JEM-EUSO

Extreme Universe Space Observatory onboard Japanese Experiment Module

Report on the Phase A Study

JEM-EUSO Collaboration

December 2008

JEM-EUSO Collaboration

JEM-EUSO is a collaborating effort of 170 members from 12 countries and 62 institutes (list updated on December 2008):

Japan: T. Ebisuzaki, H. Omori, K. Maekawa, Y. Hachisu, K. Katahira, M. Mizutani, Y. Kawasaki, Y. Takizawa, S. Wada, K. Kawai, H. Mase, K. Shinozaki, T. Ogawa (RIKEN), F. Kajino, M. Sakata, Y. Yamamoto, F. Sato, N. Ebizuka, T. Yamamoto (Konan Univ.), M. Nagano, Y. Miyazaki (Fukui Univ. of Technology), T. Shibata, N. Sakaki (Aoyama Gakuin Univ.), N. Inoue (Saitama Univ.), Y. Uchibori (National Institute of Radiological Sciences), K. Nomoto (Tokyo Univ.), Y. Takahashi (Tohoku Univ.), M. Takeda (ICRR), H. Shimizu, Y. Arai, Y. Kurihara, J. Fujimoto (KEK), S. Yoshida, K. Mase (Chiba Univ.) , Y. Mizumoto, J. Watanabe, S. Inoue, K. Asano, T. Kajino (NAOJ), H. Ikeda, M. Suzuki, H. Yano (ISAS/JAXA), T. Murakami, D. Yonetoku (Kanazawa Univ.), N. Sugiyama (Nagoya Univ.), Y. Itow (STE, Nagoya Univ.), S. Nagataki (Yukawa Institute for Theoretical Physics, Kyoto Univ.), A. Saito (Graduate School of Science, Faculty of Science, Kyoto Univ.), S. Abe, M. Nagata (Kobe Univ.), M. Chikawa (Kinki Univ.), F. Tajima (Hiroshima Univ.), M. Sato (Hokkaido Univ.)

USA: J. H. Adams, S. Mitchell, M.J. Christl, J. Watts Jr., A. English, R. Young (MSFC/NASA) , Y. Takahashi, D. Gregory, M. Bonamente, V. Connaughton, K. Pitalo, J. Hadaway, J. Geary, R. Lundquist, P. Reardon, T. Blackwell (Univ. Alabama), H. Crawford, E. Judd, C. Pennypacker (LBL, Univ. California, Berkeley), V. Andreev, K. Arisaka, D. Cline (UCLA), A. Berlind ,T. Weiler, S. Czorna (Vanderbilt Univ.), R. Chipman, S. McClain (Univ. Arizona)

France: D. Allard, J-N. Capdevielle, J. Dolbeau, Ph. Gorodetzky, J-J. Jaeger, E. Parizot, T. Patzak, D. Semikoz, J. Weisbard (APC Paris)

Germany: M. Teshima, H. Miyamoto, T. Schweizer (MPI Munich), A. Santangelo, E. Kendziorra, F. Fenu (Univ. Tübingen), P. Biermann (MPI Bonn), K. Mannheim (Wuerzburg), J. Wilms (Univ. Erlangen), T.Tajiman (LMU & MPQ)

Italy: E. Pace, M. Focardi, P. Spillantini (Univ. Firenze), V. Bratina, L. Gambicorti, A. Zuccaro (INOA/CNR Firenze), A. Anzalone, O. Catalano, G. La Rosa, M.C. Maccarone, B. Sacco (IASF-PA/INAF Palermo), G. D'Alì Staiti, D. Tegolo (Univ. Palermo), M. Casolino, M.P. De Pascale, A. Morselli, P. Picozza, R. Sparvoli (INFN and Univ. "Tor Vergata" Roma), P. Vallania (IFSI/INAF Torino), P. Galeotti, M. Bertaina, C. Vigorito (Univ. Torino), D. D'Urso, F. Guarino, F. Isgrò, S. Russo (Univ. Napoli), M. Ambrosio, C. Aramo, D. Campana, G. De Rosa, G. Osteria (INFN-Napoli), M. Ricci (INFN-Frascati)

Mexico: G. Medina-Tanco, J.C. D'Olivo, J.F. Valdés (UNAM), H. Salazar, O. Martines (BUAP), L. Villaseñor (UMSNH)

Poland: T. Batsch, B. Szabelska, J. Szabelski, T. Wibig (IPJ), T. Tymieniecka(Podlasie Univ.), Z. Wlodarczyk (Kielce Univ.), G. Siemieniec-Ozieblo (Jagiellonian Univ.)

Republic of Korea: S. Nam, I.H. Park, J. Yang, J.H. Park, T. Chung (Ehwa W. Univ.), T.W. Kim (Ajou Univ.), S.W. Kim (Yonsei Univ.), K.K. Joo (Chonnam National Univ.)

Russia: G.K. Garipov, B.A. Khrenov, P.A. Klimov, M.I. Panasyuk, I.V. Yashin (SINP MSU), D. Naumov, L. Tkachev (Dubna JINR)

Slovakia: K. Kudela, R. Bucik, R. Bobik, M. Slivka (Inst. Experimental Physics, KOSICE)

Spain: M.D. Rodriguez-Frias, L.Peral, J. Gutierrez, R. Gomez-Herrero (Univ. Alcala)

Switzerland: A. Maurissen, V. Mitev (CSEM Neuchatel)

JEM-EUSO Mission Summary

Accommodated on the Japanese Experiment Module (JEM) of the International Space Station (ISS), the Extreme Universe Space Observatory JEM-EUSO will utilize the Earth atmosphere as a giant detector of the highest energy cosmic rays, the most energetic particles coming from the Universe. Looking downward the Earth from Space, JEM-EUSO will detect such particles observing the fluorescence signal produced during their pass in the atmosphere.

The main objective of JEM-EUSO is the possibility of doing astronomy and astrophysics through the particle channel with extreme energies above 10^{20} eV, so extending, with a significant statistical evidence, the measurement of the energy spectrum of the cosmic radiation beyond the Greisen-Zatsepin-Kuzmin (GZK) cut-off. Moreover, using the atmosphere as a giant detector, JEM-EUSO could observe extremely high energy neutrinos, so opening the field of high energy neutrino astronomy. Furthermore, JEM-EUSO will contribute to the investigation of phenomena intrinsic to the Earth's atmosphere or induced by the flux of meteoroids incoming from Space.

JEM-EUSO has been designed to operate for more than 3 years onboard the International Space Station orbiting around the Earth every 90 minutes at altitude of about 400 km.

JEM-EUSO is a worldwide collaborating effort of 62 research groups from 12 countries.

Scientific Objectives

Main Objective:

Astronomy and astrophysics through particle channel with extreme energies > 10^{20} eV

- Identification of sources by the high-statistics arrival direction analysis
- Measurement of the energy spectra from individual sources to constrain acceleration or emission mechanisms

Exploratory Objectives:

- Detection of extreme energy gamma-rays
- Detection of extreme energy neutrinos
- Study of the Galactic magnetic field
- Verification of the relativity and the quantum gravity effect in extreme energy
- Global of nightglows, plasma discharges and lightning

Parameters of Instrument	
Field of View	±30°
Observational area	>1.9×10^5 km^2
Optical bandwidth	330 ÷400 nm
Focal Surface area	4.5 m^2
Number of pixels	~2.0×10^5
Pixel size	4.5 mm
Pixel size at ground and spatial resolution	750 m 0.1°
Event time sampling	≤ 2.5 μs
Duty cycle	~20%

Parameters of Mission	
Time of launch	year 2013
Operation period	3 years (+ 2 years)
Launching rocket	H2B
Transportation to ISS, international Space Station	non pressurized Carrier of H2 Transfer Vehicle HTV
Site to attach	Japanese Exposure Module JEM/ Exposure Facility EF#2
Mass	1983 kg
Power	926 W (operative), 352 W (non-operative)
Data transfer rate	285 kpbs
Orbit: height , inclination	~ 400 km, 51.64°

Table of contents

Foreword

The "Extreme Universe Space Observatory – EUSO" is the first Space Mission devoted to the exploration of the outermost bounds of the Universe through the detection of the ultra high energy ($E > 10^{20}$ eV) cosmic rays and neutrinos; it will do astronomy looking downward from the International Space Station, ISS, and using the Earth atmosphere as a giant detector.

Firstly proposed as a free-flyer, the observatory was selected by the European Space Agency (ESA) as a mission attached to the Columbus module of the ISS. The phase-A study for the feasibility of that observatory (hereafter named ESA-EUSO) was successfully completed in July 2004. Nevertheless, because of financial problems in ESA and European countries, the green-light to start the ESA-EUSO phase-B was postponed for a long time.

In 2006, Japanese and U.S. teams redefined the mission as an observatory attached to the Japanese Experiment Module/Exposure Facility (JEM/EF) of the International Space Station. They renamed it as JEM-EUSO and started with a renewed two-year-long Phase A study, targeting the launch of 2013 in the framework of the second phase of JEM/EF utilization.

This report, somewhere indicated as "the Purple Book", summarizes the JEM-EUSO Phase-A study as carried out and completed, during the year 2008, by the JEM-EUSO Collaboration.

The document is the result of the collective effort of many members of the collaboration; this is reflected in the "mosaic" of writing styles which, in spite of the best efforts of the editorial team, emerges throughout the report. The content of the main chapters has been under the responsibility of the JEM-EUSO working groups, members of which in turn represent a much larger number of scientists and technicians that would be too long to list here.

The Editorial Team

Toshikazu Ebisuzaki

Maria Concetta Maccarone

Hiroshi Mase

1. Mission Overview

JEM-EUSO (Extreme Universe Space Observatory on Japanese Experiment Module) is a new type of observatory that uses the whole Earth as a detector including the International Space Station (ISS) where a remote sensor is accommodated. It observes transient luminous phenomena taking place in the Earth atmosphere caused by particles and waves coming from Space. The sensor is a super wide-field telescope that detects particles with energy above 10^{20} eV. This remote-sensing instrument orbits around the Earth every ~90 minutes on board of the International Space Station at the altitude of ~400 km. An extremely high energy particle (EECR) collides with a nucleus in the Earth atmosphere and produces an Extensive Air Shower (EAS) that consists of numerous electrons, positrons, and photons. JEM-EUSO captures the moving track of the fluorescent Ultra Violet (UV) photons, as sketched in Fig.1-1, and reproduces the calorimetric development of the EAS.

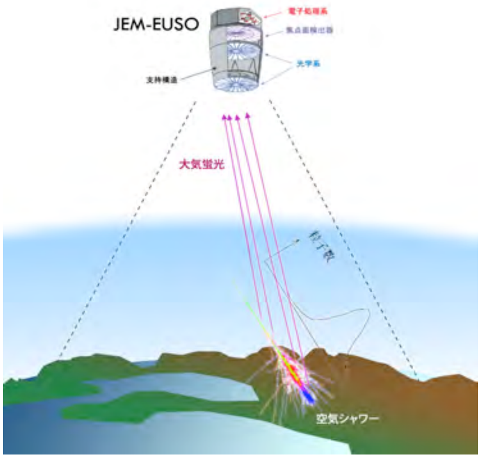

Figure 1-1. *Principle of the JEM-EUSO telescope to detect extremely high energy particles.*

The JEM-EUSO telescope has a super-wide (±30°) Field-of-View (FoV) with optics composed by Fresnel lenses; the telescope records the track of an EAS with a time resolution of 2.5 μs and a spatial resolution of about 0.75 km (corresponding to 0.1°). These time-segmented images allow determining energy and direction of the primary particles. The focal surface of the JEM-EUSO telescope is formed by about 6,000 multi-anode photomultipliers; the number of pixels is of the order of two hundred thousand.

A first EUSO observatory was originally selected by the European Space Agency (ESA) as a mission attached to the European Columbus module of the ISS. The ESA-EUSO phase-A study was successfully completed in July 2004 under ESA. However, because of financial problems in ESA and European countries, the start of phase-B was postponed for a long time. Japanese and U.S. teams re-defined EUSO as a mission attached to the Japanese Experiment Module/ Exposure Facility (JEM/EF) of ISS. They renamed it as JEM-EUSO and started the preparation targeting the launch of 2013 in the framework of the second phase utilization of JEM/EF utilization.

With respect to the first design, JEM-EUSO reduces the threshold energy down to ~10^{19} eV and increases the effective area by means of advances in technology and taking advantage of specific features of the JEM/EF module. The reduction in the threshold energy is realized thanks to new lens material and improved optical design, detectors with higher quantum efficiency, and improved algorithm for event trigger. The increase in effective area is realized by inclining the telescope from nadir (Fig.1-2); under this so-called "tilted mode", the threshold energy gets higher since the mean distance to EAS and atmospheric absorption both increase. First half of the mission lifetime will be devoted to observe lower energy region in "nadir mode" and second half of the mission to observe high energy region by "tilted mode".

Figure 1-2. *Artistic illustration of the JEM-EUSO telescope attached to the Japanese Experiment Module of the International Space Station, under nadir (left) and tilt (right) mode of observation.*

The JEM-EUSO telescope can reconstruct the incoming direction of the EECRs with accuracy better than few degrees. Its observational aperture of the ground area is a circle with 250 km radius, and its atmospheric volume above it, with a 60° FoV, is ~1 Tera-ton or more. The target volume for upward neutrino events exceeds 10 Tera-tons. The instantaneous aperture of JEM-EUSO is larger than the Pierre Auger Southern Observatory by a factor ranging from 65 to 280, depending on its observation mode (nadir or tilted, Fig.1-3).

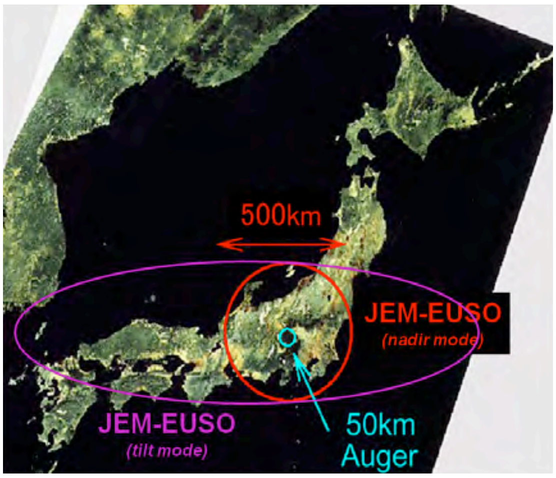

Figure 1-2. *Area observed by the JEM-EUSO telescope in one shot under "nadir" and "tilt" observation mode.*

JEM-EUSO, planned to be attached to JEM/EF of ISS, will be launched in 2013 by H2B rocket and conveyed to ISS by HTV (H-II transfer Vehicle).

2. Science Objectives

JEM-EUSO is intended to address basic problems of fundamental physics and high energy astrophysics investigating the nature and origin of the Extreme Energy Cosmic Rays, EECRs, which constitute the most energetic component ($E>5\times10^{19}$ eV) of the cosmic radiation. JEM-EUSO will pioneer the investigation from Space of EECR-induced Extensive Air Showers (EASs), making accurate measurements of the primary energy, arrival direction and composition of EECRs, using a target volume far greater than is possible from the ground. Such data will shed light on the origin of the EECRs, on the sources that are producing them, on the propagation environment from the source to the Earth and, possibly, on the particle physics mechanism at energies well beyond the ones achievable in man-made accelerators. Moreover, exploratory objectives as the detection of extreme energy neutrinos and gamma rays, the verification of the relativity and quantum gravity effect at extreme energy, and the systematic surveillance of atmospheric phenomena, complete the scenario of the JEM-EUSO science goals.

2.1. Main Objective: Astronomy and Astrophysics through the Particle Channel

The Cosmic Radiation can be considered as the “Particle” channel complementing the “Electromagnetic” one, proper of the conventional astronomy: main objective of JEM-EUSO is to initiate a new field of astronomy and astrophysics that uses the extreme energies particle channel (10^{19} eV < E < 10^{21} eV). JEM-EUSO is planned to detect more than one thousand events with energy above 7×10^{19} eV in its five years operation. Such a number of events exceeds the critical quantity to observe all the sources at least once inside several hundred Mpc and makes possible the following targets:

- Identification of sources by the high-statistics arrival direction analysis;
- Measurement of the energy spectra from individual sources to constrain acceleration or emission mechanisms.

The energy spectrum of charged particles (cosmic rays) reaching the Earth from Space is well expressed by a power law function of $\sim E^{-3}$ over eleven orders of magnitude (from 10^9 eV to 10^{20} eV; (Fig.2.1-1). The highest energy particles that we are concerned here correspond to the highest end of the spectrum with energies around 10^{20} eV. Gigantic accelerators must exist somewhere in the Universe: their acceleration energy is eight orders of magnitudes higher than those of most advanced ever man-made accelerators.

The discussion on where the break of this power law spectrum is, can be traced back to 40 years ago, which is just after the discovery of the microwave cosmic background. Penzias and Wilson [1] reported the discovery of the cosmic 2.7 K thermal black body radiation which was produced very early in the history of the Universe and which led to the undisputed acceptance of the “Big Bang” theory on the origin of the Universe. The perfect thermal character and smoothness of the CMB (Cosmic Microwave Background) proved conclusively that this radiation is indeed cosmological and that, at the present time, it fills the entire Universe with a 2.7 K spectrum of radio to far-infrared photons with a density of ~400 cm^{-3}. Shortly after the discovery of the CMB, Greisen [2] and Zatsepin & Kuz’min [3] independently predicted that pion-producing interactions of extreme energy protons with CMB photons should produce a cutoff at $\sim5\times10^{19}$eV. Since then, this predicted effect is known as the GZK (Greisen-Zatsepin-Kuz'min) effect. For protons, this occurs when the pion production threshold is reached. The reaction,

$$p+\gamma_{2.7\mathrm{K}} \rightarrow \Delta^{+} \rightarrow p+\pi^{0}, n+\pi^{+} \qquad (2\text{-}1)$$

slows down the proton and leads to an effective attenuation length of 50 Mpc for a proton of 10^{20}eV. The length of 50 Mpc is about the size of the Virgo Cluster to which our Galaxy belongs, and is just a small fraction of the total size of the Universe.

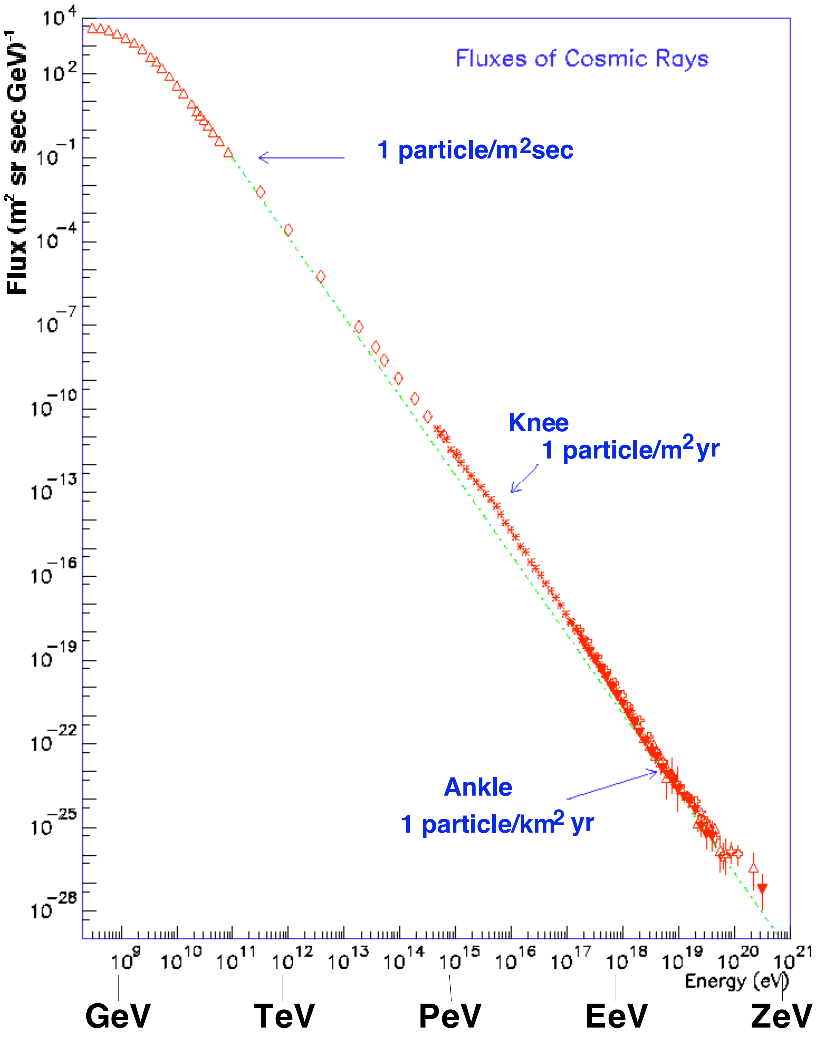

Figure 2.1-1. *Energy spectrum of cosmic rays. The flux is well expressed by a power-law proportional to* $\sim E^{-3}$ *over eleven orders of magnitude from* 10^9 *eV up to* 10^{20} *eV.*

On the other hand, a spectral steeping can be also explained by the acceleration limit in the case of bottom-up scenario. The highest energy of the particles is determined by the product of the size and the strength of the magnetic field (Fig.2.1-2). The celestial objects that satisfy the condition for acceleration up to 10^{20} eV are neutron stars with a super strong magnetic field (greater than 10^{12}–10^{13} G), jets of the active galactic nuclei (AGNs), gamma-ray bursts (GRB), radio galaxies, and clusters of galaxies. Since these sources are all lined up along the theoretical upper-limit to the energy of 10^{20} eV (as schematized by the Hillas plot, Fig.2.1-2), it is likely that the spectrum of extreme energy particles shows an acceleration limit around 10^{20} eV in addition to the trans-GZK complex. If an acceleration limit is not seen in the spectrum, it is strongly suggested that new unknown astronomical objects located in the blank region (upper-right corner) of the Hillas diagram should exist. There is no theoretical reason of the absence of such objects.

In the case of top-down scenario, EECRs are produced by a decay or annihilation of a Super-Heavy Particle (SHP: *m* ~10^{22}—10^{25} eV/c^2). The end products of this process are well studied: neutrinos and gamma rays are abundant compared with nucleons, by a factor or two of three [4, 5]. The energy spectrum is as hard as $E^{1.9}$ [6, 7, 8, 9].

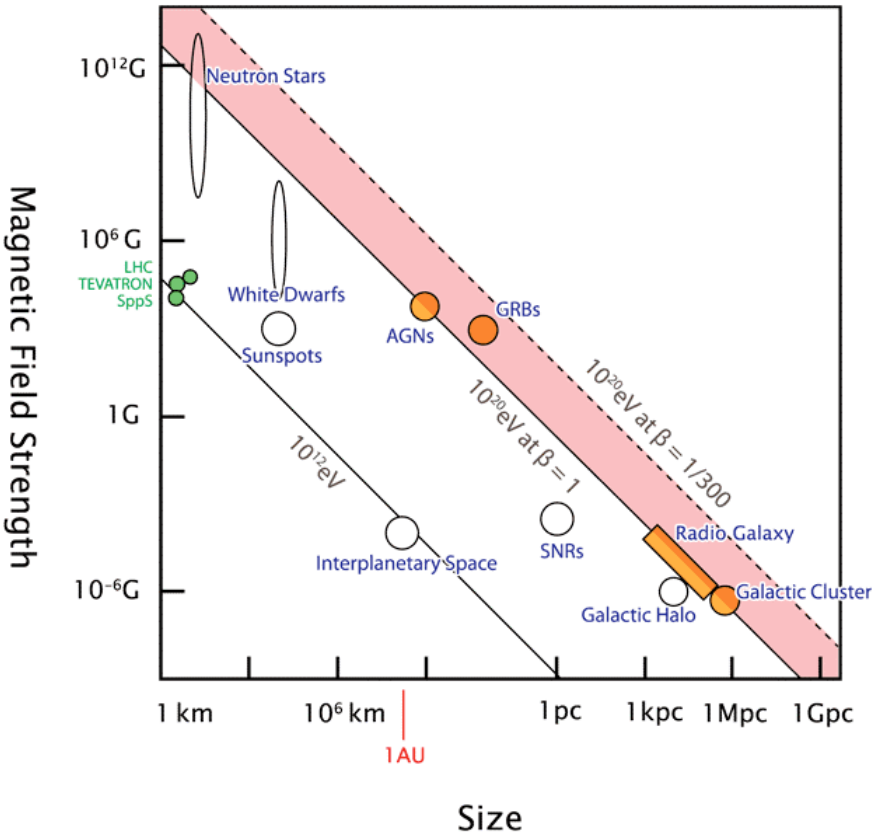

Figure 2.1-2. *Hillas diagram showing theoretical upper limits on the energy of the particle determined by the size and strength of magnetic field on the celestial objects.*

2.1.1. Identification of sources by the high-statistics arrival direction analysis

JEM-EUSO is designed to identify the origins of EECRs by the high-statistics arrival direction analysis. The extreme energy particles are not deflected by the magnetic field more than one degree (in the case of proton) and one can trace back to their origin in the measured arrival directions with accuracy better than a few degrees. The arrival direction analysis is divided in two steps: point source and global anisotropy analysis.

The point source analysis seeks small-scale clusters at the accuracy level of the instrument. In fact, AGASA experiment [14] reported small-scale anisotropy (cluster; Fig.2.1.1-1) and some correlation in the arrival direction of EECRs with AGNs (blazers). HiRes experiment [15] also indicated such a cross-correlation with AGNs. Furthermore, the Pierre Auger Southern Observatory reported a correlation between the arrival direction of the EECR events above 6×10^{19} eV and the distribution of nearby AGNs [16; Fig.2.1.1-2], though it does not reject the possibility of GRBs as the sources of EECRs: the distribution of AGN is known to have a similar behaviour to that of the matter distribution in general. If this report of the Pierre Auger Observatory is in the case, JEM-EUSO with much higher statistics will identify several dozen sources which several dozen events belong to, and will allow us to associate them to known astronomical objects

(Fig.2.1.1-3). In other words, we will know the distances to the individual sources; this makes spectral analysis much clearer than the current situation, as discussed in the next sections.

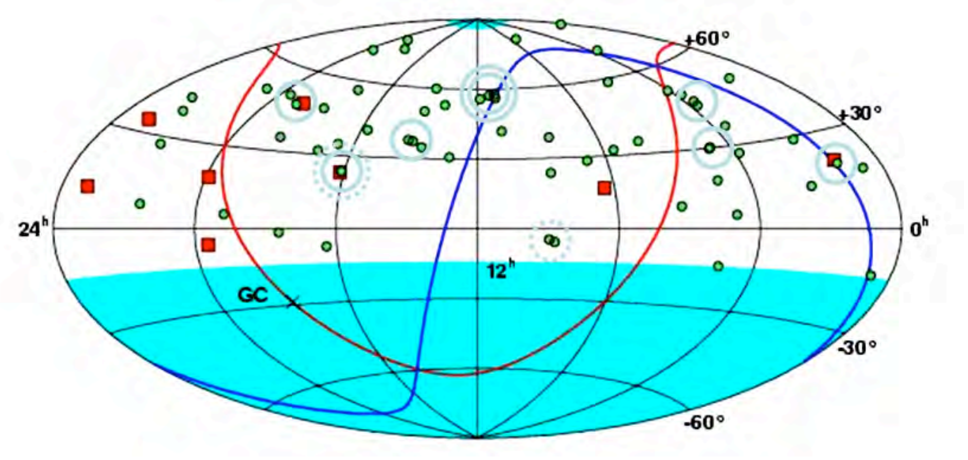

Figure 2.1.1-1. *Distribution of arrival direction of extreme energy particles by AGASA experiment [14]. Red squares and green circles denote the events above $E > 10^{20}$ eV and those with $E = (4\div10)\times10^{19}$ eV, respectively.*

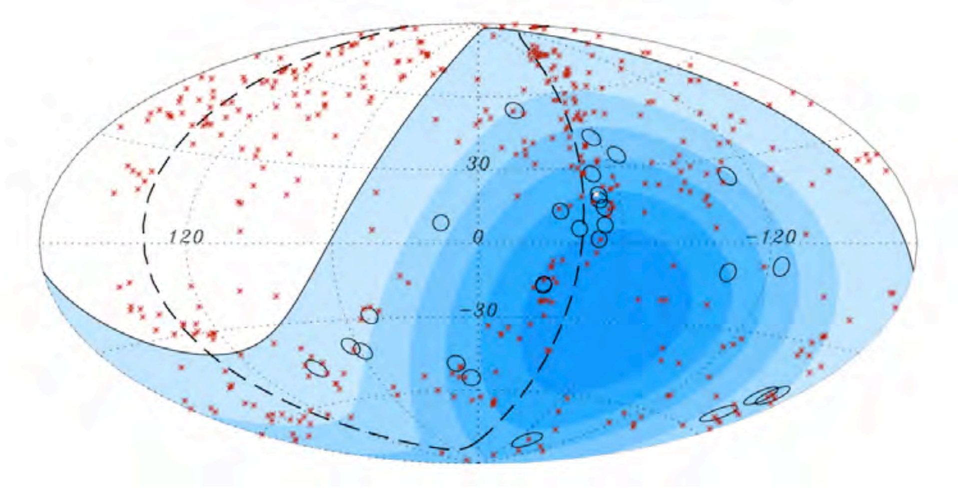

Figure 2.1.1-2. *Distribution of the arrival directions (galactic coordinates) of the events above 5.7×10^{19}eV (open circle) by the southern site of the Pierre Auger Observatory. The directions of nearby AGN within 71Mpc distance are shown by crosses [16].*

In a global anisotropy analysis, arrival directions are integrated for spherical harmonics which should reveal the source distribution of extreme energy particles. For the best analysis, the exposure must be uniform over the whole sky. ISS has an inclination of 51.6°, and onboard JEM-EUSO can equally observe both north and south sky and would offer a nearly uniform exposure for all over the entire celestial sphere.

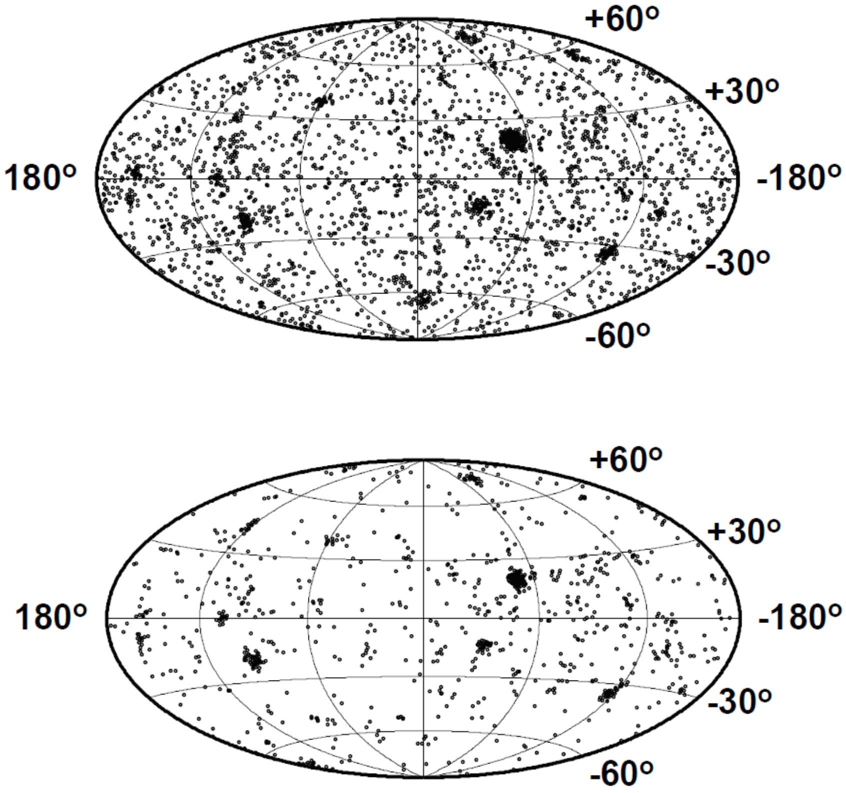

Figure 2.1.1-3. *Numerically simulated arrival direction distribution of EECRs if AGNs are the sources of EECRs[17]. Here, we assume that 42 AGNs are sources of EECRs and their particle luminosity is proportional to X-ray luminosity observed by INTEGRAL. Upper and lower diagrams correspond to the sky maps expected to be observed by JEM-EUSO for* $E>5\times10^{19}$*eV (3000 events) and for* $E>7\times10^{19}$*eV (1000 events).*

If the extreme energy particles come from cosmological distances as those of GRBs and AGNs, several dozen sources uniformly distributed in the sky will be discovered. If the sources belong to the Milky Way Galaxy, their distribution would show an enhancement in the direction of Sagittarius; if they belong to clusters of galaxies, the enhancement should appear in the directions of Virgo, Pisces, Perseus, and Hercules [19].

On the other hand, in the top-down scenario, SHPs are certainly Cold Dark Matter (CDM) that are supposed to broadly be distributed with an enhancement toward the galactic center that can also produce extreme energy particles. If the source of extreme energy particles is such a SHP dark matter, it could be concentrated in our Milky Way Galaxy and might show an enhancement in the direction of Sagittarius [20,21,22], and small clumps can be seen in the outer region [10,11,12,13].

In the Z-burst model [23, 24], which follows the standard model of the particle physics, a high energy neutrino/anti-neutrino annihilates with a relic anti-neutrino/neutrino in the galactic halo to produce charged extreme energy particles. The annihilation of a neutrino pair produces about 20 gamma rays and about 2 nucleons on average; if the annihilation takes place in nearby clusters of galaxies, daughter nucleons may arrive to the Earth without GZK loss. On the other hand, gamma rays are hardly observed, since their mean free paths are much shorter (100 kpc ÷ 1 Mpc) than the distances to the nearby clusters. If the sources of extreme energy neutrino/anti-neutrinos come from point sources, resultant charged particles show small-angle anisotropy. If the neutrino mass is heavy enough, the arrival direction of the resultant charged particles shows an enhancement towards the center of the galaxy or nearby clusters of galaxies [25]. This is recognized as the unique method to detect Cosmic Neutrino Background (CNB), which is originated from the very early Universe just one second after the Big Bang. With the information carried by CNB, one can trace back 400 thousand years before the cosmic microwave background epoch in hydrogen atoms were formed from plasma. CNB is the last undetected important component of the relic of the Big Bang. In such a way, JEM-EUSO explores the Z-burst model and aim at the detection of CNB. If the detection of neutrinos is achieved, then the key discriminator of models is if such neutrinos are abundant from the direction of super-cluster. This kind of neutrino anisotropy measurement will give a constraint on Z-burst model and give us a chance to estimate the absolute mass of neutrinos.

Such a complete arrival direction analysis can be done only with JEM-EUSO. For example, the Pierre Auger Observatory has some difficulties to make a comprehensive analysis of the arrival direction due to relatively low statistics. Since the aperture of the Auger observatory is 20 times smaller than that of JEM-EUSO, the statistics of EECR events is also significantly limited and is less than 100 events above 10^{20}eV even after 10 years operation. In addition, the Auger experiment operated in the Southern hemisphere suffers from the very strong galactic magnetic fields in the southern sky dominated by the galactic center and galactic plane. If one uses lower energy events, for example, at 4×10^{19} eV, the deflection by the galactic magnetic field (~5 times stronger) is as large as 10 degrees. That is enough to erase possible signatures of any small angle anisotropy. Furthermore, most of the southern sky is covered by zone of avoidance for which optical observations are difficult in optical wavelength. It makes very difficult to perform correlation analysis to AGNs.

2.1.2. Measurements of the energy spectra from individual sources

Many experiments, such as AGASA, HiRes, and Auger have been designed to confirm the theoretical prediction of spectral steeping by GZK process. Figure 2.1.2-1 summarizes their results [26]. HiRes [27] and Auger [28] argued that there is a spectral steeping around 6×10^{19} eV; but this steeping can be caused by the acceleration limit as well as the GZK process. However, the two effects can be separated by comparison with the energy spectra of spatially separated sources identified as known astronomical objects.

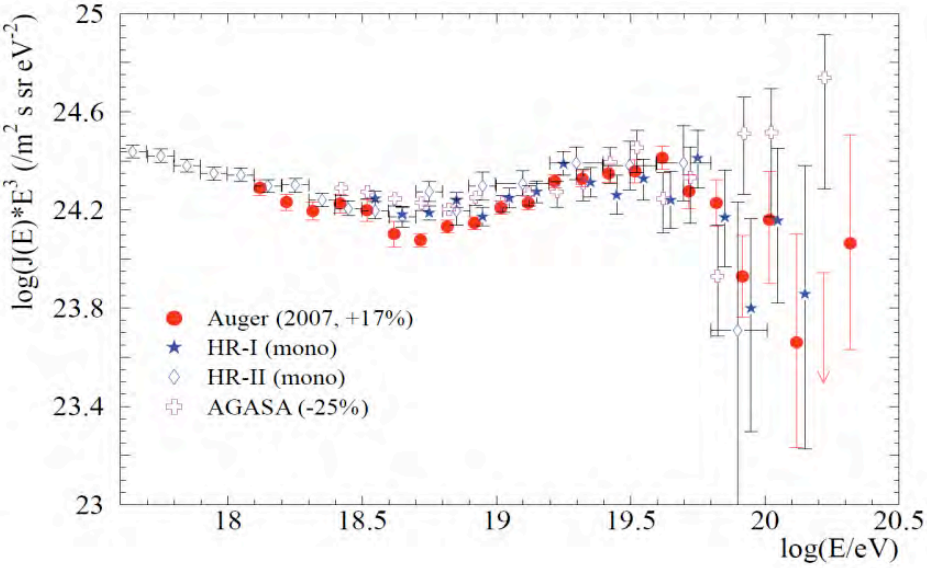

Figure 2.1.2-1. *Energy spectra of EECRs observed by Auger, HiRes, and AGASA [26]. Here, the energy scale is shifted by +17% for Auger, and by –25% for AGASA. The vertical axis is multiplied by* E^3.

Figure 2.1.2-2 shows the energy spectrum expected from the sources at different distances from the Earth. The GZK features are not prominent in the sources within 10 Mpc. In other words, we can get a direct clue to understand acceleration mechanisms by the comparison with the spectral properties of these nearby sources and the other observational facts of the identified sources in different energy bands. On the other hand, GZK features are dominantly prominent in the energy spectra from sources distant more than 50 Mpc, if GZK process is in the case [29]. When we see the spectrum breaks correlated with distance of identified objects, as expected by the GZK mechanism from these relatively distant sources, we can firmly conclude that the break is due to the GZK mechanism, and the Lorentz invariance is verified in the very high value of the Lorenz factor greater than 10^{11}.

Once it is experimentally verified, the absolute energy scale calibration is feasible by comparing the observed features of energy spectra. Note that the reported energy spectra are significantly different in energy scale. The avail of the absolute energy calibration will be breakthrough of great importance in study of the extreme energy universe. In addition to that, if a strong source lies around or outside of the GZK horizon, all of the GZK features, including GZK recovery, would be observed. It allows us to construct the firm theory of the trans-GZK complex and the acceleration limit. The comparison between theoretical and observed spectra gives us the absolute energy calibration in this energy region. This is a real breakthrough to understand the origin of high energy cosmic rays with $E>10^{15}$ eV, and to explore the extreme Universe and fundamental physics.

Furthermore, the acceleration limit is much higher than 10^{20} eV: it suggests some unknown objects (ones not in the Hillas diagram) accelerating particles or new acceleration mechanisms in bottom-up or top-down scenario.

If several sources are found with at least dozens of observed EECR events which are also identified with already known astrophysical object, the differences in spectral features among those sources will provide direct clues of understanding the particle acceleration mechanism with multi-wavelength observation. The reachable energy of the particles acceleration may differ source by source. If there are several intense sources within 50 Mpc vicinity or GZK horizon, the energy spectrum does not show GZK cutoff (see the following subsection) and the spectral cutoff appears at the energy limit of acceleration. Different from GZK effect, the energy spectrum does not recover at the highest energy end.

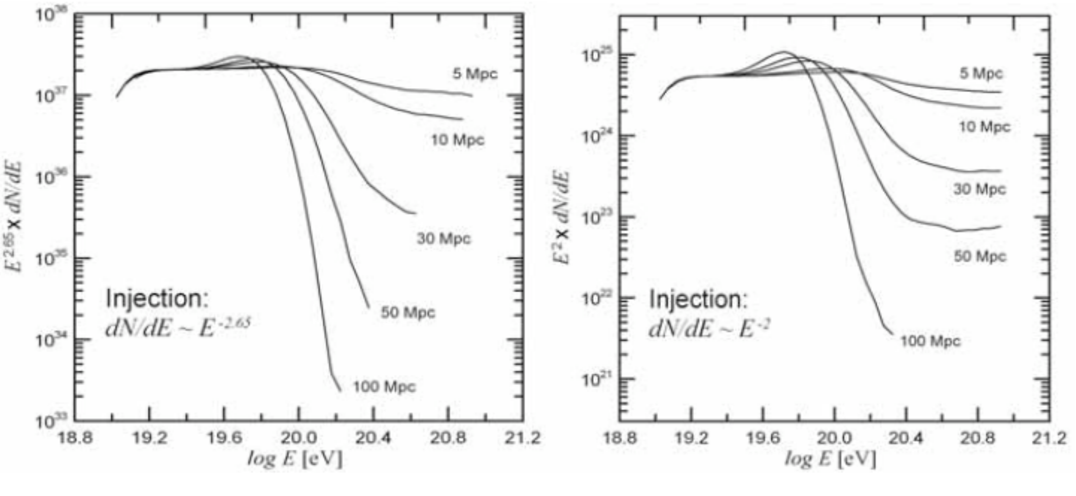

Figure 2.1.2-2. *GZK features strongly depend on the distances to the sources. Left: in the case the intrinsic spectral index is* $E^{-2.65}$. *Right: in the case the intrinsic spectral index is* E^{-2}.

Concerning the GZK energy spectrum, Stecker [31] and Berezinsky [30; Fig.2.1.2-3] independently calculated the mean energy loss time for protons propagating through the CMB in the intergalactic space as a function of energy. According to them, GZK process is responsible for the trans-GZK complex in the energy spectrum, which consists of:

1) Steepening spectral slope at $(5\div10)\times10^{19}$ eV, the so-called GZK cutoff.
2) GZK bump at $(4\div8)\times10^{19}$ eV. It is formed by particles arriving from distances of several or several dozen D_{GZK}, which lose energy on their path. The observed spectrum of such particles results from accumulation around GZK cut off energy.
3) Ankle region feature around $(0.3\div3)\times10^{19}$ eV. Highly red-shifted GZK bump made by particles coming from cosmological distances.
4) GZK recovery, that arises above 3×10^{20} eV. It consists of particles produced at distances smaller than D_{GZK}.

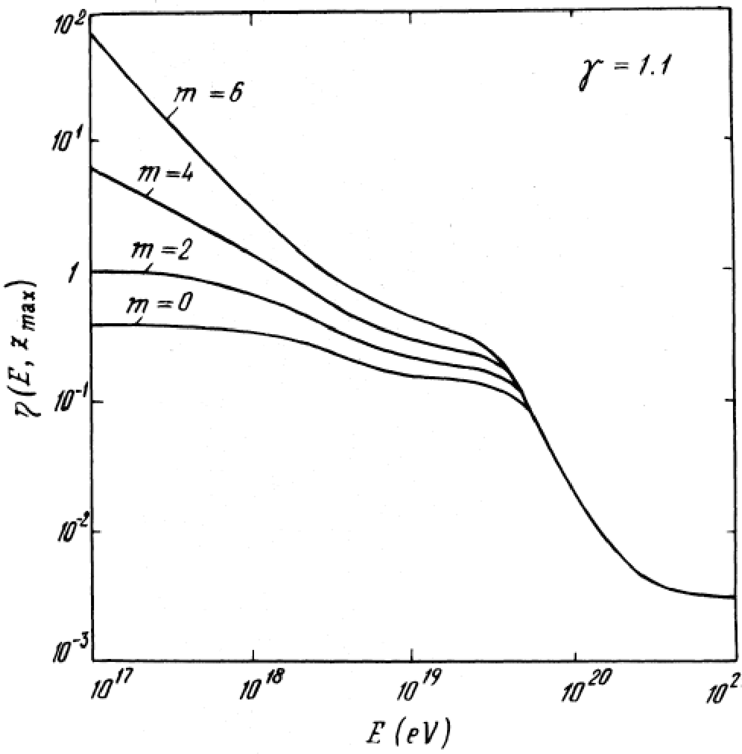

Figure 2.1.2-3. *Theoretically predicted modification function, η, of the extreme energy particles spectrum due to the effect of propagation through the Space. Here, m is a parameter that represents the degree of evolution of the primary source. The energy spectrum is the product of η with the intrinsic spectrum before propagation [30].*

The trans-GZK complex, as a whole, reflects the history of the Universe. The aspect of red-shifted GZK dump and ankle much depend on the cosmological evolution of the particle accelerating objects. Comparing the density of AGNs or the rate of GRBs, the information on the formation of astrophysical objects in Universe will be extracted. JEM-EUSO will figure out this complex by determining (1), (2), and (4) of the trans-GZK complex with much more statistics than any existing ground-based experiment. These three features give us the absolute energy calibration for the fluorescence method. The detailed comparison with the results of ground-based observatories allows us to overlap the energy spectra above the ankle region.

Here we have considered just the GZK effect and spectral modification from steady EECR sources; however, it shall be also discussed the case of transient EECR sources. If the major sources of EECRs are transient and the time scale of the emission of EECRs is shorter than the energy dependent time lag due to the propagation in the magnetized universe, the drastic change of the spectrum can be expected like a discussion by E. Waxman, i.e., the energy spectrum becomes mono energy (peak energy simply depends on the distance and the age of the explosion). With GZK effect, the resultant spectra and time evolution from the single source may become very complicated. So far there are no such dynamic calculations including the GZK effect on EECRs from transient sources. Of course, the secondary neutrino may show a very interesting energy-time development.

Ground-based observatories, such as the Pierre Auger and the Telescope Array, have major problems to perform the analysis described above. Besides the limited statistics, the Pierre Auger observatory, which uses water tanks with a stronger sensitivity to muons than electromagnetic components as ground particle detectors, suffers from a systematic error of several tens percent. This is caused by model dependence on muon production in the first collision between the extreme energy particle and the nucleus in the atmosphere, and by statistical fluctuations. The shape of the energy spectrum easily changes depending on the treatment of the muon production models. Locating in the Southern Hemisphere, the effect of deflection on EECR is larger due to the presence of the Galactic centre. The optical observation of extragalactic objects is also severely limited due to zone of avoidance, in which the Galactic gases absorb the light. Therefore, there is potential difficulty in studying cross-correlation between arrival directions of EECRs and locations of AGNs.

In case of the Telescope Array experiment, the feasible exposure by ten years operation is about 10 times of that of AGASA. Only few dozen of extreme energy events above 10^{20} eV are expected, which limits detailed discussions on their origin. Nevertheless, the Telescope Array experiment, using scintillators as its surface detectors, is relatively free from the problems of the interaction model dependence: this may provide the firm result of the energy spectrum. Against the Pierre Auger Observatory, it is located in Northern Hemisphere and hence the effect of the galactic magnetic field is moderate. This is a merit and in particular, the existence of the small angle clusters, transferring the heritages of AGASA, plays a role of guidepost for JEM-EUSO.

The observation from ground still suffers from one more problem. In the energy region above 3×10^{20} eV, EAS develop in a quite different way in the dense atmosphere near ground due to the Landau-Pomeranchuk-Migdal (LPM) effect [32,33]. Conventional energy determination method cannot be applied to EAS affected by such LPM showers. Even with ground-based fluorescence telescopes, it is difficult to determine energy with a high accuracy. For extreme energy events in most cases, they detect far distant and low elevation showers with relatively poor qualities.

Apart from the large aperture, the merit of JEM-EUSO is relatively free from the problems which ground-based experiments have. Fluorescence telescopes, including JEM-EUSO, measures the electromagnetic component that carries 90% of the energy of EAS. Observing from Space, JEM-EUSO telescope may capture EASs that develop at high altitudes (above 20 km) where the LPM effect does not work due to the low atmospheric density. Achieving high accuracy in energy determination and high statistics allow us to reveal the mystery of origin and propagation of the extreme energy particles; these expected scientific outcomes will initiate the new astronomy through the particle channel, which only JEM-EUSO is able to do.

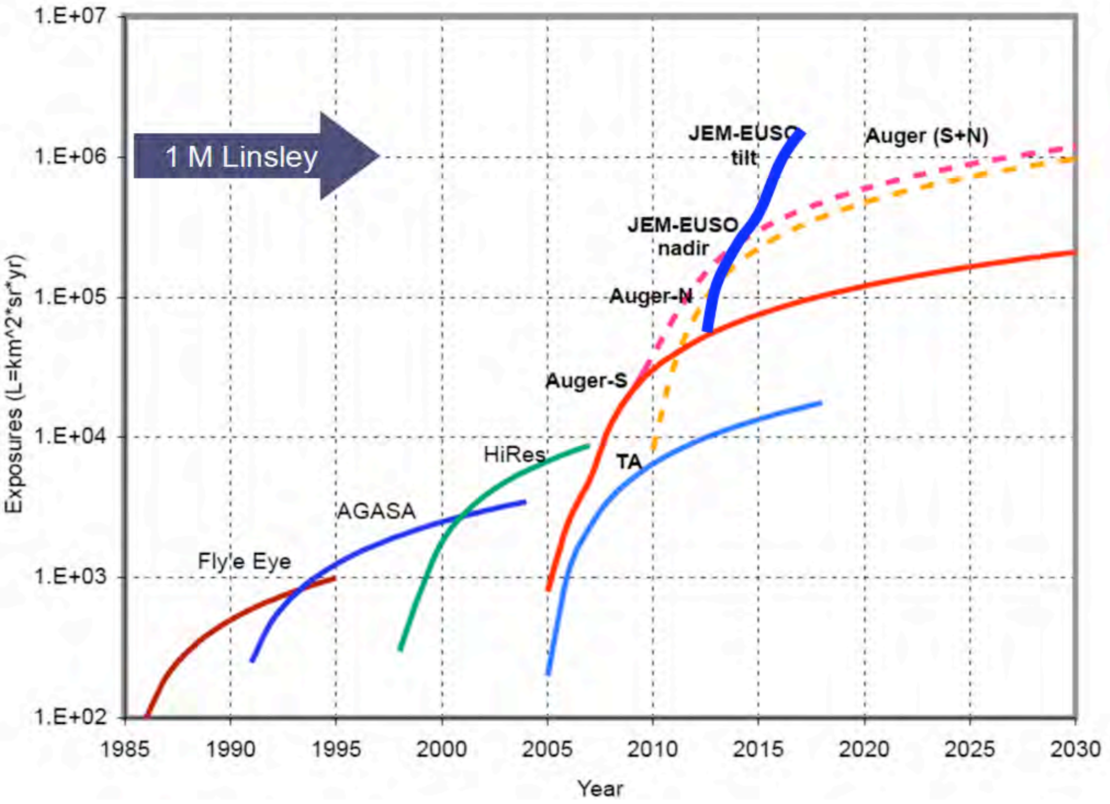

Figure 2.1.2-4. *Expected cumulative exposure, in Linsley units, of JEM-EUSO (thick blue curve). For comparison, the evolution of exposure by other retired and running EECR observatories is shown.(1 Linsley = 1 km^2· sr· year).*

2.2. Exploratory Objectives

2.2.1. Detection of extreme energy gamma rays

The air showers produced by gamma rays can be distinguished from those by nucleons and nuclei through the value of $X_{\max}$, the slant depth of shower maximum. Gamma rays with energy above 5×10^{19} eV collide in the deeper atmosphere since their collision cross section significantly shrinks due to the LPM effect; in other words, $X_{\max}$ of the gamma rays significantly increases with energy. On the other hand, gamma rays above 5×10^{19} eV interact with the geomagnetic field at the altitude of ~1,000 km from ground and produce positron-electron pairs. The electromagnetic shower including several hundred synchrotron photons has been already developed before it reaches the upper atmosphere; this process makes $X_{\max}$ smaller. Since the threshold energy of such interaction is determined by the strength of the geomagnetic field perpendicular to the direction of the particle, strong north-south effect appears in $X_{\max}$ distribution at certain energy; the gamma rays from the direction of the poles have a smaller probability for pair-creation and show larger $X_{\max}$ [34]. Figure 2.2.1-1 shows the probability of gamma rays to interact with geomagnetic field in various point of the earth [35].

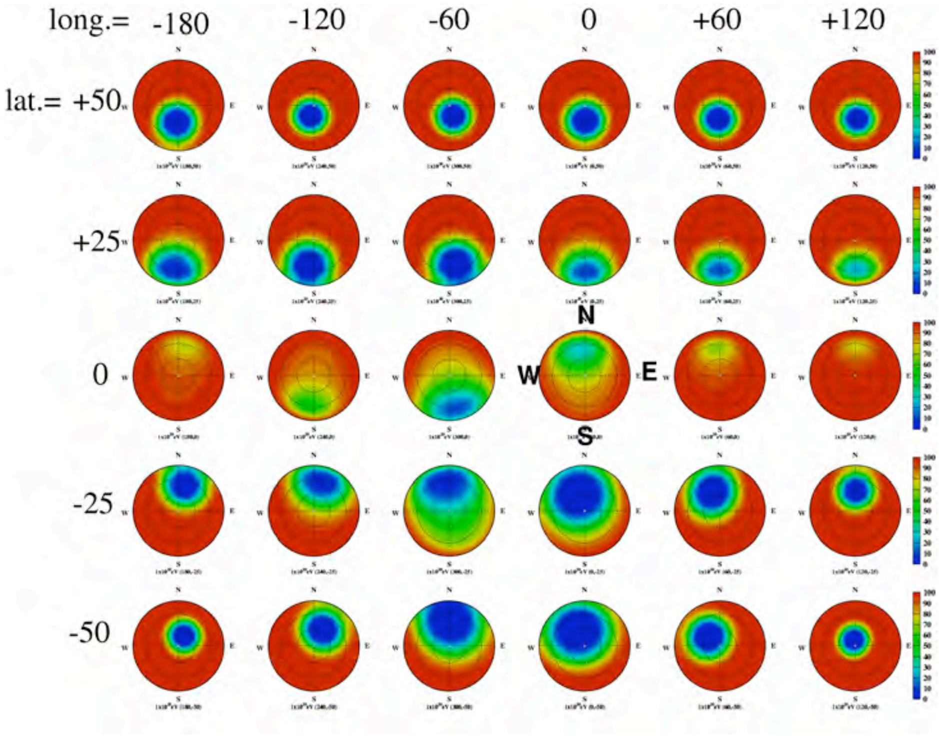

Figure 2.2.1-1. *Angular dependence of the probability of the extreme energy gamma rays interacting with the geomagnetic field [35]. Each panel shows horizontal coordinates at the different longitude and latitude on the Earth. From the bluer patches of the sky, extreme energy gamma rays are more likely to initiate an EAS with large X_{max} due to the LPM effect.*

Extreme energy gamma rays tend to produce an EAS that develop significantly slowly compared with the case of proton primaries. JEM-EUSO is capable of detecting more than 3000 (1000) events above 5×10^{19}eV (7×10^{19}eV), which enable to determine the flux of gamma ray primaries at high accuracy.

The flux of gamma rays in extreme energy is a key parameter to discriminate origin models. Figure 2.2.1-2 shows the sensitivity of gamma rays by five years operation of the JEM-EUSO Mission. The Pierre Auger Observatory recently reported the upper limit on gamma ray flux as a few percent of EECR flux above 10^{19} eV. Under null gamma ray assumption, JEM-EUSO is capable of putting more stringent upper limit by an order of magnitude at overlapping energies. To give the constraint on origin models or their parameters, the gamma ray flux above 10^{20} eV is essential and is extracted by the five years operation of JEM-EUSO.

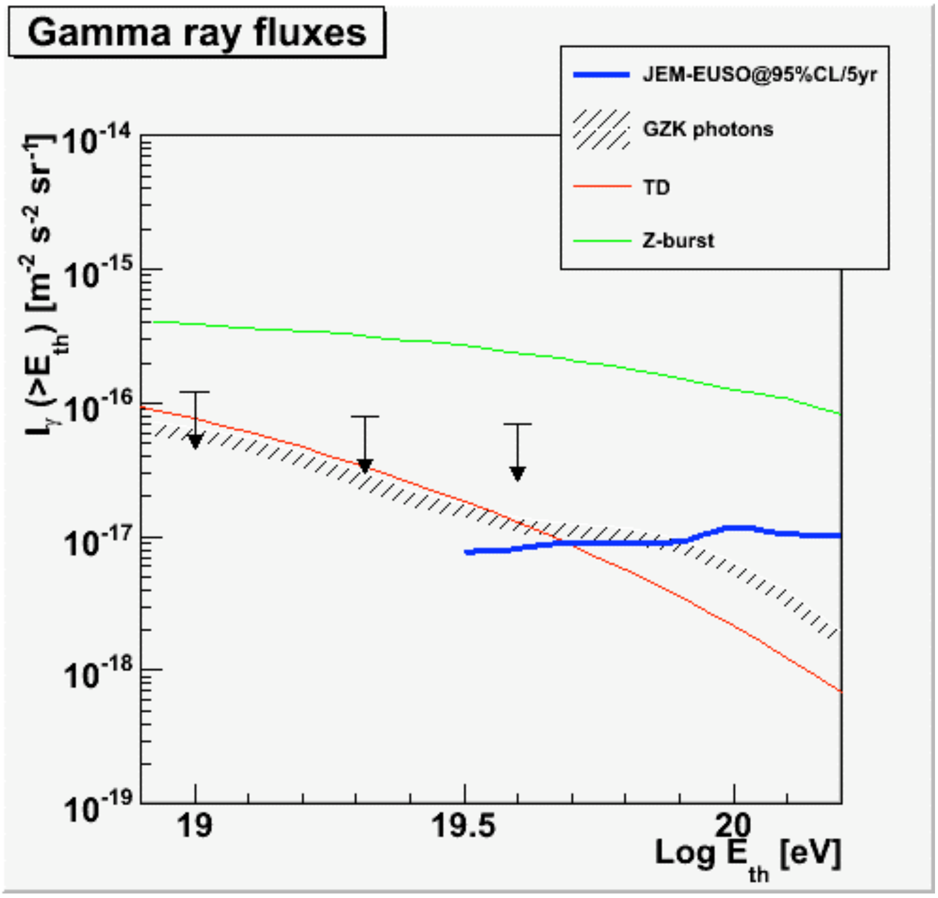

Figure 2.2.1-2. *Sensitivity of gamma rays by five years operation of JEM-EUSO Mission. The blue curve indicates the expected upper limit of gamma ray flux at 95% confidence level (CL) under a null gamma ray assumption. The arrows are the upper limits at the same CL given by Pierre Auger Observatory [36]. Green, red and shaded curves show the theoretical prediction by Z-burst [37], Topological Defect (TD) [38] and GZK photon [38] models, respectively.*

Extreme energy gamma rays create electron-positron pairs due to the CMB photons or infrared background photons and therefore they are restricted to propagate large distances (Fig.2.2.1-3). As energy increases, the off-shell component overwhelms this restriction and the Universe gets more transparent against electromagnetic component; this effect is shown in Fig.2.2.1-4: above 10^{20} eV, gamma ray detection is expected and therefore large-scale experiment is desired.

Figure 2.2.1-3. *Propagation distance of electromagnetic component in the Universe [40,41]. At higher energies, the pair creation process is suppressed by quantum gravity effect and the propagation distance sharply increases. This enables to observe the deep universe by electromagnetic component.*

Figure 2.2.1-4. *Mean free path of gamma rays through propagation in CMB photons as a function of energy [39]. Around* 10^{13} *eV, the mean free path is sharply shortened as energy increase. Below* 10^{14} *eV, the gamma rays interact with radio background and CMB photons. Curves a, b and c demonstrates the effect by different assumed infrared background flux Curves 1, 2 and 3 show the case of cutoff frequency of extragalactic radio backgrounds of 5, 2 and 1 MHz, respectively. The curve marked with small triangles indicates the case of lower limit of radio background flux.*

2.2.2. Detection of extreme energy neutrinos

Cosmogenic neutrinos may steadily be produced in the GZK process in which an extreme energy proton loses its energy through the collisions with CMB photons (Fig. 2.2.2-1). Many authors have already pointed out the possibility that neutrinos are also produced during acceleration in high-energy objects such as AGNs or GRBs. Neutrinos have so small an interaction cross-section with matter that they can directly convey the information of the site of acceleration. They escape the source region without being blocked by matter. They do not suffer from deflections by magnetic fields and propagate far longer than the distance to the cosmological horizon. This characteristic makes neutrinos be the best probe to understand EECR accelerators at cosmological distance. In Z-burst mode [23,24], neutrinos themselves are considered to be the origin of EECRs. The observation of neutrinos enables to identify the EECR sources at cosmological distances. The determination of neutrino flux is a probe for the evolution parameter of EECR production (m in Fig. 2.1.2-3) at z =1÷2 since they are highly dependent each other.

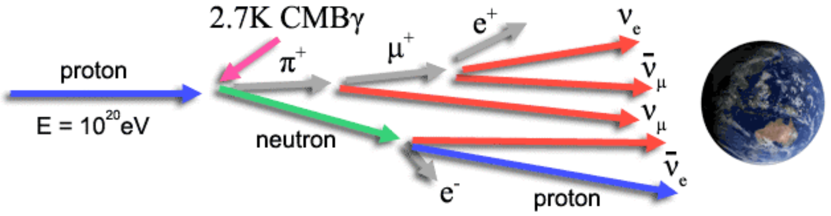

Figure 2.2.2-1. *Schematic view of cosmogenic neutrinos by the GZK mechanism. The observation of the extreme energy neutrinos enables to identify EECR origin even at cosmological distances. The flux of neutrinos depends much upon the cosmological evolution of extreme energy particle production (parameter m in Figure 2.1.2-3). It is therefore a potential key parameter to estimate the particle production rate at z=1÷2.*

The neutrino-nucleus cross-section at extreme energies is the key parameter to discuss feasibility of the neutrino detection. It is only little known and it is extrapolated from the lower energy man-made accelerator experiments. The electron-proton collision accelerator experiment HERA (Hadron Electron Ring Accelerator) reported the neutrino-nucleus cross-section to be $\sim 2\times 10^{-34}$ [cm^2] at $\sqrt{s}$ = 314 [GeV]. This corresponds to 52 TeV for a fixed target collision as the case of cosmic-ray experiments. According to the standard Quantum Chromo Dynamics (QCD) predictions and cosmogenic GZK neutrino flux calculations, JEM-EUSO is expected to observe 1÷10 neutrino events [43]. Extra-dimensional models [30] predict varieties of cross-sections. The predicted event rate is at least 100 times larger than the standard QCD rate predicts. With JEM-EUSO, it is feasible to discriminate these models.

Neutrino events are clearly distinguished by JEM-EUSO from those of protons and nuclei in terms of the shower maximum $X_{\max}$. Neutrino events are recognized as the EASs that interact deep in the atmosphere (Horizontal Air Shower, HAS) or as the Upward-going Air Showers (UAS) [29] produced by the decay of a tau-particle emitted by the interaction in the Earth's crust of an Earth-skimming or Earth-penetrating tau neutrino (Figure 2.2.2-2).

By its three-years of operation in tilted mode, JEM-EUSO can set a more stringent upper-limit on neutrino flux than the Waxman-Bahcall limit [31] around 10^{20} eV (Figure 2.2.2-3). It is expected that JEM-EUSO detects at least a few cosmogenic neutrino events (indicated as GZK(A) in Fig.2.2.2-3). If the top-down scenario for super-GZK particles (blue and green curves) is the valid case, several such events are expected in one year. On the other hand, if JEM-EUSO does not observe a significant number of neutrino events exceeding a few events, it would exclude most of the top-down models, as well as the extra-dimensional models.

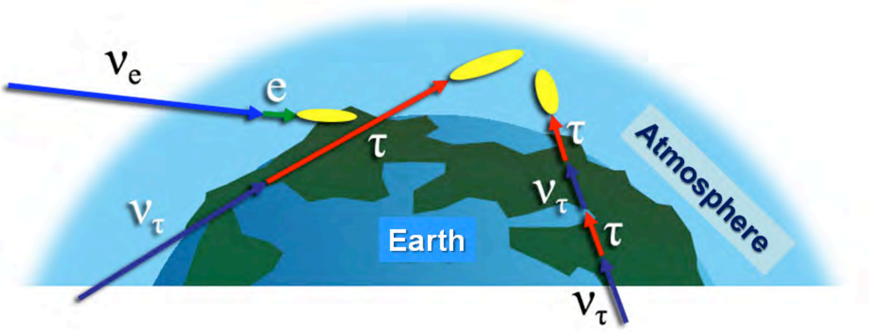

Figure 2.2.2-2. *Schematic view of EAS initiated by extreme energy neutrinos. Neutrinos at ~10^{20} eV deeply penetrates the atmosphere and may initiate EAS near the surface of the Earth. Tau neutrino events at ~10^{20} eV may be observed as the upward Earth skimming EAS. Tau neutrino events at 10^{16}÷10^{17} eV heading to JEM-EUSO are also observed by detecting Cherenkov light.*

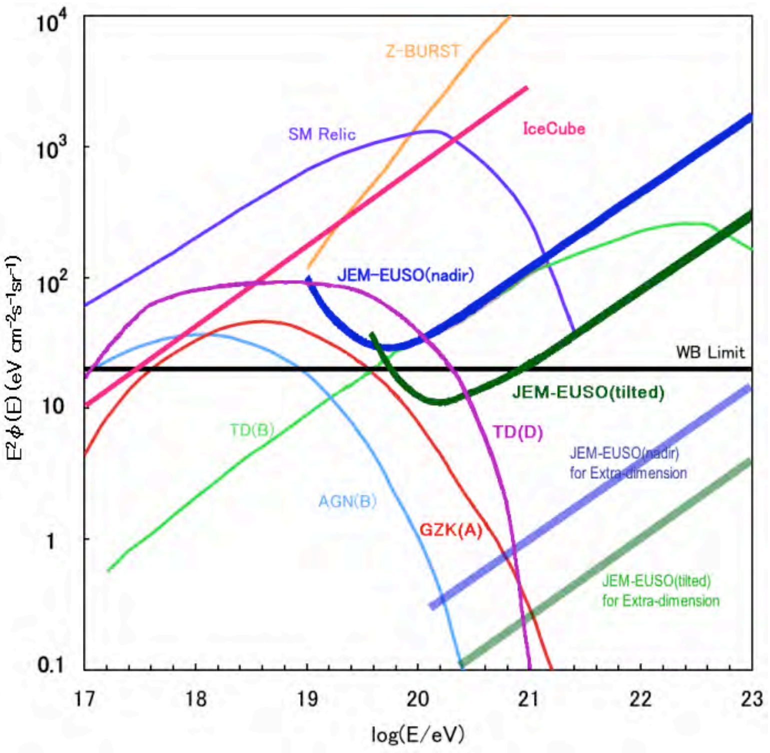

Figure 2.2.2-3. *The flux sensitivity of JEM-EUSO detecting 1 event/energy-decade per year. An observational efficiency of 25% is assumed. Blue and green dark curves show the case of nadir and tilted modes, respectively. Straight lines at high energies indicate the case of extra-dimensional model. As of IceCube (red line), 2.3 events/energy-decade per 10 years is assumed. Black line denotes the Waxman-Bahcall limit.*

Neutrinos, for example ones from GRBs, interact in the Earth crust around a few hundred meters or a few kilometres and initiate UAS. The Cherenkov beam from UAS originated by the tau-neutrino directly impinges onto the JEM-EUSO telescope and brightens only one pixel in one Gate Time Unit (GTU, 2.5 μs in the baseline design). The observable threshold energy depends upon neutrino cross-section, distance to EAS, angle to EAS, and so on. Such direct Cherenkov events in general are so strong that EAS event above 10^{16} eV are detectable (Figure 2.2.2-4). In case of a nearby (~1 Gpc) GRB event occurring in the field of view of JEM-EUSO, a bunch of upward direct Cherenkov events is expected. Such GRB events are estimated to occur ~1.2 times per year. In order to confirm such events as real UAS events, some sophisticated selection criteria have to be added to distinguish from detector noise or from the reflected Cherenkov mark of standard downward lower energy EAS.

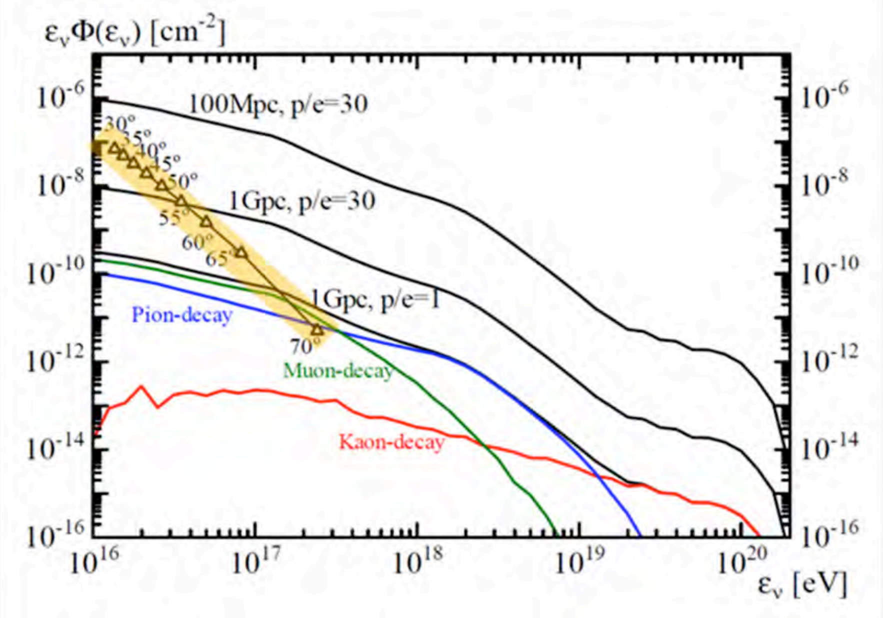

Figure 2.2.2-4 . *Expected flux of tau-neutrino from GRB as a function of energy [45]. The yellow curve marked with small triangles indicates the expected sensitivity of JEM-EUSO operating under tilted mode at different tilting angles.*

The neutrino cross-section is uncertain and highly model-dependent. The extra-dimension models [46] in which the Universe is supposed to consist of ten or eleven dimensions are among the favored models to unify quantum mechanics and gravitation theory. In these models, the neutrino cross-section is predicted to enhance more than 100 times of what predicted in the Standard model. As a result, hundreds of neutrino events are expected to be observed by JEM-EUSO and therefore the number of neutrino events may be a first experimental probe of the extra-dimension models. In addition, the ratio of events between HAS and UAS gives a quantitative estimation of neutrino cross-section around 10^{14} eV at center of mass system [43].

2.2.3. Study of the galactic magnetic field

Once the point sources are seen for events above 10^{20} eV, other events, member of these sources, can also be identified at different energies; changes in energy, magnitude and arrival direction can help to determine the Galactic Magnetic Field (GMF) [47]. Since Larmor radius is much larger than the galactic plane that dominantly contributes to GMF, particles are deflected adiabatically (Figure 2.2.3-1): GMF does not spread away the cluster of EECR events around the sources but only deforms the shape to several degrees depending on the GMF strength along the line of sight.

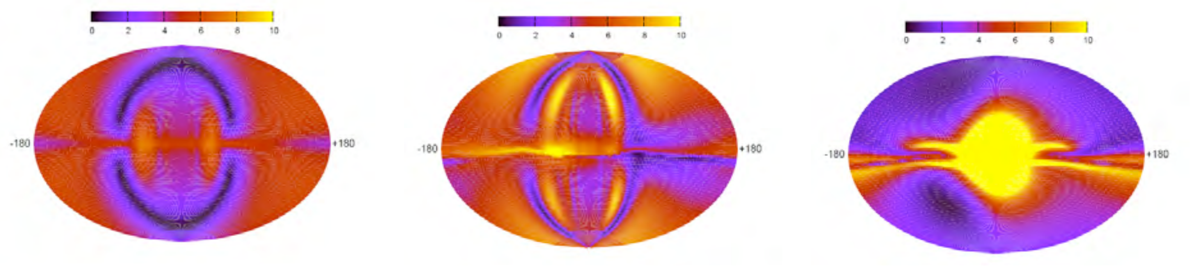

Figure 2.2.3-1. *Maps of deflection angle by different model of GMF for a rigidity of 4×10^{19} eV [47]. Left: Tinyakov and Tkachev (BBS-A)[48]. Middle: Harari, Mollerach and Roulet (BBS-S) [49]; Rigth: Prouza and Smida (BBS-S)[50]*

GMF is poorly known so far, due to the limited data only from Faraday rotation of polarized radio sources. Independent direct measurement of GMF will provide new information, which is performable by extreme energy particle deflections. When JEM-EUSO finds several bright sources less than 10 Mpc, the GMF structure will be directly determined by charged particles since the deflection by extragalactic magnetic field is negligibly small.

2.2.4. Verification of the relativity and the quantum gravity effect

The energy in the center of mass system in the interaction between an extreme energy particle and a target nucleus in atmosphere exceeds the energy reachable by the Large Hadron Collider (LHC) by more than three orders of magnitude. In the extreme energy frontier, many new physics that may change the spectral shape in the trans-GZK energies have been proposed and seriously discussed. JEM-EUSO can examine the Lorentz invariance at very high Lorentz factors of $\gamma \sim 10^{11}$. Special relativity is undoubtedly confirmed at lower energies so that the GZK cutoff is expected to be imminent. Gamma ray mean free path in vacuum is shorter than 100 kpc by interactions with CMB unless strong quantum gravity effect prohibits the $\gamma\gamma \rightarrow e^+e^-$ process. Hence, no gamma ray events are expected as extreme energy particles in the standard physics. However, if GZK-process itself would not appear as expected [32, 33, 34, 35, 36], it could imply some local limitations of Lorentz invariance in the presence of external fields. In such way, extreme energy particles offer a unique approach to experimentally test the relativity and quantum gravity theories. The standard quantum physics also predicts that EAS suffers from large fluctuations of cascading due to the LPM effect [19, 20]. It becomes considerable from 5×10^{20} eV (5×10^{21} eV) for proton (for iron nucleus). JEM-EUSO can observe such fluctuations in EAS's development with high statistics. Furthermore, the existence of super-heavy particles can be tested if they decay or annihilate into extreme energy cosmic rays delivering photons and neutrinos as well as nucleons.

2.2.5. Global observation of nightglows, plasma discharges, and lightning

JEM-EUSO will also observe atmospheric luminous phenomena such as lightning, nightglow, and meteors. The nightglow in the wavelength band 330÷400 nm is dominated by the emission from oxygen molecules in Herzberg I band around the boundary region at an altitude of 95 km between mesosphere and thermosphere; this emission is reported to have a strong correlation with the green line (557.7 nm) of oxygen atom [57]. The stripes (width of 40 km) of the green emission are observed to move in the observation from ground [58]; it is believed that these stripes are produced by the gravity wave formed in troposphere and propagated to the upper atmosphere (Figure 2.2.5-1) [58]. This propagation of gravity may affect the energy and angular momentum transfer to the mesosphere and thermosphere. In order to study these phenomena, rockets and satellite observations are actively planned [59].

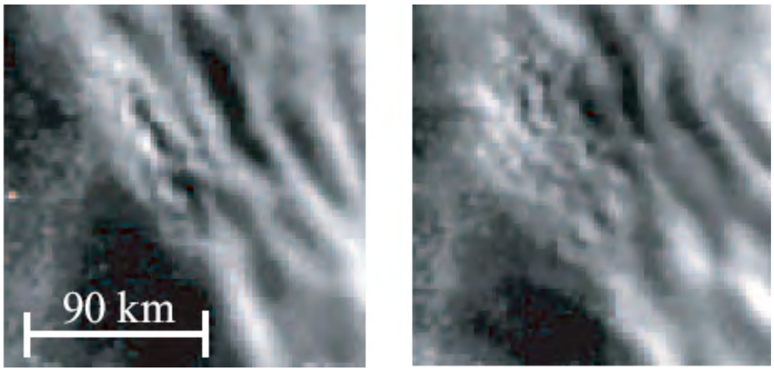

Figure 2.2.5-1. *The stripes observed in the nightglow by OH molecules. Similar stripes are expected to be observed in near UV band.*

When the heating of the ground surface has set up the severe updraft and resulting instable stratification in the troposphere, a cumulonimbus or thundercloud will develop to dissolve the instability. Generally, a thundercloud is an aggregate of convective cells that accompany severe updrafts or downdrafts whose wind speed reaches several 10 m/s. Each convective cell has its own unique life cycle, which consists of developing phase, mature phase and decaying phase. During the developing phase, collisions between ice crystals, graupels, and droplets will accelerate the electrification in the thundercloud. When the electric field between the charging layers inside a thundercloud and between the thundercloud and the ground exceeds the threshold of the breakdown electric field, a discharge will occur between them to neutralize the charges. These phenomena are called as lightning discharges.

Recently, lightning-emitted optical flashes and electromagnetic waves are successfully measured by satellites. These results are essentially useful for climatology, disaster prevention science, water cycle science, and other research fields. One of these results is derived from the FORTE (Fast On-orbit Recording of Transient Events) satellite which first succeeds in detecting electromagnetic waves emitted by lightning discharges in the VHF band. The analysis of FORTE data has shown the discharge morphology of Narrow Bipolar Events (NBEs) and Cloud-to-Ground (CG) events. NBE is a discharge event that has a time constant less than 1 μs, a discharge path length of the order of 100 m, and radiation energy greater than 100 kW. It is suggested that NBE detected at the satellite altitude is the most powerful VHF emission radiated by lightning discharges and that the optical emission related to NBE would be very weak though it has not been observed simultaneously at the satellite yet. In contrast, a CG event is the electromagnetic emission radiated from the negative leader or return stroke, which has current amplitude of several 10 kA. It is reported that NBE is only observed at the initiation phase of the negative CG discharges. From the intensive satellite and ground-based observations it is also reported that the NBE is strongly related with the cloud-to-cloud discharges occurring at the 10÷20 km altitude. Gurevich and Zybin 2004 [62] suggested that NBE would reasonably be explained by the runaway breakdown triggered by EAS that consists of mainly 3 MeV relativistic electrons. Thus, the wavelength of the optical emission related to NBE is not in the visible range but in the near UV range (330÷400 nm) same as EAS. This scenario is consistent with the observational result showing that the visible optical emission of NBE is very weak. Optical energy of NBE is estimated to be 10÷100 J, which can be detected by JEM-EUSO (16 J corresponds to 10^{20} eV). Specific mission to study Transient Luminous Events (TLE), are currently under development, as the JEM-GLISM (Global LIghtning and Sprite Measurement) to be installed onboard ISS in 2011. If the simultaneous observation of NBE using optical and electromagnetic instruments of JEM-EUSO and JEM-GLISM missions is realized, it may be possible to obtain direct observational evidence showing that NBE is generated by cosmic rays, and lightning discharges are triggered by cosmic rays. Research groups of the JEM-EUSO mission initiated the establishment of the agreement of the future collaborative observations with the JEM-GLISM and ASIM (Atmosphere-Space Interactions Monitor), a lightning and TLE observation mission led by ESA.

New type of lightning-associated discharge phenomena above thunderclouds has been identified in 1990s, called as sprites, elves, and blue jets (Figure 2.2.5-2). It is suggested that sprites are phenomena related to cloud-to-ground discharges, which generate quasi-electrostatic field above the thundercloud and accelerate ambient electrons. Recently it is implied that the electromagnetic pulse from the horizontal lightning current may play an important role to determine the occurrence condition of TLEs. In order to clarify them, it is essential to carry out nadir observation of sprites and to identify horizontal distribution of sprites. However, it is difficult to carry out nadir observation of TLEs since the optical instruments naturally watch both lightning and TLE emission almost simultaneously. It is known that the lightning discharges generating TLEs has a time constant of ~1 ms and that the delay time of sprites from the parent lightning discharges is >1 ms. Thus, one solution to distinguish both emissions is to employ high-speed imaging technique with the time resolution of no more than 1 ms. Since the time resolution of JEM-EUSO imaging observation is 2.5 μs, it is possible to identify the spatial distribution of sprites and clarify their generation mechanism. Moreover, JEM-EUSO has enough potential to detect weak optical emission originated from the streamers, which may precede the main discharges of TLEs.

Furthermore, satellites detect several GRBs probably associated with lightning from the Earth [64]. Such runaway electrons produced by cosmic rays might be accelerated by the quasi-static electric field of the discharge associated with lightning. JEM-EUSO would keep monitoring both EECR tracks and runaway phenomena to see whether there is any recognizable relationship.

Other atmospheric phenomena that would be observable by JEM-EUSO have been included in the mission studies.

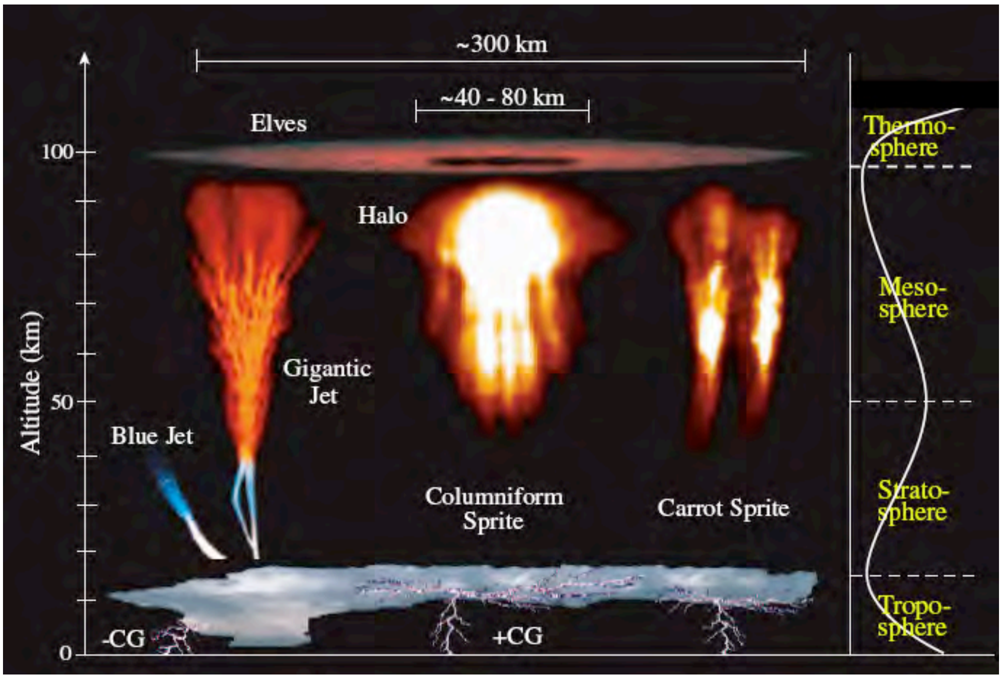

Figure 2.2.5-2. *Various transient luminous events associated with lightning.*

3. Observation Principle and Requirements

3.1. Observation Principle

In the JEM-EUSO Mission, the EECR observation is based on the measurement of the fluorescence and Cherenkov photons produced by the extensive air shower phenomenon, induced by the primary EECR particle, as it progresses through the atmosphere.

An EECR, colliding with air nuclei, produces secondaries that in turn collide with the air atoms giving rise to a propagating cascade of particles, known as EAS, Extensive Air Shower. The number of the secondary particles in an EAS is proportional to the energy of the primary EECR: in a 10^{20} eV EECR, for example, as many as an order of 10^{11} particles are produced along the shower axis. The most numerous secondary particles are electrons which, moving through the atmosphere, ionise the air and excite metastable energy levels in its atoms and molecules, in particular Nitrogen. With a short relaxation time, electrons from those Nitrogen levels return to ground state emitting a characteristic fluorescence light. In air the peaks of such a fluorescence light are at wavelengths from 330 nm to 450 nm, in the Ultraviolet (UV) region. The emitted light is isotropic and proportional to the shower energy at any given depth in the atmosphere. Moreover, because the velocities of the secondary EAS particles are higher than the local velocity of light, it is also present the emission of Cherenkov photons, highly beamed within a cone of ~1.3° radius along the shower axis; part of these Cherenkov photons are scattered along the EAS path, due to the molecular and aerosol content in the atmosphere; one part will be isotropically diffused due to the impact of the Cherenkov beam on clouds, land or sea. An EECR-induced EAS then forms a significant streak of scintillation light along its passage in the atmosphere, depending on the energy of the primary EECR and the angle with the vertical axis.

Looking from Space downward the dark Earth atmosphere, JEM-EUSO will capture this scintillation light and images the motion of the streak every few microseconds, allowing to determine the arrival direction of the primary EECR. As sketched in Fig. 3.1-1, JEM-EUSO will observe the fluorescence light, and the accompanying Cherenkov radiation, at distance from the shower axis, so capturing the cascade profile of the EAS. The shower appears as a relatively small disc-shaped luminous object; when viewed continuously, the object moves on a straight path with the speed of light. As it does so, the disc luminosity changes from so faint to be undetectable up to a maximum followed by a gradual fading. The resulting event seen by the JEM-EUSO telescope looks like a narrow track in which the recorded amount of light is proportional to the shower size at the various depth in the atmosphere. The integral of light recorded in the track and the light signal at the shower maximum are proportional to the energy of the primary EECR. The cascade shape (especially the position of the shower maximum as a function of the penetration depth) gives an indication about the nature of the primary: for example, showers initiated very deep in the atmosphere indicate an origin by neutrinos because the neutrino-air nuclei interaction cross section is several orders of magnitude lower than the cross section for hadrons or photons.

The time profile of a typical EAS induced by a proton of energy 10^{20} eV, arriving from 60° zenith angle, is shown in Fig.3.1-2. The vertical axis denotes the number of photons reaching the JEM-EUSO optical system. The green and blue curves represent the fluorescence and Cherenkov components, respectively, and the red one is the sum of both the two components. For comparison, the black dotted histogram indicates the case when the atmosphere transmission effects are neglected. The sharp peak at the end of the profile is the so-called Cherenkov "footprint" or "mark"; it is due to the photons reflected from the impact point of the Cherenkov beam (from the sea, in the figure) and its identification will help to locate where EAS lands.

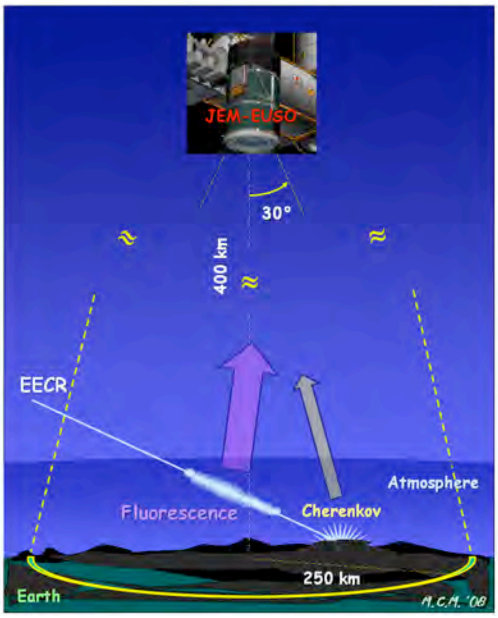

Figure 3.1-1. *Artistic view of the JEM-EUSO principle of observation. Both fluorescence and Cherenkov light, produced by the EAS through the atmosphere, are captured by the telescope.*

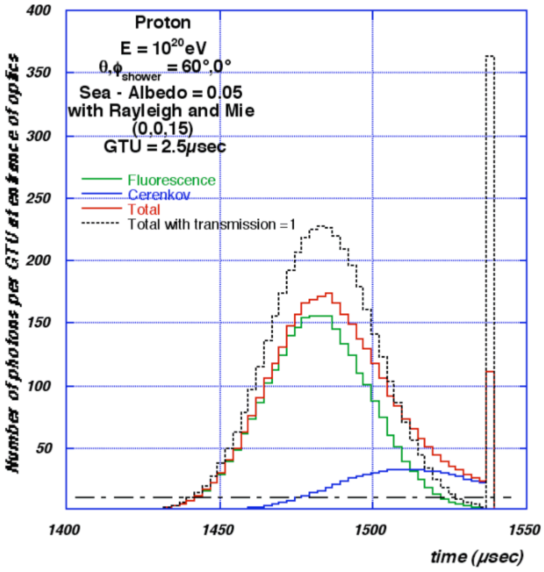

Figure 3.1-2. *Time profile of photons from a typical EAS. Green and blue curves represent the fluorescence and Cherenkov components, which sum is reported in red; the black curve represents the full atmospheric transmission.*

The International Space Station, on which JEM-EUSO will be accommodated, orbits around the Earth at ~7 km/s at an average altitude of 400 km with an inclination of 51.64°. As minimum value, when operating in nadir mode, JEM-EUSO will monitor an area of ~200,000 km^2 on the surface of the Earth corresponding to an atmosphere fiducial volume of 10^{12} tons. Under such a configuration, the merits and advantages of JEM-EUSO with respect to the ground-based EECR observatories can be summarized as follows:

- Wide aperture, at least more than one order of magnitude with respect to the current limit reachable for ground-based observatories of EECRs. Main advantages: high statistics, allowing to detect at least 1000 EECRs in three-years operation; determination of the Cherenkov footprint; detection of rare neutrino interacting events.
- Full sky coverage. The entire celestial sphere will be observed, allowing to consider several different celestial objects as candidate sources of EECRs, even in regions far from the Galactic centre.
- Limited uncertainty in distance to EAS. The Extensive Air Showers only develop within ~20 km from the Earth surface, a very small thickness with respect the altitude of the JEM-EUSO observation; this strongly reduces the systematic errors and ensures that one can determine luminous fluorescence events as being EECR events.
- Limited uncertainty in atmospheric absorption of photons from EAS. The sources of attenuation of the signal in the atmosphere are reduced; the observation from Space is much less sensitive to the presence of most of the aerosols.

3.2. Accuracy of Observables

The JEM-EUSO observational approach mainly relies on the fact that, thanks to the huge amount of UV light emitted during the EAS path through the atmosphere, a substantial fraction of these photons will reach the JEM-EUSO telescope that is looking downward to the Earth from an average height of 400 km. Nevertheless, in order to capture these photons, JEM-EUSO must satisfy several requirements (as described in the next paragraphs), and the accuracy in measuring the observables must be guaranteed. Such an accuracy is obviously related to the JEM-EUSO telescope performance and to the ISS orbit parameters. In this section we will deal with some essential requirements (effective area, time resolution, pixel size, pixel minimum content) needed to assure the capability of JEM-EUSO of observing a 10^{20} eV EECR-induced EAS passing through the atmosphere at a zenith angle of 60°.

3.2.1. Effective area

The saturated effective area is determined by the following equation:

$$A_{eff} = \eta_c \cdot \eta_0 \cdot (1 - \tau_{dead}) \cdot \pi \cdot h^2 \cdot \tan^2 \gamma_M \tag{3-1}$$

where h =400 km is the mean orbital altitude of the JEM-EUSO detector, γ_M ~30° is half of its field of view, η_o ~0.20÷0.25 is the duty cycle and η_c is the efficiency due to cloud presence, estimated to ~0.7 by the TOVS instruments database of the International Satellite Cloud Climatology Project, ISCCP. Compared with the effective area of the Pierre Auger Observatory, JEM-EUSO observatory must satisfy the following relationship:

$$\eta_0 \cdot (1 - \tau_{dead}) \cdot \tan^2 \gamma_M \geq 0.066 \tag{3-2}$$

to exceed by an order of the effective area.

3.2.2. Time resolution, collecting aperture, pixel size, X_{max}

The key parameters that define the fundamental telescope performance are effective aperture of photon collection (including focusing power, filter transmittance and response of the photon detector), pixel size and time resolution.

The optimal time resolution δ_T is required to be short enough to dissolve the time profile of the EAS development. In case of a typical EAS event, the duration of its development is ~ 60 □s and therefore a time resolution δ_T of the order of μs is desired. The optimal δ_T is chosen to be comparable to the time scale of the light crossing a distance corresponding to the pixel size:

$$\delta_T = \left(\frac{\delta \cdot h_0}{c} \right) = 2.3[\mu s] \cdot \left(\frac{\delta}{0.1^\circ} \right) \cdot \left(\frac{h}{400[km]} \right) \tag{3-3}$$

where δ is the angle corresponding to the pixel dimension. In order to avoid pile-up of the signal from the Cherenkov mark, the effective time resolution is required to be as short as 10 ns to assure the wide enough dynamic range.

The optimal definition of effective optical aperture S_{eff} and pixel size δ needs some more preliminary considerations. In case of the typical EAS of interest, ~550 photons per square meter arrive to the JEM-EUSO telescope. The length of the EAS track, L_{EAS}, is ~1.5° and its duration, T_{EAS}, is ~60 μs. The total number of photons from EAS, N_{EAS}, is expressed as:

$$N_{EAS} = n_0 \cdot S_{eff} \tag{3-4}$$

where n_o~ 550 photons/m^2 is the density of photons reaching JEM-EUSO. If the focal spot size is comparable to the pixel size, the contaminating night sky background signal, N_B, within the pixels receiving the EAS track, is expressed as:

$$N_B = n_B \cdot \delta \cdot L_{EAS} \cdot S_{eff} \tag{3-5}$$

where n_B = 500 [photons / m^2 ns sr] is the typical night sky background flux in the UV region. The scientific requirements on energy and angular resolutions are 30% and 2.5°, respectively; to assure the margin to the shower reconstruction procedure, we herein require the half of these resolutions as in the following relationships:

$$\frac{\sqrt{N_{EAS}+N_B}}{N_{EAS}} \leq 0.15 \tag{3-6}$$

$$\Delta\beta = \left(\frac{\delta}{L_{EAS}} + \frac{\delta_T}{N_{EAS}}\right) \cdot \sqrt{\frac{N_{EAS}+N_B}{N_{EAS}}} \leq 1.25° \tag{3-7}$$

Figure 3.2.2-1 shows the permissible parameters region for S_{eff} and δ in case of a constant δ_T=2.5 μs. The red and blue curves draw the lower limits of S_{eff} as a function of δ that are defined by Eqs. (3-6) and (3-7). To obtain that an EAS event triggers the JEM-EUSO data acquisition system , at least 5 photoelectrons per pixel are needed around the maximum of the EAS development. This limit is shown by green line in the figure. The star represents the S_{eff} and δ parameters for the baseline detector design which satisfy all the above three conditions.

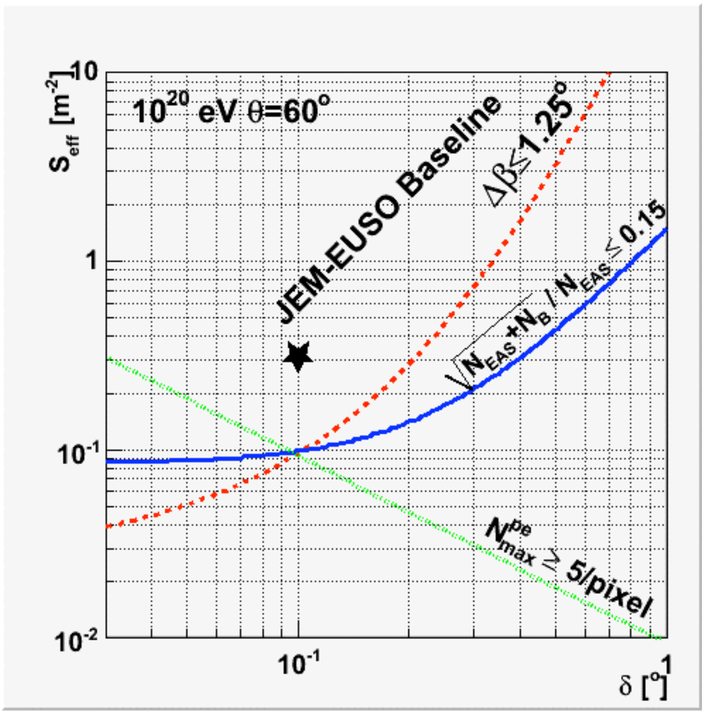

Figure 3.2.2-1. *Permissible lower limit of S_{eff} as a function of δ. Herein, the value δ_T=2.5μs is assumed. The red and blue curves draw the lower limits from Eqs. (3-6) and (3-7). The green line draws the lower limit for at least 5 photoelectrons per pixel detected at the maximum of the EAS development. The star refers to the baseline detector design.*

The determination error of X_{max}, which is the key EAS parameter to discriminate primary particles, is required to be less than 120 g/cm^2 from the scientific objectives . Assuming the EAS development profile as a Gaussian function, its root mean square is L_{RMS} = 0.4°. An “ad hoc” estimate of the angular position of the EAS development maximum is determined with an accuracy of ~ $L_{EAS}\cdot\sqrt{\frac{N_{EAS}+N_B}{N_{EAS}}}$ if only statistical error is taken into account. The corresponding error in X_{max} is evaluated by the equation:

$$\Delta X_{\max}\approx\left(\frac{L_{RMS}}{[rad]}\right)\cdot\frac{\sqrt{N_{EAS}+N_B}}{N_{EAS}}\cdot\left(\frac{h}{1[cm]}\right)\cdot\left(\frac{\rho_{air}}{1[g/cm^3]}\right)/\sin\theta \qquad (3\text{-}8)$$

where ρ_{air} id the density of air at the maximum of the EAS development. In case of a typical EAS event (note that the zenith angle of arrival is 60°), it reaches the maximum around 7 km above sea level where is $\rho_{air}\sim 0.6\times10^{-3}$ g/cm^3. If the number of photons from EAS exceeds the limit of Eq. (3-6), then the error on X_{max} is smaller than 30 g/cm^2 and therefore the requirement for X_{max} is satisfied.

3.2.3. Dark current and night sky background

The dark current level is required to be less than ~50 GHz. This limit is far smaller than the level of night sky background which is $(3\div10)\times10^{11}$ Hz over the entire focal surface detector.

3.3. Requirements

The scientific objectives and goals of the JEM-EUSO mission, described in Chapter 2, convert in a set of scientific, observation and instrument requirements, as listed in the next paragraphs. All the requirements are strictly related each another; such inter-relations are defined in each proper paragraph and summarized in the flow-chart drawn in Fig.3.3-1.

3.3.1. Scientific requirements

[SR1] Statistics: ≥ 1000 events detection above 7×10^{19} eV.

[SR2] Angular resolution: better than a few degrees to investigate EECR origin.

[SR3] Energy resolution: trans-GZK structure in cosmic ray energy spectrum.

[SR4] EECR primary identification capability: discriminating among nucleus, gamma ray and neutrino.

3.3.2. Observation requirements

[OR1] Acceptance: ≥ 7×10^5 $(h[\text{km}]/400)^2$ [km^{2}sr] (E=10^{20} [eV] and 60° zenith angle) [SR1]

[OR2] Angular resolution: ≤ 2.5° (E=10^{20} [eV] and 60° zenith angle) [SR2]

[OR3] Energy resolution: ≤ 30% (E=10^{20} [eV] and 60° zenith angle) [SR3]

[OR4] $X_{\max}$ determination error: ≤ 120[g/cm^2] (E=10^{20} [eV] and 60° zenith angle) [SR4]

[OR5] Energy threshold: ≤ 7×10^{19} [eV] [SR1]

3.3.3. Instrument requirements

[IR1] Observation duty cycle: ≥ 10% [SR1]

[IR2] Instrumental duty cycle: ≥ 30% [SR1]

[IR3] Lifetime: longer than two years. Two years storage is also required before the launch [SR1]

[IR4] Attitude determination accuracy: ≤ 0.05° (this may be achieved by offline analysis) [OR2, OR3, OR4]

[IR5] Precision of Absolute time: ≤ 1 μs [OR2]

[IR6] Wavelength band: containing EAS fluorescence lines in 330÷400 nm [OR1,OR2,OR3,OR5]

[IR7] Synchronization precision among subsystems: ≤ 200 [ns] [ASR1]

[IR8] Protection against stray light: less than GHz level [OR5,OR2]

3.3.3.1. Optics

[OPR1] Effective aperture: ≥ 1.5 [m^2] (taking into account photon collection efficiency [OR3,OR5,OR2]

[OPR2] Field of view: ≥ 60° full [OR1]

[OPR3] Spot size: ≤ 5 [mm] (root mean square) [OR2,OR3,OR5]

[OPR4] Focusing power: ≥ 50% (on-axis) [OR3,OR5,OR2]; ≥ 30% (30° off optical axis)

[OPR5] Transmittance of filter: ≥ 90% (degrading during operation period should be less than 10% level) [OR3,OR5,OR2]

3.3.3.2. Focal surface detector

[FSR1] Shape of focal surface: spherical

[FSR2] Photon detection efficiency: ≥ 0.12 [OR3,OR5,OR2]

[FSR3] Average pixel size: ≤ 4.5 mm [OPR3]

[FSR4] Focal surface area: ≥ 3.6 m^2 [OPR2]

[FSR5] Trigger efficiency: ≥ 0.95 (E_0=10^{20}eV, zenith angle 60°) [OR5]

[FSR6] Gate time: ≤ 2.5 μs [OR2,OR3,OR4]

[FSR7] Dynamic range: 200 photons within gate time (TBC) [SR2]

[FSR8] Dead time: ≤ 3% [OR1]

[FSR9] Dark current noise: ≤ 50 GHz [OR5]

3.3.3.3. Calibration system

[CSR1] Wavelength: 330÷400nm [IR6]

[CSR2] Accuracy: ≤ 18% (TBC) [OR2,OR3,OR4]

3.3.3.4. Atmospheric monitoring

[ASR1] Accuracy of cloud top altitude: ≤ 500 m over field of view [OR3,OR4]

3.3.4. Miscellanea

- Robustness, compactness, low mass, small volume, low power consumption, structure, radiation tolerance, magnetic field tolerance (against ~gauss level) and stability in 3÷5-year operation.
- Mountable on International Space Station.
- Telescope protected against potential hazards.
- Instrumental success criterion: more than 80% instruments work in good order after five years operation. The mission success probability should be more than 95% that fulfil the above instrumental success criterion.
- Detectors and their circuits are modularized and are capable of self-operation.

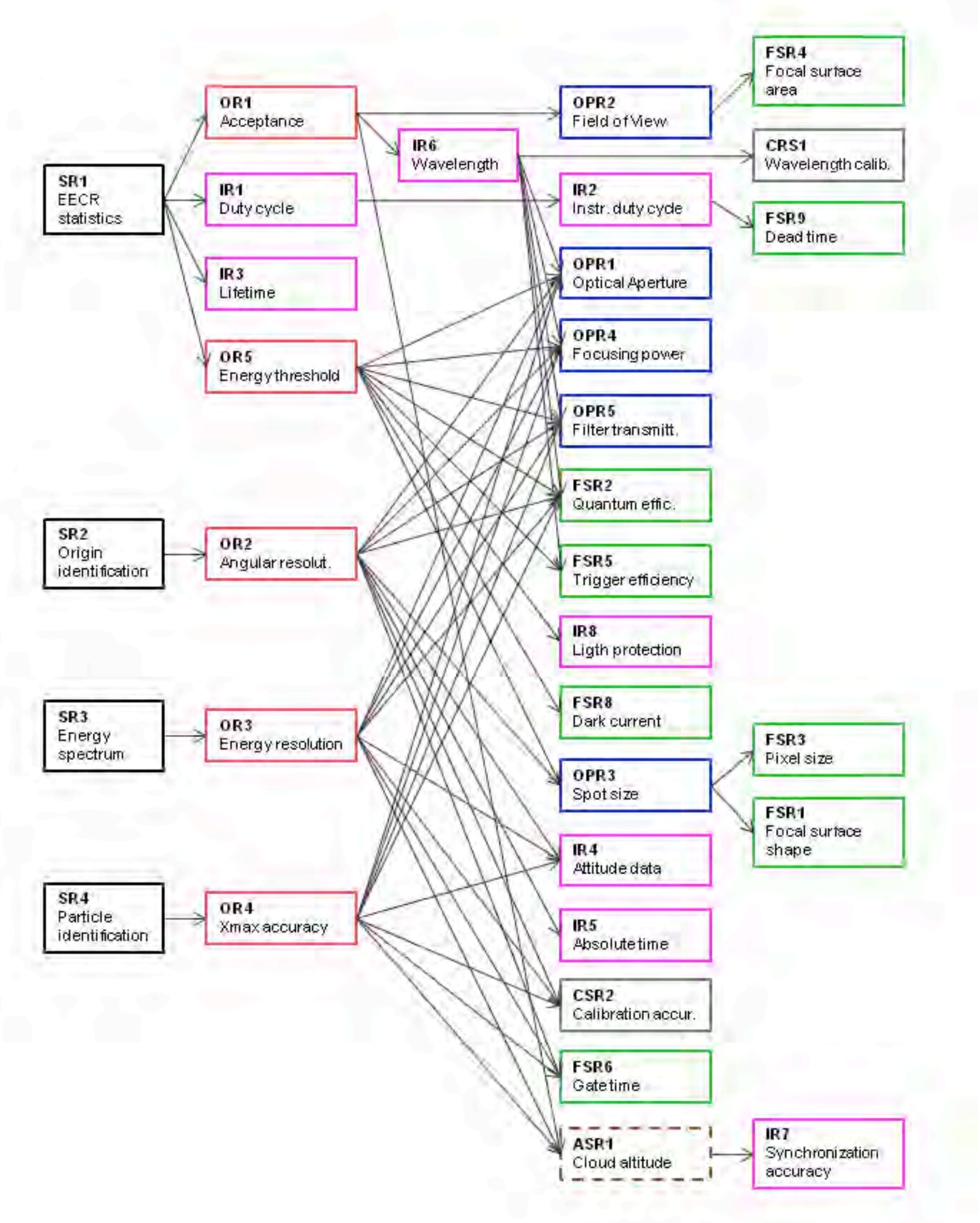

Figure 3.3-1. *Tree of scientific, observational and instrumental requirements in JEM-EUSO.*

3.4. Success Criteria

The accomplishment of some or all the scientific requirements will determine the success of the JEM-EUSO mission at different levels as defined by the following criteria:

Minimum success:	The criterion of minimum success of JEM-EUSO Mission is acquisition of more than half of the statistical requirement of EECR events [SR1], namely ≥ 500 events above 7×10^{19} eV.
Full success:	Advent of new generation astronomy via EECR particles [SR1, SR2, SR3, SR4].
Extra success:	Achieving one or all subjects described in the exploratory scientific objects.

4. Instrument

4.1. Overview

As described in previous chapters, the first EUSO observatory, hereafter named ESA-EUSO, was originally selected by the European Space Agency (ESA) as a mission attached to the European Columbus module of the International Space Station (ISS). The ESA-EUSO phase-A study was successfully completed in July 2004, accompanied by the issue of detailed report [65]. In 2006, the mission was redefined as an observatory attached to the Japanese Experiment Module/Exposure Facility (JEM/EF) of the ISS. Thereafter, Japan is supervisor of the mission and of the concept design of the whole observatory, renamed JEM-EUSO.

The JEM-EUSO instrument, i.e. the experimental apparatus to be accommodated on JEM/EF (Fig.4.1-1), is an upgraded version of the ESA-EUSO design that can be considered as the minimum set-up for such a kind of EECR telescope from Space; with respect to it (somewhere indicated as ESA-EUSO(min) in this document), JEM-EUSO aim to reduce the threshold energy and to increase the effective area by taking advantage of the technological progresses and of specific features of the JEM/EF module, as will be described in the following paragraphs.

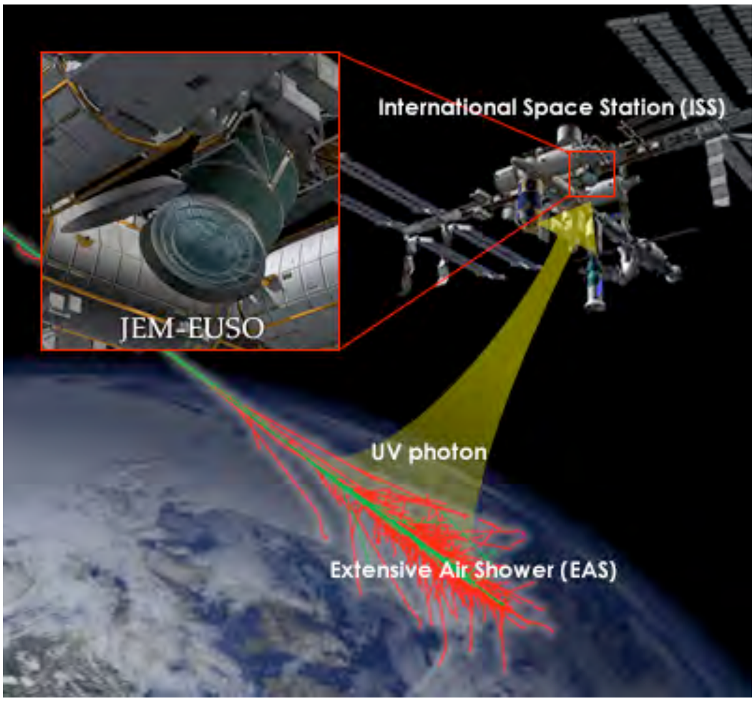

Figure 4.1-1. *Artistic view of the JEM-EUSO instrument accommodated on the ISS.*

The JEM-EUSO instrument basically consists of an EECR telescope assisted by an atmosphere monitoring device and controlled by a calibration system.

The JEM-EUSO telescope is a fast, high-pixelized, large-aperture and large field-of-view digital camera, working in the near-UV wavelength range (330 ÷ 400 nm) with single photon counting capability. The main components of the telescope are the collecting optics, the focal surface detector, the electronics and the structure, as shown in Fig.4.1-2. The optics system is composed of two Fresnel lenses and one diffractive precision lens. With an aperture of ±30° field of view (FoV), the optics focuses the UV light incident onto the front lens (numbered as lens #1 in figure) toward the focal surface with a spatial resolution of 0.1°. The focal surface detector is composed by a grid of ~6000 multi-anode photomultipliers (MAPMT) which convert the energy of the incoming photons into electric pulses with duration of 10 ns. The electronics counts-up the number of the electric pulses in time periods of 2.5 μs and records them to the memory; when a signal pattern coming from extreme energy particle events is found, the electronics issues a trigger signal and transmits all the useful data to the ground operation center, tracking back the image information stored in the memory.

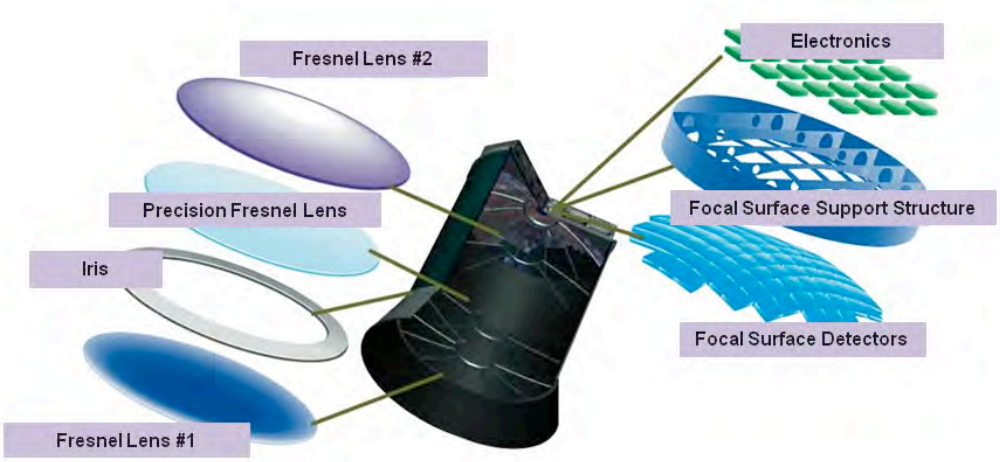

Figure 4.1-2. *Schematic view of the JEM-EUSO telescope.*

For what concerns the atmosphere monitoring, JEM-EUSO will use an infrared (IR) camera and a Lidar (LIght Detection and Ranging) with ultraviolet laser to observe the conditions of the atmosphere in the FoV of the EECR telescope, with the objective of determining effective observation time, and of increasing the reliability of the events around the energy threshold. With respect to ESA-EUSO(min), JEM-EUSO reduces the role of the Lidar to the following: to observe the condition of clouds in several points of the JEM-EUSO field of view, and to calibrate with high accuracy the transformation table between altitude of cloud tops and their temperature, obtained by the analysis of the IR camera images. Being the wavelength of the laser (355 nm) in the range of interest for JEM-EUSO, the focal surface detector of the EECR telescope will be used as Lidar receiver unit.

JEM-EUSO will be calibrated through instrumentation both onboard and on ground. The onboard calibration system of JEM-EUSO is composed of a set of three LEDs (TBC) with different wavelengths (from 300 to 500 nm) that will be installed in the telescope cylinder as diffusive light sources. By measuring with the focal surface detector the light from these light sources passing through the optics and reflected from the interior side surface of the lid, we will calibrate gain and detection efficiency of the detector. Moreover, Xenon flasher lamps will be installed in a dozen of sites on the ground and when JEM-EUSO passes over them, once a day or so, it will detect such lights and measure the total atmospheric UV absorption and, therefore, calibrate the device. In order to estimate the systematic error in the energy and arrival direction of the primary cosmic rays, JEM-EUSO telescope observes the ultraviolet laser from the ground as the simulated EAS. This observation also allows us to estimate the transmittance of the atmosphere as a function of the altitude. In addition to the calibration of the devices before the launch, all the above calibrations will be complementarily used to obtain the possible influences caused by the long-term variation in the sensitivity of the device and by the variable atmospheric environment.

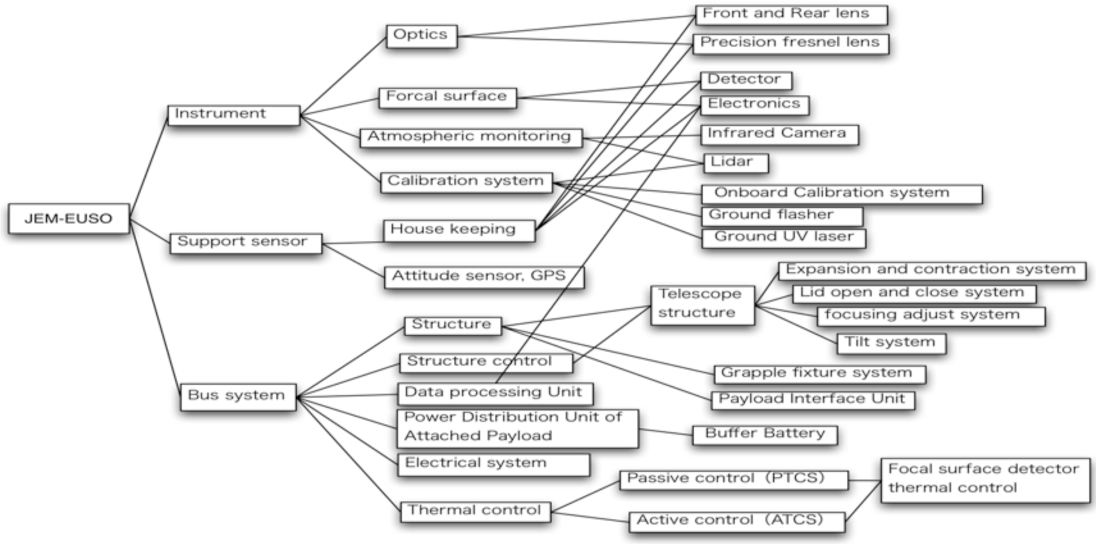

Figure 4.1-3. *Breakdown of the JEM-EUSO system.*

The whole JEM-EUSO system, whose breakdown is shown in Fig.4.1-3, will be technically detailed in all its components, together with requirements and constraints, in the next paragraphs; Moreover, a comparison with the ESA-EUSO original design is included whenever useful, to underline the advantages obtained or expected thanks to the improvements performed during the JEM-EUSO Phase-A study.

4.2. Optics Module

4.2.1. General

The definition of the JEM-EUSO Optics Module (OM) follows and improves what done during the ESA-EUSO Phase-A study [65], where OM was essentially constituted by two curved double-sided Fresnel lenses in PolyMethil-MethaAcrylate PMMA-000 material (Mitsubishi Rayon Co. product). After that, the study for an improved OM has been continued, reaching today a new baseline for JEM-EUSO as well as the option for a more advanced design. Both the designs have been verified during the JEM-EUSO Phase-A study, as reported in this document.

The JEM-EUSO "Baseline" optics maintains the PMMA-000 material as verified and selected in [65], and adds one intermediate curved precision Fresnel lens between the two curved double-sided Fresnel ones, to correct for chromatic aberration.

The JEM-EUSO "Advanced" option presents changes in both the material and the geometrical design, with respect to the baseline; in fact, the two curved double-sided Fresnel lenses are in CYTOP material (AGC Co. product), while the PMMA (a fine grating structure from the manufacturing point of view) is maintained for the precision lens, that presents now a flat surface.

The conceptual design of the JEM-EUSO optics module is included in the sketch of Fig.4.2-1. All the details about baseline and advanced OM design will be described in the following sections where we will mainly refer to the configuration for a 2.5 m diameter telescope; this was the size foreseen for the original EUSO configuration. Nevertheless, to take advantage of all the available room on the HTV vehicle to transfer JEM-EUSO onboard the ISS, the size of the lenses can be extended in one dimension and a further geometrical design has been studied, as will be discussed in next paragraphs; briefly, such a design considers lenses with maximum extension of 2.65 m (diameter) and minimum extension of 1.9 m, obtained by cutting two parallel sides of the lenses.

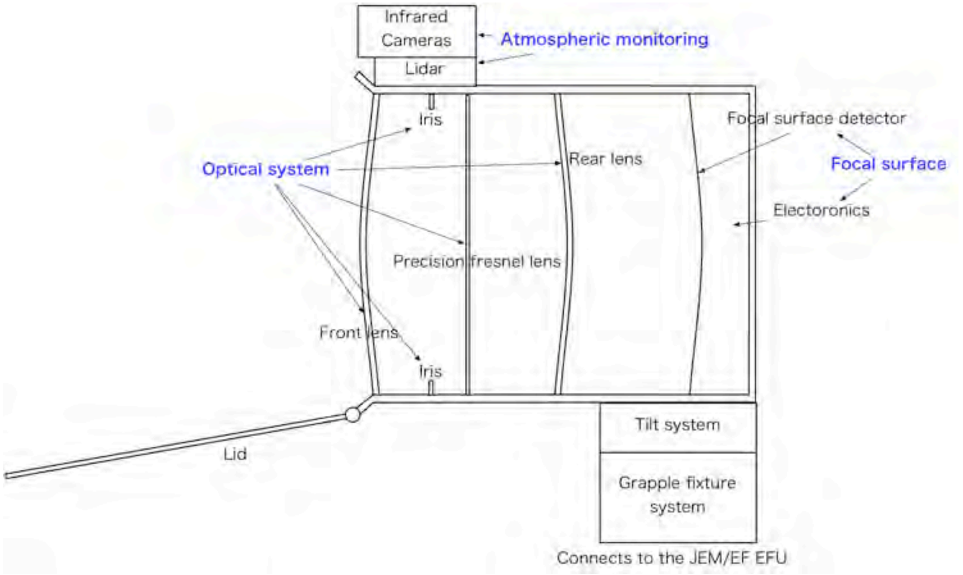

Figure 4.2-1. *Conceptual design of the JEM-EUSO telescope.*

4.2.1.1. Definitions

JEM-EUSO optics focuses the incoming photon toward a pixel of the detector set on the optical focal surface. The collection of photons by the optics requires:

- Field of view of optics larger than ±30°.
- Spot size smaller than the pixel size of the focal surface detector.

Coordinate system:

- The origin of the coordinate axes is a cross point of 1st lens surface and optical axis.
- Z-axis accords with optical axis. Its "plus" direction is from the 1st lens to focal surface.
- X-axis is parallel with the direction of the ISS movement, when observation mode is nadir mode. Its positive direction is anti-direction of ISS.
- Y-axis is defined by the Cartesian coordinates of the above-mentioned X and Z axes.

Location:

Optics is set to focus on the focal surface detector.

Main parts:

Optics consists of the following parts:

- 1st lens (Curved doublet Fresnel lens)
- Stop (Iris)
- 2nd lens (Precision Fresnel lens)
- 3rd lens (Curved doublet Fresnel lens)
- Filter
- Lens frame
- Focusing adjust system
- Housekeeping sensor

Lifetime:

Optics has lifetime defined by the JEM-EUSO system design.

4.2.1.2. Requirements

Performance requirements:

- Optics is able to detect atmospheric fluorescence and Cherenkov light from EAS.
- Optics is able to determine the emission point with spatial resolution of 0.1°.
- Optics is able to collect photons (330÷400 nm wavelength band) to a pixel of the focal detector as higher efficiency as possible.
- Spot size satisfies that the spatial resolution is 0.1° or less.
- Life span of optics is 5 years or more.
- Optics is “space qualified”.

Physical requirements:

- Mass of optics is defined by the JEM-EUSO system design.
- Centre of gravity of optics is on the Z-axis with TBD mm or less.
- Optics must be totally included in the JEM-EUSO telescope envelope.

Temperature requirements:

Optics basically depends on the surrounding environment. Fluctuations of each lens have to 10°C or less.

4.2.2. Lens material

CYTOP is an amorphous, soluble perfluoropolymer (AGC Corp. product). CYTOP combines the excellent properties of highly fluorinated polymers with solubility in selected perfluorinated solvents to provide outstanding coatings for optical, electronic and other applications. CYTOP has a 95% high transmittance between UV and near-IR.

PMMA-000 is a special Grade UV transmittance polymetyl metacrylate (Mitsubishi Rayon Corp. product). Table 4.2.2-1 shows the characteristics of CYTOP and of PMMA-000 [66].

Table 4.2.2-1. *Characteristics of the CYTOP and PMMA-000 materials.*

	CYTOP	PMMA000
Product Company	AGC (Asahi Glass Co.)	Mitsubishi Rayon Co.
Density (25 °C)	2.03 g/cm^3	1.19 ~ 1.20 g/cm^3
Glass transition temperature	108 °C	105 ~ 120 °C
Water absorption	< 0.01	0.3
Coefficient of linear expansion	7.4×10^{-5} cm/cm/°C	8.0×10^{-5} cm/cm/°C
Mechanical properties:		
Rupture strength	40 MPa	65 ~ 73 MPa
Break elongation	150%	3 ~ 5%
Yield strength	40 MPa	(65) MPa
Tensile strength	1200 MPa	3000 MPa

4.2.2.1. Refractive index

Refractive index of CYTOP and PMMA-000 in the near-UV region.

Refractive indexes of the two materials CYTOP and PMMA-000 in the near UV region are shown in Fig.4.2.2.1-1. The refractive index dispersion of CYTOP is smaller than PMMA-000; therefore, CYTOP reduces colour aberration effect as compared with PMMA-000.

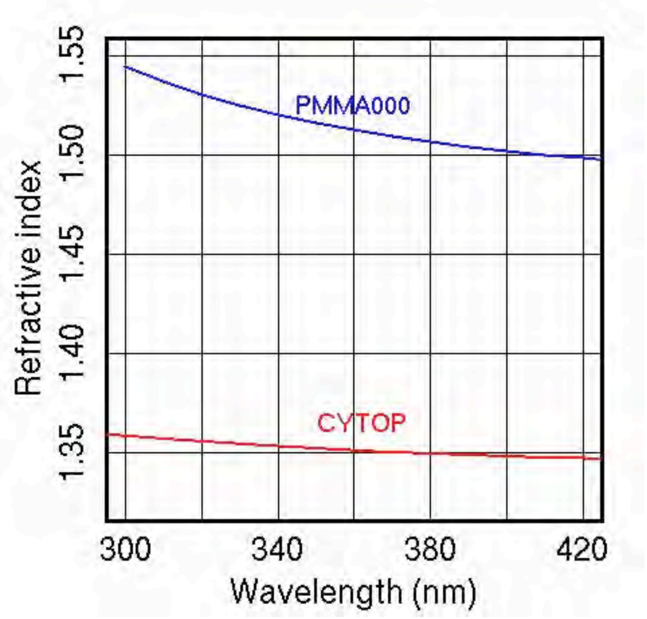

Figure 4.2.2.1-1. *Refractive index of CYTOP and PMMA-000 in the near-UV region.*

Temperature dependence of the refractive.

JEM-EUSO orbits around the Earth in ~90 minutes. Therefore, each lens has a thermal cycle synchronizing orbit. Refractive index is shifted by temperature changes which cause de-focusing effect. Thermal analyses predicted that each lens shifts ±10°C from the equilibrium temperature (see Tables 4.2.2.1-1 and 4.2.2.1-2). On the other hand, optics analysis by numerical ray-tracing method requires that temperature shift amount is below 0.0013/10°C. The measurement results of temperature dependence of refractive index are shown in Table 4.2.2.1-3 (CYTOP) and Table 4.2.2.1-4 (PMMA-000). The temperature shift amount is 0.0007/10°C (CYTOP) and 0.0009/10°C (PMMA-000); we confirmed that each value is below the requirement of 0.0013/10°C.

Table 4.2.2.1-1. *Thermal analysis of baseline optics design*

Part	Max temperature °C	Min temperature °C	Differential value °C
1st lens front side	-15.65	-19.00	3.35
1st lens back side	-14.73	-16.46	1.73
2nd lens front side	-6.51	-6.70	0.19
2nd lens back side	-4.10	-4.86	0.16
3rd lens front side	6.90	6.88	0.02
3rd lens back side	10.86	10.82	0.04

Table 4.2.2.1-2. *Thermal analysis of advanced optics design.*

Part	Max temperature °C	Min temperature °C	Differential value °C
1st lens front side	-15.77	-19.63	3.36
1st lens back side	-14.41	-15.92	1.51
2nd lens front side	-6.47	-6.65	0.18
2nd lens back side	-4.73	-4.87	0.14
3rd lens front side	6.54	6.51	0.03
3rd lens back side	12.47	12.42	0.05

Table 4.2.2.1-3. *Temperature dependence of refractive index (CYTOP, 404.656 nm h-line).*

Temperature	Refractive index	Differential refractive index value from 0 °C
25 °C	1.3481	-0.0018
0 °C	1.3499	0.0
-18 °C	1.3511	0.0012

Table 4.2.2.1-4. *Temperature dependence of refractive index (PMMA-000, 404.656 nm h-line).*

Temperature	Refractive index	Differential refractive index value from 0 °C
25 °C	1.5060	-0.0024
0 °C	1.5084	0.0
-18 °C	1.5100	0.0016

4.2.2.2. Transmittance

The transmittance curves for a 20 mm thickness layer of CYTOP and PMMA-000 are shown in Fig. 4.2.2.2-1.

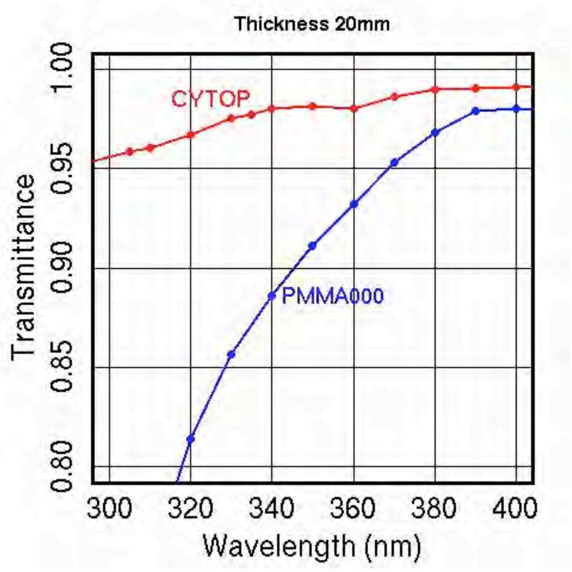

Figure 4.2.2.2-1. *Transmittance of CYTOP and PMMA-000 (20 mm thickness).*

4.2.3. Optics design

Cross-section views of Baseline and Advanced optics design are shown in Fig.4.2.3-1; the related parameters are listed in Tables 4.2.3-1, 2, and 3. The throughput curves in Fig. 4.2.3-2 show how much higher is the performance of the Advanced design with respect to the Baseline. The level of performance depends on several elements as, among them, surface roughness, surface reflection and corresponding scatter loss, and material absorbance. Advanced optics has better performance than Baseline because CYTOP has better transmittance than PMMA-000; furthermore, Advanced optics can select smaller spot size (2.5 mm) than Baseline optics, because CYTOP presents a smaller dispersion of refractive index than PMMA-000.

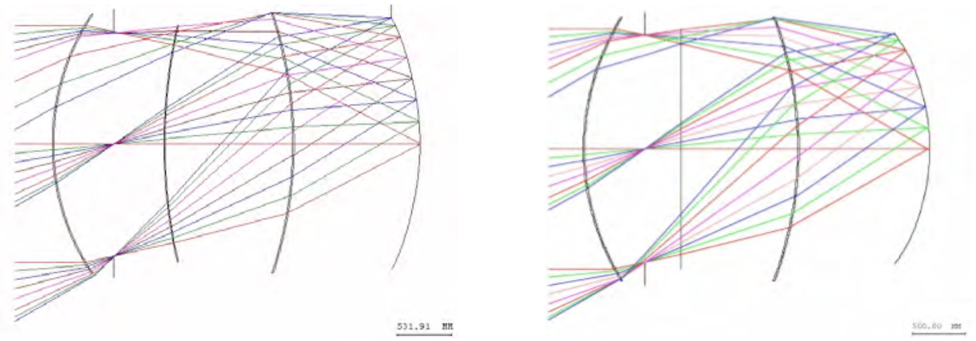

Figure 4.2.3-1. *Cross section views of Baseline (left) and Advanced (right) optics design .*

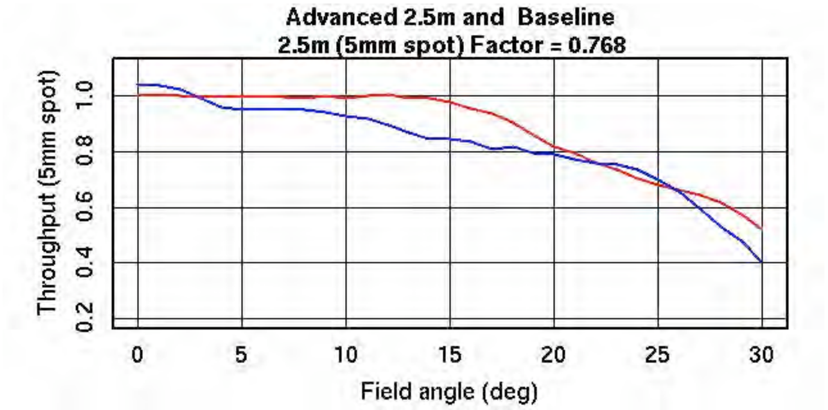

Figure 4.2.3-2. *Comparison of throughput performance between Baseline (blue) and Advanced (red) optics design. Each curve is normalized to the throughput advanced optics value with 0° incident angle.*

Table 4.2.3-1. *Requirements and parameters for the Baseline and Advanced optics design.*

	Requirements	Baseline optics	Advanced optics
f/# (F number)	< 1.25	1.0	1.0
Lens diameter	≥ 2.5 m	2.5 m	2.5 m
Spot size (RMS)	≤ 5 mm	5.0 mm	5.0 mm (2.5 mm)
Throughput	50% @ 0°÷10° 40% @ 10°÷20° 30% @ 20°÷30°	59% @ 0°÷10° 52% @ 10°÷20° 39% @ 20°÷30°	62% @ 0°÷10° 58% @ 10°÷20° 42% @ 20°÷30°
Filter transmittance	≥ 90%	>90%	> 90%

Table 4.2.3-2. *Lens parameters for the Baseline optics design.*

	1st lens	**2nd lens**	**3rd lens**	**Focal surface**
Material	PMMA-000	PMMA-000	PMMA-000	See Sect.4.3
Lens type	Curved doublet Fresnel	Curved Fresnel (precision lens)	Curved doublet Fresnel	Not Applicable
Diameter [mm]	2500.	2366.895	2500.	2289.268
Radius of curvature [mm]	2278.382	5175.611	4052.703	
Thickness [mm]	15.	10.	15.	Not Applicable
Weight (BEE) [kg]	95.4	59.3	89.8	See Sect.4.3

Table 4.2.3-3. *Lens parameters for the Advanced optics design.*

	1st lens	**2nd lens**	**3rd lens**	**Focal surface**
Material	CYTOP	PMMA-000	CYTOP	See Sect.4.3
Lens type	Curved doublet Fresnel	Flat Fresnel (precision lens)	Curved doublet Fresnel	Not Applicable
Diameter [mm]	2500.	2241.433	2500.	2212.
Radius of curvature [mm]	2432.7	Not Applicable	3632.1	
Thickness [mm]	15.	10.	15.	Not Applicable
Weight (BEE) [kg]	163.	51.	157.	See Sect.4.3

4.2.3.1. Detail of the lenses

To correct for chromatic aberration, the JEM-EUSO optics adds one intermediate precision Fresnel lens between the two curved double-sided ones. The curved double-sided Fresnel lenses in PMMA-000 material had been deeply investigated during the ESA-EUSO Phase-A study, confirming their basic performance; all details can be found in the related report [65]. In this section we will then report only to the newly added intermediate precision lens, indicated as the 2nd lens. In particular we will refer to the Advanced option, where the intermediate lens, in PMMA-000 material, presents one flat surface, and where the 1st and 3rd lenses are in CYTOP.

The two surfaces of the 2nd lens in the JEM-EUSO Advanced optics are characterized by:

- **Flat Fresnel surface**, acting as a “field lens”. This surface is able to make the spot size to be sharper. RMS spot size is improved from 5 mm to 2.5 mm, when this surface is added. Surface structure is shown in the Fig. 4.2.3.1-1. The Fresnel structure’ facets are only 26. Therefore, scatter loss of facet back-cuts is negligible.

- **Precision Fresnel surface**. The refractive index dispersion of the CYTOP material is lower than PMMA-000; therefore, the color aberration effect is reduced by using CYTOP as material for the 1st and 3rd lenses. Role of the precision surface on the 2nd lens is to reduce the still remained color aberrations by using diffractive effect. The concept of diffractive effect is shown in the Fig 4.2.3.1-2. Diffractive lens has opposite dispersion of the refractive ones, so being able to completely eliminate the remaining color aberration.

The precision Fresnel surface of the 2nd lens has grooves of height 0.694 μm and width varying from 6 μm to 100 μm. The manufacturing accuracy of groove height requirement is ±10% of 2λ, λ= 357 nm, that is below ±0.072 μm. A diameter 10 cm manufacturing result was ±0.036 μm.

This value satisfies the requirements of accuracy of groove height, and its surface roughness was below 16 nm (RMS), which value fulfils the requirement to be below 20 nm (RMS) (see 4.2.8.1).

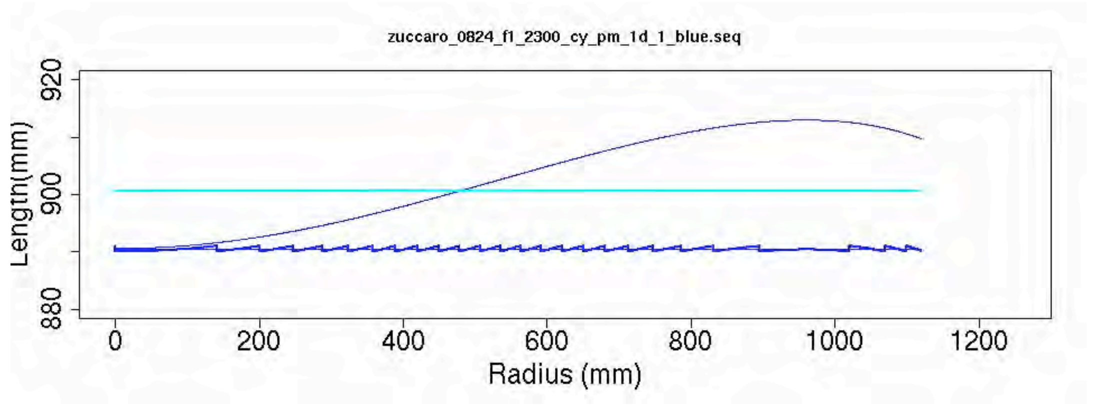

Figure 4.2.3.1-1. *Flat Fresnel surface of the 2^{nd} lens. Light blue line: precision Fresnel surface; blue line: Fresnel surface (blue curve line superimposed on Fresnel surface).*

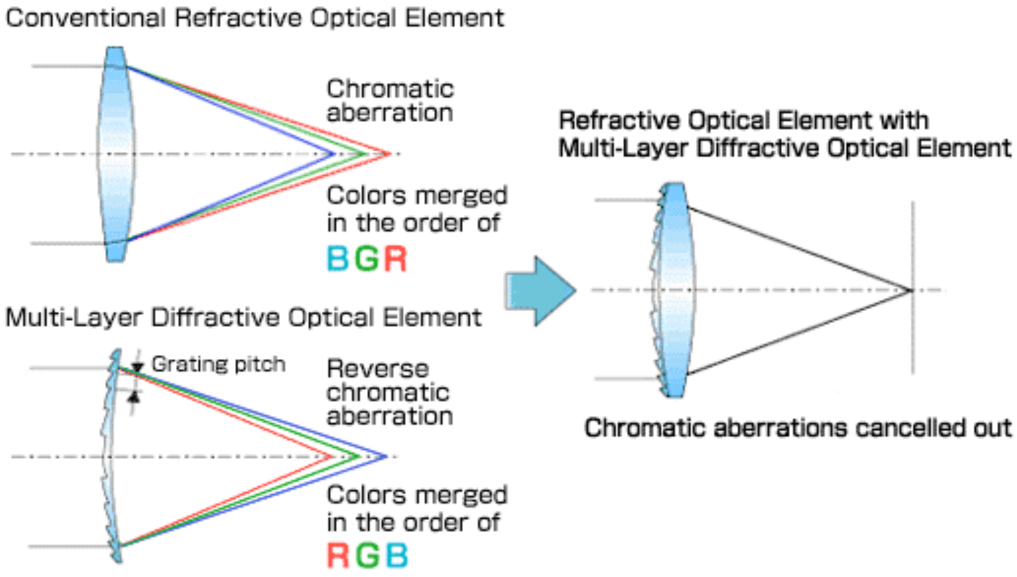

Figure 4.2.3.1-2. *Concept of colour aberration cancels by using diffractive element.*

4.2.4. Performance

In this section we will refer to the 2.5 m in diameter optical system (HTV install type side cut optics will be described in section 4.2.4.1). Let us define:

- **Encircled Energy** (EE): it is the ratio between the number of photons in the spot area and the photons which reached the focal surface;

- **Throughput** is the ratio between the number of photons in the spot area and those which passed through the iris.

EE and throughput were estimated by using a ray-tracing code that takes into account the material absorption, the Fresnel structure, and the surface reflection. The loss due to the surface roughness and to the depth error of the precision Fresnel structure are estimated by formulas which were verified during the ESA-EUSO Phase-A study.

The loss in transmittance due to the surface roughness is shown in Fig. 4.2.4-1 and Fig.4.2.4-2 where the transmittance is estimated by the formula

$$T = \exp\left[-\left(\frac{2\pi}{\lambda}\cdot RMS\cdot\Delta n\right)^2\right] \qquad (4\text{-}1)$$

where λ is the wavelength [nm], Δn is the difference of optical index between vacuum and material, and RMS refers to the surface roughness [nm].

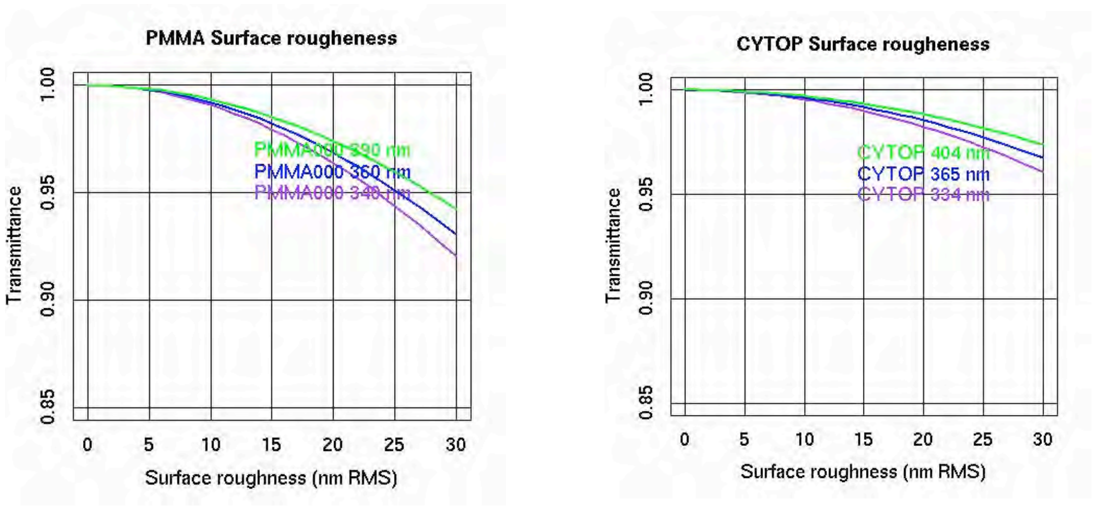

Figure 4.2.4-1. *Loss of transmittance due to the surface roughness for PMMA-000 (left) and CYTOP (right) materials at different wavelengths.*

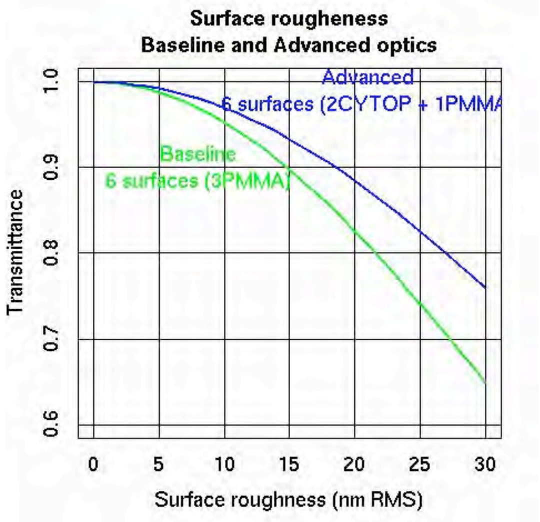

Figure 4.2.4-2. *Loss of transmittance due to the surface roughness. Comparison between Baseline and Advanced JEM-EUSO optics.*

The loss due to the depth error of the precision Fresnel structure is shown in Fig. 4.2.4-3 where the transmittance is derived from η efficiency defined as

$$\eta(\Delta z,\lambda) = \mathrm{sinc}^2\left[\left(\frac{\lambda_0 - \Delta z}{\lambda} - 1\right)\cdot \Delta n\right] \quad \text{here,} \quad \mathrm{sinc}(x) = \frac{\sin(\pi x)}{\pi x} \qquad (4\text{-}2)$$

where Δz is the depth error [nm], λ is the wavelength [nm], λ_0 is the optimized wavelength [nm], Δn is the difference of optical index between vacuum and material. Assuming that Δz follows a Gaussian distribution (σ nm RMS), the transmittance can be expressed as:

$$T(\lambda,\sigma) = \frac{1}{\sigma\sqrt{\pi}} \int \eta(z,\lambda)\cdot e^{-\left(\frac{z}{\sigma}\right)^2} dz \qquad (4\text{-}3)$$

Moreover, the loss due to the support structure obscuration is of the order of 12%, while the 10% loss due to the Fresnel facet back-cuts can be evaluated applying the Root & Peak error tool. All the losses are summarized in Table 4.2.4-1.

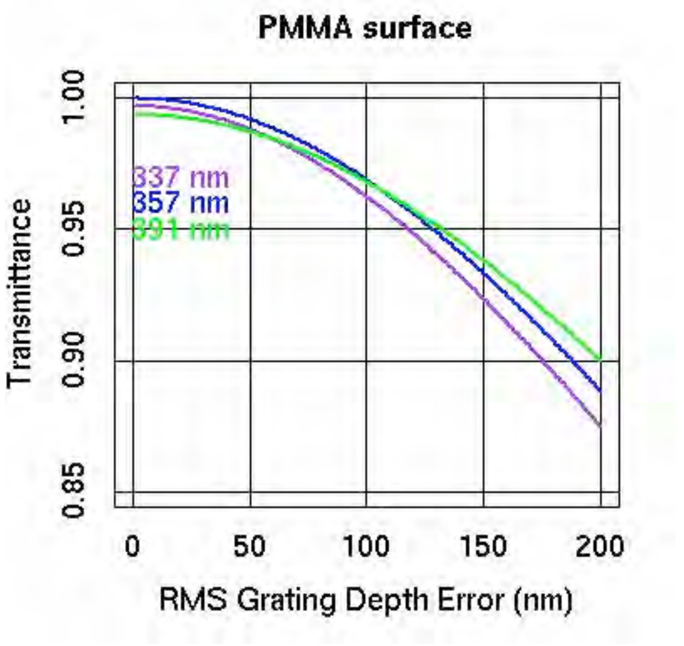

Figure 4.2.4-3. *Loss of transmittance due to the precision Fresnel structure depth error at the wavelength of the three main fluorescence lines.*

Table 4.2.4-1. *Summary of LOSS items.*

Item	**Loss factor**
Surface roughness	3% (15 nm RMS)
Precision Fresnel structure depth error	1%
Fresnel facet back-cuts Root & Peak tool error	10%
Support structure obscuration	12%

The addition of the Fresnel surface on the 2nd lens allows to improve the RMS spot size from 5 mm to 2.5 mm. Spot diagrams are shown in Fig. 4.2.4-4.

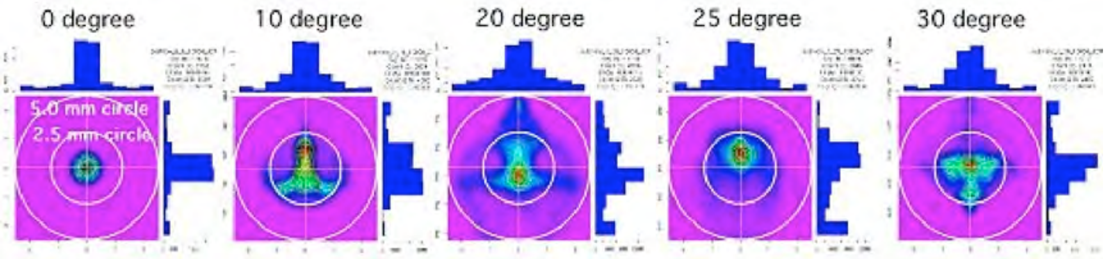

Figure 4.2.4-4. *Spot diagrams for Advanced optics at different angles (outer circle: 5 mm diameter; inner circle: 2.5 mm diameter).*

The improvement in the spot size reflects in the behaviour of both the Encircled Energy and the throughput for the JEM-EUSO Advanced optics, as shown in Fig. 4.2.4-5.

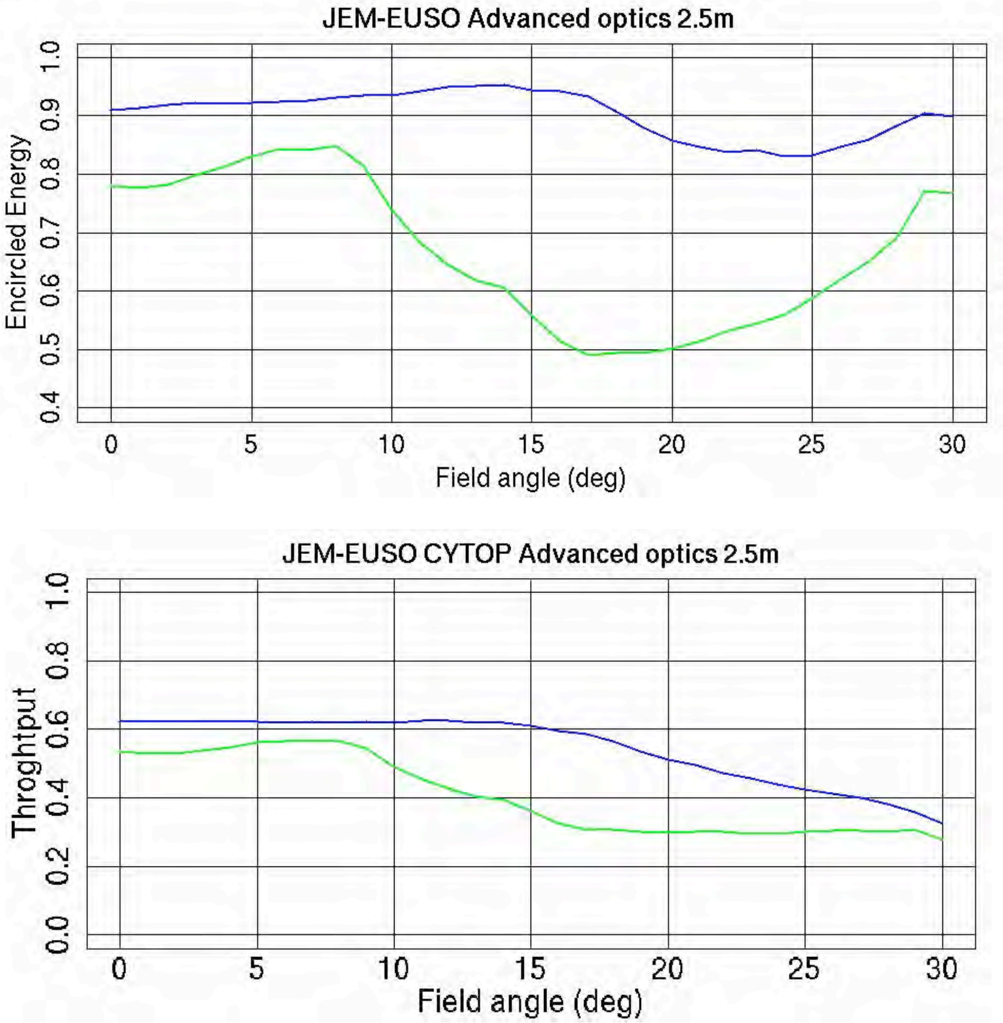

Figure 4.2.4-5. *The Encircled Energy (top panel) and the throughout (bottom panel) for the JEM-EUSO telescope, 2.5 m diameter, with Advanced optics. Two spot sizse are compared: 5 mm (blue curve) and 2.5 mm (green curve).*

4.2.4.1. The performance of the HTV stowing type optics

We have a telescope design to fit configuration of HTV stowing. Details of the design are described in section 4.7.1. Optics is enlarged from 2.5m to 2.6 m in diameter and cut side. The lens shape is 2.65m in diameter, 1.9 m in width. The side cut optics has ~90% aperture of 2.5m in diameter lens (original design). Performance of the side cut optics is shown in Fig 4.2.4.1-1. The HTV stowing optics keeps performance of 2.5m optics till 15° field angle; the field of view of side cut direction is limited to ~24°.

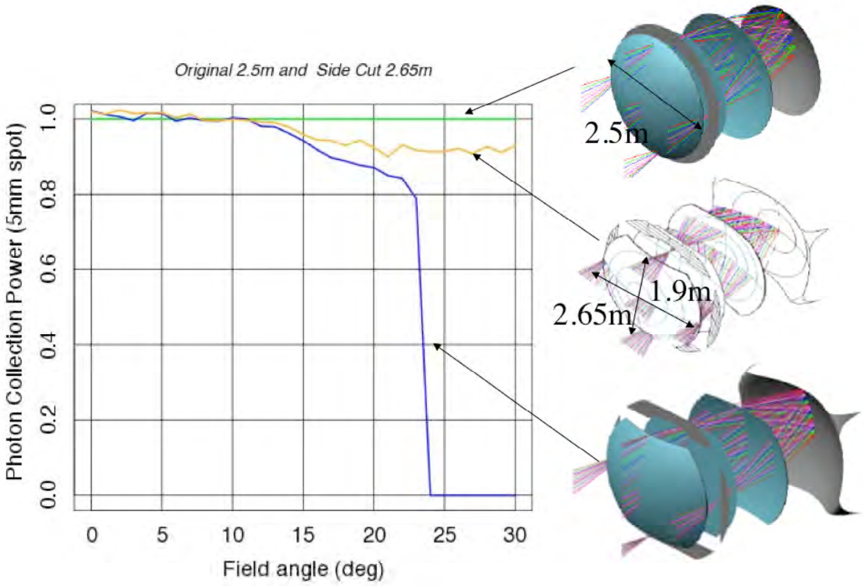

Figure 4.2.4.1-1. *Performance of the HTV stowing type optics, normalized with respect to the 2.5 m diameter case (green line). Blue curve: vertical direction from side cuts; yellow curve: parallel direction from site cuts.*

4.2.5. Tolerance analysis

JEM-EUSO optics does not need diffraction limit resolution like astronomical telescope. JEM-EUSO angular resolution tolerance is roughly 300 thousand times larger than the diffraction limit. Tolerance of the optics is much lower than astronomical telescope. JEM-EUSO optics tolerances an error of less than the spot size, because the f/# number is 1 and the incident angles of rays to the focal surface are less than 30 degrees.

We verified tolerance under two spot sizes, 5mm and 2.5mm, by using a ray-tracing code. The result for the 5mm case is similar to what obtained during the EUSO-ESA-Phase-A study [1]. We define tight tolerances based on spot size 2.5mm for securing possibility of using small pixel size detector. Each component of optics has 3 degrees of freedom, namely the axial displacement, the lateral displacement and the tilt (see Fig 4.2.5-1). The tolerances are shown in Table 4.2.5-1.

Table 4.2.5-1. *Tolerance requirements on the degrees of freedom.*

Degree of freedom	Requirement
Lateral displacement	Less than ± 2.5 mm
Tilt	Less than ± 2.5 mm
Axial displacement	Less than ± 2.5 mm

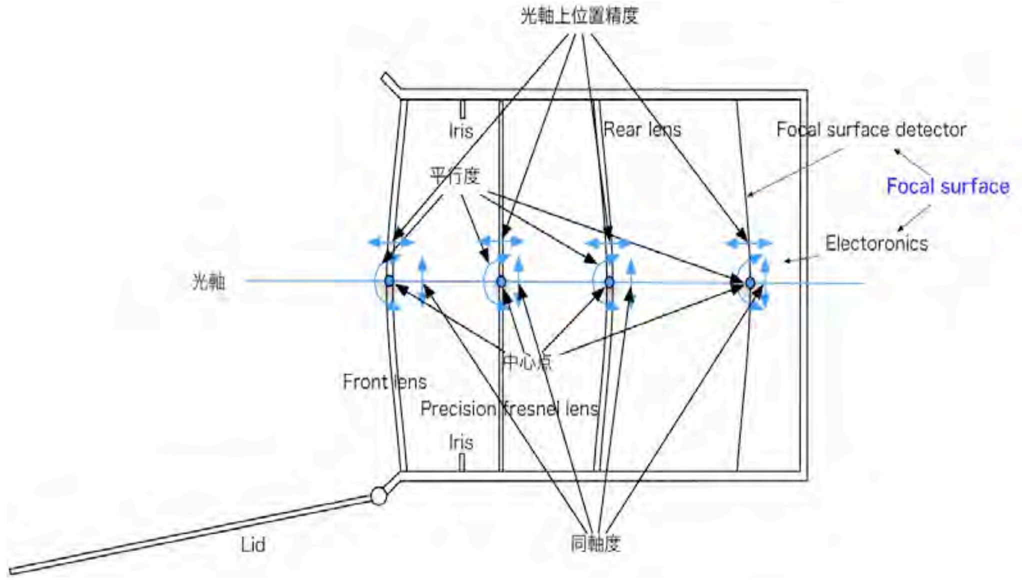

Figure 4.2.5-1. *Definition of the degrees of freedom.*

JEM-EUSO optics has a focusing adjust mechanism at the focal surface or 3rd lens to control thermal expansion of telescope structure, etc. The preliminary adjust stroke and step values are in Table 4.2.5-2; they will be reviewed when the details of the telescope structure will be defined. A conceptual design (by IHA aerospace) of a focusing adjust mechanism is shown in Fig. 4.2.5-2.

Table 4.2.5-2. *Requirements for focusing adjust mechanism.*

Item	Requirement
Adjust stroke	Longer than ± 12.5 mm
Adjust step	Less than ± 1.25 mm

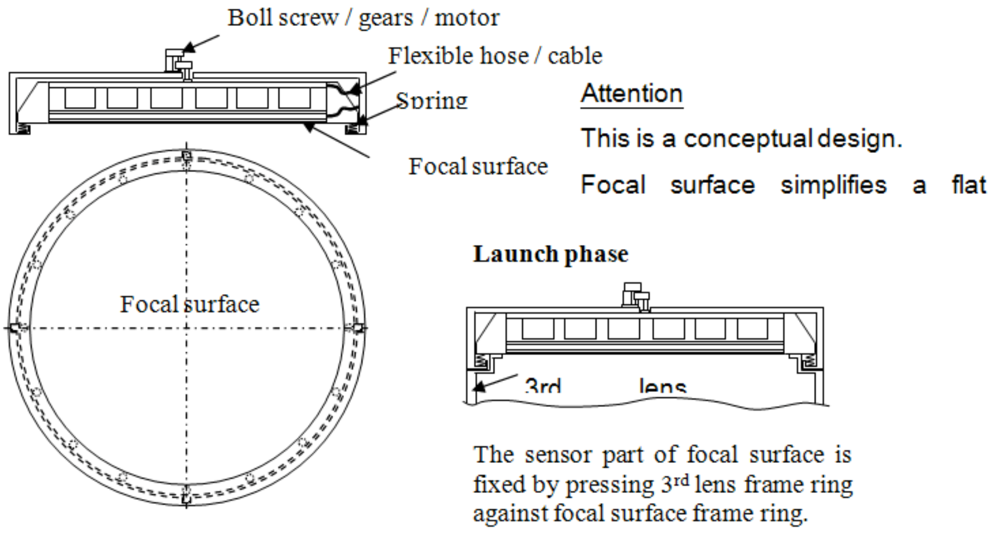

Figure 4.2.5-2. *Conceptual design of a focusing adjust mechanism (provided by IHA Aerospace Co.).*

4.2.6. Lens support structure

The basic design for the lens support structure corresponds to what already performed during the EUSO-ESA Phase-A study [65]. For what concerns the HTV stowing telescope configuration for JEM-EUSO, it will be defined during the next months.

4.2.7. Filters

4.2.7.1. BG3 baseline filters

The JEM-EUSO optics uses band-pass filters (330÷400 nm) to cut photons above 400 nm wavelength. The filters are set directly on the window of each photo-multiplier forming the focal surface detector, as sketched in Fig.4.2.7.1-1. The Schott BG3 absorption filter has been selected as baseline for JEM-EUSO; its transmittance curve is shown in Fig.4.2.7.1-1.

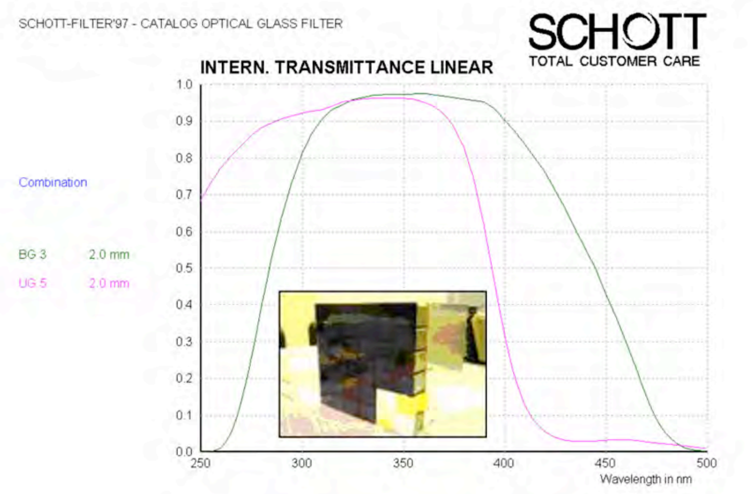

Figure 4.2.7.1-1. *Transmittance of the BG3 band-pass filter (green curve), to be set on each MAPMT .*

4.2.7.2. Advanced filters

The atmospheric fluorescence emission of interest for JEM-EUSO resides in the three Nitrogen lines (337nm, 357nm, 391nm). BG3 baseline filter, however, transmits photons between 250 nm and 500 nm. JEM-EUSO observes Nitrogen lines and background photons. Therefore, the signal-to-noise (S/N) ratio of detector is not the best under the influence of background photons.

Advanced filter is able to pass through only around the three Nitrogen lines. Advanced filter is a multilayer filter, which has 25 pair layers of Ta_2O_5/SiO_2. We coated the multilayer and tested its transmittance performance. If advanced filter is used, S/N ratio is improved 1.4 times high. Advanced filter performances are shown in Fig 4.2.7.2-1.

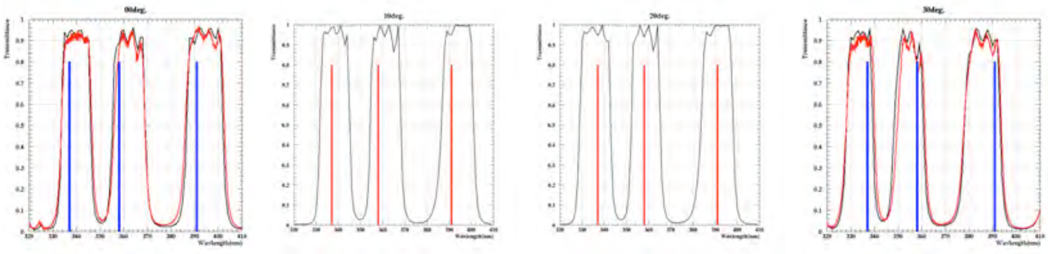

Figure 4.2.7.2-1. *Transmittance performance of the advanced filter as increasing incidence angle (0°, 10°, 20°, 30° from left to right panels).*

4.2.8. Lens manufacturing

4.2.8.1. Test piece manufacturing

The test piece refers to a 10cm diameter piece in CYTOP and PMMA-000 material.

CYTOP Fresnel structure manufacturing

Fresnel structure was manufactured by the Materials Fabrication Laboratory of RIKEN. We confirmed that the surface roughness is less than 15 nm (RMS), which satisfied the requirement maximum value of 20 nm (RMS).

Figure 4.2.8.1-1. *Pictures of manufacturing and test piece.*

PMMA-000 precision Fresnel structure manufacturing

Precision Fresnel structure is manufacturing on PMMA-000 by Materials Fabrication Laboratory of RIKEN. Grating depth of precision Fresnel structure is 0.694 μm. Grating pitch has various values between 6 μm and 100 μm. Grating depth requirement is smaller than ±0.072μm, which is 2λ of ±10%, to concentrate diffraction efficiency on the first order. Here, wavelength λ is 357 nm.

Manufacturing result was ±0.036 μm. This value is half of grating depth requirement. Surface roughness is less than 15 nm (RMS), which satisfied the requirement value of 20 nm (RMS).

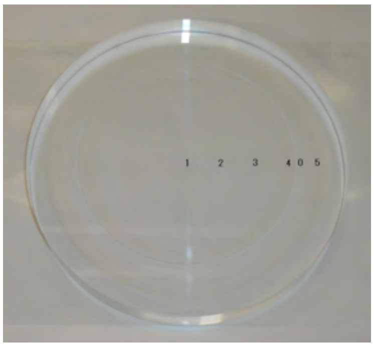

Figure 4.2.8.1-2. *PMMA-000 precision Fresnel structure manufacturing.*

4.2.8.2. Large lens manufacturing and test

Manufacturing

On June 2008, the UTD-3400 (Toshiba Machine Corp. product) machine was installed at IKEGAMI Mold Corp. The machine is able to manufacture lens up to 3.4 m in diameter lens (see Fig. 4.2.8.2-1 4). UTD-3400 has been under tuning-up phase from June to August 2008. Then UTD-3400 will start to manufacture three subscale PMMA-000 lenses (>1.5m in diameter) from September 2008. A reason for why we will manufacture PMMA-000 lenses is we had confirmed that the machine which has capability to manufacture PMMA-000 has capability to manufacture CYTOP by the 10 cm in diameter test piece manufacturing. These lenses will be transported to NASA and they will undergo to optical test by using NASA's facility.

Figure 4.2.8.2-1. *Large lens manufacturing machine UTD-3400 (Toshiba Machine Co.).*

Test and Verification for the Phase-B demonstration system

To assist in raising the Technology Readiness Level (TRL) of the JEM-EUSO optics, our U.S. partners at NASA/MSFC will propose to the MSFC management the use of Technology Investment Program (TIP) funds for testing two demonstration systems that will be manufactured in Japan. The first system will be a subscale prototype and is made up of the central 1.5 meters of all three optical elements, assembled in a non-flight structure and used for optical testing. The second system will be a single flat PMMA-000 disk of 2.6 meters diameter that has a series of cuts between 0.75 and 1.3 meters radius. The cuts should demonstrate manufacturing the most difficult parts of the JEM-EUSO optical prescription, the Fresnel pattern and the blazed grating on the diffractive surface at the edge of the lenses.

Currently, the characterization of standard Fresnel lens by Industry includes a visual inspection of groove geometry using a high-powered microscope followed by an optical performance test. Techniques for evaluating the unique performance of the multiple element JEM-EUSO optical system have not been addressed in Industry but were developed by the U.S. EUSO team during their MIDEX Phase-A, and reported in the Concept Study Report.

If the TIP proposal is accepted, in the U.S. we will measure the surface roughness and the local profiles of the Fresnel and diffractive surfaces of both demonstration systems in the radial and tangential directions at the centre of the lenses and the edges using a special optical instrument developed for measuring the Chandra X-ray telescope mirrors and a contact profilometer. The results of these measurements will be compared to manufacturing errors (tolerances) required for the optics to meet JEM-EUSO requirements as determined by optical simulations. These simulations should establish limits on surface roughness (or errors at high spatial frequency), on radial and tangential slope errors (at lower spatial frequencies) and on plunge cut depth errors in the blazed grating. The comparison will allow the verification of the manufacturing processes and machines that will be used to make the 2.6m flight optics.

In addition, if the TIP proposal is accepted, using a 2 meter collimator located at a facility at the U.S. Army in Huntsville, Alabama, we will perform a full aperture optical test of 1.5m prototype at 300-400 nm at incident angles from 0 to 30 degrees. Planned measurements of the optical properties include: imaging accuracy and resolution, photometric influence distribution, and veiling glare and stray-light measurements.

All these measurements and test results will be used to validate our models for the JEM-EUSO optics so that we can predict the true performance of the 2.6 meter diameter flight optics system.

Test and verification for the 2.6m flight system

If the U.S. EUSO proposal to NASA is accepted, the U.S. project will conduct extensive verification on the Optical System (OS) to ensure that it meets all requirements. Our verification approach will rely heavily on the testing of the flight hardware as shown on Figure 4.2.8.2-2 and discussed below. Other verification methods will include analysis, and inspections.

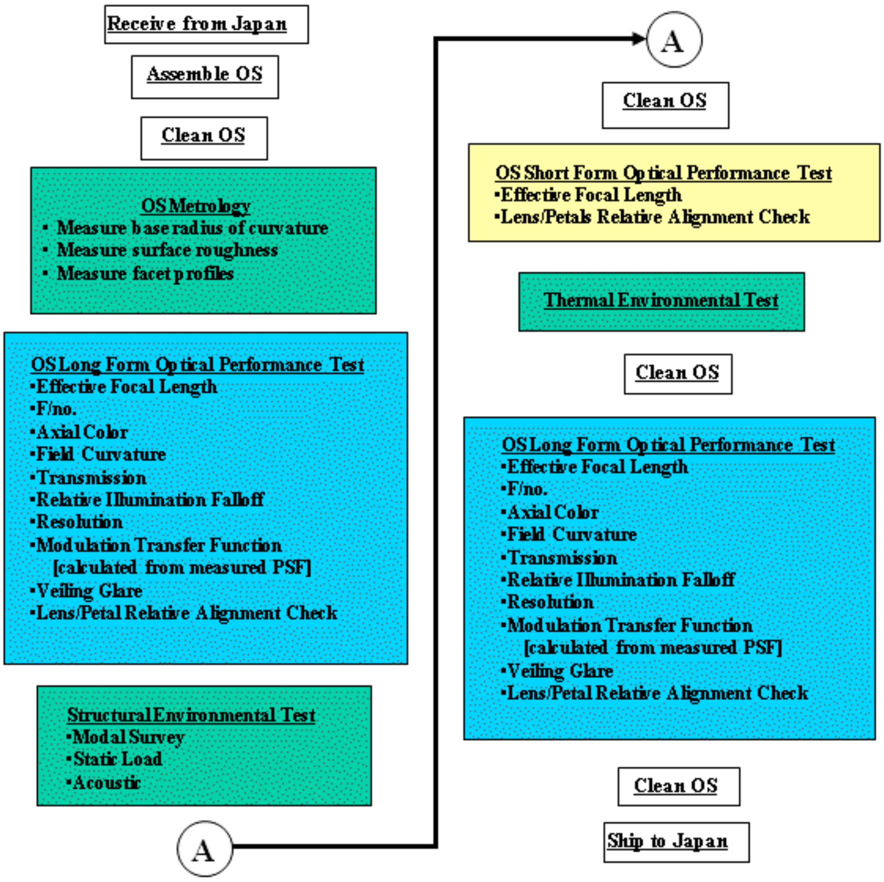

Figure 4.2.8.2-2. *Optical System test flow.*

The U.S. EUSO team will follow a proto-flight test program. Proto-flight is a term used to indicate the type of testing program that will occur at the subsystem level and means that the deliverable end item used for flight will also be used to qualify the design for the expected environment and to provide acceptance for design and performance requirements. Two complete OS units will be built. One set will be the flight unit, and the other will be used as a spare.

After the optical element frames, the focusing mechanisms, the Ground Support Equipment (GSE) metering structure and the shipping container have been completed, they will be assembled. After the optical elements have been manufactured and inspected, they will be mounted in the frames and aligned using laser retro-reflectors to establish reference points (see Fig. 4.2.8.2-3). These retro-reflectors will be utilized during all phases of the optics testing to ensure the alignment of the lens segments and the lenses relative to each other. The frames will then be installed in the GSE metering structure whose purpose is to hold the lenses in the same relative positions as they will be on orbit, so that their optical performance may be measured and baselined prior to delivery. The GSE metering structure containing the lenses in their frames will be shipped to MSFC.

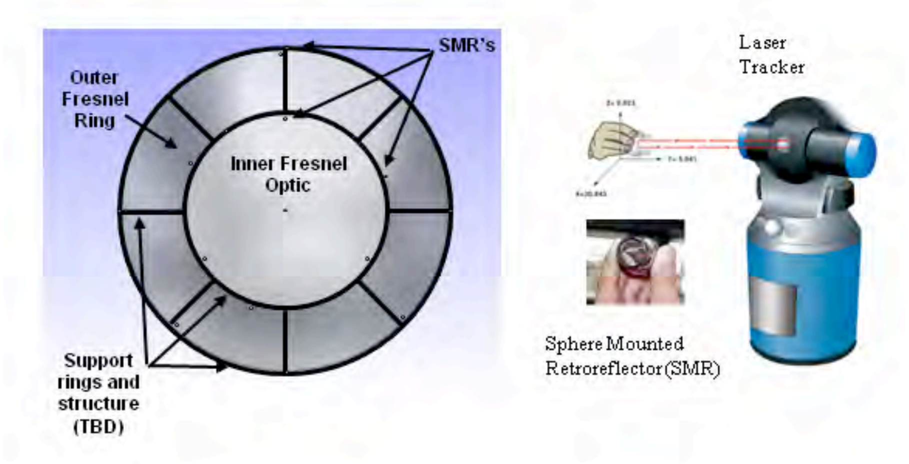

Figure 4.2.8.2-3. *Alignment concept.*

At MSFC, a modal survey will be made of the lens/frame assemblies. The lens/frames assemblies will then be cleaned and placed in a thermal vacuum chamber to measure thermal conductance across attach points. These data are necessary for system thermal analysis by JAXA.

Following testing at MSFC, the lens/frame/metering structure assembly, along with a GSE focal surface attachment for mounting light detectors, will be placed in its shipping container and taken to Wright-Patterson AFB for optical performance testing. After attachment of the focal surface and detectors, the assembly will be placed in a chamber with a large-diameter collimated light source to measure and baseline the system's ability at full aperture to concentrate and focus light across the full field of view. These tests will be conducted in vacuum and at temperatures over the range expected in flight. They will include tests of the focusing mechanism.

Following the Optical Performance Test, the assembly will be brought back to MSFC for cleaning and inspection and then returned to its shipping container and transported to Japan. JAXA will complete the integration and system testing there, including thermal vacuum bake-out.

Environmental test philosophy

For the JEM-EUSO Instrument, the environmental testing philosophy is to develop and test a proto-flight unit, verifying design via the subscale prototype and incorporating knowledge from its testing into the proto-flight unit. Testing will provide confidence that the designs will perform as expected in the prescribed environments, which will be defined by JAXA in ICD's to be provided at the beginning of Phase B. Sufficient margin will be included in the designs to satisfy both NASA and JAXA requirements applicable to HTV transport and ISS installation.

The testing of U.S. provided hardware is necessarily limited to the component and subassembly levels of integration. These tests will cover mechanical structure, thermal and material properties, and space environmental effects. Specifically, the tests will include acoustic-vibration environments relevant to ground and HTV transportation, and ensure thermal-vacuum compatibility and compliance with both HTV and ISS environments.

4.2.9. Operation

The optics will have to fulfil different operations during the various phases of the mission.

Table 4.2.9-1. *Operation of optics*

Operation phase	**Operation mode**
Before launch	Keeps constant temperature and keeps out of shocks. Covers on lens surfaces to protect from falling objects.
Transportation to ISS	
Launch time	Follows environment of HTV un-pressurized module. Protect from falling objects by using lid.
Stand-by phase to attach the ISS and attaching phase	Follows environment of ISS. Protect form debris and sunlight by closing lid.
Observation phase	
Normal operation	Follows environment of ISS. Open/close the lid synchronizing with orbit to protect from debris and sunlight.
Approaching transportation vehicle phase and ISS attitude controlled phase	Closes the lid. If needs, transforms to HTV stowing mode.
Onboard calibration mode	Adjusts focal position by using focal adjust system.
End of mission	Transforms to HTV stowing mode.

4.2.10. Summary

4.2.10.1. Specifications

Table 4.2.10.1-1. *Optics requirements.*

Code	**Item**	**Required value**	**Note**
IR1	Wavelength	330÷400 nm	Including 337, 359, 391 nm lines of Nitrogen.
OPR1	Aperture diameter	≥ 2.5 m	
OPR2	Field of View, FoV	≥ ±30°	
	F number (f/#)	≤ 1.25	OPR1/OPR2
OPR3	Angular resolution	≤ 0.1°	For determining the arrival direction of the primary particle within few degrees.
OPR3	Spot size	≤ 5 mm in diameter	Corresponding to the light detector pixel size less than 4.5 mm. Corresponding to less than 0.1° in spatial resolution.
OPR4	Photon collecting efficiency (Throughput)	50% @ 0°÷10° 40% @ 10°÷20° 30% @ 20°÷30°	Indicating the focus efficiency on a spot size 5 mm in diameter on the focal surface. Upon consideration of: structure of Fresnel lens (back-cuts, etc.), transmittance of materials, reflection on lens surface, error in diffractive optics manufacturing, error in Fresnel lens manufacturing, and loss in lens support structure.
OPR5	Filter transmittance	≥ 90%	Should avoid a degradation of the performance by more than 10% during the mission.

Table 4.2.10.1-2. *Optics technical readiness levels.*

Code	Item	Technical Readiness Level (TRL) and its reason when selected in Febr.'07	Verification status of TRL and reason (as of Apr.'08)	Expected TRL and activities at SDR time (Mar.'09)
IR1	Observational wavelength	TRL4 Verified by observed spot size with test lens of 20 cm, 40 cm, and 1 m diameter; lens in EUSO-ESA Phase-A Study [65]. Wavelength dependence of CYTOP material on refraction and transmittance was verified.	TRL4 In addition to the left column, the following four verifications were accomplished: - Verification of the optical performance in case of CYTOP by using optics design software CodeV. - Optimization of designing to reduce the spot size to ½ by using CodeV. - Measurement of refractive index and its temperature dependence and transmittance in case of the usage of CYTOP. - Verification of the manufacturing CYTOP lens using a small piece of 10 cm diameter.	TRL5 Fabricate 2.5 m lens dividing it in two parts: a central part of 1.5 m, and the circular ring part. Optical performance of the central part to be verified (before March '09).
OPR1	Entrance diameter	TRL3 Verified by using CodeV. Further enlargement of the diameter and stowing capability in HTV to be verified.	TRL4 Stowing capability in HTV was verified by enlarging the diameter to 2.65 m diameter (cutting lateral parts).	TRL5 The same as above.
OPR2	Field of View	TRL4 Verified by using CodeV.	TRL4 Refer to IR1.	TRL5 The same as above.
OPR3	Angular resolution	TRL4 Verified by using CodeV.	TRL4 Refer to IR1.	TRL5 The same as above.
OPR3	Spot size	TRL3 Verified by using CodeV. There is some room to optimize the design for a further improvement of the performance by reducing the spot size.	TRL4 Refer to IR1.	TRL5 The same as above.
OPR4	Photon collecting power (Throughput)	TRL3 Verified by using CodeV. It is necessary to verify the possibility of processing CYTOP material.	TRL4 Refer to IR1.	TRL5 The same as above.

Table 4.2.10.1-3. *Optics main parts (PFM, Pre-flight model; FM, flight model).*

Item	Number	Supplier	Result of test	Notes
1st lens Baseline: PMMA-000 Advanced: CYTOP	2 (PFM, FM)	Manufacturing: RIKEN Material: Mitsubishi Rayon Material: AGC	Space qualification: see [65] Manufacturing: verified by test piece manufacturing	
2nd lens Baseline: PMMA-000 Advancd: PMMA-000	2 (PFM, FM)	Manufacturing: RIKEN Material: Mitsubishi Rayon	Space qualification: see [65] Manufacturing: verified by test piece manufacturing	
3rd lens Baseline: PMMA-000 Advanced: CYTOP	2 (PFM, FM)	Manufacturing: RIKEN Material: Mitsubishi Rayon Material: AGC	Space qualification: see [65] Manufacturing: verified by test piece manufacturing	
Lens frame	1 (share with PFM and FM)	IHI Aerospace Co. Nippi Co.	Under designing	
Focusing adjust system	1 (share with PFM and FM)	IHI Aerospace Co. Nippi Co.	Under designing	

Table 4.2.10.1-4. *Optics temperature requirements*

Item	Operation temperature	Non-Operation temperature	Comments
3 lenses + frame	T_0±10°C (-30°C < T_0 < +30°)	-45°C ~+45 °C	Each lens has an independent equilibrium temperature T_0.

Table 4.2.10.1-5. *Optics house-keeping requirements*

Item	Requirement
Temperature monitor	15 points, 5 point per lens (center, 1 point; circular parts: 4 points)
Sampling	10/12 samplings per orbit
Focus adjust system position monitor	1 sampling per orbit

Table 4.2.10.1-6. *Mass budget (Baseline optics).*

Parts	BEE [kg]	Margin [%]	Total [kg]	Comments
1st lens	89	15	103	PMMA-000 15 mm thickness
Frame of the 1st lens	-	-	-	Included in pallet frame
Stop (iris)	-	-	-	Included in 2nd lens frame
2nd lens	55	15	64	PMMA-000 10 mm thickness
Frame of the 2nd lens	55	15	64	
3rd lens	84	15	97	PMMA-000 15 mm thickness
Frame of the 3rd lens	55	15	64	
Focusing adjust system	20	15	23	
Total	***358***		***415***	

Table 4.2.10.1-7. *Mass budget (Advanced optics).*

Parts	**BEE [kg]**	**Margin [%]**	**Total [kg]**	**Comments**
1st lens	150	15	173	CYTOP 15 mm thickness
Frame of the 1st lens	-	-	-	Included in pallet frame
Stop (iris)	-	-	-	Included in 2nd lens frame
2nd lens	47	15	55	PMMA-000 10 mm thickness
Frame of the 2nd lens	55	15	64	
3rd lens	144	15	166	CYTOP 15 mm thickness
Frame of the 3rd lens	55	15	64	
Focusing adjust system	20	15	23	
Total	***471***		***545***	

Table 4.2.10.1-8. *Optics power budget.*

Parts	**BEE [Watt]**	**Margin [%]**	**Total [Watt]**	**Comments**
Focusing adjust system	10	15	12	

Table 4.2.10.1-9. *Optics telemetry budget.*

Parts	**BEE [kbps]**	**Margin [%]**	**Total [kbps]**	**Comments**
Focusing adjust system	TBD	15	-	
Housekeeping, HK	TBD	15	-	

4.2.10.2. Cost

The following table shows the cost, in US Dollars, subdivided in Financial Years (FY) from 2008 to 2013.

Table 4.2.10.2-1. *Cost [US$]*

	FY08	**FY09**	**FY10**	**FY11**	**FY12**	**FY13**
Phase A/B	183,124	4,049,433	1,199,981			
Phase C/D			9,093,931	7,136,476	6,490,009	4,044,885
Phase E						247,639
Phase F						
PI Mission Cost	**183,124**	**4,049,433**	**10,293,912**	**7,136,476**	**6,490,009**	**4,292,524**
Contributions	461	3,786	5,833	5,999	6,176	134,716
SEO Activities	0	0	0	0	0	0
Total Enhanced Mission Cost	183,585	4,053,219	10,299,745	7,142,475	6,496,185	4,427,240

Total cost: 32.6 M$ ≈ 3.3 BYen

4.2.10.3. Schedule

Schedules of FY 2008 and after FY 2008 are shown in Table 4.2.10.3-1 and 4.2.10.3-2. We will manufacture three subscale lenses of baseline optics by using the UTD-3400 machine by the end of November 2008. Seizes of these lenses are larger than 1.5m in diameter. These lenses will be sent to NASA after the end of November 2008. US team will do optical test of the three subscale lenses of baseline optics and report by April 2009.

Table 4.2.10.3-1. *Optics schedule of FY 2008.*

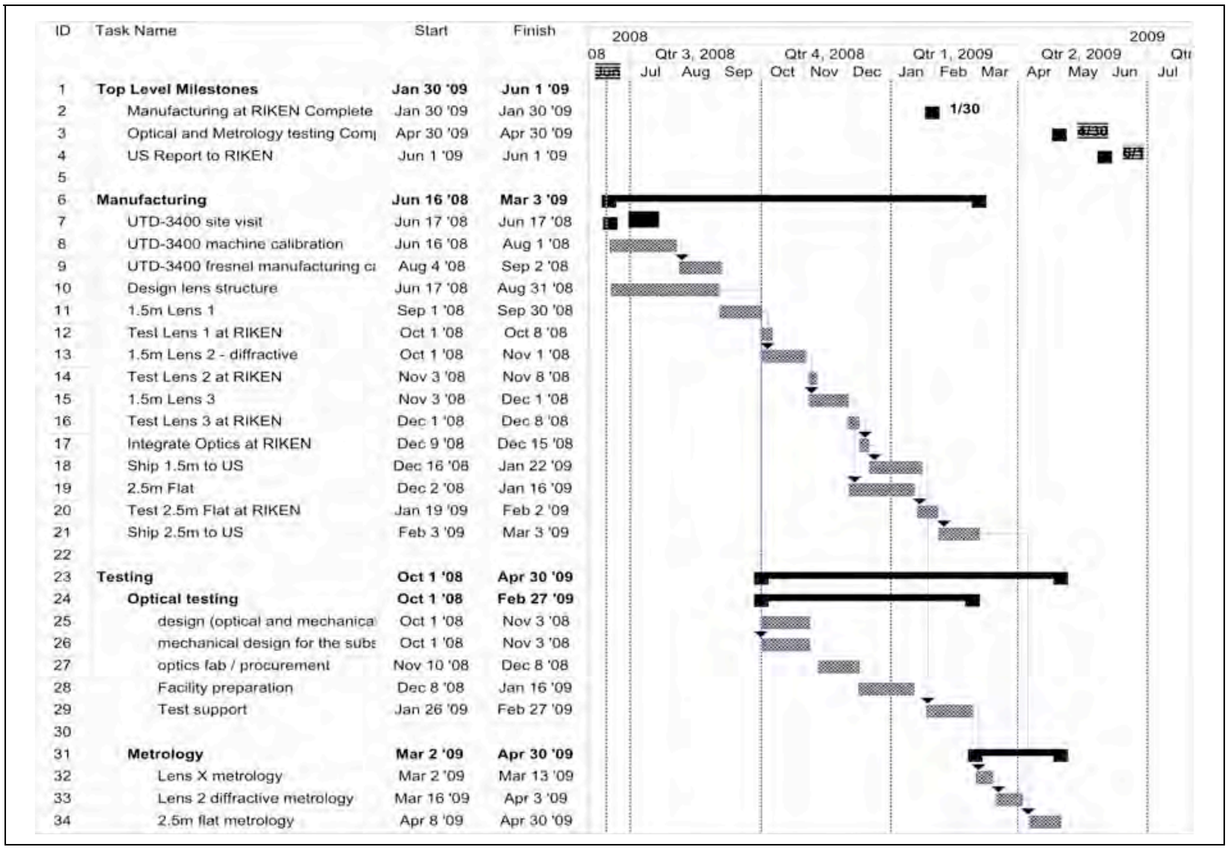

ID	Task Name	Start	Finish
1	**Top Level Milestones**	**Jan 30 '09**	**Jun 1 '09**
2	Manufacturing at RIKEN Complete	Jan 30 '09	Jan 30 '09
3	Optical and Metrology testing Com	Apr 30 '09	Apr 30 '09
4	US Report to RIKEN	Jun 1 '09	Jun 1 '09
5			
6	**Manufacturing**	**Jun 16 '08**	**Mar 3 '09**
7	UTD-3400 site visit	Jun 17 '08	Jun 17 '08
8	UTD-3400 machine calibration	Jun 16 '08	Aug 1 '08
9	UTD-3400 fresnel manufacturing c	Aug 4 '08	Sep 2 '08
10	Design lens structure	Jun 17 '08	Aug 31 '08
11	1.5m Lens 1	Sep 1 '08	Sep 30 '08
12	Test Lens 1 at RIKEN	Oct 1 '08	Oct 8 '08
13	1.5m Lens 2 - diffractive	Oct 1 '08	Nov 1 '08
14	Test Lens 2 at RIKEN	Nov 3 '08	Nov 8 '08
15	1.5m Lens 3	Nov 3 '08	Dec 1 '08
16	Test Lens 3 at RIKEN	Dec 1 '08	Dec 8 '08
17	Integrate Optics at RIKEN	Dec 9 '08	Dec 15 '08
18	Ship 1.5m to US	Dec 16 '08	Jan 22 '09
19	2.5m Flat	Dec 2 '08	Jan 16 '09
20	Test 2.5m Flat at RIKEN	Jan 19 '09	Feb 2 '09
21	Ship 2.5m to US	Feb 3 '09	Mar 3 '09
22			
23	**Testing**	**Oct 1 '08**	**Apr 30 '09**
24	**Optical testing**	**Oct 1 '08**	**Feb 27 '09**
25	design (optical and mechanica	Oct 1 '08	Nov 3 '08
26	mechanical design for the subs	Oct 1 '08	Nov 3 '08
27	optics fab / procurement	Nov 10 '08	Dec 8 '08
28	Facility preparation	Dec 8 '08	Jan 16 '09
29	Test support	Jan 26 '09	Feb 27 '09
30			
31	**Metrology**	**Mar 2 '09**	**Apr 30 '09**
32	Lens X metrology	Mar 2 '09	Mar 13 '09
33	Lens 2 diffractive metrology	Mar 16 '09	Apr 3 '09
34	2.5m flat metrology	Apr 8 '09	Apr 30 '09

Table 4.2.10.3-2. *Optics schedule after financial year FY 2008.*

Lens	FY08	FY09	FY10	FY11	FY12	FY13
Prototype model	Manufacturing					
Preflight model		Manufacturing & Testing				
Flight model			Manufacturing & Testing			Deployment

4.2.10.4. Organization

Subsystem leaders: Roy Young (NASA/MSFC), Yoshiyuki Takizawa (RIKEN).

Members: H. Omori, K. Maekawa, Y. Hachisu, T. Katahir, M. Mizutani (RIKEN), J. H. Adams, S. Mitchell, M.J. Christl, J. Watts Jr., A. English, R.Young (NASA/MSFC) , Y. Takahashi, D. Gregory, M. Bonamente, V. Connaughton, K. Pitalo, J. Hadaway, J. Geary, R. Lindquist, P. Reardon, T. Blackwell (Univ. Alabama), H. Crawford, E. Judd, C. Pennypacker (LBL, Univ. California ,Berkeley), V. Andreev, K. Arisaka, D. Cline (UCLA), A. Berlind ,T. Weiler, S. Czorna (Vanderbilt Univ.), R. Chipman, S. McClain (Univ Arizona).

The following two references must be checked; where are they cited in this 4.2 paragraph ?

~~[2]:~~ Optics design file, 1114_f1_2300_pm_1d_3

[~~3]:~~ Optics design file, 0824_f1_2300_cy_pm_1d_1

If related to some particular graphics, these references could be cited in the proper figure caption, and not in the general list of References.

4.3. Focal Surface Detector and Electronics

4.3.1. General

The Focal Surface (FS) of JEM-EUSO has a curved surface of about 2.3 m in diameter, and it is covered with more than 5,000 Multi-Anode PhotoMultiplier Tubes, MAPMT, (Hamamatsu R8900-M36). The FS detector consists of Photo-Detector Modules (PDMs), each of which consists of 9 Elementary Cells (ECs) arranged in an array of 3×3. About 1,233 ECs, corresponding to about 137 PDMs, are arranged on the whole FS (Figure 4.3.1-1).

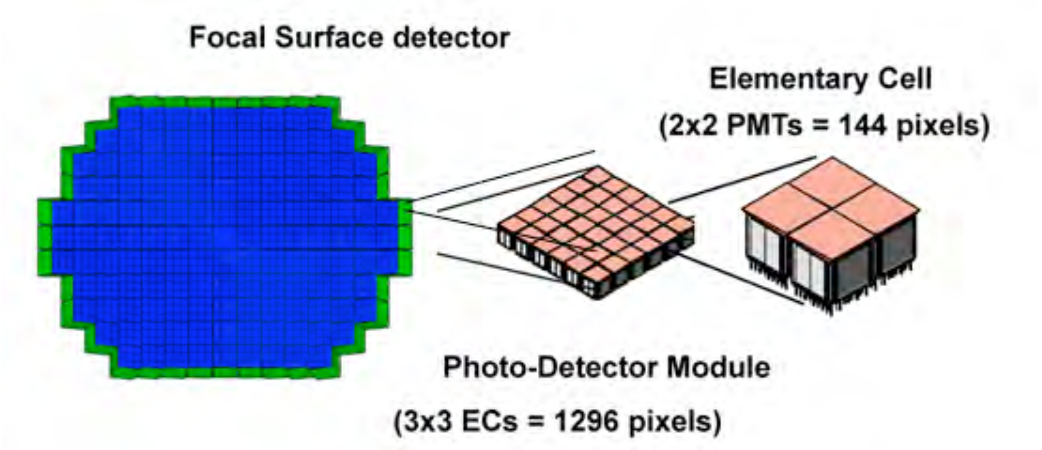

Figure 4.3.1-1. *Focal surface detector and its structure.*

4.3.1.1. Definitions

The FS of the JEM-EUSO instrument, located onto the focal surface of the optics, consists of the Photo-Detector (PD) and the Read-Out electronics.

Coordinate system:

The coordinates within the FS are defined as follow:

- Origin of the Cartesian axes at the centre (vertex) of the FS.
- The Z-axis passes by the centre of the optics, in the direction from the FS to the optics, i.e., towards Earth.
- The X-axis is parallel to the moving direction of the ISS, in the same direction as the ISS.
- The Y-axis, together with the above X- and Z-axis, is defined by the right-handedness of the coordinate system.

Location:

The surface of the FS-Photo-Detector is accommodated on the focal surface of the optics.

Main parts:

The FS main components are:

- FS Detector, and
- FS Electronics.

Lifetime:

The lifetime of the FS is defined in the JEM-EUSO system specification.

4.3.1.2. Requirements

Performance requirements:

- The FS shall be capable to detect the EAS by observing the fluorescence light produced during the EAS development and the Cherenkov light.
- The FS shall be capable to determine the position of the arriving photons as a function of time and to follow the space-time development of the EAS.
- The FS shall have single-photon sensitivity in the 330 nm ÷ 400 nm wavelength range to detect EAS as faint as possible.
- The FS shall have fast response (well below 0.1 μs) to follow the space-time development of the EAS.
- The FS pixel size shall correspond to a pixel size on Earth no greater than $\Delta\alpha=0.1°$.
- Cross talk between neighbouring pixels shall be less than 10 % (TBC).
- The noise rate shall be two orders smaller than the rate of the night airglow background.
- Overall detection efficiency shall be good and uniform. The overall detection efficiency, averaged over all the FS, shall be $\varepsilon_{PD} \geq 0.12$.
- The FS shall cover the optical focal surface with a sensitive area as large as possible by reducing dead or inefficient areas.
- The FS shall have low sensitivity to magnetic fields of the order of magnitude of ~ 1 Gauss.
- The FS shall be highly reliable and stable over at least a 5 years' time.
- The FS shall be compatible with the requirements imposed by a Space Mission.

Physical requirements:

- The mass is required by the JEM-EUSO Instrument System.
- The centre of gravity shall be on the Z-axis with a tolerance of less than TBD mm.
- The FS structure shall be able to be installed within the JEM-EUSO telescope envelope.

Thermal requirements:

- The FS shall be designed so that the temperature does not exceed 50 °C at any time, to protect the bialkali photocathode.
- To figure out the property of the device, we will measure the temperature with the accuracy within $\Delta T = \pm 5$ °C on the whole region of the focal surface.
- The FS shall be designed so that the temperature must not fall below -30°C for the operation safety of the electronics.

Shape assumption:

The FS generated by the optical system has an aspheric shape given by the following equation (in cylindrical coordinates).

$$z[r] = \frac{r^2}{\left(1+\sqrt{1-\frac{(1+k)r^2}{\rho^2}}\right)\rho} + a\,r^4 + b\,r^6 + c\,r^8 + d\,r^{10} + z_0 \qquad r \equiv \sqrt{x^2+y^2}$$

where: $\rho = -2551.41$ mm; $k = 0.480130$; $a = -0.\ 430458\times 10^{-10}$ mm^{-3}; $b = 0.\ 138070\ 10^{-15}$ mm^{-5}; $c = -0.\ 126951\ 10^{-21}$ mm^{-7}; $d = 0.\ 353757\ 10^{-28}$ mm^{-9}, and z_0 is the quota of the vertex of the FS.

On the other hand, on the FS detector, modules of identical shape are arranged on an approximate spherical shape. The shape of the FS shall be assumed to be a spherical surface:

$$z_s[r] = \sqrt{\beta^2 - r^2} - \beta \qquad r \equiv \sqrt{x^2+y^2}$$

where $\beta = 2114.15$ mm.

4.3.2. FS detector

The detector on the focal surface is essentially composed by:

- Photo-detector, PD (array of multi-anode photomultipliers, MAPMTs)
- MAPMT support structure
- Components of the PD-Module, PDM
- High Voltage divider
- High Voltage power supply
- FS structure

4.3.2.1. Photo-detector

JEM-EUSO is a photon-hungry experiment and its FS detector should have high detection efficiency. The FS detector should have the single photon counting capability in near-ultraviolet wavelength region to avoid the systematic errors, which may be introduced through the gain drift. It should be reliably and stably operational in Space environment for at least 3 or 5 years mission period. For the above reason, Multi-anode photomultipliers (MAPMT) with UV-glass entrance window are employed as sensors of the FS detector.

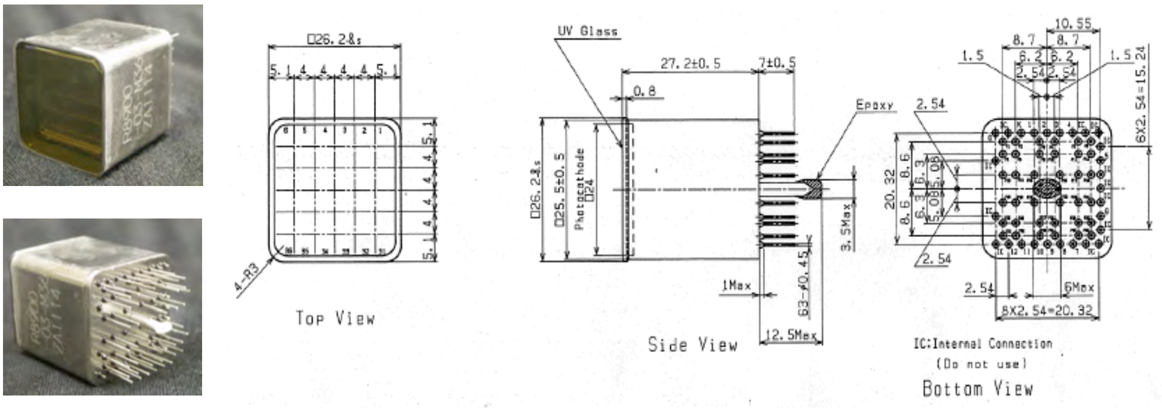

Figure 4.3.2.1-1. *The MAPMT for the JEM-EUSO photo-detector (R8900-03-M36).*

MAPMT specification

Present baseline choice is the Hamamatsu R8900-03-M36 (see Fig. 4.3.2.1-1), which has been developed by RIKEN in collaboration with Hamamatsu Photonics K.K. It has an ultra-bialkali photo-cathode which transforms photons into electrons then focuses them by means of a weak electric field, and amplifies photo-electrons by means of a stack of metal channel dynodes. The signals are taken from the anode that is formatted as an array of 6×6 squares. Compared with the former R7600 series, selected at the beginning of EUSO-ESA Phase-A study, the R8900 MAPMT has 1.75 times higher quantum efficiency and 1.9 times larger sensitive area. The total detection efficiency of R8900 is over 3 times higher than that of R7600 (see Fig. 4.3.2.1-2).

The main specifications of R8900-03-M36 are as follows:

- The 6×6 square pixels have a side of 4.3 mm and a pitch of 4.3 mm, giving a maximum sensitive area of 24 mm × 24 mm.
- The physical dimension of the MAPMT section is 25.7 mm × 25.7 mm (26.2 mm maximum) and the length is 27.2 mm. The mass is 27.3 g.
- The tube is equipped with an ultra-bialkali photo-cathode and a 0.8 mm thick UV-transmitting window. This ensures quantum efficiency higher than 35% (maximum 40%) for wavelengths from 330 nm to 400 nm.

- Detection efficiency (ε_3) of photons has the following temperature dependence: $d\varepsilon_3/dT = a\varepsilon_3$, $a = -0.37\%$ per °C.
- The device has a metal channel dynode structure with 12 stages, providing a gain of the order of 10^6 at 0.9 kV with a tapered voltage divider.
- The anode pulse rise-time is about 1.5 ns.
- The transit time spread is about 0.3 ns.
- Cross talk is about 7%.
- Gain non-uniformity between different anodes on the same MAPMT is 1:3.
- Average gain non-uniformity between different MAPMT is within 1:2.
- The anode MAPMT capacitance is about 2.8 pF.
- The overall anode dark current after 30 minutes storage in darkness is of the order of 1 nA.
- The voltage divider ratio: PK (0.6,1.8,2.4,1,1,1,1,1,1,1,1,1,1,1) A.

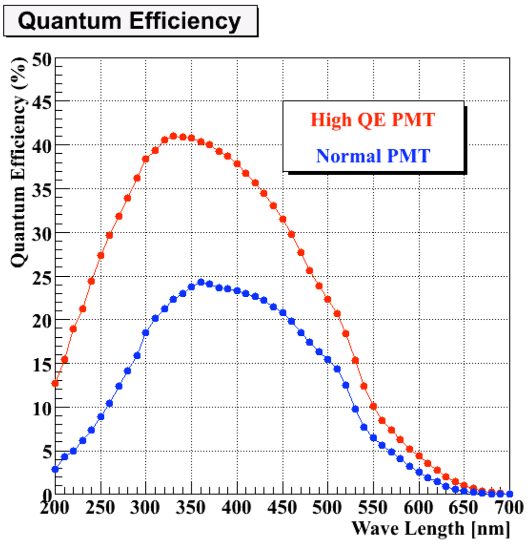

Figure 4.3.2.1-2. *Quantum Efficiency of the photocathode; comparison between ultra-bialkali (High QE PMT) and normal-bialkali photocathode.*

The environmental specification for R8900-03-M36 is:

- Optimal operating temperature: -10°C < T < +30°C.
- Non operating temperature: -30°C < T < +50°C.
- Temperature of each MAPMT should be monitored with the accuracy of ±4.5°C or better.
- Max acceleration: 18 Grms [break-point is beyond 20 Grms by test].
- Magnetic field effects: 0.1 relative gain variation at 2 Gauss.
- Gain goes down after 3(+2) years operation: 81%(78%).
- Reliability for 3(+2) years operation: 99.1%(98.5%).

Requirements of systematic errors

The following requirements shall reduce systematic errors within ±5% (TBC):

- Uncertainty on the sensor efficiency ($\Delta\varepsilon_{PMT}/\varepsilon_{PMT}$): ±5% or smaller.
- Uncertainty on threshold value of Front-end-comparator ($\Delta x/x$): ±25% or smaller.
- Accuracy of the High Voltage supply (ΔHV): ±24V or smaller.
- Temperature uncertainty (ΔT): ±13.5°C or smaller.
- Anode cross talk uncertainty: ±5% or smaller.
- Dynode and pre-amplifier gain uncertainty: ±5% or smaller.

Radiation environment

The radiation influences the transparency of the entrance window. The influence on the cathode sensitivity and electron amplification is negligibly small compared with the transparency degradation. The transparency is degraded to 90% beyond 1.4×10^{-5} R for gamma-rays in the MeV energy region, or is degraded to 95% beyond 100 krad for 70 MeV protons. The estimated radiation dose in 5 years mission period is around 10 krad.

Vacuum monitoring

The voltage applied to the MAPMT is around -1 kV. Accidental increase of local pressure in the range of 100-1000 Pa may cause a fatal damage due to the discharge, therefore a pressure monitor will turn off the high voltage power supply. In addition for security reason, all the HV lines are supposed to be potted with a suitable resin (Dow Corning DC-93500 etc.).

UV environment

When the lid of the JEM-EUSO telescope does not close by some failure, the daylight of the Earth illuminates the FS. In such a case, the HV Power Supply of the photomultipliers is turned off, and the dynodes are not damaged. However, the photocathode itself may be damaged. Therefore, we have measured the damage of the photocathode by means of a strong UV light illumination with the power supply switched off. We did not recognize any damage for the UV light illumination which is equivalent to 10 years daylight from the Earth (see Fig. 4.3.2.1-3).

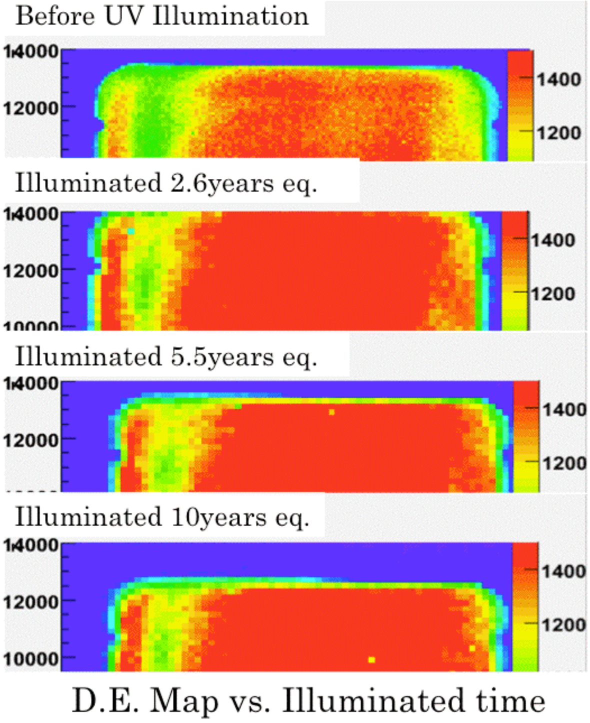

	Sensitivity	**Uniformity**
Before	1.00	1.4
2.6 years eq.	1.11	1.4
5.5 years eq.	1.11	1.4
10. years eq.	1.10	1.4

Figure 4.3.2.1-3. Sensitivity variation for UV-light illumination.

4.3.2.2. MAPMT support structure

The main functions of the MAPMT support structure are:

- To allow packing of the MAPMT as close as possible with precise relative positioning.
- To have common high voltage inputs and every anode signal outputs.
- To be able to support MAPMTs safely against the vibration at the launch.
- To minimize outgas.

The main specifications of the prototype model of the MAPMT support structure, sketched in Fig. 4.3.2.2-1, are:

- It supports 4 MAPMTs.
- It has a pair of high voltages input and provides them to 4 MAPMTs.
- It has every anode signal output.
- It doesn't destroy the MAPMT when the PDM is vibrated with 20 Grms.
- Physical dimension: 56 mm × 56 mm × 7 mm.

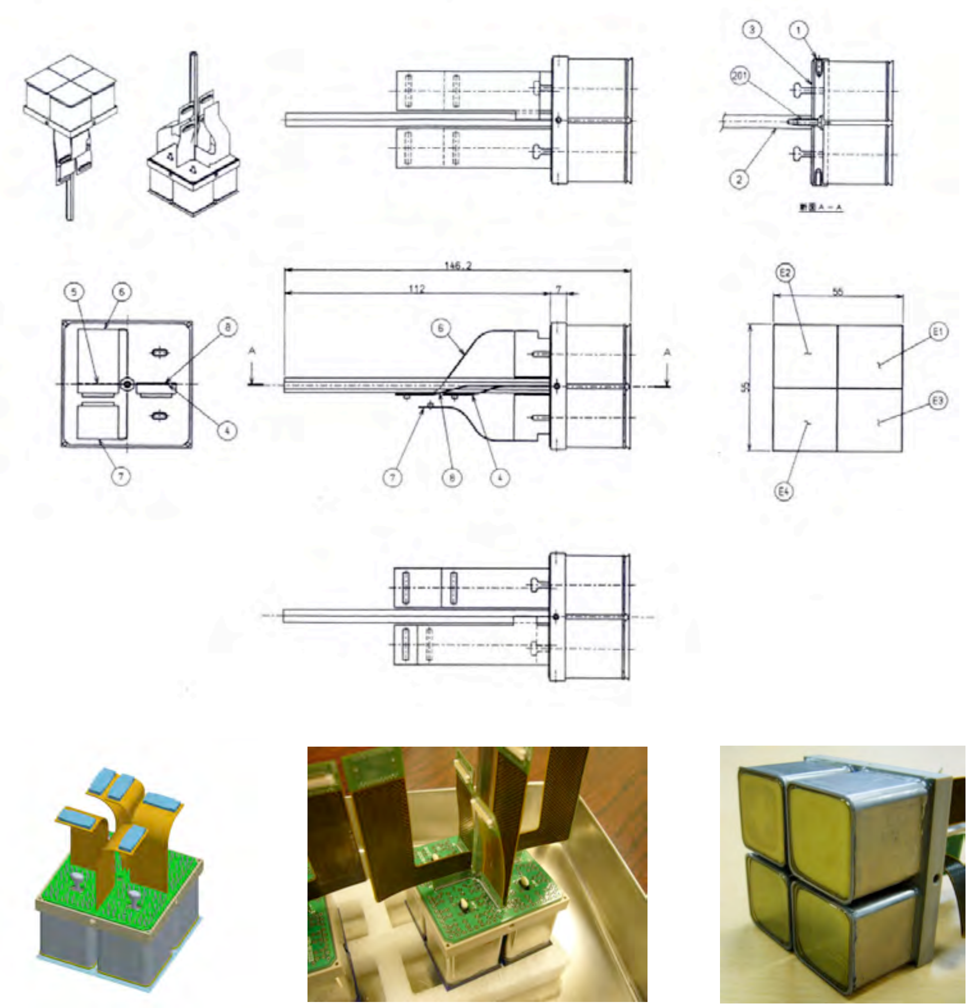

Figure 4.3.2.2-1. *Drawings of the MAPMT support structure and its prototype.*

4.3.2.3. PDM structure

The main functions of the structure of the Photo-Detector-Module, PDM, are:

- To allow packing of the MAPMT Support Structure as close as possible.
- To have the EC electronics boards and the PDM electronics board inside.
- To have a High-Voltage Power Supply inside.
- To be able to endure vibrations at the launch.
- To minimize outgas.
- To evacuate efficiently the heat from internal circuits.

The main specifications of the PDM structure, sketched in Fig. 4.3.2.3-1, are:

- It supports 9 MAPMT Support Structures.
- It has 3 EC electronics boards and the HV Power Supply system.
- It endures vibrations of the PDM with 20 Grms.

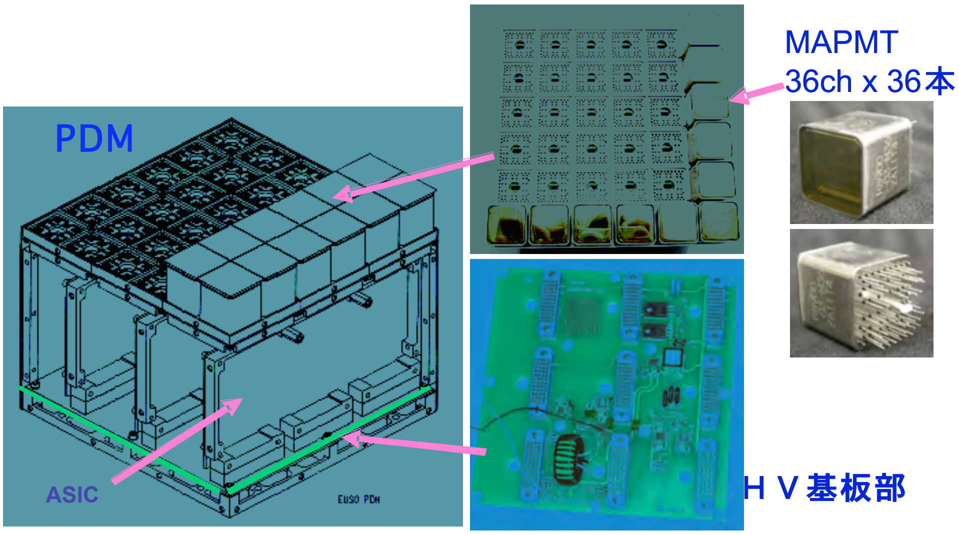

Figure 4.3.2.3-1. *Drawings of the PDM structure and its prototype.*

4.3.2.4. High Voltage divider

Active high-voltage dividers of power saving type (as schematized in Fig. 4.3.2.4-1) are used to supply high voltage to the MAPMT dynodes. In addition, the divider current is defined as 10 times than the anode current for the standard nightglow background. The High-Voltage power supply is designed to supply arbitrary voltage in the range between 0 V and 1000 V. The above characteristics have been verified through the designing, production, electrical tests, radiation tests and a balloon flight, etc.

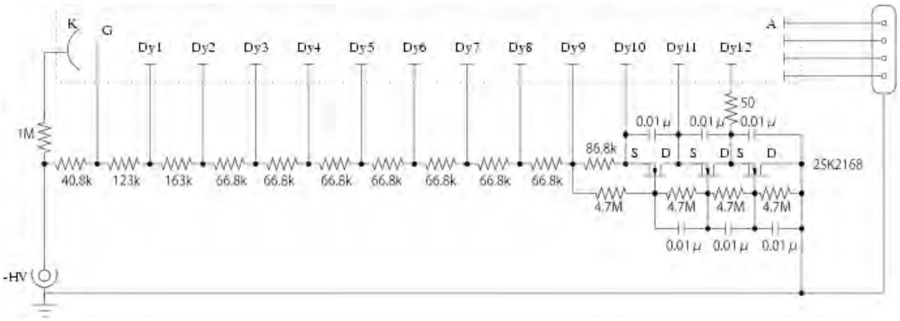

Figure 4.3.2.4-1. *Active High Voltage divider.*

In addition, we have developed the high-voltage divider including a protection circuit. It protects the MAPMT from an instantaneous large amount of light such as the lightning. We can operate it more safely by quickly interrupting the photoelectron multiplication using a Photo-MOS relay, as sketched in Fig. 4.3.2.4-2.

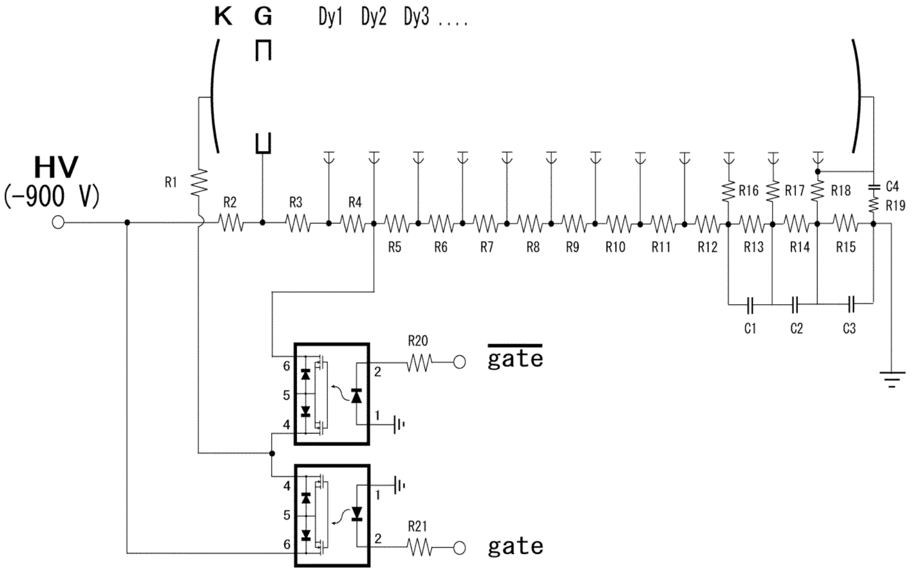

Figure 4.3.2.4-2. *Test circuit of the HV divider with protection from large amount of light.*

4.3.2.5. High Voltage power supply

The High-Voltage Power Supply, HV-PS, system is designed to decrease the failure rate, the complexity of wiring and the danger associated with it, by means of the distributed control method shown in Figure 4.2.3.5-1.

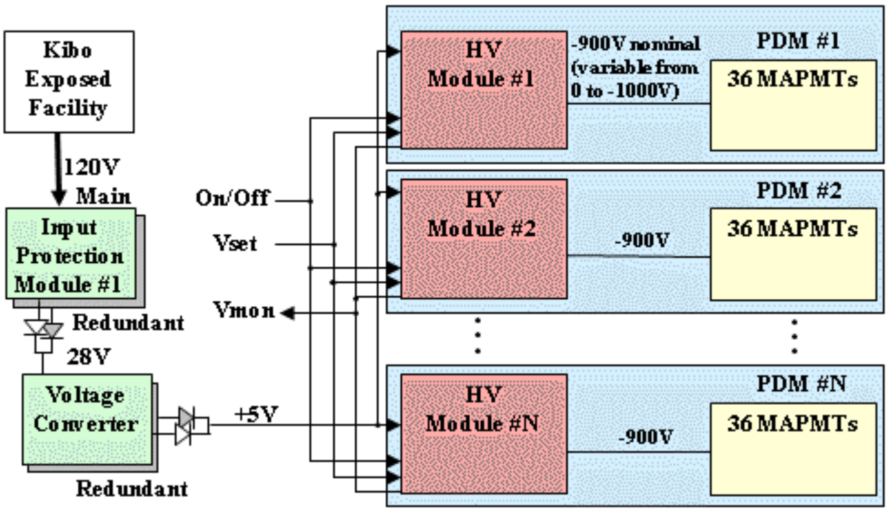

Figure 4.3.2.5-1. *Basic diagram of the HV-PS system for the JEM-EUSO focal surface. Each HV-PS module is mounted on the PDM. The module drives 36 MAPMTs of each PDM.*

The structure of each HV-PS is shown in Figure 4.3.2.5-2. Trigger Control Unit (TCU) gives instructions of the high voltage value, and then it is converted to an analog value from 0 to +5 V, by the DA converter. When the DC-HV converter receives this voltage, it generates a high voltage from 0 V to 1000 V. This is then transferred to the Bleeder resistance of the MAPMT, which starts its operation. This voltage is supposed to be monitored through the AD converter after reducing its value.

This high voltage device was stowed on a balloon flight and its operation has already been verified. In addition, its radiation tolerance has also been tested at the National Institute of Radiological Sciences, by using proton beams. [ref.?]

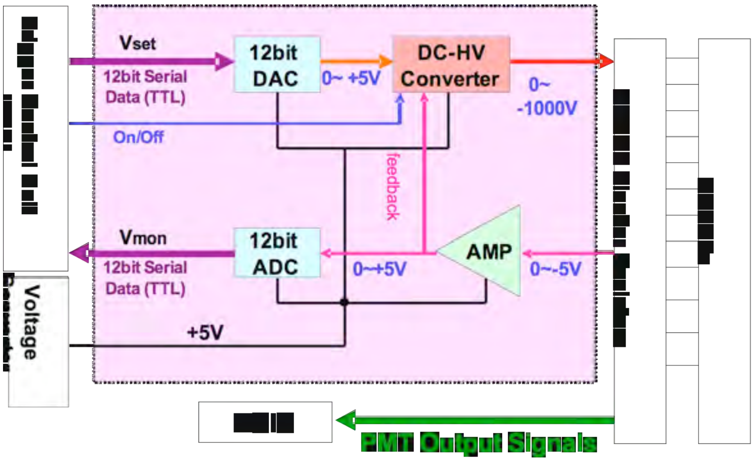

Figure 4.3.2.5-2. *Basic block diagram of the HV-PS module.*

4.3.2.6. FS structure

The shape of the focal surface is a spherical surface with about 2114 mm radius. The PDMs should have a layout which minimizes the gaps on that surface. Figure 4.3.2.5-1 shows the PDM layout in case of 137 PDMs.

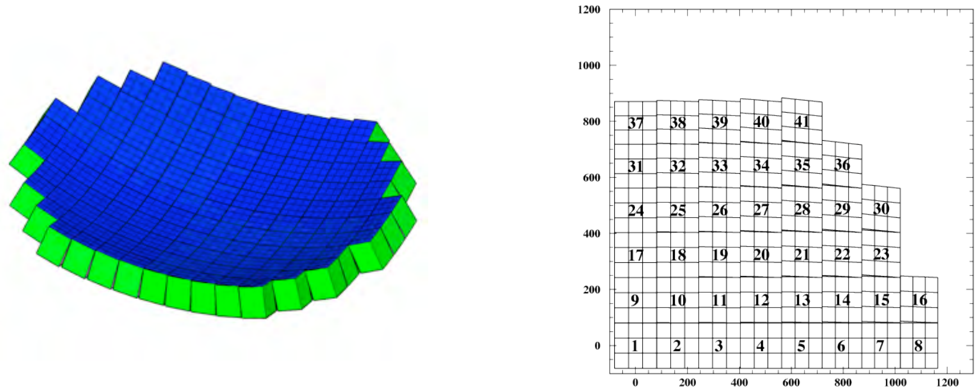

Figure 4.3.2.6-1. *The PDM layout. The scheme on the right shows the PDM layout covering 1/4 of the whole FS.*

4.3.2.7. Advanced option

If we can make the spot size of optics smaller, in parallel the S/N ratio will improve. This will make possible to reduce the pixel size of the focal surface. Therefore, we can expect an improvement in the detection efficiency of cosmic rays.

In the baseline design, to match the spot size of 5 mm, we use the M36 type MAPMTs, which are 1"×1" and 6×6 channels. If the spot size becomes half, 2.5 mm in diameter, the corresponding pixel size of M144 is the most appropriate. In this case, the pixel size becomes 2.2 mm, which is difficult to realize with the currently existing MAPMTs, so it becomes necessary to adopt the Silicon PhotoMultiplier SiPM. In addition, we studied both MAPMT and SiPM cases for M64, which is in between M36 and M144. If we reduce the pixel size as a consequence of the fact that the spot size becomes smaller, the size of the air shower signal, which is the point light source, remains unchanged, while the intensity of the background light becomes smaller in proportion to the dimension of the pixel. Therefore, S/N ratio will improve. As we know from the analysis, the energy threshold to trigger cosmic ray air shower roughly varies inversely with S/√N; if the pixel size is reduced, the energy threshold becomes lower.

In addition, we esteem that by using SiPM, the photon detection efficiency improves by 1.5 times or higher. This fact also contributes to a further improvement of the S/N ratio. On the other hand, if the pixel size is reduced, the total pixel number on the focal surface becomes larger. This fact may cause some demerits such as the increase of package density of the readout electronics and the increase of electric power consumption for readout, etc. The following table shows the summary of the above effects.

Table 4.3.2.7-1. *Effects of the different number of pixels and type of sensor device.*

Pixel number and type	MAPMT		SiPM	
	M36 (Baseline)	**M64**	**M64 equivalent**	**M144 equivalent**
S/√N	1.00	1.33	2.00	3.00
Power	1.00	1.33	1.02	1.75

MAPMT with reduced pixel size

Although the pixel size of current MAPMT is reduced, the expected effect is not completely achieved due to the signal cross-talk. Therefore, we modified a dynode structure design with M64 and M100 MAPMT, which have 8×8 and 10×10 channels in 1" square, respectively. The following figure is a preliminary design of M100 MAPMT. The sensitive area is slightly smaller.

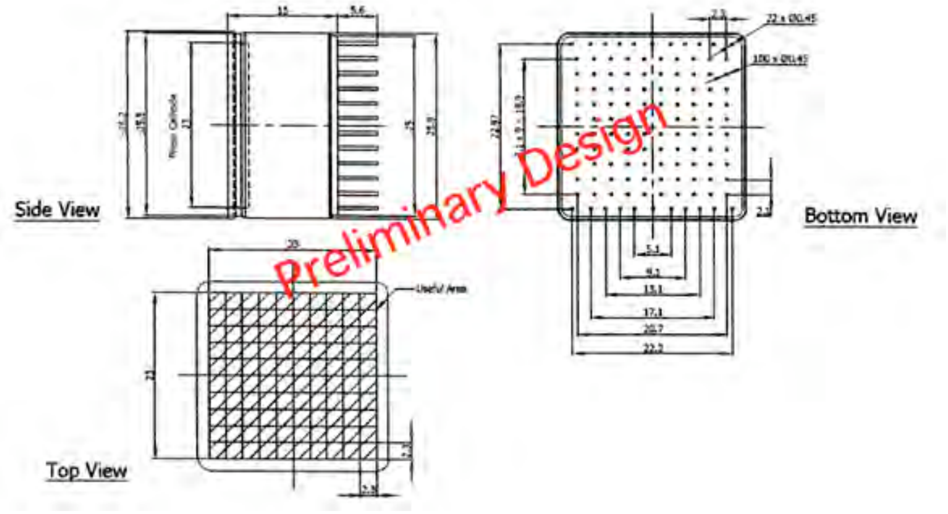

Figure 4.3.2.7-1. *Preliminary design drawing of M100 MAPMT.*

SiPM

Introduction

A Silicon Photomultiplier (SiPM) is a novel type of optical semiconductor elemental device which has the photon counting ability. It is compact, low cost, it has a high quantum efficiency, high multiplication factor, and fast response (< 100 ps). It also has the big advantage, compared to Photomultiplier Tubes (PMT), of being able to operate at low voltages (< 100 V), without being affected by magnetic fields.

A SiPM consists of multiple, from several hundreds to around ten thousands, of avalanche Photodiodes (APDs), which are operated in Geiger mode. APD is a high-speed and high-sensitivity photo-diode, whose photo-electric current is multiplied by applying a reverse bias voltage. If the reverse bias is set above its breakdown voltage, the inner electric field becomes higher and the multiplication factor suddenly rises up (10^5~10^6). This phenomenon is called Geiger mode. In this case, each APD pixel is operated in binary mode, which outputs a fixed signal current, regardless of the detected number of photons. Eventually, the output signal from a SiPM is the total charge of all the APD signals, which is proportional to the number of the detected incident photons.

The PDE (Photon Detection Efficiency) of a SiPM depends on the transmittance of the surface, the fill factor of the sensitive area, the quantum efficiency (QE), and on the Geiger efficiency of the device:

$$PDE = Transmittance \times Fill\_Factor \times QE \times Geiger\_Efficiency$$

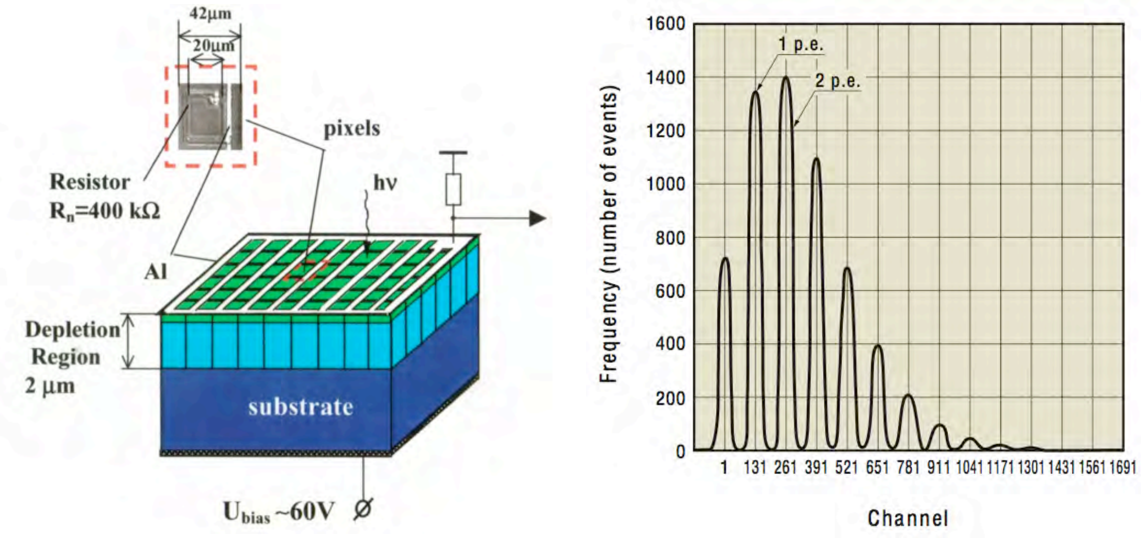

Figure 4.3.2.7-2. *About the Silicon Photomultiplier. Left: schematic view of a SiPM, consisting of a multiple array of APDs operated in Geiger (binary) mode. The output of a SiPM is an analogue signal which is the sum of all APD signals and is proportional to the number of incident photons. Right: example of charge histogram of the output pulse. Light intensity can be measured by single photon counting.*

Status of SiPM development

Several kinds of SiPMs, as candidates for JEM-EUSO focal surface detector, are being developed by Hamamatsu, MPI-HLL (Max-Planck Institute for Physics – Halbreiter Semiconductor Laboratory), and MPI-MEPhI (Max-Planck Institute for Physics – Moscow Engineering Physical Institute).

Hamamatsu: MPPC

Multi-Pixel Photon Counter (MPPC) was developed and released by Hamamatsu. They have a high sensitivity in the short-wavelength region. Compared to many other SiPMs, they have less thermal noise, as shown in Fig.4.3.2.7-3, left panel.

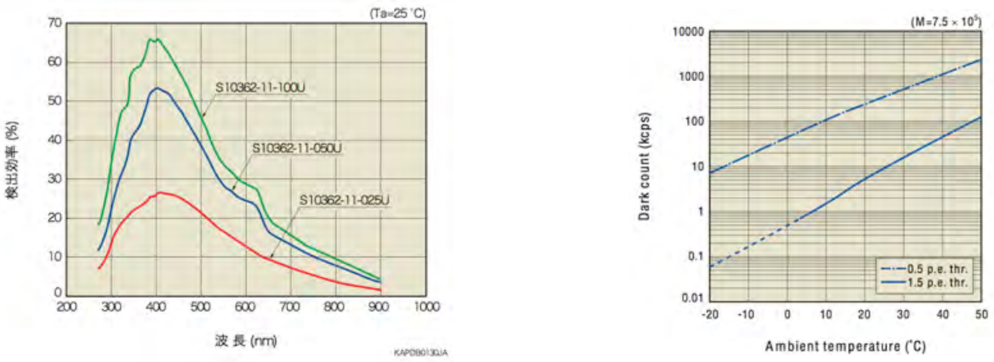

Figure 4.3.2.7-3. *About the MPPC by Hamamatsu. Left: wavelength dependence of the Photon detection efficiency, PDE. The green, blue and red lines represent the PDE for 100, 50, and 25 micron pith MPPC, respectively. Right: temperature dependence of dark current. The rate is ~100 kHz/mm^2 at -15°C at single photoelectron level. A 3×3 mm^2 device would have a rate of ~100 kHz at that temperature.*

Hamamatsu already developed and released several types of MPPC. In addition, arrays of 2×2 or 4×4 of 3mm× 3mm size are being developed. The test of the 2×2 array is going on at MPI.

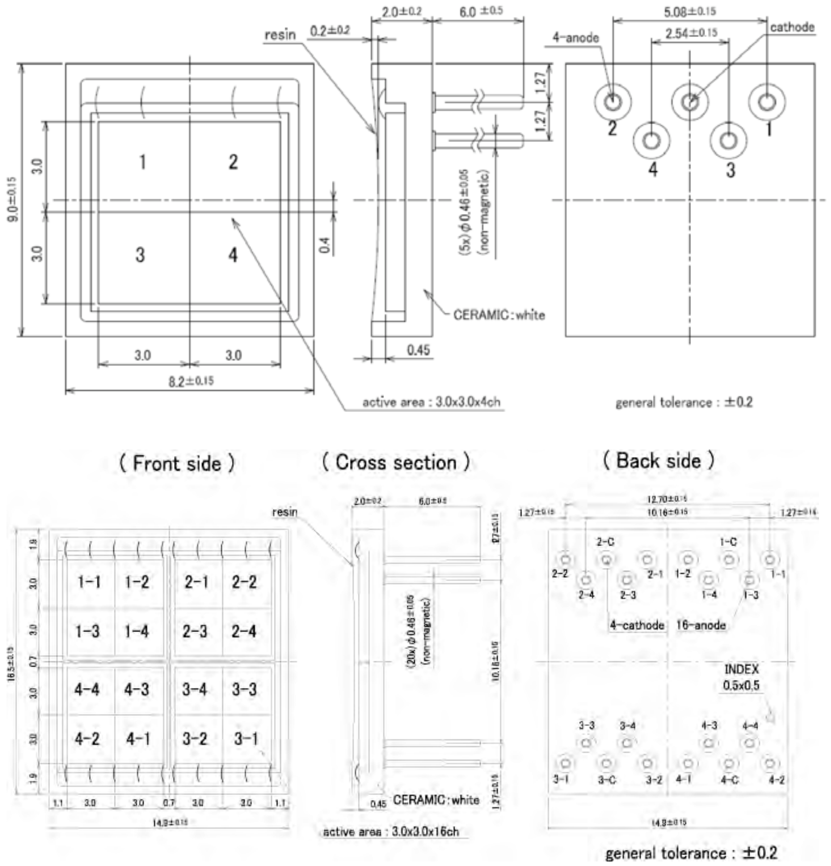

Figure 4.3.2.7-4. *Design drawing of 2×2 (upper) and 4×4 (lower) array of 3×3 mm^2 sized MPPCs.*

MPI-HLL: SiMPL

MPI for Physics and MPI Semiconductor Laboratory are developing a bulk resistor type of SiPM named SiMPL. In the normal SiPM, the quench resistors and signal lines are placed on the surface, where the incoming radiation hits the detector, while SiPML doesn't have this structure on the surface, therefore we can improve the filling factor dramatically. In addition, by effectuating anti-reflection coating, we can improve the photon detection efficiency. In this way, we expect to achieve 60% or higher PDE.

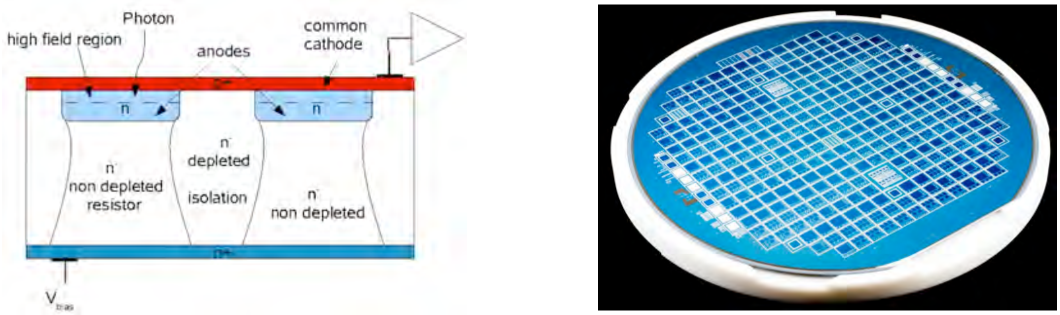

Figure 4.3.2.7-5. *About the SiMPL by MPI-HLL. Left: schematic view of SiMPL (bulk register type) with P-on-N structure, which makes it sensitive to UV. By removing a complicated structure on the surface of the incoming radiation, we can increase the filling factor. As the structure is simple, it can be produced at low cost. Right: first silicon wafer of the prototype of SiMPL. As of June 2008, it is tested at wafer level and device tests are ongoing.*

MPI-MEPhI: SiPM

SiPMs have been developed by MPI for Physics and MEPhI for more than 6 years.The former N-on-P structure was not UV sensitive (< 400 nm), while the new structure, P-on-N type, is UV sensitive. The dark noise rate at the room temperature is relatively high but low enough around the JEM-EUSO operation temperature (-10 ±5 °C) (~500 kHz/3×3mm^2).

Application of SiPMs

The temperature dependence of SiPM gain is one of the most important things to consider in the case of SiPM application to JEM-EUSO. The temperature dependence of gain is ~ -3% per °C at a certain bias voltage. We developed a bias voltage compensation circuit using a thermistor as shown in Fig. 4.3.2.7-6 which enables us to reduce the temperature coefficient down to around 0.3% per °C, equivalent to a PMT.

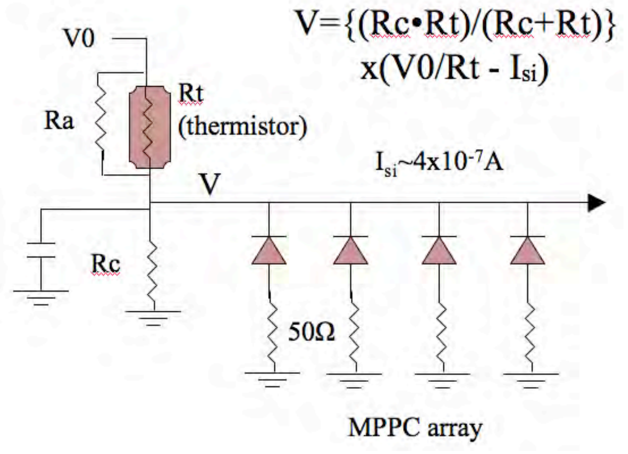

Figure 4.3.2.7-6. *A circuit diagram for temperature compensation of SiPM bias voltage.*

The circuit, whose bias voltage is regulated following the temperature, works as shown in Fig. 4.3.2.7-6. By using this circuit, we obtained a static gain fluctuation stabilized within 0.1% per °C, and ~0.5% per °C in the case of rapidly changing ambient temperature; the Fig. 4.3.2.7-7 shows plots of the device temperature and the gain fluctuation of a Hamamatsu MPPC as a function of time while the device temperature was changed periodically from -8 ºC to -18 ºC in a sudden way. The vertical axis of the upper plot is the MPPC gain and bottom one is the device temperature, and the horizontal axes of both top and bottom plots indicate time. We found that in case of a wider temperature range, the gain fluctuations are stabilized within 0.5%/ºC using this circuit. By decreasing thermal resistance between the thermistor and the MPPC device, even less gain fluctuation is expected.

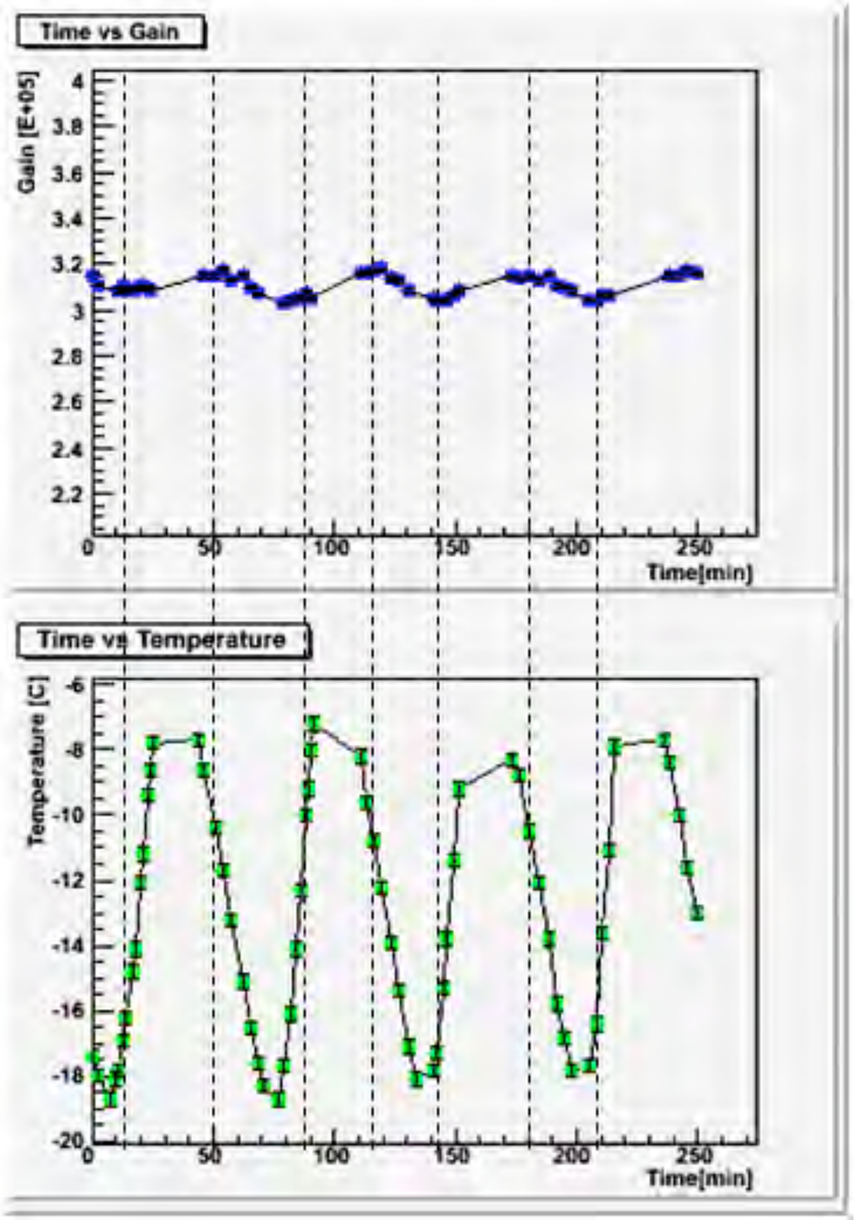

Figure 4.3.2.7-7. *We operated a MPPC with a temperature compensation circuit to control the bias voltage. The gain fluctuation is within 0.5%/ºC. We consider the gain fluctuation at this level is acceptable with a careful on-line calibration.*

SiPM vs PMT

The following table summarizes the main differences between the two types of devices.

Table 4.3.2.7-2. *SiPM vs PMT.*

Parameter	**MAPMT (UBA)**	**MPPC**	**SiMPL**	**SiPM**
PDE (400 nm)	0.7 × 40%	50%	61%	40%
Operation Voltage	900 V	70 V	40 V	40 V
Effect of magnetic field	Yes	No	No	No
Charge resolution (ability of counting the number of photons)	good	very good	very good	very good
Price per pixel	￥4,200	￥4,300	￥5,000	￥5,000
Sensitive area per pixel	4×4 mm^2	3×3 mm^2	3×3 mm^2	3×3 mm^2
Weight per pixel	1.4 g	0.11 g	--	--
Dark count (-15 °C)	~ kHz	~ 100 kHz	--	~ 500 kHz
Matrix type	6×6	2×2, 4×4	1	1
Status	on sale	on sale	prototype	prototype

Outlook for the SiPM application to JEM-EUSO

With the objective of applying SiPM/MPPC to JEM-EUSO, we aim to further improve their photo-detection efficiency at device level, and quickly design the module and the prototype which have a more stable and safe operation in Space. We construct an optimized front-end electric circuit considering gain, impedance, floating capacitance associated to its implementation, which matches with the read-out circuit. Then, as the last evaluation of their performance, we will observe Cherenkov light by implementing in parallel a camera composed of SiPM/MPPC with another one composed of MAPMT to a ground based telescope.

We should consider in concrete the following points:

- Stability of gain (< ~0.3%/°C). As mentioned before SiPM/MPPC normally have around 3%/°C of temperature dependence of gain, however, we can limit it till around ~ -0.1%/°C by using an adequate thermistor as temperature compensation circuit. We should design the detection module so that the temperature of SiPM/MPPC inside it is uniform and stable.
- Dark current (< ~100 kHz). In the advanced design of JEM-EUSO, the environmental temperature of JEM-EUSO can be decreased till -15°C ±2~3°C, therefore, the noise rate caused by the dark current by SiPM/MPPC becomes low enough. However, in the design, we should place SiPM/MPPC as much as possible far away from the heat of the front-end electric circuit.
- Radiation Tolerance. Radiation might cause the increase of the dark current of SiPM/MPPC, and a degradation of the resolution, because the collision of protons or neutrons produces defects in the lattice structure of the silicon crystals. There is small influence of electrons and γ-rays. Radiation tolerance tests have already been done inside and outside Japan and we concluded that there was no problem in their use in JEM-EUSO for more than 5 years at the altitude of the International Space Station. However, we should design protections from unexpected huge flares from the Sun. In addition, we should also study in advance the influences on trigger and recorded data in case of degradation.

- Stability of photon detection efficiency. Photon detection efficiency may vary due to the damage of the entrance window. Therefore, we should do a measurement of radiation tolerance and stability of photon detection efficiency at the same time.
- Designing focal surface and focal surface modules. We assume to use Hamamatsu 3×3 mm^2 MPPC in a 4×4 matrix (Fig. 4.3.2.7-4). As in figure 4.3.2.7-8, we fix the basic module using a 4×4 matrix placed on a grid of 8×8, and provide a common bias voltage adjusting the temperature by means of thermistor-based temperature compensating circuit. We will keep the temperature of the whole module uniform by supporting it with copper plate. We estimate that the temperature of the focal surface will be low enough to keep the optimal gain and the dark noise rate. However, to realize more stable operation, we will uniform the temperature inside the module with the abovementioned copper plates. In addition, we will minimize the dead space by installing Winston Cones in each MPPC array. Furthermore, we will uniform the temperature by adhering and fixing the MPPC array, copper plates and the PCB for bias voltage supply and pulse readout by means of thermal conductive adhesive.
- Readout circuit. We should design carefully the part which transmits the pulse to the readout circuit considering sufficiently the following points: impedance matching between SiPM/ MPPC, degradation of time character of pulse due to floating capacitance, increase of electric noise accompanied with the implementation, electric interference among channels.

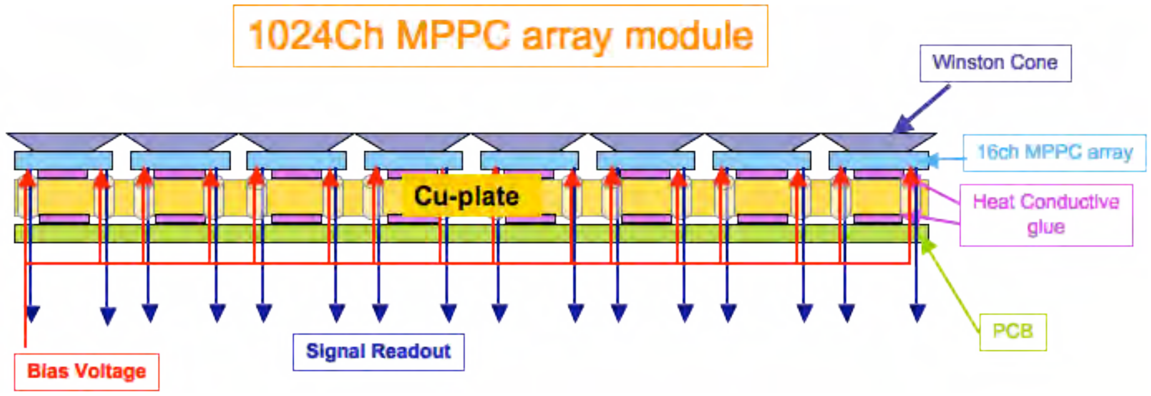

Figure 4.3.2.7-8. *Conceptual design of the FS basic module with 16ch MPPC. First, make the heat of the whole module uniform by attaching Winston Cones to each MPPC placed in an 8×8 array form by means of optical adhesive. Then, attach and fix it again to the PCB and aluminium panel by means of thermal conductive adhesive. The gain of MPPC will be kept stable by means of thermistor-based temperature compensation circuit.*

4.3.3. FS electronics

The Focal Surface Assembly (FSA) position-sensitive layer consists of a large array of MAPMTs. The Focal Surface Assembly includes proximity electronics for MAPMT data collection, MAPMT driving circuit. A LIDAR and an IR camera assembly will also be provided for atmosphere sounding, which is an important complement for the main data analysis. A Control Electronics will manage all those subsystems and will provide the electrical interface between JEM-EUSO and the ISS via the JEM (Japanese External Module) platform. Other ancillary subsystems, such as Thermal Control and Calibration, Alignment and Monitoring will also be managed by the Control Electronics.

The principal electronics of JEM-EUSO are then Focal Surface Electronics and Control Electronics. Focal Surface Electronics is located inside the FS structure, and Control Electronics (CPU etc.) is located both in normal and redundant electronic boxes. The places of the following electronics have to be decided.

The FS Electronics includes:

- front end electronics (ASIC)
- PDM electronics
- Cluster control electronics
- FSA power supply system (DC/DC converters to generate LV and HV)

The Control Electronics includes:

- ISS (JEM) communication interface (I/F)
- ISS (JEM) power I/F
- FSA communication I/F
- Scientific Functions management system
- HK collection management system
- LIDAR management system
- IR camera management system
- Thermal Control management system
- Calibration, Monitoring and Alignment devices management system (TBD)
- Lid mechanism management system
- Management of the system to determine the instantaneous absolute orientation of the JEM-EUSO Instrument (TBC)

4.3.3.1. Functions

The main functions of the Focal Surface Electronics are as follows:

- The Front End Electronics, FEE, directly interfaces the MAPMTs and provides the first main level of trigger (analogue and digital).
- The PDM circuit provides the second and third Main level of trigger and provides the ring memory buffers and the communication I/F between the FSA and the control electronics.
- The FSA power supply system provides the power to the MAPMT (HV) and to the first and second front end electronics (LV).
- The ISS (JEM) communication I/F provide the JEM-EUSO communication capability with the external world for commands and data collection.
- The ISS (JEM) power I/F provides the JEM-EUSO powering capability from the JEM provided power busses.
- The FSA communication I/F provide the link between the FSA and the Control Electronics for command and data.
- The Scientific Functions management system includes all the science relevant HW and SW such as the trigger system, the data acquisition system and the temporary onboard storage capability.
- The HK collection management system provides the regular collection of engineering HK data from various locations within the instrument.
- The LIDAR and IR Camera management system provide all what is needed for the proper operation of the atmospheric sounding system, including power supply, configuration commands issuing, data retrieval and storage.
- The Thermal Control management system provides the instrument thermal control by means of proper temperature sensor readout and heaters activation.
- The Calibration, Monitoring and Alignment devices management system drives the devices used for calibration of the different instrument parts (TBD), those used to monitor the relative alignment of different Instrument parts (TBD) and those used to monitor important parameters.
- The Lid mechanism management system provides the proper motors drive capability and position sensors conditioning to operate the instrument lid.

- The system to determine the instantaneous absolute orientation of the JEM-EUSO Instrument will monitor the absolute orientation of the JEM-EUSO Instrument in case the available standard resources (normally from ISS, etc) are not able to provide this information with sufficient precision (TBC).

4.3.3.2. Trigger and read-out: concept design and definitions

Trigger philosophy specifications

The overall JEM-EUSO trigger philosophy is at the core of the concept of the instrument. Therefore, it has to be clearly described in this chapter.

The goal of the trigger system is to detect the occurrence of a scientifically valuable signal among the background noise detected by the JEM-EUSO telescope.

Since the total number of pixels in the array is very large (~ 2×10^5), a multi-level trigger scheme was developed. This trigger scheme relies on the partitioning of the Focal Surface in subsections, named PDM (Photo Detector Module), which are large enough to contain a substantial part of the imaged track under investigation (this depends on the energy of air shower and the zenith angle). PDMs will have a suitable shape and will be identified by a pair of coordinates XPDM, YPDM as well as the pixels inside the PDMs, generally named (X,Y).

The general JEM-EUSO trigger philosophy asks for a System Trigger organized into three trigger-levels (TBC). The three levels of trigger work on the statistical properties of the incoming photon flux in order to detect the physical events hindered in the background, basing on their position and time correlation.

The trigger is issued in accordance with the three stages (EC, PDM, PDM cluster).Table 4.3.3.2-1 gives a synthetic idea of the expected rate of signals at each stage, and the expected rejection power. The numbers here reported give a first rough estimation of the requirements. The exact power rejection of each trigger level will be optimized in future. The last row gives also a reference number on the expected rate of cosmic ray events, which could fluctuate by around one order of magnitude depending on the effective threshold of the detector.

Table 4.3.3.2-1. *Outline of noise reduction capability.*

Level		**Rate of signals/triggers at PDM level**	**Rate of signals/triggers at FS level**
1st level trigger (EC)	Photon trigger	~5.2×10^8 Hz	~7.8×10^{10} Hz
	Counting trigger	~4.0×10^5 Hz	~6.0×10^7 Hz
2nd level trigger (PDM)		~7 Hz	~10^3 Hz
3rd level trigger (PDM cluster)		~6.7×10^{-4} Hz	~0.1 Hz
Expected rate of cosmic ray events		~6.7×10^{-6} Hz	~10^{-3} Hz

The First trigger level has the two following types of triggers:

- Photon trigger. Anode-level trigger, basically edge and width counters coupled with a Q-t (electric charge-time) conversion, which act as a single photon counting method, in order to recognize the arrival of a signal over threshold, which will be identified as a single photoelectron. At this trigger-level, the electronic noise effect is greatly reduced due to the fact that the “strong” anodic pulses are easily discriminated above the preamplifier electronic noise.
- Counting trigger (Red pixel trigger and Yellow pixel trigger). Counting trigger consists of a gated counter and two digital comparators (*high* and *moderate levels*). The gate time is

named GTU (from Gate Time Unit), and its duration is about 2.5 μs (TBC). The counting trigger is issued whenever the number of single-photoelectrons exceeds a pre-set digital threshold value. In every GTU, all the pixels in a PDM will be tagged depending on the number of single photo-electrons detected by each of them. Pixels that passed the *high level* threshold will be tagged as *Red pixels*, while those passing only the moderate level threshold will be tagged as *Yellow pixels*. All the other pixels will be discarded for the rest of the trigger stages.

At the First-level trigger, the random background (randomly arriving photons) can be greatly reduced by setting the digital threshold value above the observed background fluctuations. The threshold on Red pixels will be set in order to have ~1 pixel over threshold per PDM every few GTU (1-10). The threshold on Yellow pixels will be set so to have <100 pixels/GTU on a PDM.

The Second-level trigger is issued at PDM level and it is devoted to a further reduction of the background, by operating a 'space proximity test' of 'hits' in consecutive GTUs. The algorithm working as a 2nd level trigger, presently proposed for JEM-EUSO, is called 'Linear Track Trigger' method (LTT), which searches for light points moving with the light speed at 400 km ahead. The main aim of this trigger level is to further decrease background events, bringing the rate of triggered events at the level of ~1Hz/PDM or below.

The Third-level trigger is issued at the cluster level and according to this trigger we make the final decision to start the readout procedure. The Third-level trigger logic must collect data coming from the whole Focal Surface divided in 18 subsections consisting of 8 PDMs. The Third-level trigger logic will provide a decision about the presence of any interesting feature, by collecting the Second level trigger coming from each PDM. The decision will be made in accordance with the optimized "trigger modes" for the different phenomena to be observed. At this level, the remaining statistical noise will be reduced to the point that only the "event-like" patterns will initiate the readout sequence.

The system-level trigger will be fully in-flight programmable in order to allow for any adjustment in the trigger modes.

Trigger mode specifications

The System Trigger shall be fully in-flight programmable in order to set it for all triggers modes. The following trigger modes have been identified:

- Standard EECR (Extreme Energy Cosmic Rays) mode
- Slow mode
- Fast mode
- Analog Trigger (sub-mode)

The EECR mode shall be the standard one where the trigger looks for signals which rise above the Third-level trigger for a duration between about 30 μs and about 300 μs (the exact value shall be in-flight programmable). The Extreme Energy Cosmic Rays (EECRs) are observed by means of this mode. Event which does not match the above duration window will be ignored.

The Slow mode shall be normally not active; it will be activated by telecommand when required by the observers or as a programmed feature in the System Trigger. When the Slow mode is activated, the signals with Third-level trigger activity lasting more than a pre-set time (e.g. 300 μs) will be anyway recorded, however, with a slower sampling frequency (GTU). Most atmospheric phenomena (e.g. meteoroids) are observed with this mode.

The Fast mode shall be normally not active; it will be activated by telecommand when required by the observers. When the Fast mode is activated, the sampling frequency is increased by a factor 8 with respect to the EECR mode, and signals with 3rd level trigger activity lasting less than a pre-set time (e.g. 30 μs) will be anyway acquired. This feature will be used during on board calibration.

What about the Analog Trigger ?

Read-out specifications

For every detected event within the foreseen classes, the JEM-EUSO electronics shall be able to record a set of raw data on a pixel-by-pixel base. By making use of the "free running" techniques, data are continuously sampled with fine time resolution (GTU) and sequentially stored into cyclic buffer memories. The buffer memories are designed to be properly deep in order to keep the maximum expected time-length for a track. Unless a read-out is started by the System-Trigger, the older data are dropped from the memory buffer in order to make room for the new ones. When a read-out is started by the System Trigger, the track data stored into the memory buffer is simply read out. As a baseline, the sampling period shall be related to trigger mode following the table below:

Table 4.3.3.2-2. *Trigger modes and sampling periods.*

Trigger mode	Position sampling period	Remarks
Standard (EECR)	2.5 μs (TBD)	Gate Time Unit, GTU
Slow	40 μs (TBD)	16 × GTU
Fast	0.156 μs (TBD)	1/8 of GTU
Auxiliary (sub-mode)	According to the selected mode	

The general readout scheme is based on the PDM areas, used independently for the Second level trigger. As a baseline, the data readout shall take place from the PDM that originated the trigger and from its "first neighbours".

4.3.3.3. Trigger and read-out hardware

The purpose of the system trigger is to discriminate, at detector level, the "event-like" signatures against the natural diffuse background noise. The requirements for the abovementioned overall JEM-EUSO trigger philosophy are as follows.

There are three Trigger levels within the detector:

- First Level (EC);
- Second Level (PDM);
- Third level (PDM cluster);

The location of these trigger levels within the instrument is shown in Fig. 4.3.3.1 together with the basic associated HW function. A detailed description for each level of trigger is given in the next sections.

First-level trigger (EC)

The trigger at MAPMT level is caused by an UV photon that impinges on the photocathode causing an avalanche multiplication of photoelectrons emitted by the photocathode and the dynodes. The produced photoelectrons will be amplified to $3\div5\times10^5$ electrons, and reach the opposite laying anode. The anodic pulse described above is then delivered to the proper anodic input of the front-end ASIC. At front-end ASIC level, two trigger functions are performed:

- Analog threshold on the pulse amplitude: photon trigger
- Digital threshold on the pulse counts (see next paragraph): counting trigger

The First-level trigger function is related to the discrimination of the anode signals coming from the MAPMT. This is the only analog section of the trigger.

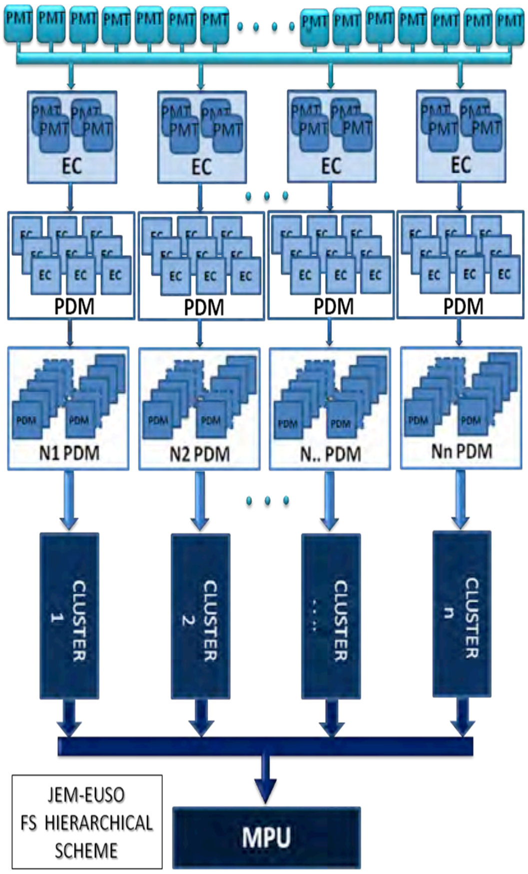

Figure 4.3.3.3-1. *Structural scheme of the different levels of trigger.*

The front-end ASIC for JEM-EUSO includes an impedance matching circuit, integrator circuit and comparator circuit as well as current-source and current-sink circuits which feed currents at the input node of the integrator (Fig.4.3.3.3-2). The impedance matching circuit acquires a pulse from a multi-anode PMT with low-impedance, and reduces cross talk between channels. Furthermore, the impedance matching circuit protects the entire circuit from a possible electro-static discharge. The output of the impedance matching circuit is sent to a comparator circuit via the integrator circuit. The comparator circuit delivers a logic H when the integrator's output exceeds a pre-determined level. Once the comparator circuit delivers H, the current-source circuit is activated to linearly damp the integrator output voltage until the integrator output goes below the comparator threshold.

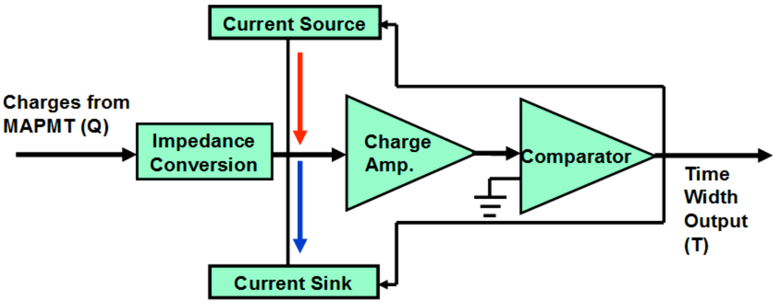

Figure 4.3.3.3-2. *Block diagram of the front-end ASIC.*

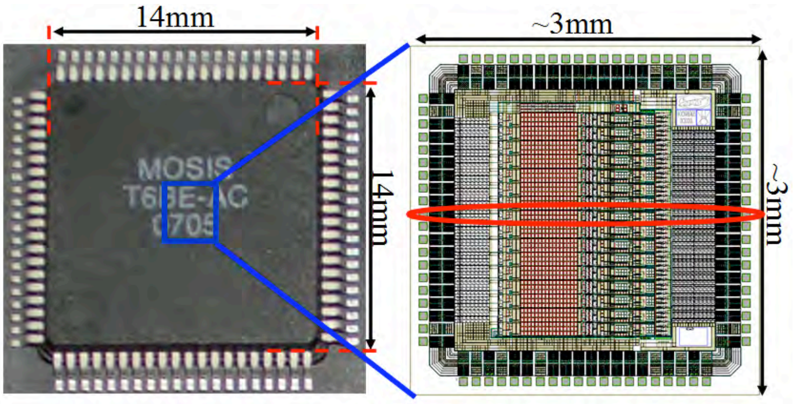

Figure 4.3.3.3-3. *80pin QFP package (left) and the ASIC layout of a bare chip (right).*

When the pulse from the integrator circuit falls below the comparator threshold, the current-sink circuit is activated to very slowly raise the integrator output voltage (more slowly than that of the electric source circuit), and then the comparator delivers a short pulse under a low period. However, its level remains enough lower than the effect of a background light. If the effective electric charge is injected from MAPMT, the input charge amount is converted to the output pulse duration.

The front-end ASIC has been designed and simulated using T-SPICE of Tanner Research Inc. The first version of the ASIC named “KI01” has been made by MOSIS Integrated Circuit Fabrication Service in 2006 (Fig. 4.3.3.3-3). There are 16 channels for the Q-T conversion circuit and various control circuits in a chip. The second version, named “KI02”, was made in 2007.

Regarding the above ASIC, we have tested and confirmed the followings:

- Measured power consumption is 1.8 mW/channel, which is conform to the designed value.
- Measured dynamic range of the Q-T conversion is at least 1÷300 photoelectrons/2.5μs, which satisfies the designed value (Fig. 4.3.3.3-4).
- Various adjust mechanisms work as designed.

This ASIC has been connected to the MAPMT and the output charges from the MAPMT were fed into the ASIC. It has been verified that the charges (Q) are converted to time width (T). Fundamental designed functioning of the ASIC was proved to work.

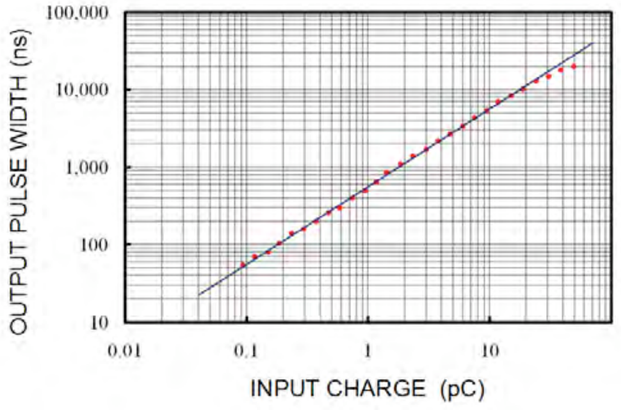

Figure 4.3.3.3-4. *Measured output pulse width as a function of input charge for the Q-T conversion ASIC.*

The circuit design of the next version with the following improvements has almost been finished.

- Power consumption will be decreased to 0.7 mW/channel, which may be decreased till around 0.4 mW/channel by the optimization.
- Further noise reduction of the electric circuits.
- Detection circuits of the single event upsets (SEU) caused by the radiation will newly be added.
- The value of the Supply voltages will be changed for easy handling.

High-density bare chip mounting board will be adopted to be able to pack the required number of channels in the limited space.

Second-level trigger (PDM)

The Second-level trigger is implemented in a dedicated FPGA chip of the PDM module. Each PDM module is connected to 9 pieces of ECs (36 MAPMTs), handling 1296 channels in total. Together with "segment_counters" (PH_CNT) of each pixel and tag data from red and yellow pixels, issued by the First-level trigger for every GTU, the Second-level trigger performs the "Linear Track Trigger", which aims to search for correlated hits during the track trigger time period (Δt = 11 GTU) along the predefined track angles. The trigger issue is done in each GTU based on the saved data in ring buffer of the FPGA. If the trigger is issued, it will be sent to the Third-level trigger.

The trigger algorithm is explained in detail in the section 4.3.3.4. However, it requires computing the sum of all pixel hit counts. Total of 16 predefined track directions are tested with trigger track time. The positive trigger decision is made when the hit sum is bigger than the Second-level trigger threshold for at least one of the 16 trigger track angles.

The key idea to perform the trigger logic computation, which has to be completed in the period of a GTU (2.5 μs), is to pick up simultaneously all relevant pixels data of track trigger time along a track direction under test, and to sum them up at a time.

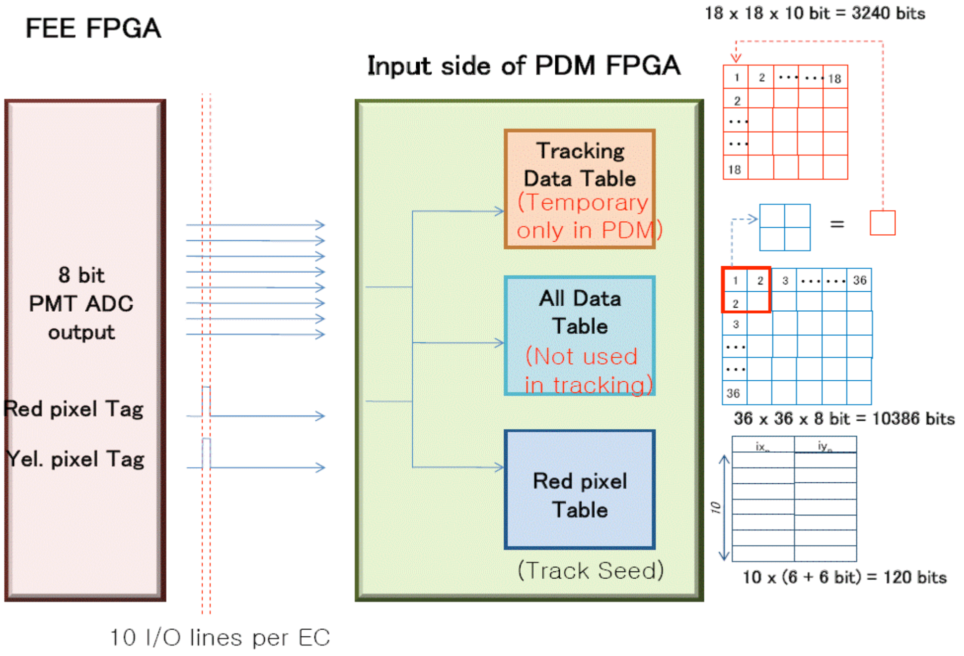

Figure 4.3.3.3-5. *Data flow from the First-level trigger. A total of 22 lines are needed to receive the all data from 36×36 pixels (two 8 bits lines), information of trigger type (two 1 bit lines), a Clock line of 100MHz, and a Token line.*

In order to carry out this trigger logic, three types of data tables are prepared (Fig. 4.3.3.3-5.): All Data Table (ADT), Tracking Data Table (TDT), and Red Pixel Table (RPT).

- ADT: a table containing *PH_CNT* data of all channels in an array of 18×18 pixels. Each pixel size is 8 bits. This table is not used in the trigger logic, but is stored in the ring buffer until the trigger decision is made.
- TDT: a summary table of *PH_CNT* in an array of 18×18 elements. Each element of the table is the sum in 10 bits of *PH_CNT* data of corresponding 2×2 channels.
- RPT: a list of pixel tagged as “RED”. This table has two columns for the pixel coordinates in X and Y direction (each 6 bits).

The above three tables are filled with multiplexed data coming from the First-level trigger. Considering the number of channels, GTU width, number of FPGA I/Os, and FPGA logic clock speed, total 22 input data lines are assigned between the First and the Second level trigger FPGAs: all 36×36 pixel data (two 8 bits lines), color definition information (two 1 bit lines), a Clock line, and a Token line. The FPGA is set to run in the clock speed of 100 MHz.

Fig. 4.3.3.3-6 shows the overall structure of FGPA logic in the Second-level trigger. The three data tables filled with new data, every GTU are saved in the ring buffers. The depth of ring buffer should be at least over track trigger time (11 GTU). However, the depth for ADT should be more than 100 GTUs to store initial part of shower data in case that the trigger is issued at the maximum of the shower.

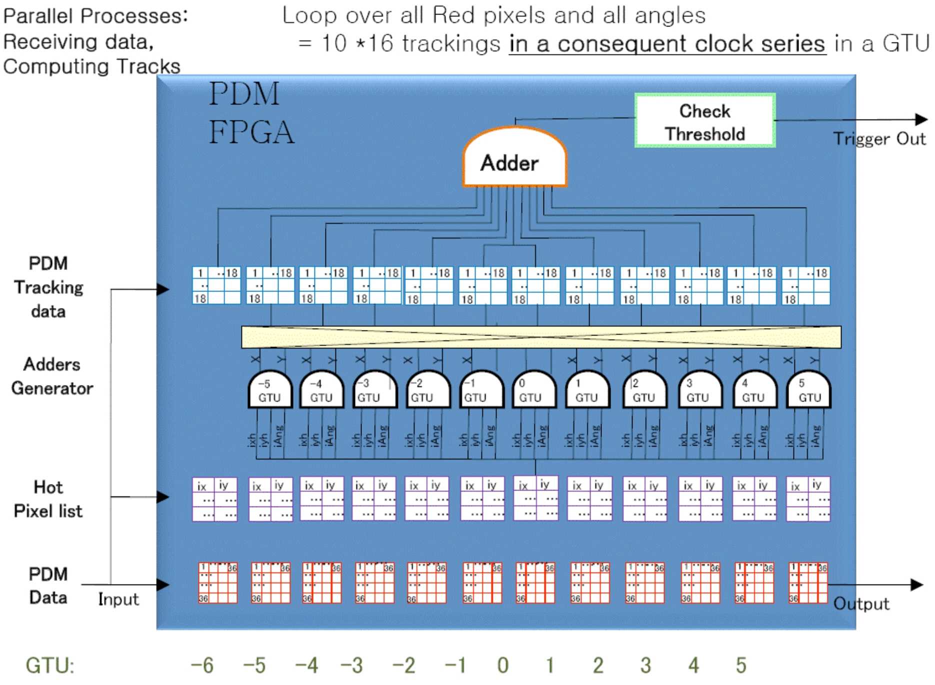

Figure 4.3.3.3-6. *The structure of FPGA logic in Second Level Trigger. Starting from a red (=hot) pixel in a GTU, it checks the sum of charge amount of Yellow pixels in 11 GTUs along one of 16 predefined track angles and judge if the value surpasses the threshold.*

The trigger determination starts with reading out the Red Pixel Table (RPT) of each GTU. The position information (ix, iy) of a Red pixel is sent to 9÷11 pieces of Address Generators (AG) (sketched in Fig. 4.3.3.3-7) together with the angle number for the test. This AG is the key mechanism in Second-level trigger. The position of Red pixel in the RPT (iX_{red}=ix, iY_{red}=iy) will be mentioned in the memory address (iX_{out}, iY_{out}) in TDT (Tracking Data Table) of the pixel along a test track. The AD does not need more than a couple of logic clocks because it refers to the look-up table stored inside.

Once the AG outputs become available, elements from 9÷11 pieces of Tracking Data Table will be compared with the Second-level trigger threshold. And this logic will be repeated for all the 16 predefined track angles as well as for all the elements in Red Pixel Table for a GTU.

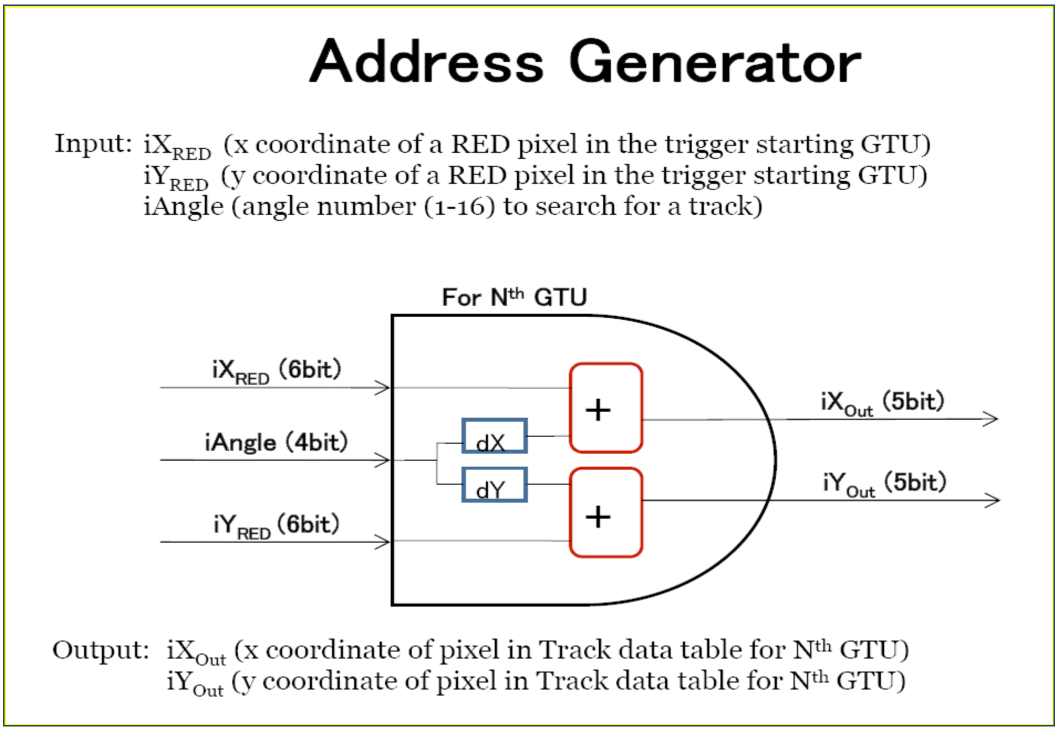

Figure 4.3.3.3-7. *Address Generator in Second-level trigger Logic. Direction of pursuit (iAngle) is given to a memory address line, and the increased amount of the address of pixel, which corresponds to the direction of corresponding memory cells, will be added to the address of Red pixel, and then outputted.*

Third-level trigger

The output from each 8 PDM board is transmitted via dedicated LVDS protocol to one of 21 Cluster Control Boards (CCB), then CCBs in turn transmit pixel information which passed the fine trigger conditions via SpaceWire interfaces to the Mission Data Processor (MDP).

The heart of the CCB is a Digital Signal Processor (DSP). Currently we foresee to use the Texas Instruments TMS320C6713B chip, which is available in two speed grades for the extended temperature range from - 40°C to 105°C, either as 167 MHz or 200 MHz version. Even at a clock frequency of 167 MHz, the TMS320C6713B delivers up to 1000 million floating-point operations per second (MFLOPS) and 1240 million instructions per second (MIPS). In addition, the chip needs two supply voltages, 1.2 V for the core of the processor, and 3.3 V for the I/O ports.

The group at IAAT (Institut für Astronomie und Astrophysik Tübingen) has some experiences with Texas Instruments DSPs for the German eROSITA project. In eROSITA project, a similar DSP was used to process the pixel data from a 384×384 pixel frame store CCD. The prototyping board for this processor was developed at IAAT. During Phase-B, we will use a hard and software development kit of Texas Instruments to investigate the performance of the DSP for application for the project.

Advanced option

In addition to the system trigger of the baseline, we are improving the function of FPGA of the 1st level trigger to do the filtering of events more efficiently. If it works as expected, we can reduce the number of events for the 2nd level trigger, and then we can reduce the energy consumption of the whole system trigger.

The First-level trigger in the advanced option is a three sub-levels trigger detailed here below:

- 1st sub-level. Anode-level trigger, basically an analog discriminator to recognize the arrival of a single photoelectron event at each anode. At this sub-trigger level the electronic noise effect is greatly reduced due to the fact that the "strong" anodic pulses are easily discriminated above the preamplifier electronic noise.
- 2nd sub-level. Pixel-level digital trigger, basically a gated counter and a digital comparator. The gate time is named GTU (from Gate Time Unit), its duration is about 2.5 μs (TBC). This sub-level trigger is issued whenever the number of single-photoelectrons recorded by an anodic chain within a GTU exceeds a pre-set digital threshold value. At this sub-trigger level the random background (randomly arriving photons) is greatly reduced by setting the digital threshold value above the observed background fluctuation.
- 3rd sub-level. PDM digital trigger, basically a gated counter and a digital comparator. This sub-level trigger is issued whenever the activity above the 2nd sub-level persists (persistency trigger) in consecutive GTUs, in a PDM or subset of it, up to a pre-set value. Whenever the activity above the 2nd sub-level persists, dedicated pixel-counters are increased and the sum of the grouped pixels (2×2 or 3×3 pixels) is compared with a pre-set value when the persistency is met, otherwise the pixel counters are reset.

In the advanced option, the 1st sub-level trigger is implemented using a fast discriminator designed within each channel of the front-end ASIC coupling the discriminator directly to the MAPMT anode and it is located inside the Charge to Time ASIC device. The sensitivity of the discriminator is such that it allows the discrimination of a single photoelectron pulse. The discriminator threshold can be set in between the electronic noise level and the single photoelectron average pulse amplitude. The speed of the discriminator is such that it allows the discrimination of pulses within a time separation as low as 10 ns. If the discriminator analog threshold is exceeded, a fast pulse is generated. The output signal (DISCR_OUT) is a short pulse (less than 10 ns duration) with standard shape and amplitude. The DISCR_OUT signal is used to increment a dedicated pixel-counter (note: one counter for each pixel) which is periodically re-set by an external signal (GTU_CLOCK). The period of the GTU_CLOCK is named "GTU", from Gate Time Unit. The counter value is continuously compared with a previously set Digital Threshold value: a Pixel_Trigger signal is issued whenever the counter reaches the Digital Threshold value (2nd sub-level trigger). The Pixel_Trigger level stays active for all the remaining part of the GTU. Moreover, when the pixel trigger is active, a gate is enabled to let the single photon pulses go through for the remaining part of the GTU. In other words, the Photon Count fast output pulse (N1) is issued each time the comparator is fired while the pixel trigger is active. The Gate Time Unit is a parameter that can be set from ground and that can be changed autonomously on board. The value of this parameter is related to the speed of propagation of a particle shower. A reference value for GTU is 2.5 μs when running in the normal (EECR) mode.

The 2nd sub-level trigger is implemented in digital way as follows. The signals (DISCR_OUT) coming from the 36 ASIC's hosted in 9 Elementary Cells (i.e. one "standard" PDM) are collected and managed by the FPGA in the Read-Out & Control Board of the PDM. The pixel-counter is periodically reset every GTU. A sufficient size for the counter is 8 bits. The counter value is continuously compared with a previously set Digital Threshold value (N) and a trigger signal (N1) is issued to the 3trd sub-level trigger whenever the counter reaches the threshold value. The N1 stays active for all the remaining part of the GTU and, at the beginning of the next GTU, it is reset. In addition, the counter value is stored in a dedicated ring memory at the end of each GTU.

With reference to a “standard” PDM, pixel-counters belong each Elementary Cell are grouped (2×2 or 3×3) and the sum (S) is compared with a pre-set value. The OUT_EN signal will be activated only if the 3rd sub-level trigger met the persistency condition P.

The 3rd sub-level trigger is implemented in digital way as follows. Each time a PMT_TRIG signal is issued by one PDM, that PDM is marked as active for the current GTU. The logic implemented in the FPGA looks for an activity continued for several contiguous GTU’s. If any pre-set criteria for a valuable pattern are met, the system trigger waits for the pre-set (mode-dependent) exposure time and then issues a ALERT_TRIGGER signal to the Second Main Trigger level.

An auto-level-trigger function will be implemented within the First level trigger: this will use the persistence rate measurements (number of consecutive active PDM_trigger) as the input of a software algorithm that calculates the proper setting for the two digital trigger levels (level 2 and level 3). This would allow for the instrument to set the optimum trigger levels in case of varying background conditions due to slowly transient phenomena (moon phase, clouds coverage, large urbanized area and so on). This special auto-trigger mode will be switchable ON/OFF and be fully re-programmable in flight.

Failure tolerance and reliability specifications

Any single point failure shall not cause a loss of more than TBD % in the total number of pixel readout capability of JEM-EUSO. This requirement asks for the subdivision of the JEM-EUSO electronics into a suitable number of independent blocks so that the loss of each of them does not affect the whole functionality by more than the specified percentage. Any single point failure in any JEM-EUSO functional subdivision will not propagate to any of the others. All integrated circuits parts shall be mil 883/B level as minimum (TBC).

4.3.3.4. Trigger and read-out software

The basic Trigger & Readout algorithm shall be as follows:

(i) The instrument normally stays in a “waiting” status or “free running mode”, in which background noise is continuously written into the PDM ring memories. The written data are the PDM pixels array.

(ii) At the occurrence of an event (i.e. when 3rd level trigger fires), a dedicated signal runs the instrument for data acquisition.

(iii) The instrument continues to write data into the memories for a pre-set amount of time (exposure time).

(iv) At the end of the exposure time, the instrument goes in a “hold” status and the read-out phase starts.

(v) During the read-out and write-out phase, the content of the memories of the “hit” PDMs is downloaded into the CPU data buffer.

(vi) At the end of the data download, the instrument re-starts from the “waiting” status.

First-level trigger (EC)

The System Trigger logic flow shown in Fig. 4.3.3.4-1 summarizes the case when the instrument is set for standard EECR observation with automatic slow-mode enabled.

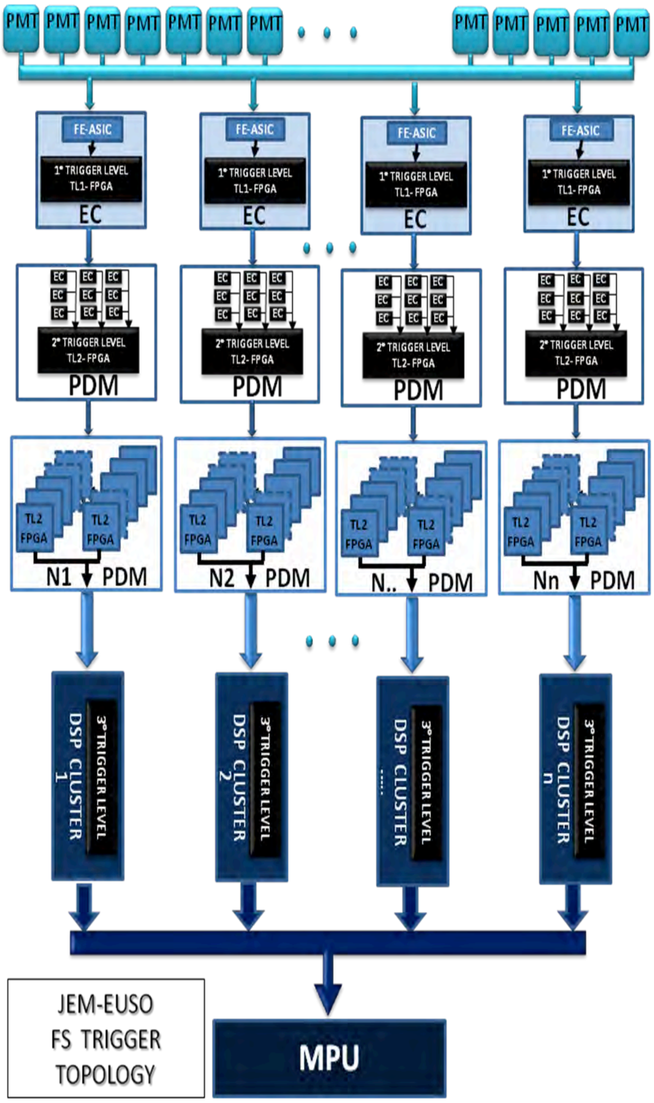

Figure 4.3.3.4-1. *Trigger flow diagram.*

With reference to Fig. 4.3.3.4-1, the instrument is normally waiting for trigger. If a MC_TRIG persistency is detected, i.e. a given MC_TRIG stays active for a selected number of GTUs, then the System Trigger is run. The System Trigger then checks the duration of the detected persistency until one of the following cases happens:

a) the persistency disappears;

b) the persistency duration exceeds a given duration of N2 (e.g. N2=300) GTUs and continues.

In case b), the System Trigger autonomously switches the instrument in “slow mode” and continue to monitor the event evolution until case a) happens. A “stuck check” routine is also executed in order to restart the System Trigger in case it is “stuck”. Basically, this routine should work as a sort of watchdog. In the “slow mode”, a *SLOW_DOWN* signal is sent in order to slow down the X and Y ring memories updating rate in order to keep trace of what is likely to be a long lasting event like e.g. a meteoroid. The *PH_CNT* ring memory continues to be updated at the standard speed.

In case a), the System Trigger checks if the event duration exceeds a given duration of N1 (e.g. N1=30) GTUs, then:

- if the answer is **"no"** (a-a), the System Trigger checks if the Fast Mode is enabled;
  - if the Fast mode is not enabled (a-a-b), then the trigger is restarted and the instrument restarts waiting for a next event (that means the event is considered as a spurious transient);
  - if the Fast mode is enabled (a-a-b), then it is activated so to acquire possible interesting non-EECR phenomena and collect the data.
- if the answer is **"yes"** (a-b), then after a pre-set "exposure time" (e.g. 300 GTUs), the System Trigger issues the *SAVE_FRAME* signal and initializes the readout routine.

All the settings related to the System Trigger (N1, N2, "exposure time" etc.) will be in-flight programmable as part of the instrument initialization routine to be run at the beginning of each observation.

Second-level trigger (PDM)

The algorithm working as a 2nd trigger level, presently proposed for JEM-EUSO, is called 'Linear Track Trigger' method (LTT) which searches for light points moving with the light speed at 400 km ahead. This method is implemented in the PDM electronic circuit. The strategy of the Track Trigger Method is as follows:

(i) When a 1st trigger level is issued, the pixels of the entire PDM are divided into three categories (Red, Yellow, and White pixels). Red pixels are defined to have a high signal ($N_{phe} \geq N_{thr,r}$). The trigger algorithm starts on a Red Pixel. Yellow pixels hold a moderate signal ($N_{thr,y} \leq N_{phe} < N_{thr,r}$). Only Yellow and Red pixels are used to integrate the signal of the track for triggering purposes. White pixels have low or absent signal. These pixels are discarded immediately, and not used anymore for the trigger analysis. The thresholds of $N_{thr,y}$ and $N_{thr,r}$ depend on the background noise level. Because of the limited computational capacity, the thresholds are set in order to have, in presence of pure background, $N_{red} < 1$ Red pixel and $N_{yellow} < 100$ Yellow pixels every GTU.

(ii) This algorithm searches tracks developing with specific directions at the speed of light, taking into account such fundamental characteristics that distinguish an air shower from noises. In the following, we define θ and ϕ respectively as the zenith (θ=0° means the nadir direction of JEM-EUSO) and azimuth angles of the air shower. Such angles are related either to the ΔX and ΔY distances imaged by the track on the X-t and Y-t projections and to the on-ground pixel size (ΔL) by the following relationships [67]: $\phi=\tan^{-1}(\Delta Y/\Delta X)$; $\theta=2\cdot\tan^{-1}(C\cdot\sqrt{(\Delta X^2+\Delta Y^2)})$; $C=\Delta L/(c\cdot GTU\cdot\Delta t)$, being "c" the speed of light. Assuming a fixed time length Δt (i.e. Δt =9÷11 GTU), inclined showers will be detected as tracks moving through several pixels, while almost vertical EAS will be seen as spots insisting always on the same pixels. We consider implementing inside the FPGA of 2nd level, 16 different directions, chosen to cover homogeneously the entire θ, ϕ plane. As in the case of Red and Yellow pixels, the total number of directions is decided at an acceptable level within the computational capacity.

(iii) Upon receiving the alert by a Red pixel, the algorithm defines a 'box' of maximum N_{pix}/GTU around the Red pixel that gave the alert, and for N_{pers} GTU persistence centered on the GTU_0. The content of the Yellow and Red pixels inside the 'box' are integrated. The location of the 'box' varies from GTU to GTU in accordance with the specific direction in analysis. In particular, if the algorithm is analyzing a vertical shower, the box will insist on the same pixels for the entire N_{pers} GTU, while in the case of horizontal showers, the box will shift by about one row and/or one column of pixels of every GTU. The two parameters, N_{pix} and N_{pers}, are related respectively to the width and length of the tracks, as well as to the total number of angular trials and computational capacity. In the present setup, N_{pix} equals 4, and N_{pers} equals 9÷11. The width of the track is related to the EAS energy, to the spot size of the optics (~4 mm), to the position of the spot on the FS (in the center of a pixel, or in between pixels), and to the response of the PMT (cross-talk). The final configuration will depend on a trade-off between number of directions, dimension of the boxes, and thresholds on Red and Yellow pixels.

(iv) After defining the location of the 'box' in the N_{pers} GTU, the content of the Yellow and Red pixels of such boxes is integrated and the total number of photoelectrons (Σ_{track}) is compared to a preset threshold THR (bkg), that depends on the average background level. The THR (bkg) as well as the $N_{thr,r}$ and $N_{thr,y}$ strongly depend on the average background level and on the rate of fake events that is acceptable for the experiment. At present, the thresholds (in particular THR(bkg)) are set in order to achieve a trigger rate on fake events between 0.1 Hz/FS and 1 kHz/FS. The stricter condition is applied to match the signaling speed to the ground. It is important to be aware that the rate of real events detected will probably not exceed few events per hour (~10^{-3} Hz/FS) on the entire Focal Surface, FS (see Table 4.3.3.2-1).

Third-level trigger (PDM cluster)

The software for the 3rd level and Lidar is implemented in the DSP tip which is stowed on the cluster control board (CCB). The 2nd trigger level operates at PDM level. However, some tracks will develop crossing different PDMs, typically in case of showers of large zenith angle. It is therefore important to trigger also these events. At the same time, artificial lights such as city lights, seem vertical air showers at few GTU scale. It is also important to avoid such events. For the above reason, the 3rd trigger level is being developed, based on the Track Trigger Method and it has the following characteristics:

- more refined and more number of directions will be scanned;
- higher flexibility in the starting point of the track;
- limits on the total number of GTUs in which the signal exceeds the average background;
- lower threshold for events in which near-by PDMs issue a 2nd level trigger in a close time window and space location;
- monitor possible failures or anomalies at PMT, EC or PDM levels and, temporarily inhibits their functions.

4.3.3.5. Data acquisition and handling

General considerations

JEM-EUSO Data Acquisition and Handling System is designed to maximize detector observation capabilities to meet the various scientific goals, to monitor system status, autonomously taking all actions to maintain optimal acquisition capabilities and handle off-nominal situations. CPU and electronics are based on hardware successfully employed in Space experiments such as Pamela, Agile, Altea, Sileye-3, …, taking into account recent technological developments in microprocessors and FPGA. Acquisition techniques and algorithms also benefit from the development performed in these missions. Rad-hard technology will be employed, with ground beam tests (e.g. GSI, Dubna, Himac) to qualify and test resistance of new devices. Space qualified devices will be employed wherever required by safety and agency requirements.

Particular care will be taken to the use of off-the-shelf technologies in the development of the laboratory models and breadboard systems used to refine and test the various trigger and data reduction algorithms. The same approach will be followed in the use of communication protocols and interfaces (e.g. VHDL, SpaceWire, 1553, 1355 protocols) and in the realization of the Ground Support Equipment. This will allow for a fast development of the software in parallel to the engineering and flight boards, reducing costs and integration time.

Hot/Cold redundancy will be implemented in all systems and in all stages of data processing with the exception of intrinsically redundant devices such as the focal surface detectors.

Data budget

Data acquisition is based on a hierarchical architecture designed to reduce at each level the amount of data through a series of triggers controlling an increasingly growing area of the focal surface. It is necessary to pass from the ≈ 10 GB/s on the Focal Surface to the ≈ 250 kbps which can be down-linked on the ground. Each board and data exchange protocol is compliant to the handle the data and send them to the higher level when needed. As an advanced option it is foreseen to use physical storage on hard disk on board the ISS and send them to the ground. In this case a factor 2 or 3 improvement in the data budget is expected.

Table 4.3.3.5-1. *Data budget and transmission speed at various acquisition levels.*

Level	From	To	Trigger rate	Reception rate	Total DH Budget	Reception speed from each subsystem
1st PDM Control Board	EC *9 EC*	PDM Control Board	200 kHz/EC	1.8 MHz (total trigger rate on 1 PDM from 9 EC)	518.4 MBytes/s on a PDM	57.6 MB/s each EC
2nd CCB Cluster Control Boards	PDM Control Board *8 PDM*	CCB Cluster Control Boards	7 Hz/PDM (trigger rate from each PDM)	56 Hz/CCB (total trigger rate from all PDM)	18.56 MB/s	2.32 MB/s from 1 PDM to CCB
3rd CPU	CCB *21 CCB*	CPU	5.3 mHz/CCB (maximum allowed trigger rate including background)	0.11 Hz/CPU (total FS trigger rate including background)	36.5 kB/s to mass memory/ISS (total from all CCB) + Lidar + IR camera + HK	1.73 kB/s from CCB to CPU (each CCB can send about this value of data to CCB); central section more

Communication protocol

Communication between different layers operates with LVDS to minimize interference and reduce power consumption. All lines are redundant, with each line employing double ODU connectors at each end to increase reliability of the system and resistance to vibrations and thermal stresses. High level communication protocol between CCB and CPU is based on SpaceWire.

Commands from ground

Slow control communication from/to ground is based on MIL-STD-1553B bus, a slow speed reliable bus used for transmission/reception of critical information. A 1553B bus consists of two twisted, shielded pairs of copper wires, as sketched in Fig. 4.3.3.5-1. The speed of the bus is 1 Mbit/second (as compared to fiber optic networks which operate at approximately 100 Mbit/second), but it follows the Military Standard 1553B protocol. Although speed is sacrificed by using this protocol, there are several positive reasons for using the 1553B bus. Specifically, the 1553B is well-proven in Space. Additionally, it has significant built-in redundancy capabilities that make it a good choice for space applications.

In JEM-EUSO the 1553B bus is employed to:

- Switch on/off the instrument or sections.
- Issuing of telecommands from ground.
- Set general acquisition parameters based on detector status. Furthermore they can be used to patch (reprogram) part of the software at CPU, DSP or FPGA levels and dump the memory of each level in case of debugging.
- Reception of keep-alive information from the detector, of nominal events, alarms.
- Switch from mail to spare channel (acquisition, power supply).

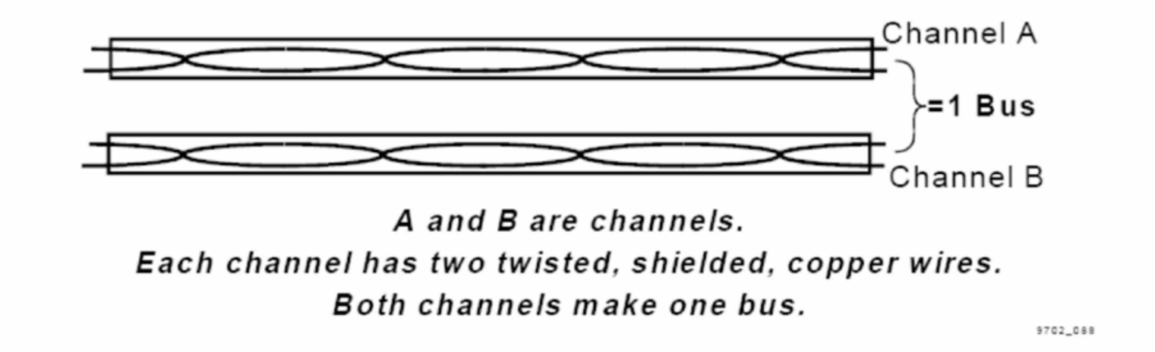

Figure 4.3.3.5-1. *The 1553B .bus*

Downlink/Download

Data download to ISS uses Ethernet protocol for high speed data transfer. Data are subsequently downlinked to the ground via TRDS link or stored on Hard Disks.

Data transmitted to the ground consists mostly of events coming from the FS but include also:

- Housekeeping information
- Alarm
- Calibration data
- Ancillary information
- Experimental data

According to available bandwidth data are sent to the ground with highest priority given to housekeeping and alarm information. Experimental data are sent to ground with main priority to high energy particle data and special trigger (e.g. luminous phenomena). Part of the data is stored on board ISS on disk server. Disks are then periodically sent to the ground with Soyuz capsules. Disks storage is expected to triple available bandwidth on board allowing to lowering the energy threshold of the apparatus or to save specific triggers belonging to particular classes of physics events.

4.3.3.6. CPU system

The CPU System is composed of a number of boards devoted to different tasks:

- CPU
- Mass Memory
- Internal Housekeeping interface (I-HK)
- ISS interfaces (1553 and Ethernet)
- Fast bus interface for event acquisition

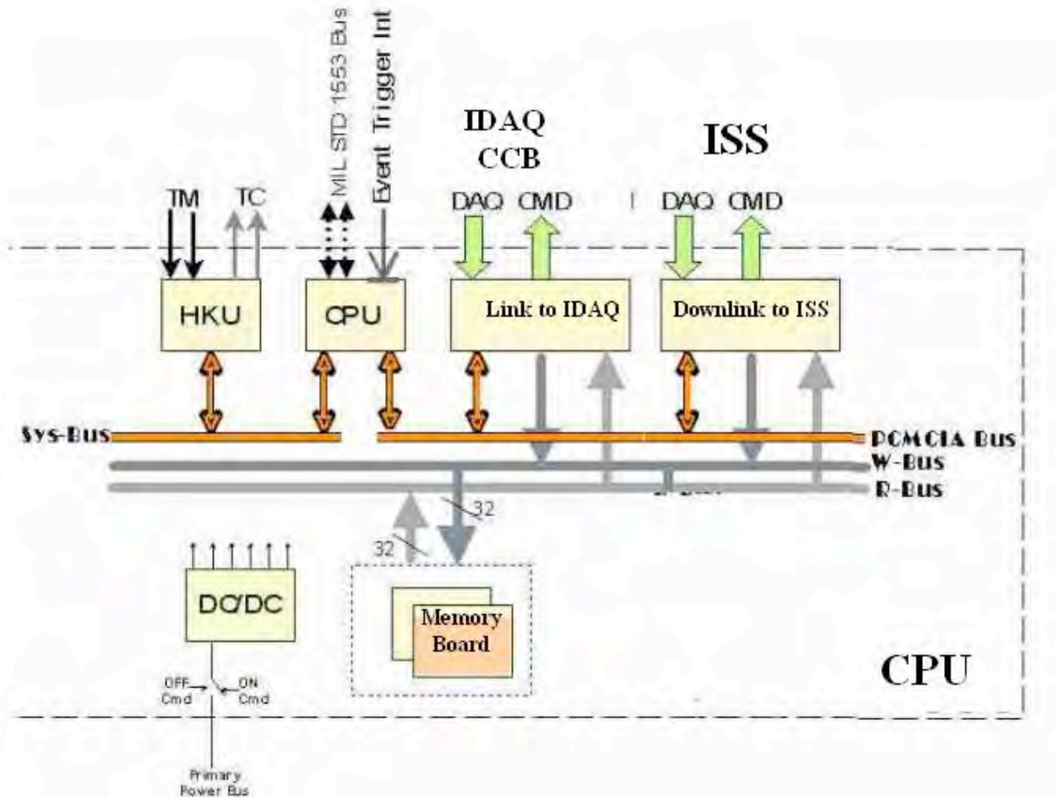

Figure 4.3.3.6-1. *The CPU internal block diagram and interfaces with other subsystems.*

The CPU is devoted to the control of the apparatus and the general optimization of the performance of the instrument in terms of data budget and detector status. It is expected to function autonomously and to reconfigure the working parameters with little or no intervention from the ground. It will handle alarm and contingencies in real time minimizing possible damage to the instrument. Long term mission operation and observation planning from the ground will be implemented from the ground with specific telecommands used to overrule the specific operation parameters of the instrument. By sending immediate or time-delayed telecommands it will be possible to define the various operation parameters of the instrument in terms of specific physics objectives or specific situations.

In this scheme most of the computational power resides in the CCB (Cluster Control Boards), with the CPU being charged with trigger handling, telecommand reception and implementation, housekeeping monitor and so on.

The main CPU tasks are:

- Power on/off of all subsystems
- Perform periodic calibrations
- Start acquisition / Run
- Define trigger mode acquisition
- Read Housekeeping
- Take care of real time contingency planning
- Perform periodic download/downlink
- Handle 1553 commands

CPU chip

CPU core for high level data acquisition and processing is based on Atmel AT697 Leon Chip. It is a Rad Hard 32-bit SPARC V8 embedded processor, an implementation of the European Space Agency (ESA) Leon2 fault tolerant model.

The baseline configuration for JEM-EUSO CPU core is based on the Leon2 architecture, although different configurations (Leon3, HIREC) are also being considered. Baseline chip is AT697E, with AT697F as advanced option which is expected to have passed qualification tests by the end of 2008. AT697F is pin compatible to the AT697E, and it will have improved radiation resistant capabilities, >300 krads.

The AT697 is a highly integrated, high-performance 32-bit RISC embedded processor based on the SPARC V8 architecture. By executing powerful instructions in a single clock cycle, the AT697 achieves throughputs approaching 1 MIPS per MHz, allowing the system designer to optimize power consumption versus processing speed. The internal block diagram of the Amtel AT697 chip is sketched in Fig.4.3.3.6-2. The AT697 contains an on-chip Integer Unit (IU), a Floating Point Unit (FPU), separate instruction and data caches, hardware multiplier and divider, interrupt controller, debug support unit with trace buffer, two 24-bit timers, parallel and serial interfaces, a watchdog, a PCI interface and a flexible memory controller. The design is highly testable with the support of a Debug Support Unit (DSU) and a boundary scan through JTAG interface. An idle mode holds the processor pipeline and allows timer/counter, serial ports and interrupt system to continue functioning. The processor is manufactured using the Atmel 0.18 μm CMOS process; it has been especially designed for Space applications, by implementing on-chip concurrent transient and permanent error detection and correction.

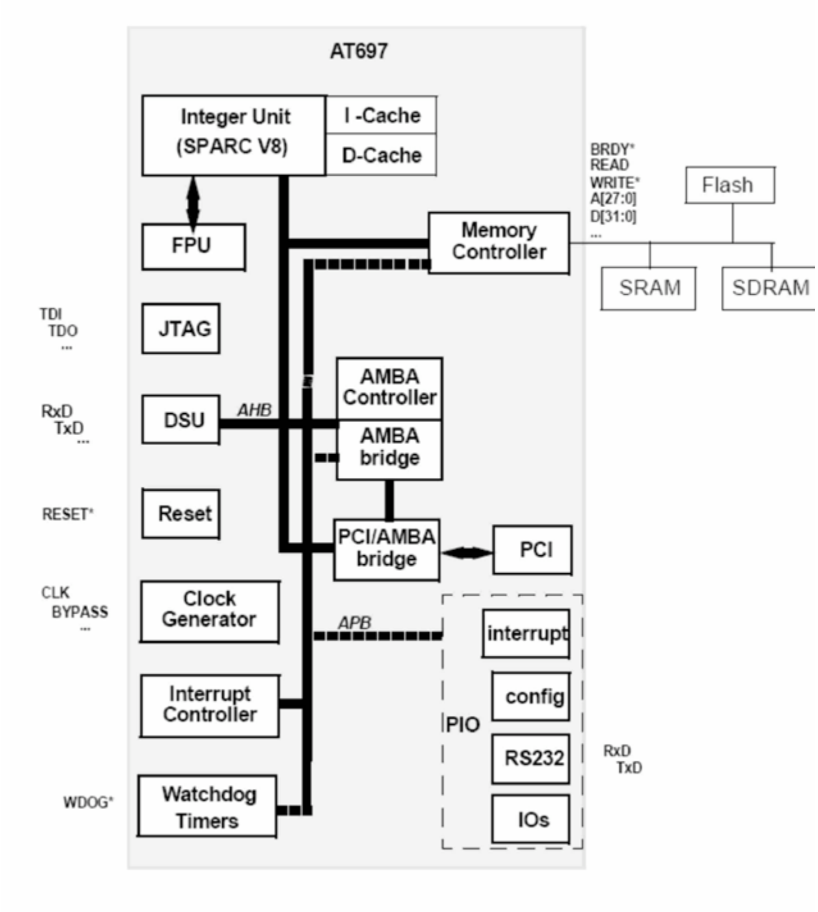

Figure 4.3.3.6-2. *The AT697 internal block diagram.*

Software

CPU software is written in C using ERC32 Cross Compilation System (ERC32CCS). This platform was developed by ESA for Space applications. ERC32CCS-v2.0.7 is a GNU-based cross-compiler system for ERC32 allowing software development and testing on Linux-based emulator machines. The same code can then be recompiled for the target application (Atmel chip).

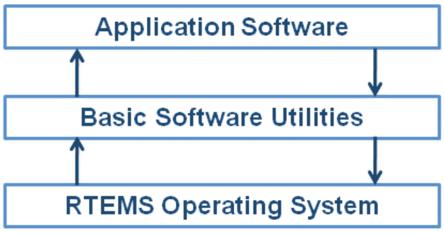

Figure 4.3.3.6-3. *Application and operating system layers. Data acquisition and all procedures are implemented at an application software level.*

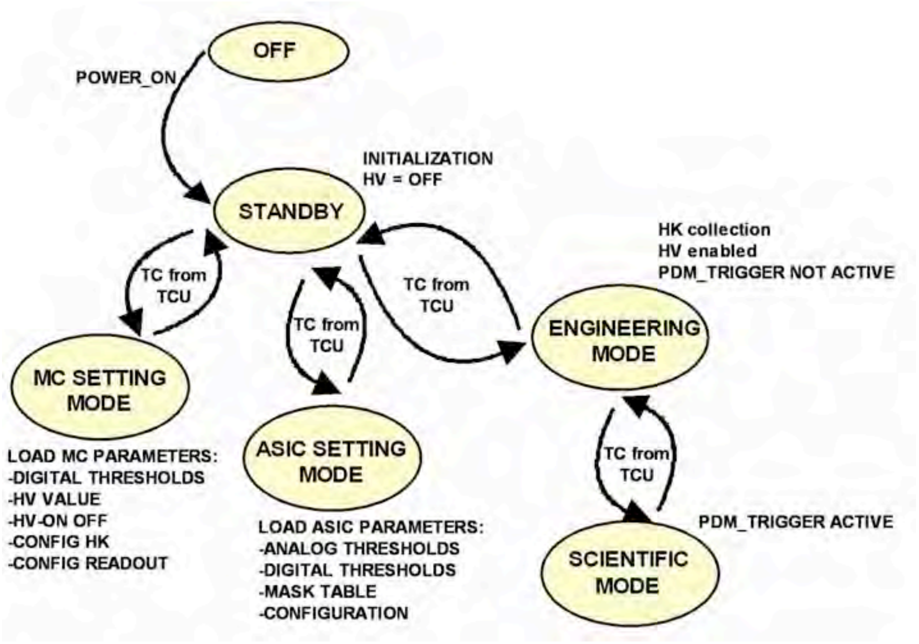

Figure 4.3.3.6-4. *CPU software operational models.*

Current framework for ERC32 consists of:

- GNU C/C++ compiler (egcs-1.1.2)
- GNAT Ada 95 compiler (gnat-3.11p)
- Linker, assembler, archiver, etc. (binutils-2.9.1)
- Standalone C-library (newlib-1.8.1 from Cygnus)
- RTEMS real-time kernel with ERC32 support (rtems-4.0.0)
- ERC32 boot-prom utility (mkprom-1.2.7)
- Standalone ERC32 simulator (sis-3.0.5)
- GNU debugger with ERC32 simulator (gdb-4.17 + sis-3.0.5)
- DDD graphical user interface for gdb (ddd-3.1-3)
- Work-arounds for all FPU rev.B/C errors

The ERC32CCS allows cross-compilation of single or multi-treaded C, C++ and Ada95 applications for ERC32. Using the gdb debugger, it is possible to perform source-level symbolic debugging, either on the simulator or on a remote target.

Memory board

Memory board is based on rad hard chips (3d cube). Storage is performed on 10 bit / byte, with one bit flip automatic error correction and two bit flip error detection. A total of 4 Gbytes are foreseen. Main task of the memory board are temporary storage of data prior to transmission to ISS. This allows added flexibility during periods of absence of downlink to ground or special operations.

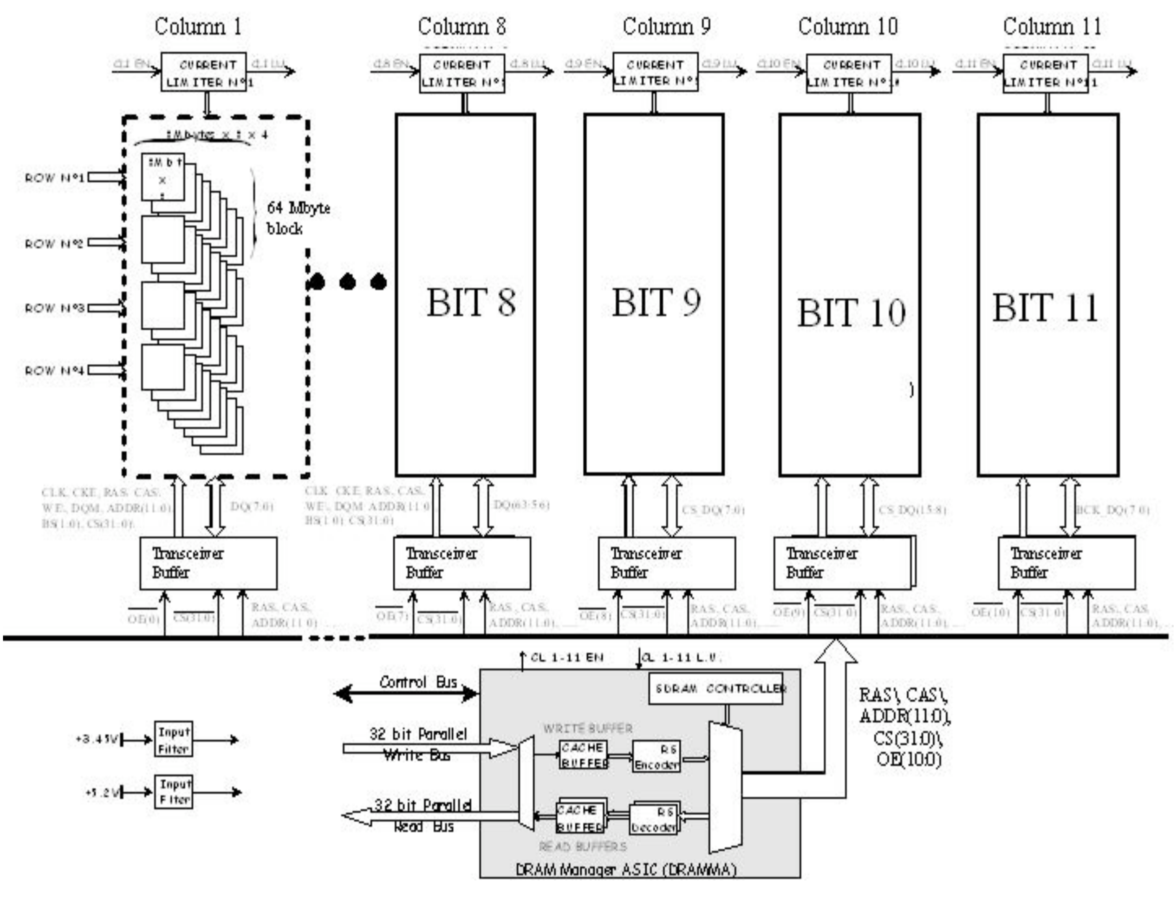

Figure 4.3.3.6-5. *Memory module block: 10 bits are used for error correction of one bit flip and detection of two bits flips. 11th bit is used for spare.*

The functional module is housed on an “extended” Double Europe PCB (200×233 mm). This module is in charge of four main functions:

(i) To Send Commands to the experiment Front-End (FE) via a parallel CMD I/F.

(ii) To Receive Science Data Packets (SDP), through a parallel Data Acquisition Interface (DAQ I/F), from the experiment Front-End.

(iii) To manage the Mass Memory (MM) for storing Science Data Packets received from the experiment Front-End or Data Packets coming from the internal CPU module.

(iv) To manage the downlink of data files stored in Mass Memory towards an external Telemetry Adapter Module via a dedicated parallel TAM I/F.

Fast bus interface

The main building blocks of this module are:

- The parallel CMD I/F that is composed of 10 LVDS differential lines (8 Data out, 1 Strobe out, 1 Ack in).
- The parallel DAQ I/F that is composed of 10 LVDS differential lines (8 Data in, 1 Strobe in, 1 Ack out).
- The parallel TAM I/F that is composed of 10 LVDS differential lines (8 Data out, 1 Strobe out, 1 Busy in).
- A “PIF Core Controller” FPGA including all the module’s control functions, as:
    - PCMCIA Bus I/F
    - CMD DMA management
    - DAQ DMA management
    - MM Parallel Write Bus management
    - MM Parallel Read Bus management

Housekeeping modules

Two different housekeeping modules are foreseen: one internal (I-HK) to the CPU system, linked via serial bus and one external (E-HK), linked to the CPU via digital line. The housekeeping modules interface the CPU with the aim to distribute command to the CPU users and to collect telemetry for monitoring purposes and optimization of observational parameters.

The internal housekeeping module is devoted to monitor of critical systems, power on/off of secondary power supply, etc. I-HK is turned on together with the CPU and enables power on to all subsystems, including E-HK. Task of the latter is the general slow control and monitoring of the status of the apparatus.

The I-HK functional module is housed on an “extended” Double Europe PCB (200×233 mm). Both single (upon request) or cyclic (periodic) acquisition/commanding operating mode are possible according to the status of the acquisition.

According to the type of signal different acquisitions and control are foreseen. For instance all relays for switch on/off secondary power supply and subsystems are controlled by High Level signals. This approach has the advantage of a great degree of flexibility keeping at the same time a strong robustness and reliability.

A summary of the commanding and acquisition electrical interfaces provided by the module is given here below:

- Voltage monitor (Primary – 120V 28V; Secondary: +-5V +12V , +3.3V -700V
- Current monitor
- Temperature monitor
- Contact closure (Lid status, relays)
- Digital Communication Protocol (Cam Bus)

The internal housekeeping block scheme is shown in Fig. 4.3.3.6-6, with commands as detailed in Table 4.3.3.6-1.

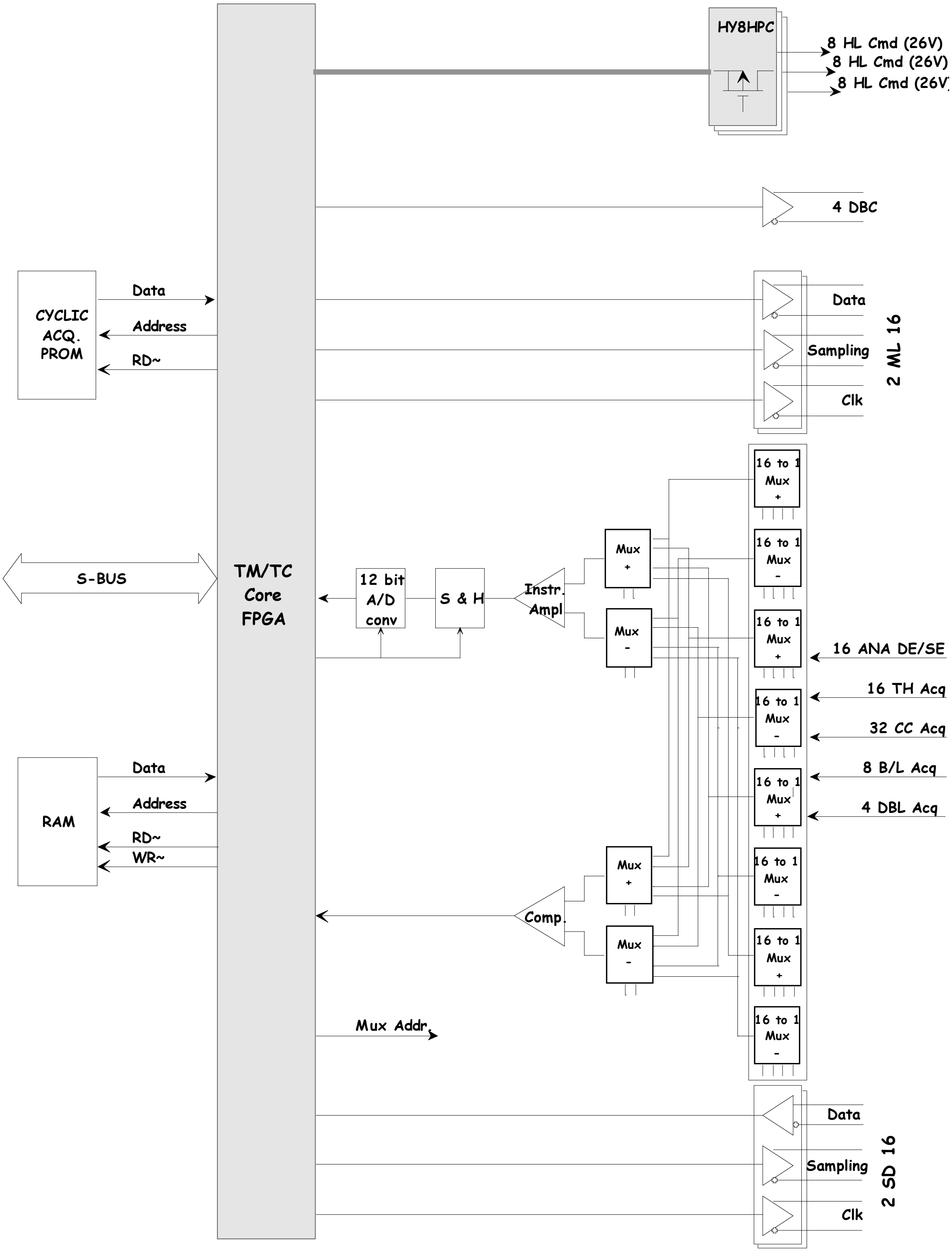

Figure 4.3.3.6-6. *Internal housekeeping (I-HK) block scheme.*

Table 4.3.3.6-1. *Internal HK details (see Fig.4.3.3.6-6).*

Commands	**Quantity**
High Level 26V (**HL26**) pulsed commands. These are power command used to pilot directly the relays of the power supply and DC/DC system. In this way we do not need to go through the secondary lines and we can control the switch on/off of the power supply (main/spare) and control the power on procedure in order to switch on gradually the whole apparatus.	50
Memory Load 16 bit (**ML16**) serial commands. This is the output digital line for controlling the CAM bus and the additional housekeeping board. It is basically a Digital output port. Four of them issue commands to different boards independently.	4
Differential Bi-Level (**DBC**) commands. Output command to issue commands where ground is an issue or in noise-robust environment.	8
Acquisitions	**Quantity**
Contact Closure (**CC**) acquisitions. Check if a relays has been closed and monitor the start-up procedure.	50
Bi-Level (**Bi-L**) acquisitions. Read the status of one system (8 systems in total)	8
Differential Bi-Level (**DBL**) acquisitions. Read the status of one system in differential in order to be independent from different grounding.	4
Analogue Double Ended (**DEA**) acquisitions. Acquisitions (slow control) through 12 bit ADC, differential related (voltage, current, etc)	50
Analogue Double Ended Thermistor (**TH**) acquisitions (Betatherm 10 kΩ @ 25 °C). Thermal resistors readout.	50
Serial Digital 16 bit (**SD16**) acquisitions. Input port 16 bit for readout of digital messages from the various boards.	4

IDAQ board

IDAQ board handles all communication with CCB and other subsystems. It is an FPGA-based interface board taking care of:

- Event packing and data transfer from CCB to Mass memory
- Issuing of commands from CPU to CCB
- Issuing of commands from CPU to FPGA boards
- Patch/dump of software of CCB and lower level boards
- Pass-through commands between CCBs

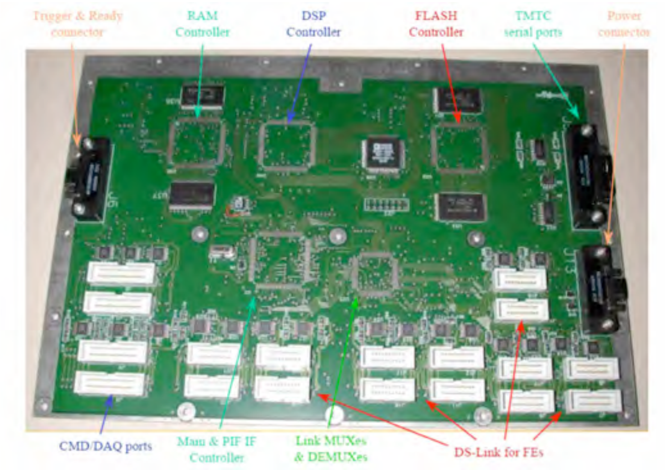

Figure 4.3.3.6-7. *Prototype of the IDAQ board based on Pamela development.*

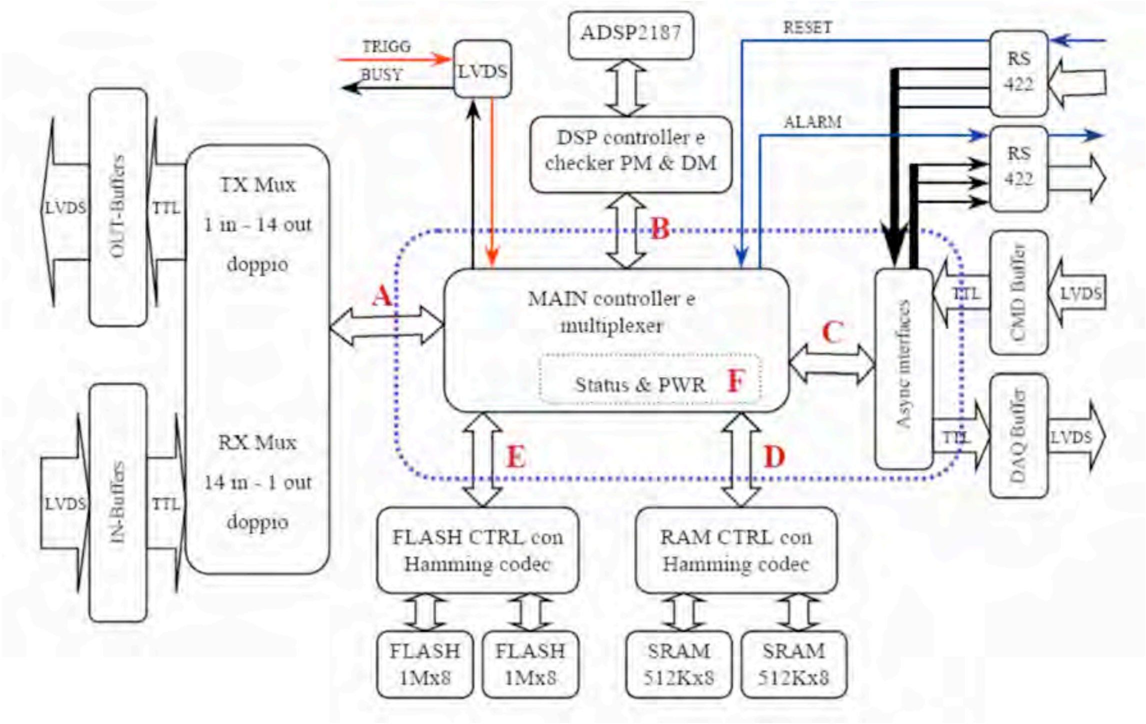

Figure 4.3.3.6-8. *Functional scheme of the IDAQ board.*

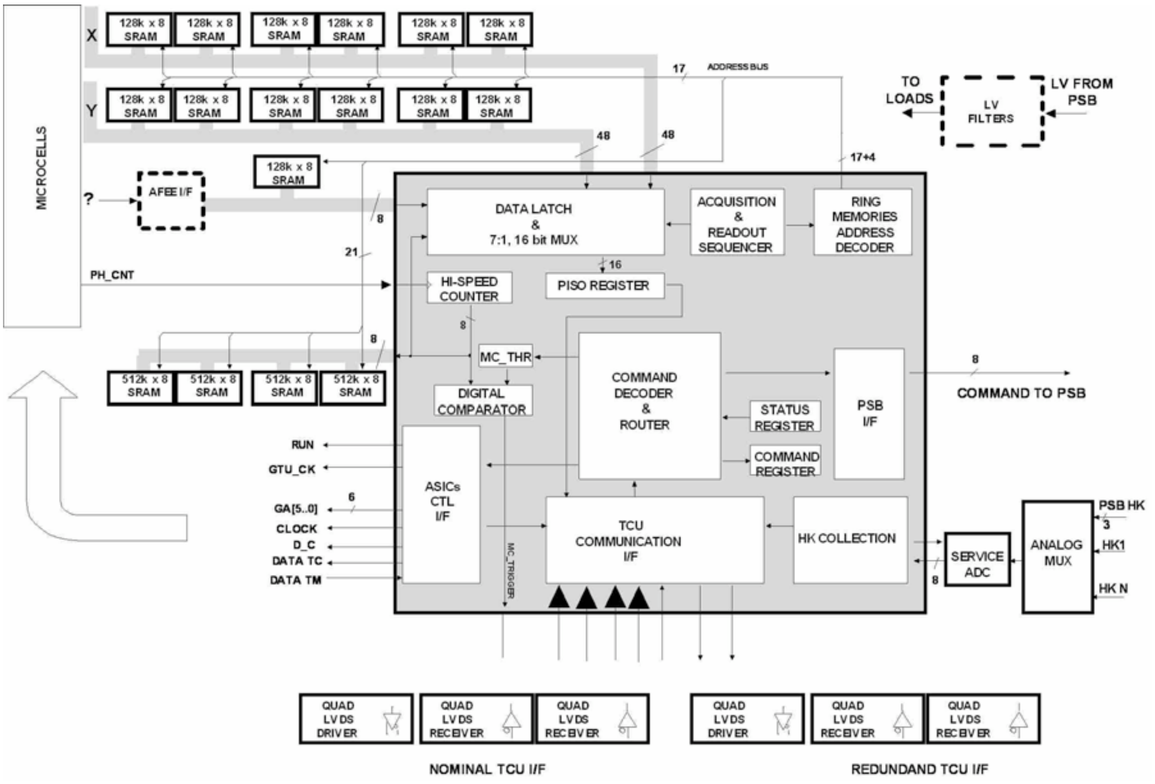

Figure 4.3.3.6-9. *Detailed design of the IDAQ board.*

Power supply distribution

ISS provides +120V and +28 V current. DC/DC converters will provide all secondary power supplies to the CPU system and all subsystems. At power on, the following procedure is followed:

(i) Power on of primary.

(ii) Power on of secondary power for CPU system.

(iii) CPU starts up, checks all internal systems.

(iv) I-HK board checks status of the experiment.

(v) I-HK board switches on all secondary power supplies.

(vi) I-HK board enables power to all subsystems in predefined sequence to avoid large inrush currents and unbalanced power to critical systems.

(vii) E-HK board checks status of subsystems and monitors it in real time.

(viii) In case of failures or contingencies subsystems are switched off.

Note that this approach has the advantage to allow the CPU of JEM-EUSO to keep under control the power on and off of the experiment and monitoring it at all times. A direct power on of the subsystems has the disadvantage of not being able to take care of contingencies or unbalances in the power supply.

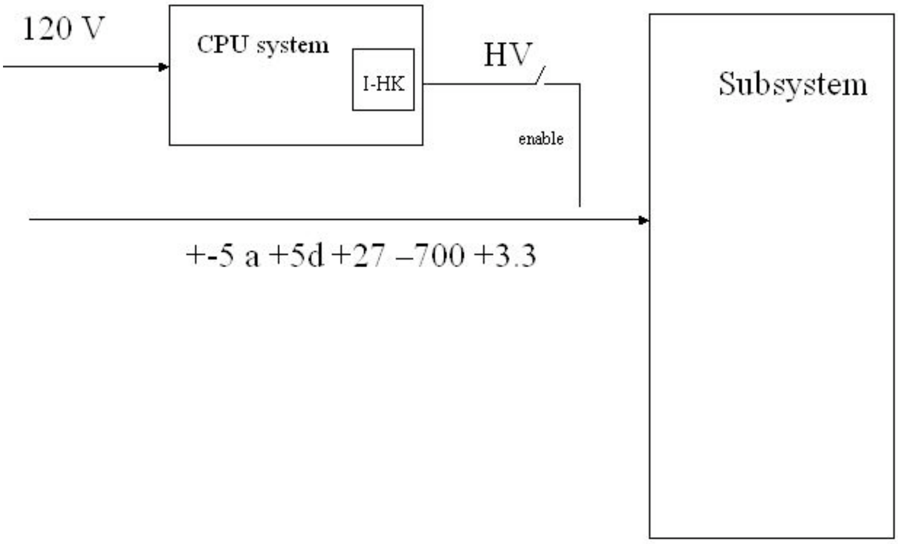

Figure 4.3.3.6-10. *Logical scheme of power supply: power to all sub-systems is enabled from I-HK board in the CPU system.*

Cluster control board

Cluster control board (CCB) is devoted to high performance (1 Gflop) trigger system. Each of the 21 CCBs performs trigger recognition on a part of the Focal Surface covered by 8 PDM.

CCB performs data reduction by three orders of magnitude. In case of track recognition, if the track is close to the boundary of the CCB, data is requested to nearby CCB. Both primary and secondary CCB transfer data to the mass memory of the CPU via the IDAQ.

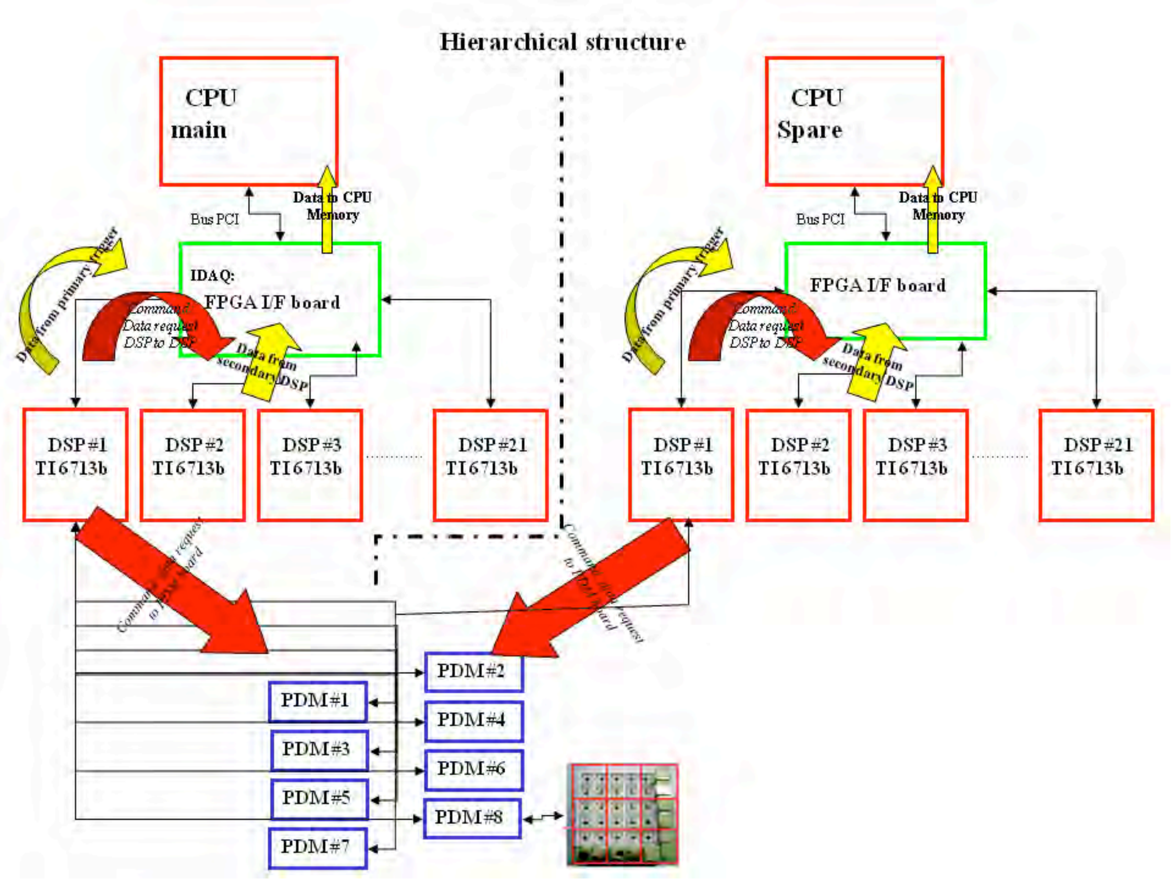

Figure 4.3.3.6-11. *Scheme of the acquisition system of JEM-EUSO. The Structure is organized in a hierarchical system with the CPU controlling, via IDAQ, the 21 CCBs with Texas 6713 DSPs. Each CCB controls operations of 8 PDM boards, each devoted to 9 elementary cells.*

Development scheme, laboratory and engineering models

In experiment realization is of critical importance to parallelize development of subsystems on one hand and HW and SW on the other hand. Furthermore, given the distributed nature of the collaboration, a number of laboratory and engineering prototypes are needed in all stages of development. To meet these requirements, thus reducing integration time and associated costs, we foresee to use off the shelf boards.

In case of the Atmel CPU the boards, based on GR-CPCI-AT697 from Gaisler research, support identical functionalities to the flight ones. In case of Hirec model a similar approach is foreseen.

Engineering model will be naturally identical to flight model.

Software development will be performed on the emulator systems, with the ERC32 code compiled to run on standard Linux machines (taking advantage of the cross-complier characteristics).

The hardware characteristics for lab model are:

- AT697 Leon2-ft0.18 @ 100 MHz, with full FT (TMR cells, cache parity, regfile EDAC)
- Meiko FPU
- InSilicon Master/Target PCI core
- 100 MHz operation
- 8 Mbyte flash prom (2M × 32)
- 4 Mbyte static ram with ECC (1M × 40)
- Up to 256 Mbyte PC133 SDRAM with ECC (64M × 40)
- 10/100 Mbit Ethernet MAC
- 33 MHz, 32-bit PCI interface with host/satellite/target capability
- Standard RS-232 UART port for DSU
- 120-pins memory and custom I/O expansion connectors (AMP-177-984-5)
- 2 × RS-232 drivers
- 4 × RS-232 drivers
- 4 × RS-422 drivers
- 4 × LVDS drivers

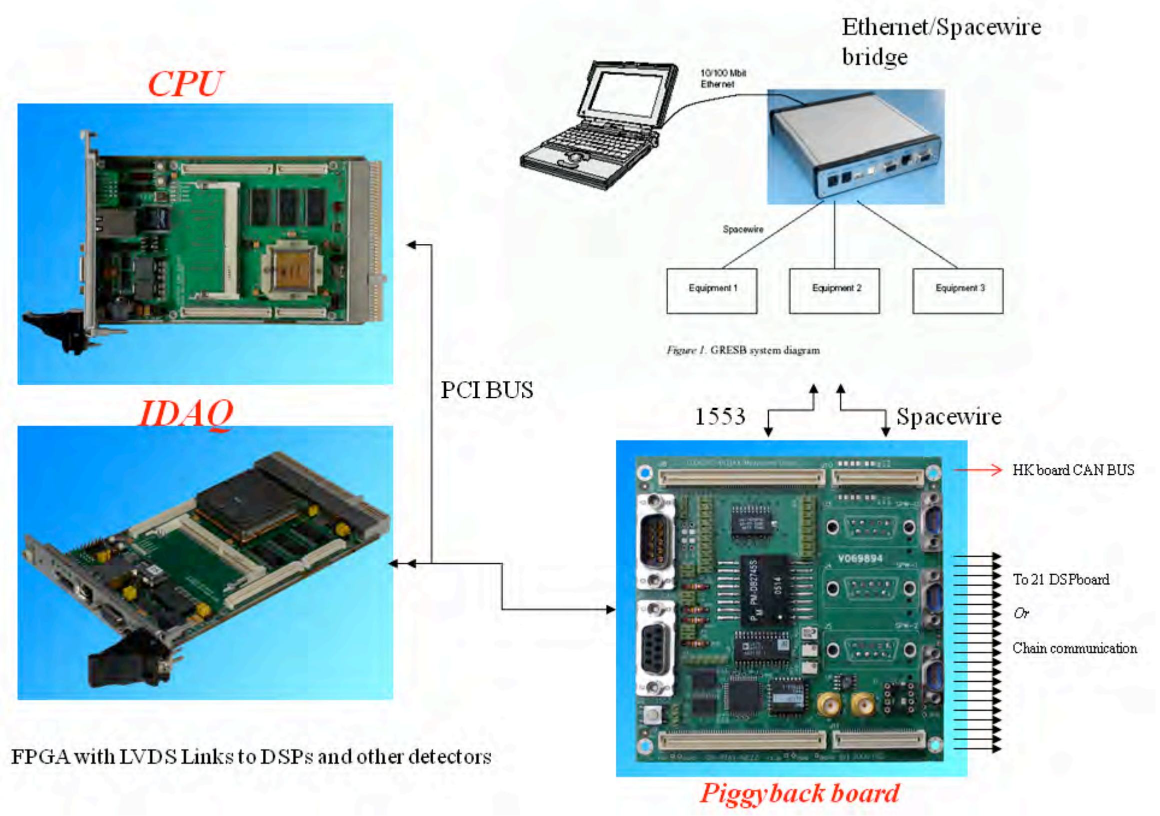

Figure 4.3.3.6-12. *Board breakdown for laboratory model of the CPU system. Connection between CPU and IDAQ board is via PCI bus. CPU and IDAQ are emulated by devoted FPGAs. Link with ISS simulator occurs in SpaceWire protocol. Data command is implemented in 1553 protocol.*

EGSE simulator

The EGSE (Electronic Ground Support Equipment) is devoted to the simulation of all systems connected to the CPU box. In this way it is possible to develop and test HW and SW of the CPU in parallel to other systems and to shorten considerably the time of integration and debugging. They include: the 1553 command simulator (to send commands from ISS/ground and receive replies/status), the terminal/debugger console, linked to the engineering connector of the CPU to monitor register status of the processor and debug SW, the Monitor/Control Command Stimuli, connected to the Housekeeping port (simulates housekeeping such as temperature and current), the IDAQ/High Speed link simulating event data acquisition ,and so on …

All parts of the EGSE are fully interchangeable with the engineering/flight model version, allowing for gradual integration of one subsystem at a time. Furthermore the EGSE is used to test the logic of working of the experiment, simulating failures and critical conditions in ways not otherwise possible with the real hardware.

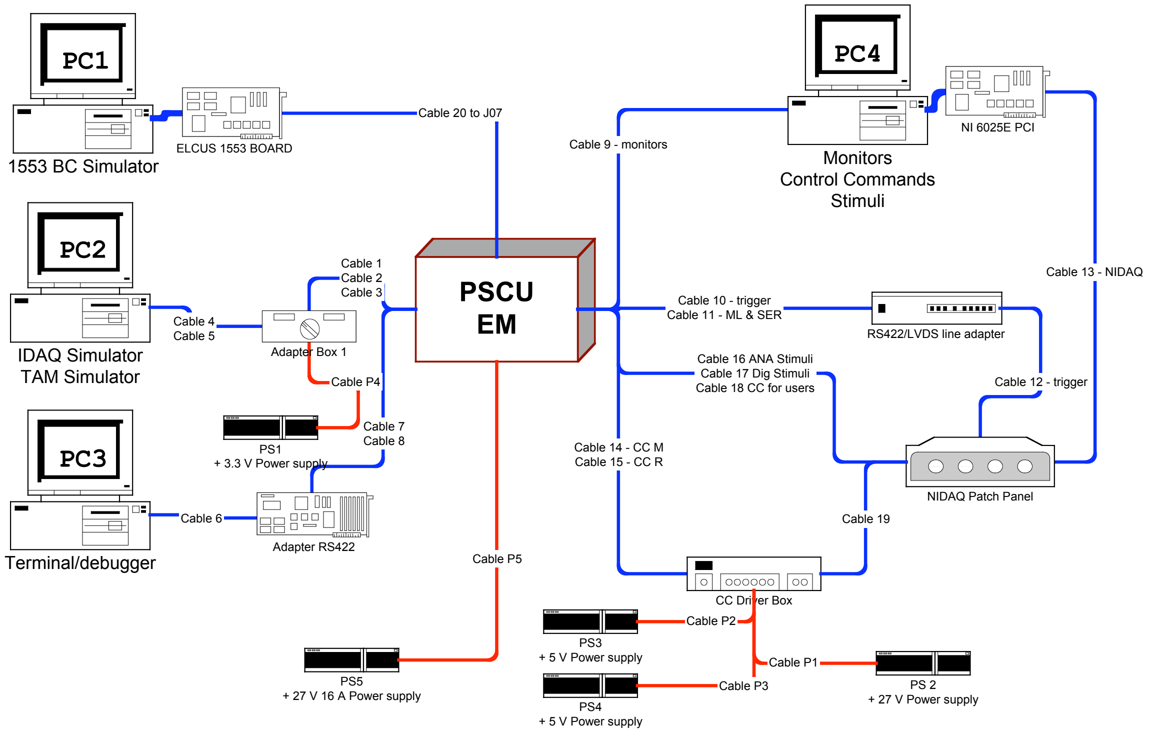

Figure 4.3.3.6-13. *Scheme of the EGSE of the CPU and acquisition system of JEM-EUSO. The CPU system is interfaced to different computer devoted to emulation of specific detector and system function.*

4.3.4. Operation

4.3.4.1. Before launch

Keeps constant temperature and keeps out of shock. Covers on the detector surfaces to protect from falling objects.

4.3.4.2. Transportation to ISS

Launch

Follows environment of HTV un-pressurized module. The FS Electronics is in STAND-BY mode. Especially, the HV Power Supply must be power off.

Standing-by phase to attach the ISS and attaching phase

Follows environment of ISS. The FS Electronics is in STAND-BY mode.

4.3.4.3. Observation phase

Normal operation

The FS is in science observation mode synchronizing with the orbit.

Approaching transportation vehicle phase and ISS attitude controlled phase

The FS Electronics is in STAND-BY mode.

Onboard calibration mode

The FS Electronics obtains the calibration data.

4.3.4.4. End of mission

The FS Electronics is in STAND-BY mode or power off.

4.3.5. Summary

4.3.5.1. Specifications

Table 4.3.5.1-1. *Focal Surface requirements.*

Code	Item	Required value	Note
FSR1	Shape of the Focal Surface	spherical	
FSR1	Gap on the positions between designed FS and the detector	< 2 mm	
FSR2	Photon detection efficiency	> 0.12	Effective area ratio × photoelectric quantum efficiency × photoelectron collection efficiency
FSR3	Average pixel size	< 4.5 mm	Corresponding to a FoV of 0.11° (1 mm = 0.023÷0.027)
FSR4	Dimension of the FS	4.45 m^2	Corresponding to a 30° view angle of the telescope
FSR5	Trigger efficiency	95% @ 10^{20} eV	
FSR6	Gate Time (GTU)	< 2.5 μs	
FSR7	Counting capacity	200/GTU	
FSR8	Electrical noise rate	< 50 GHz	< 250 kHz per pixel
FSR9	Deadtime	< 3%	

Table 4.3.5.1-2. *Focal Surface technical readiness levels.*

Code	Item	Technical Readiness Level (TRL) and its reason when selected in Febr.'07	Verification status of TRL and reason (as of Apr.'08)	Expected TRL and activities at SDR time (Mar.'09)
FSR1	Shape on the focal surface	TRL3 Structure design as in ESA-EUSO Phase-A study: EUSO-FS-REP-007 [68], EUSO-FS-REP-011 [69].	TRL3	TRL4 To be verified doing an optimal performance test.
FSR1	Gap on positions between designed FS and the detector	TRL3 The same as above.	TRL3	TRL4 The same as above.
FSR2	Photon detection efficiency	TRL4 0.148 was verified by R8900-M36 during ESA-EUSO Phase-A study, EUSO-FS-REP-006 [70]	TRL4 By upgrading the photocathode, the improvement up to 0.207 was confirmed.	TRL4 Verification by means of element tests on the trial manufactured PDM.
FSR3	Average pixel size	TRL4 The same as above.	TRL3 Same as FSR1.	TRL4 The same as above.
FSR4	Dimension of the FS	TRL4 The same as above.	TRL3 Same as FSR2.	TRL4 The same as above.
FSR5	Trigger efficiency	TRL3 Original design evaluation.	TRL3 98.7 % was confirmed by trigger SW simulation.	TRL4 The same as above.
FSR6	Gate Time, GTU	TRL3 EUSO-PI-REP-005 [65] and original design evaluation.	TRL3 Design evaluation by trigger SW simulation	TRL4 The same as above.
FSR7	Counting capacity	TRL3 Original design evaluation.	TRL3	TRL4 The same as above.
FSR8	Electrical noise rate	TRL3 Original design evaluation.	TRL3	TRL4 The same as above.
FSR9	Deadtime	TRL3 Original design evaluation.	TRL3	TRL4 The same as above.

Table 4.3.5.1-3. *Focal Surface main parts.*

Part (main)	Part (sub)	Total #
Detector	PMT	4932
	High Voltage	137
	HV Divider	1233
EC	EC ASIC	4932
	EC FPGA	1233
PDM	PDM FPGA	137
CCB	DSP	36
MDP	MPU	2

Table 4.3.5.1-4. *Focal Surface temperature requirements.*

Item	**Operation temperature**	**Non-Operation temperature**
Detector	T_0±10°C (0°C < T_0 < +20°)	-30°C ~+50 °C
Electronics	-10°C ~+50 °C	-30°C ~+50 °C

Table 4.3.5.1-5. *Focal Surface HK requirements.*

Part	**Control**			**Monitor**		
	Item	**Width (bit×#)**	**Cycle**	**Item**	**Width (bit×#)**	**Cycle**
PDM × 137	EC status	8 × 9	1 per orbit	EC status	8 × 9	8 s (TBC)
				FS temper.	8 × 3 ?	
				FEE temper.	8 × 9 ?	
	HV value	8 × 1		HV value	8 × 1	
				LV	8 × 1	
				1st trigg. rate	8 × 1	
				2nd trigg. rate	8 × 1	
	PDM status	16 × 1		PDM status	16 × 1	
CCB × 19	CCB status	16 × 1		CCB status	16 × 1	
				3rd trigg. rate	8 × 1	
				LV	8 × 1	
MDP × 2	MDP status	16 × 1		MDP status	16 × 1	
				LV	8 × 1	

Table 4.3.5.1-6. *Mass budget.*

Parts	**BEE [kg]**	**Margin [%]**	**Total [kg]**	**Comments**
PMT	138	15	159	28 g/PMT × 4932
Electr. board	91	15	105	PMT support, PDM_BOX, CCB, MDP
Cables	86	30	112	
Total	***315***		***376***	

Table 4.3.5.1-7. *Focal Surface power budget for science observation.*

Item	BEE [Watt]	Margin [%]	Total [Watt]	Comments
HV for PMT	72.0	30	93.6	
EC	208.4	30	271.0	ASIC: 141.0, FPGA: 67.4
PDM	31.0	30	40.3	
CCB	13.0	30	16.9	
MDP	1.0	30	1.3	2 systems
Loss of V Trans.	172.6	30	224.4	120 V → 28 V, 28 V → HV:0.5, 28 V → 5V
Total	***498***	***30***	***648***	

Table 4.3.5.1-8. *Focal Surface telemetry budget.*

Item	BEE [kbps]	Margin [%]	Total [kbps]	Comments
Science Data	202	15	233	Trigger rate: 0.1 Hz

4.3.5.2. Cost and schedule

Table 4.3.5.2-1. *Focal surface: cost [Yen] and schedule*

Item	H20 2008	H21 2009	H22 2010	H23 2011	H24 2012	H25 2013	Total (MYen)
PMT evaluation	Evaluation	Mass production					
	40	442	422	345	295	56	1,600
FS construction	Structure design	Trail prod.	1st production		2nd prodct.		
Electr. making	30	464	419	350	290	47	1,600
	BBM eval.	EM eval.	PFM making & Ttest		Test		

4.3.5.3. Organization

Focal Surface: Hirohiko M. Shimizu (KEK), Yoshiya Kawasaki (RIKEN)
FS Detector: Yoshiya Kawasaki (RIKEN)
FS Electronics: Tokonatsu Yamamoto (Univ. Konan), Marco Casolino (Univ. Rome)
ASIC & 1st Trigger: Tokonatsu Yamamoto(Univ. Konan)
PDM (2nd Trigger): Shinwoo Nam (Ehwa W. Univ.)
CCB (3rd Trigger): Andrea Santangelo (Univ. Tubingen)
MDP: Marco Casolino (Univ. Rome)
Trigger Algorithm: Mario Bertaina (Univ. Torino), Osvaldo Catalano (IASF-PA/INAF)

4.4. Atmosphere Monitoring System

4.4.1. General

The aim of the Atmosphere Monitoring system is to observe the condition of the atmosphere in the field of view of the telescope. The strength of the fluorescent light and Cherenkov light emitted from EAS and their transmission process depend on the transparency of the atmosphere, the cloud coverage and the height of cloud top. These must be determined by the Atmosphere Monitoring system of JEM-EUSO.

In the case of events above 10^{20} eV, the existence of clouds can be directly detected by the signals from the EAS [65, 71]. However, the monitoring of the cloud coverage by the JEM-EUSO Atmosphere Monitoring system is important to estimate the effective observing time with a high accuracy and to increase the confidence level in the events just above the energy threshold of the telescope. The JEM-EUSO mission, therefore, has its own Atmosphere Monitoring (AM) system whose impact onto mass and power budget is not-significant. The AM system consists of: Infrared camera, Lidar, and analysis of slow data of the JEM-EUSO telescope. These elements are planned to measure the height of cloud top with accuracy better than 500 m (Figure 4.4.1-1) as minimum. During 2007, we determined the basic specifications of the instruments and the conceptual design of them; in the following paragraphs we will describe the design and the problems to be solved.

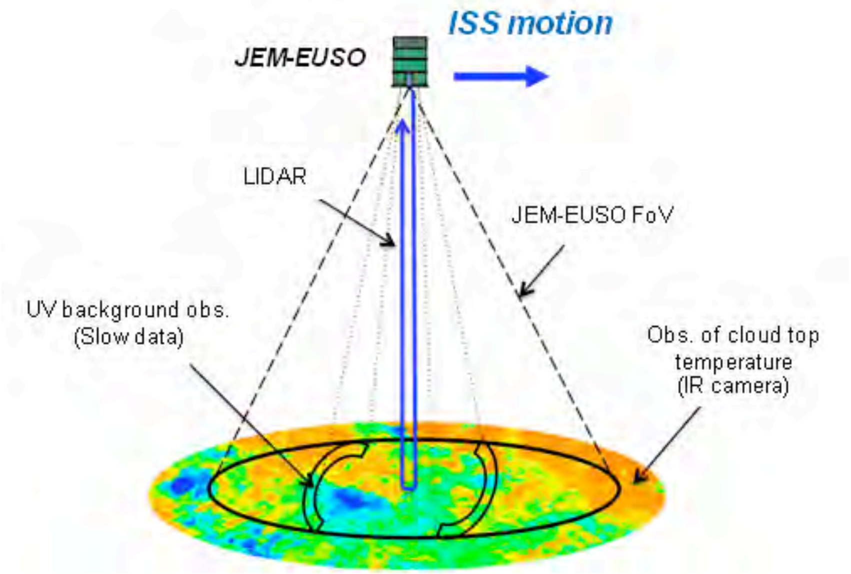

Figure 4.4.1-1. *Concept of the atmospheric monitor.*

4.4.2. Infrared camera

The Infrared (IR) camera consists of refractive optics made by Gelium material and uncooled micro bolometer array detector. Interferometer filters that transmit 10÷12 μm are used as the filters of wavelength bands. The IR camera is 60° field of view, totally matching that of the main EECR telescope. The angular resolution, which corresponds to one pixel, is about 0.25° at the center of the field of view. The temperature controlled shutter in the camera and mirrors are used to calibrate background noise and gains of the detector to achieve the absolute temperature accuracy of 3K, as well as sea temperature that are observed by the other satellites. Though the IR camera takes images continuously at the frequency of video frame rate (1/30 sec), transfer of the images takes place every 30 seconds, in which ISS moves half of the field of view of JEM-EUSO telescope (the requirements for the IR camera are listed in Table 4.4.2-4).

Uncooled bolometer array can be small, light weight, and less power consumption, since it is different from semiconductor detectors such as HgCdTe, GaAs, InGaAs, which require the cooling system. In recent years, the performance is dramatically advanced and is used in Space environment in Mars Odyssey and Space Shuttle mission STS-85. Planet-C/VCO (Venus Climate Orbiter), scheduled launch in 2010, is also adopted an infrared camera in mid-infrared (LIR) with a uncooled micro bolometer array detector. A wide field is achieved by the Germanium refraction optics developed in JAXA for the stratosphere platform mission. On the other hand, EADS/SODERN has experience of the development of IR cameras with an uncooled micro bolometer array for METOP1 and CALIPSO satellites. In the infrared camera of the JEM-EUSO mission we will use these already developed technology as far as possible.

4.4.2.1. The accuracy of the cloud top height evaluation

The Infrared camera will acquire images in the field of view of JEM-EUSO; these images are analyzed to determine the cloud coverage and the cloud top height. The data, together with what obtained from the Lidar, are then used in the estimation of the effective observational volume and for the reconstruction of the events. For this purpose it is important to obtain a high level of accuracy in the determination of the cloud top height.

The accuracy of the cloud top height is determined by the requirement for the accuracy of the estimation of the effective volume for the cosmic-ray events, i.e., the accuracy of the spectrum determination. In the following, we will describe the process of requirement determination for the infrared camera.

First of all, the flux of EECRs is determined by:

$$Flux \propto \frac{N}{S \cdot T \cdot \Omega}$$

where $N=N_{total}$ is the total of events of EECRs, S is the effective exposure, T is observational time, Ω is the solid angle of the cosmic-rays incident to the Earth. Since we can safely assume that both T and Ω are constants, the flux is proportional to N_{total}/S:

$$Flux \propto \frac{N_{total}}{S}$$

where N_{total} is the number of EECRs "golden events" N_{golden} with Cherenkov mark plus the number of those EECRs events N_{cloud} that impinge to the cloud area and reflect Cherenkov light at the cloud top. On the other hand, we assume that the effective exposure S is the sum, in the field of view of JEM-EUSO, of the area of clear sky, S_{golden}, and the area of the cloudy sky, S_{cloud}:

$$\frac{N_{total}}{S} = \frac{N_{golden} + N_{cloud}}{S_{golden} + S_{cloud}}$$

Here, we assume that $N_{golden} + N_{cloud}$ is a constant. The effective exposure of the clear sky will be 30% of the area, S_{EUSO}, corresponding to the field of view of the JEM-EUSO as reported in ESA-EUSO Phase-A study [65], for an ISS altitude of 430 km:

$$S_{EUSO} = \pi \cdot (430 \cdot \tan 30°)^2 = 1.94 \times 10^5 \quad [km^2]$$

$$S_{golden} = 0.3 \cdot S_{EUSO} = 5.81 \times 10^4 \quad [km^2]$$

Next, in order to obtain the cloudy area S_{cloud}, we use the statistics data of cloud height and optical depth estimated by TOVs data as shown in Table 4.4.2.1-1 [65]. Assuming that the

Cherenkov light is reflected only at clouds with the optical depth (OD) deeper than 1, the resulting number of the total events is N_{cloud}. We interpolate the data by a linear function between cloud top height and coverage, and then we get:

$$S_{cloud} = 4551.2 \cdot h + 27753 \quad \lfloor km^2 \rfloor$$

This equation allows us to evaluate the cloudy sky area, S_{cloud}, [km^2], at any arbitrary h height.

Table 4.4.2.1-1. *Abundance of clouds estimated from the TOVs database as a function of optical depth, OD, and cloud top altitude. The clear sky fraction is 30%. The total probability exceeds 100% because a supplementary fraction of sub-visible clouds at high altitudes have been added.*

	TOVs: cloud presence			
Cloud Top Altitude [km]	**OD < 0.1**	**0.1 < OD < 1**	**1 < OD < 2**	**OD > 2**
h > 10	1.6 %	17.9 %	3.0 %	6.1 %
7 < h < 10	0.5 %	3.6 %	3.5 %	6.3 %
3 < h < 7	0.7 %	2.2 %	2.9 %	5.8 %
h < 3	1.3 %	5.6 %	5.1 %	16.1 %

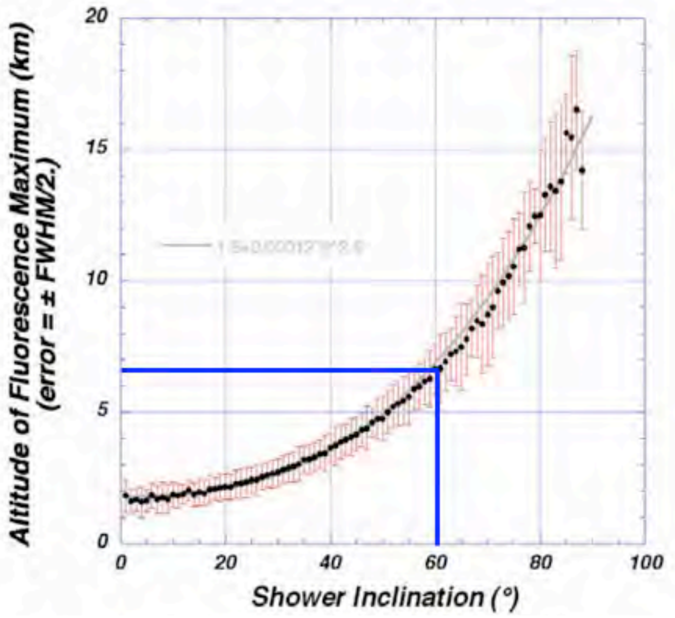

Figure 4.4.2.1-1. *Average altitude of the maximum of the shower signal (for proton primary), as a function of shower inclination. The error bars represent the FWHM fluctuations.*

The average height of the maximum for a shower induced by primary proton with the energy of 10^{20} eV is given in Fig.4.4.2.1-1 [65]. In case of 60° zenith angle, the average height of the shower maximum is about 6.8 km (crossing point of the blue lines in figure). Here, we neglect the the uncertainty on the first interaction point (red bars in the figure) for simplicity. For a zenith angle of 60° and clouds lying below 6.8 km, the event can be reconstructed; the evaluation of the cloud area in such a case is equivalent to determining the area for a cloud lying in 0÷6.8 km:

$$S_{cloud}(h = 6.8\,km) = 5.87 \times 10^4 \quad \lfloor km^2 \rfloor$$

The relation between cloud coverage and cloud top height is shown in Fig. 4.4.2.1-2. Assuming that the accuracy of the cloud top height determined by infrared camera is Δh = 1 km, then the cloud top height for a shower at 60° zenith angle is determined as 6.8±1 km; the error in the cloud top height (green lines in figure) is the same as the error of the cloudy sky area, ΔS_{cloud} (red lines in figure), obtained as

$$\Delta S_{cloud} = 4551.2 \cdot \Delta h = 4.55 \times 10^3 \ [km^2]$$

We can evaluate these errors in a similar way for various zenith angle of 0°, 10°, 20°, … , 80°. The results are summarized in Table 4.4.2.1-2. The cloud top heights are also obtained in a similar way for the cases with cloud top height error equal to ±0.5 km and ±0.2 km.

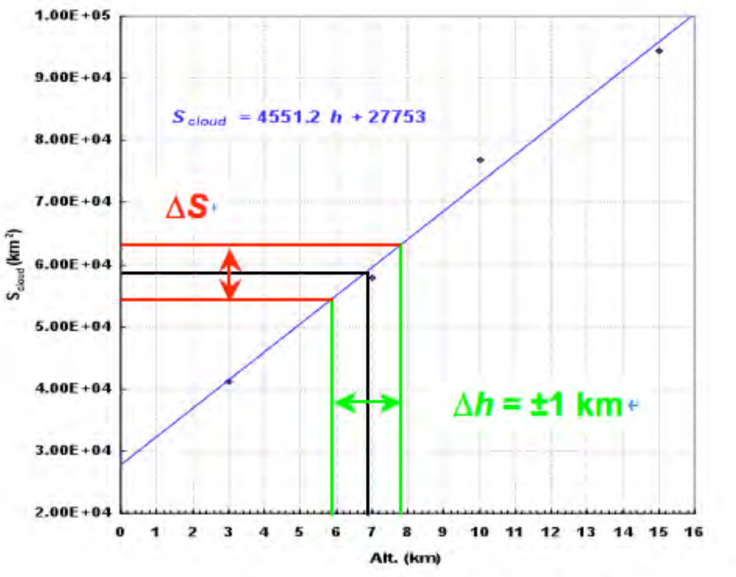

Figure 4.4.2.1-2. *Relation between cloud coverage and cloud top height.*

Table 4.4.2.1-2. *The error in the effective observation area as function of the cosmic ray incident angle when the accuracy of the cloud top height is ±1 km .*

θ angle	X_{max} alt	S_{golden}	S_{cloud}	Δh = ± 1 [km]	
[deg]	[km]	[km^2]	[km^2]	ΔS [km2]	Error [%]
0	1.5	5.81×10^4	3.46×10^4	4.55×10^3	4.91
10	1.8		3.59×10^4		4.84
20	2.2		3.78×10^4		4.75
30	2.6		3.96×10^4		4.66
40	3.6		4.41×10^4		4.45
50	4.7		4.91×10^4		4.24
60	6.8		5.87×10^4		3.90
70	9.3		7.01×10^4		3.55
80	12.3		8.37×10^4		3.21

JEM-EUSO is expected to detect more than one thousand "golden" events in three years operation. The relation between golden and cloud events can be expressed by:

$$N_{cloud} = \frac{S_{cloud}}{S_{golden}} \cdot N_{golden}$$

which allow us to determine the statistical fluctuations for detected events arriving from different zenith angles, as listed in Table 4.4.2.1-3, if N_{golden}=1110.

The results of our analysis are summarized in Fig. 4.4.2.1-3. By setting an accuracy level less than ±0.5 km in the determination of the cloud top height, the related errors (blue dotted curve in figure) are at the same level of the statistical ones (black curve); for an accuracy level of ±0.2 km (green curve), these errors are significantly smaller than the statistical errors.

In brief, the accuracy in determining the cloud top height is required to be less than ±500 m. The temperature decrease in troposphere is almost constant, with a value of ~ 0.6° C / 100 m: the difference in height of 500 m corresponds to a difference in temperature of 3K.

Table 4.4.2.1-3. *Statistical fluctuations for detected events.*

θ angle [deg]	**X_{max} alt [km]**	**S_{golden} [km^2]**	**S_{cloud} [km^2]**	**N_{golden}**	**N_{cloud}**	**N_{total}**	**$1 / \sqrt{N_{total}}$ [%]**
0	1.5	5.81×10^4	3.46×10^4	1110	661	1771	2.38
10	1.8		3.59×10^4		687	1797	2.36
20	2.2		3.78×10^4		722	1832	2.34
30	2.6		3.96×10^4		756	1866	2.31
40	3.6		4.41×10^4		843	1953	2.26
50	4.7		4.91×10^4		939	2049	2.21
60	6.8		5.87×10^4		1122	2232	2.12
70	9.3		7.01×10^4		1339	2449	2.02
80	12.3		8.37×10^4		1600	2710	1.92

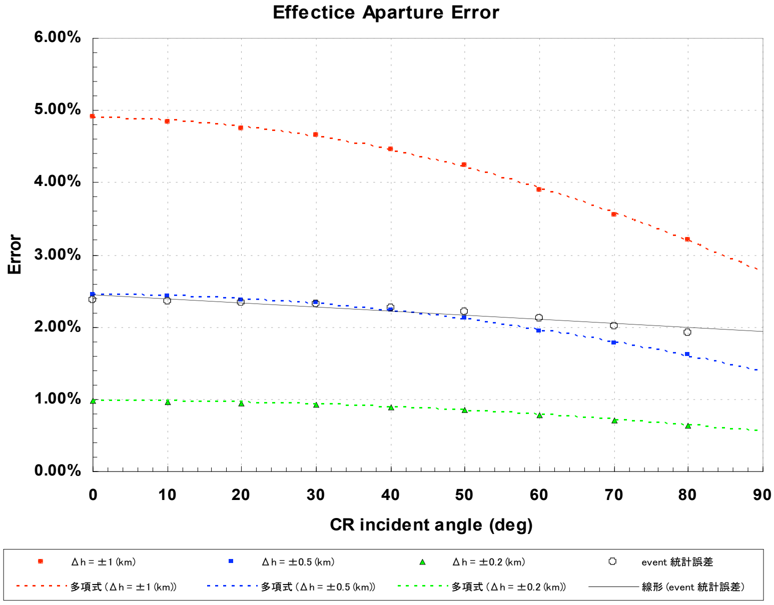

Figure 4.4.2.1-3. *Error in cosmic ray flux for several incident angles.*

4.4.2.2. Requirements for the Infrared camera

The following table summarizes the specification for the JEM-EUSO Infrared camera.

Table 4.4.2.2-1. *Specifications for the JEM-EUSO Infrared camera.*

Parameter	Requirement
Temperature range	220 ÷ 300 K
Wavelength	10 ÷ 12 μm
Field of View	60 °
Spatial resolution	0.25° @ FoV center (= 4.4 mrad) 0.22° @ FoV edge (= 3.8 mrad)
Absolute temperature accuracy	3 K
Optics	Ge refractive optics
Detector	Un-cooled microbolometer array
Digitizing resolution	12 bit
Integration time	33 ms/mage (= video frame rate)

We contacted EADS/Sodern, Aerospace Company in France, to confirm the feasibility to build infrared camera attached to JEM-EUSO. EADS/Sodern has experience to build the infrared camera (IIR) onboard CALIPSO satellite and that of METOP1satellite (IIS), that are working fine until now. Both IIR and IIS Infrared cameras use uncooled micro-bolometer array made by Boeing to make them small and light weight. EADS/Sodern reported us that they can make Infrared camera of JEM-EUSO based on the technology of IIR and IIS, though some minor modifications are necessary. We have started further optimization of the infrared camera such as pixel size, design of the wide field optics, and onboard calibration instruments. Table 4.4.2.2-2 summaries the feasibility report of EADS/Sodern with the necessary modifications from IIR or IIS, which we briefly describe here below.

Temperature and wavelength range.
It is achievable with currently available technologies in EADS/Sodern.

Field of view of Optics
EADS/Sodern developed infrared camera with narrow field of view (Fig. 4.4.2.2-1) and performs survey observations of a wide area by the scanning mirror. On the other hand JEM-EUSO requires one wide-field optics to reduce cost and weight and to avoid mechanics. The field of view of 60 degrees, however, can be achievable relatively easily, since it has been already achieved by other several missions. The concrete specifications will be determined not later than SRR (System Requirement Review).

Absolute temperature accuracy
It is achievable with currently available technologies of EADS/Sodern. If we use calibrator module that onboard in CALIPSO satellite, even that of 1K would be also achievable. Onboard calibrator will not be used in JEM-EUSO in the case that absolute temperature accuracy of 3K is achievable without it, since it may increase mass, size, and power considerably. Conversion curve from the temperature to height can be calibrated directly by Lidar or slow data of the main telescope. This issue will be studied with EADS/Sodern and decided by the time of SRR.

Detector
Most confident detector is the uncooled microbolometer sensor made by Boeing; and EADS/Sodern developed IIR and IIS with them. We will investigate along this line for the JEM-

EUSO mission. Although a microbolometer array by Boeing has 320×240 pixels, ERADS/Sodern uses only 64×64 pixels. Read-out electronics may have to be newly developed for JEM-EUSO where full pixel will be used. In the case of 320×240 pixels, spatial resolution is about 1.8 km/pixel in the direction of Nadir. This is more than two times larger than the pixel of the JEM-EUSO telescope (0.75 km/pixel) and allowable.

Mass Size and Power
It is achievable by the current technologies of EADS/Sodern and expected considerably lower than the specification of JEM-EUSO.

In summary, all the specification can be satisfied if they apply the technologies that used in IIR of the CALIPSO satellite, although some minor developments are necessary for the field of view and pixel size needs. The flight model can be manufactured in five years by the cost of 5.5 M€.

Table 4.4.2.2-2. *Feasibility of the Infrared camera specifications.*

Parameter	Target value	CIM compatibility
Survey temperature range	220 ÷ 300 K	OK
Wavelength	11 ÷ 13 μm	Filter to be modified
Field of View, FoV	60 °	Optics to be modified
Spatial resolution	0.25° @ FoV center (= 4.4 mrad) 0.22° @ FoV edge (= 3.8 mrad)	Depending on the image size
Absolute temperature resolution	3 K	OK *
Optics	Ge dioptric system (f/# = 1.0)	OK * Temperature stability to be discussed
Detector	Uncooled microbolometer array device	OK
Image pixel number	320 × 240	64×64 or 128×128 or 240×256
Pixel size	37 μm	50 μm
Image resolution	12 bit	OK
Exposure time	33 ms/mage (= video frame rate)	OK
Mass	7 kg	5 kg without calibration device *
Dimension (L × W × H)	200 × 280 × 320 mm	130×250×250 without calibration device *
Power	20 W (operative) 7 W (non-operative)	8 W (operative) without calibration device *

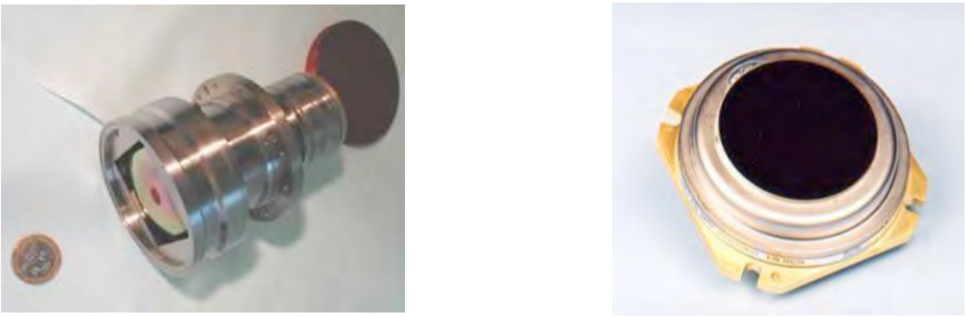

Figure 4.4.2.2-1. *Optics of IIR.*

4.4.3. Light detection and ranging (Lidar)

Images of the two-dimensional distribution of clouds are obtained using an infrared camera: the brightness temperature at the cloud top is derived from the IR camera collected data, and the altitude of the cloud top is obtained by estimating the temperature distribution in the altitude direction at the measurement position using an atmospheric model. The cloud distribution and the cloud-top altitude are important parameters for improving the reliability in estimating the energy of EECRs from the air shower EAS profile. However, the accuracy in determining the cloud-top altitude using images obtained with the infrared camera is around ±500 m; thus, it is not possible to satisfy the required accuracy (temperature: ±1.4 K, altitude: ±200 m) using the data obtained using the IR camera alone.

The purpose of Lidar is to carry out ranging measurements at several positions in the field of view of JEM-EUSO so to achieve the determination of the cloud-top altitude with high accuracy. The direct observation data of the cloud-top altitude obtained by Lidar serves as calibration data for what obtained by the IR camera. The ranging resolution of Lidar is 30 m; from data by both IR camera and Lidar, the 3-dimensional cloud distribution and cloud-top altitude are determined.

The Lidar system of JEM-EUSO is composed of transmission and receiving systems. The transmission system comprises a Nd:YAG laser and a pointing mechanism for the irradiation beam. The third harmonic (λ=355 nm) of the Nd:YAG laser is used. The JEM-EUSO telescope itself is used for the receiving system of Lidar. Four photodetectors are placed on the focal surface to measure the backscattered light, so that there is a visual field in the laser irradiation direction from Lidar. Because the wavelength of the laser from Lidar is in the range of λ=330÷400 nm, which is the range of atmospheric fluorescence and Cherenkov light, the focal surface detector (the MAPMTs) of JEM-EUSO can also be used as a Lidar receiver unit.

4.4.3.1. Transmission device

The laser unit of the Lidar transmission system of JEM-EUSO is almost identical to the laser unit of the BepiColombo laser altimeter (BELA), which is planned to be mounted on a Mercury exploration satellite that is being developed by the European Space Agency [72]. A German research group is in charge of the development of the laser unit. The launch of the BepiColombo satellite is planned for 2012, and the BELA laser unit is still in the development phase. The specifications required for the BELA laser unit are a pulse frequency of 20 Hz and a wavelength of 1064 nm. As a result of discussions with a developer and manufacturer of measurement devices used in Space, it was confirmed that changing the pulse frequency from 20 Hz to 50 Hz or 100 Hz and the use of the third harmonic (λ=355 nm) of the 1064 nm wavelength are possible. The Solid-State Optical Science Research Unit, lead by Dr. Wada of RIKEN, can realize a laser that satisfies the above requirements.

The Lidar transmission system is mounted on the JEM-EUSO telescope. The beam is diffused with approximately the level of spatial resolution of the JEM-EUSO telescope used as the receiving system. The control of the irradiation direction of the laser is carried out by means of the beam pointing mechanism, for which two possibilities are considered, i.e., 1) 2-4 laser beams fixed in different directions with each beam irradiated according to a corresponding program, and 2) a micro electro-mechanical system (MEMS) mirror developed by a research group of Ewha Womans University (Korea).

The specifications of the laser system are summarized in Table 4.4.3.1-1; we will explain the outline of the laser system developed by RIKEN to satisfy the specifications in the table. For the excitation module, a laser rod is placed at the centre, around which host crystals not doped with fluorescent ions are fused in a triangular shape to protect the main laser rod. This technique is achieved using ceramic crystalline technology developed in Japan. Furthermore, we adopt a method in which the laser rod is excited using laser diodes, which are placed at the vertices of the triangle of host crystals. For cooling, direct conduction cooling in the metal, without the use of a solvent, is planned. For the resonator, a U-shaped laser resonator with a pair of prisms is used so that the resonator is robust to vibration and torsion. Figure 4.4.3.1-1 shows the cross section of the excitation module of the laser system. Figure 4.4.3.1-2 shows the arrangement of the resonator optics.

Table 4.4.3.1-1. *Specifications for the JEM-EUSO Lidar.*

Parameter	Requirement
Wavelength	355 nm
Repetition rate	50 Hz
Pulse width	5 ÷15 ns
Pulse energy	20 mJ/pulse
Beam divergence	0.1 mrad
Bandwidth of filter and transmittance	3 nm / 50%
Telescope for detection	JEM-EUSO
Detector	MAPMT (JEM-EUSO)
Range resolution	30 m
Steering of output beam	±15° to a vertical axis (TBD)
Exposure time	0.01 s/shot
Integration time	0.1 s (=5 shots)
Mass	17 kg
Dimension	450×350×250 mm
Power	< 70 W

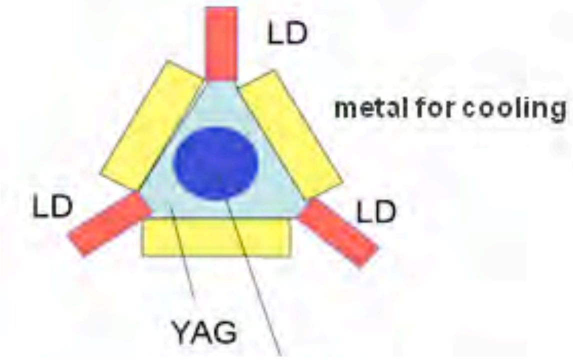

Figure 4.4.3.1-1. *Lidar pump module (cross section).*

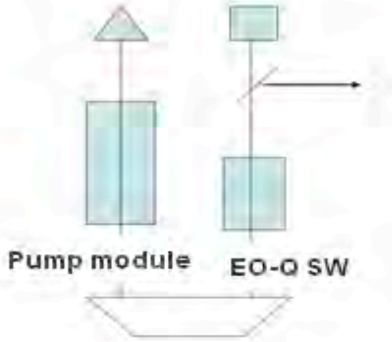

Figure 4.4.3.1-2. *Lidar cavity configuration.*

By June 2008 we had succeeded in obtaining an output of 200 mJ/pulse using the excitation module alone by pseudo-CW excitation from three directions with water cooling. Furthermore, frequencies of up to 400 Hz were obtained by a repeated output of 100 mJ/pulse with 20 nm wavelength using a resonator having an electro-optical Q (EOQ) switch, and the basic specifications required for the atmospheric monitoring system were obtained at a fundamental wave of 1064 nm in the laboratory. By the wavelength conversion of this fundamental wave, the third harmonic (λ=355 nm) was generated. Under the current conditions, an output of approximately 30 mJ/pulse can be obtained using lithium triborate (LBO) crystals.

Figure 4.4.3.1-3 shows the expected mounting location of the laser oscillator. It is planned to be fixed using screws on an aluminium fringe that protrudes from a surface perpendicular to the observation direction. Heat is planned to be radiated from this contact surface; thus, rubber with high thermal conductivity is placed between the laser oscillator and the aluminium fringe.

The laser system is driven by a power source of DC 28 V supplied from the main system. The power source and electrical components for controlling the laser, such as the pulse light control circuit, are placed between the main laser system and the laser oscillator for pulse operation. The specifications of the control signal and the control method are currently under consideration.

Two steering methods for the laser beam used in Lidar are currently being examined. The progress of the development of the MEMSs, which is one candidate, is described below.

Figure 4.4.3.1-4 shows the structure of the MEMS under development. Using the electrostatic force generated at the comb-like sections on the outer actuator side and mirror operating side, rotations around the X-Y axes and the axis perpendicular to the X-Y axes are induced. This method has already been tested in an actual space environment. Currently, the steering angle is set at ±6° and the mirror system is composed of 8 pixel × 8 pixel, 3 mm × 3 mm mirrors, realizing a fill factor of 90%.

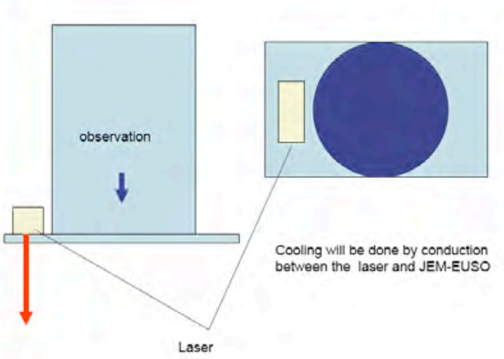

Figure 4.4.3.1-3. *Accommodation of the Lidar.*

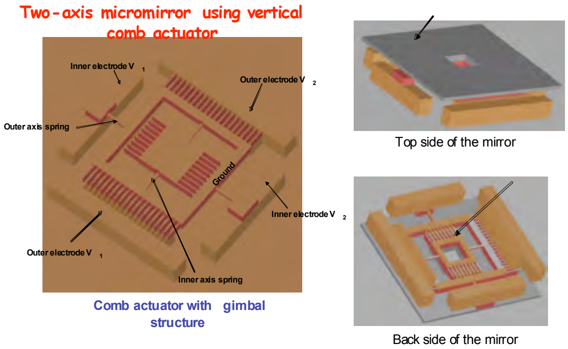

Figure 4.4.3.1-4. *Basic structure of two-axis micro-mirror.*

4.4.3.2. Receiving device

The backscattered light of Lidar is expected to be detected by the photocounting method. A photomultiplier tube (PMT) with the specifications shown in Table 4.4.3.2-1 is expected to be used as the photodetector. Note that a PMT, the specifications of which are equivalent to those of a multipixel-type MAPMT with high sensitivity in the near-UV range and used for JEM-EUSO, can also be used as the photodetector in Lidar.

4.4.3.3. Simulation

The JEM-EUSO telescope itself is used as the Lidar receiving system. Therefore, a laser beam with a wavelength of 355 nm, which is the third harmonic of the seed laser (1064 nm), is used for Lidar in order to minimize the changes that arise in the optical system of the telescope and the focal-plane detector owing to the mounting of Lidar.

The performance of Lidar was evaluated by simulation. The variables and their values used in the simulation are summarized in Table 4.4.3.3-1. The variables associated with clouds and their values are summarized in Table 4.4.3.3-2. As the atmospheric model, US Standard Atmosphere 1976 was used.

Table 4.4.3.3-1. *Subsystems specifications assumed in the JEM-EUSO Lidar under specification simulation.*

Item		**Value**
Transmitter	Wavelength	355 nm
	Repetition rate: nominal mode, burst mode	10, 100 pulse/s
	Pulse energy	10 mJ
	Beam divergence	0.1 mrad
	Optical efficiency	80 %
Receiver	Receiver aperture	210 cm
	FoV (Lidar detector pixel)	0.25 mrad
	Bandwidth of a filter, FWHM	3 nm
	Transmittance of a filter	50 %
	Transmittance of optical system	25 %
Detector	Quantum efficiency	25 %
	Dark noise	500 counts/s
Acquisition	Range resolution	30 m
	Injection time	1
ISS	Altitude	500 km

Table 4.4.3.3-2. *Optical parameters of the clouds used for Lidar simulation. SR (Scattering Ratio) and OD (Optical Depth) are defined at 532 nm.*

Cloud	**SR peak altitude [m]**	**Width of altitude [m]**	**SR at the peak altitude**	**Ext-to-backsc ratio *) [sr]**	**Angsr exp**	**OD**
Opaque	3000	1500	500	20	0	6.28
Subvisible (cirrus)	9000	1000	10	22	0	5.12×10^{-2}

The results from the simulation for one laser shot and 100 integrated laser shots are shown in Figs. 4.4.3.3-1 and 4.4.3.3-2, respectively. The abscissa indicates the altitude and the ordinate indicates the scattering ratio (SR) of the clouds and the signal-to-noise ratio (SNR). The SR in the two figures is obtained when the wavelength is 355 nm, and is different from that given in Table 4.4.3.3-2. As shown in the figures, only opaque clouds are detectable using Lidar with the current specifications in the case of one shot, whereas subvisible clouds are detectable with SNR=9 in the case of 100 integrated shots.

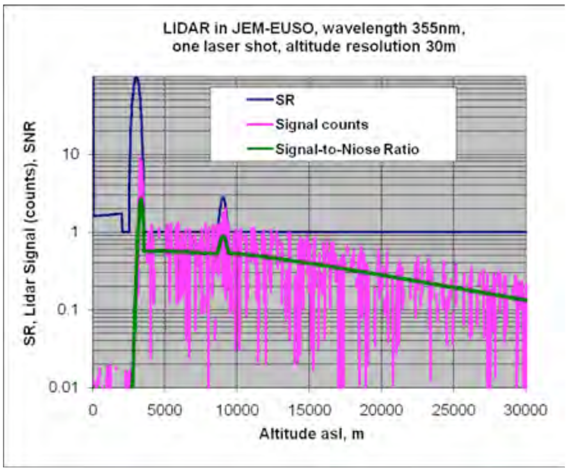

Figure 4.4.3.3-1. *Calculated signal counts and SNR for single shot measurement with Lidar.*

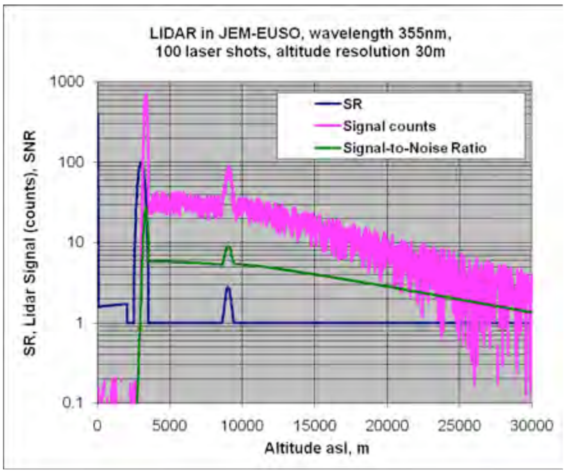

Figure 4.4.3.3-2. *Calculated signal counts and SNR for integration of 100 measurements with Lidar.*

4.4.4. Slow data

Among the focal surface detector module (PDMs) of JEM-EUSO, two of them are installed with function to collect slow data; they are arranged parallel and orthogonal to the travelling direction of the International Space Station. Slow data are collected in the slow trigger mode (see paragraph 4.3.3.2) with the purpose to perform:

- continuous observation of the background light intensity (the altitude of the cloud top is estimated by analyzing a stereo image of the observed data), and
- observation of airglow and meteors.

The photoelectron signals from MAPMT are converted into digital signals using an application-specific integrated circuit; then, the digital signals are counted at an interval of 2.5 μs for the aim of observing the extensive air shower using a counter. Along with this observation, counts for a 40 μs time band are continuously recorded at an interval of 3.5 s. The obtained slow data are input to the two parallel PDMs, and each PDM continuously observes the background near-ultraviolet light. Because the two PDMs observe two discrete spaces that are spatially distant, the altitude of the cloud top can be estimated by analyzing the stereo image [73, 74].

The emission of the Herzerg I band of oxygen molecules at an altitude of approximately 95 km, the boundary between the mesosphere and the thermosphere, is prominent in night airglow in the wavelength band of 330-400 nm. It is considered that this emission has a stripe structure with a stripe width of approximately 20-300 km in correlation with the atmospheric gravitational wave, and that the observation of such a structure in detail will be possible by examining the slow data obtained by JEM-EUSO.

4.4.4.1. Specifications required for the FPGA of the counter

Ultraviolet light reflected by clouds and incident on the MAPMT is intermittently collected at an interval of 3.5 s with a gate time of 20 μs. The amount of background light incident on the MAPMT in photoelectrons (p.e.) is estimated to be 1 p.e./2.5 μs. Therefore, for the integration time of 50 μs, approximately 20 p.e. of light is expected. It is possible to set the gate time width via appropriate commands to the FPGA, so that the amount counted is within 8 bits, even when the lunar phase and the distribution of clouds change. The specifications required for the FPGA are summarized in Table 4.4.4.1-1.

Table 4.4.4.1-1. *Requirement performance for the JEM-EUSO slow data.*

Parameter	**Requirement**
Wavelength	330÷400 nm
Resolution	0.1 °
Detector	MAPMT (JEM-EUSO)
Count resolution	8 bit
Count integration time	50 μs
Time interval for a detection	3.5 s

4.4.5. Operation

Each device used for the JEM-EUSO atmosphere monitoring carries out observation while the ISS passes over the night side of the Earth. Commands are transmitted from the ground station, and the operation sequences of the atmosphere monitoring devices, that are orbiting around the Earth, are programmed by the ISS. Each device performs observation according to a defined sequence. The data collection is basically only carried out when the ISS is passing over the night side of the Earth, however, these devices are turned on or off according to the following rules.

Infrared camera
The temperature of the uncooled bolometer arrays is controlled using a Peltier device. The sensors and cooling element are always turned on when the ISS passes over the day side. The collection of IR image data is only carried out when the ISS passes over the night side.
Lidar
In order to maintain Lidar stability, the laser head is always turned on when the ISS passes over the day side as well as over the night side. Ranging measurements and data collection are only carried out when the ISS passes over the night side.
Slow data
The on/off switching during slow data collection conforms to the operation of the JEM-EUSO focal-plane detector.

4.4.6. Summary

4.4.6.1. Specifications

Table 4.4.6.1-1. *Requested specifications for the JEM-EUSO InfraRed camera.*

Parameter	**Requirement**
Measurement temperature range	220 ÷ 300 K
Wavelength	10 ÷ 12 μm
Field of View	60 °
Spatial resolution	0.25° @ FoV center (= 4.4 mrad) 0.22° @ FoV edge (= 3.8 mrad)
Temperature resolution	3 K
Optical system	Geospatial system
Detector	Microbolometer
Resolution	12 bit
Integration time	33 ms/mage (= video frame rate)

Table 4.4.6.1-2. *Specifications for the JEM-EUSO Lidar (Japanese version).*

Item	Value
Wavelength	355 nm
Repetition rate	50 Hz
Pulse width	5 ÷15 ns
Pulse energy	20 mJ/pulse
Beam divergence	0.1 mrad
Interference filter, FWHM	3 nm / 50%
Telescope for detection	JEM-EUSO
Detector	MAPMT (JEM-EUSO)
Range resolution	30 m
Output beam direction	±15° to a vertical axis
Exposure time	0.01 s/shot
Integration time	0.1 s (=5 shots)
Mass	17 kg
Dimension	450×350×250 mm
Power	< 70 W (measurement)

Table 4.4.6.1-3. *Specifications for the JEM-EUSO Lidar for one module (German version). Four modules are used simultaneously.*

Item	Value
Wavelength of fundamental	1064 nm
Repetition rate	20 Hz
Pulse width	3 ns
Pulse energy	50 mJ
Beam divergence	0.1 mrad
Optical efficiency	5.3 %
Wavelength for Lidar	355 nm
Pulse energy	10 mJ
Beam divergence	0.1 mrad

Table 4.4.6.1-4. *Specifications for the JEM-EUSO Lidar with 4 laser modules (German version).*

Item	Value
Wavelength	355 nm
Repetition rate	80 Hz
Pulse energy	40 mJ

Table 4.4.6.1-5. *Specifications for the JEM-EUSO slow data.*

Item	Value
Wavelength	330÷400 nm
Spatial resolution	0.1 °
Detector	MAPMT
Count resolution	8 bit
Count integration time	50 μs
Exposure time	3.5 s

Table 4.4.6.1-6. *Budget of the JEM-EUSO InfraRed camera.*

Item	Value
Mass	5 kg
Dimension	130×350×250 mm
Power	8 W

Table 4.4.6.1-7. *Budget of the JEM-EUSO Lidar.*

Item	German version	Japanese version
Mass	30 kg	17 kg
Dimension	missing	450×350×250 mm
Power	100 W (on), 20 W (off)	70 W (on), 35 W (off)

4.4.6.2. Cost

The following table shows the cost for the Atmosphere Monitoring system including research and development cost. French researchers will organize budget and research group. Budget is estimated under the assumption that the development is performed in Japan; as reference, the budget for the Lidar development by Japanese group is listed.

Table 4.4.6.2-1. *Cost, in MYen, for the JEM-EUSO atmosphere monitoring instruments.*

Item	FY 2008	FY 2009	FY2010	FY 2011	FY 2012	Total (M¥)
IR camera (French vers.)	10	400	300	100	70	880
Lidar (German vers.)	0	80	320	320	320	1040 *
Lidar (Japanese vers.)	10	30	30	100	100	270

* The total cost of Lidar, German version, includes:	
- Lidar transmission art (4 units):	2800 kEuro
- Control electronics of 4 sets of laser:	1600 kEuro
- Manufacturing nad test of the prototype:	1600 kEuro
- Integration and verification:	900 kEuro

4.4.6.3. Schedule

Table 4.4.6.3-1. *Schedule for the IR camera development.*

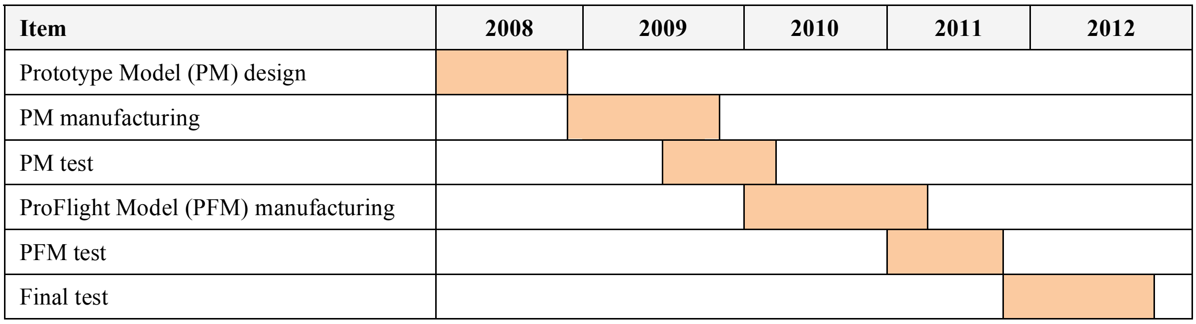

Item	2008	2009	2010	2011	2012
Prototype Model (PM) design	▨				
PM manufacturing	▨	▨			
PM test		▨	▨		
ProFlight Model (PFM) manufacturing			▨	▨	
PFM test				▨	
Final test				▨	▨

Table 4.4.6.3-2. *Schedule for the Lidar development (Japanese version).*

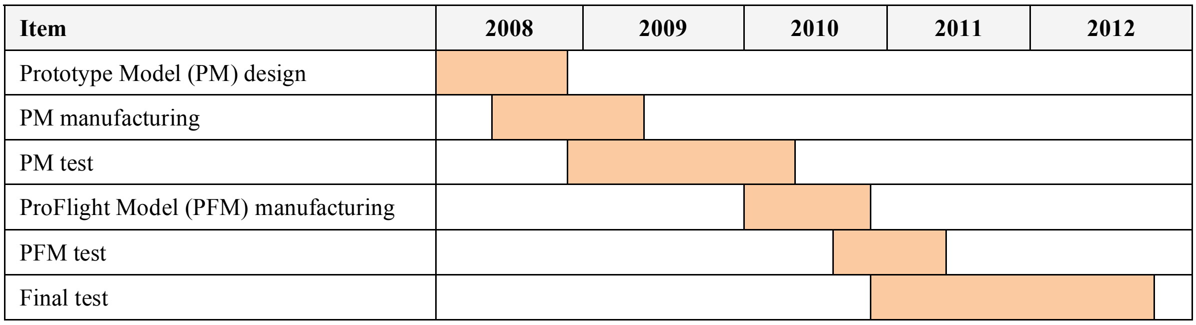

Item	2008	2009	2010	2011	2012
Prototype Model (PM) design	▨				
PM manufacturing	▨	▨			
PM test	▨	▨	▨		
ProFlight Model (PFM) manufacturing			▨		
PFM test			▨	▨	
Final test			▨	▨	▨

4.4.6.4. Organization

Atmospheric Monitor: Valentin Mitev (CSEM), Satoshi Wada (RIKEN)

4.5. Calibration System

4.5.1. General

The calibration system is the apparatus that measures the efficiencies of the optics, the focal surface detector and the data acquisition electronics with a precision necessary to determine energy and arrival direction of the EECRs.

In the EAS induced by an EECR in the atmosphere, only the billions of secondary electrons are of interest here. The number of produced electrons strongly depends on the local density; such a density cannot be measured directly, only the altitude above ground at which such a production happens can be evaluated. The transformation of altitude in density relies on models, themselves based on prior observations with specialized instruments like balloons equipped with manometers and thermometers. Indeed, the altitude to density relation is well known, and knowing if it is winter or summer is generally enough; the accuracy is a few percent.

The electrons ionize the air nitrogen and produce photons in a few bands from 300 to 430 nm. This transformation is called the N_2 fluorescence yield. It is known with a 5% accuracy at 1 bar, 20°C and no pollutants. It is known to 10÷15% at lower pressures. The JEM-EUSO Collaboration will measure in lab this fluorescence yield with unprecedented accuracy from 0.1 to 1 bar, -50°C to +30°C, and with different pollutants like water and methane. The emission of the produced photons is isotropic. The shower electrons produce also Cherenkov light, along a cone whose axis is the shower development axis. This light will splash on the ground, and a certain fraction of it (from 5 to 10 %) goes back isotropically. Some N_2 and Cherenkov photons will reach JEM-EUSO instrument and will be detected by the Focal Surface detector.

The energy of a primary cosmic ray is essentially proportional to the amount of detected light. In order to determine the maximum in the EAS development, it is required to determine the emitted amount of light accurately. Therefore it is necessary to know attenuation and conversion factors between the source and the detector.

The detected number of photoelectrons (ΔS) from the light source (intensity ΔQ) at distance *r* is expressed by the following equation:

$$\Delta S = \frac{\varepsilon \cdot \kappa \cdot \eta \cdot g \cdot T_l \cdot T_f \cdot T_e \cdot T_\alpha}{4 \cdot \pi \cdot r^2} \cdot \Delta Q$$

where ε is the quantum efficiency of the detector, η is the collection efficiency of the detector, g is the relative variation of the detector gain, κ is the fraction of light which reaches the designed pixel, T_l is the throughput of the Fresnel lens system, T_f is the transmittance of the optical filter, T_e is the trigger efficiency (count loss), T_α is the transmittance of the atmosphere, A is the entrance pupil area of the telescope ,and r is the distance to the light source. The terms ε, η, κ, g, $T_{f,}$ T_e and T_l are related to the instrument and are determined from the efficiency measurements of the Fresnel lenses, the optical filter, the focal surface detectors, and the trigger electronics. The amount of detected light is affected by the atmosphere (T_α), so that characterization of the atmosphere is necessary. Since onboard measurements of the atmosphere are detailed in the section of Atmospheric monitor, only the atmospheric monitor on ground is described in this section.

Fresnel lenses have a certain transmittance, measured before launch (this is an efficiency measurement). This transmittance can deteriorate, so that the variations have to be measured in order to take them into account during the analysis of the events. This will be accomplished by sending a light through them up to the FS. This light will be absolutely determined by taking a known percentage of the emitted photons towards a NIST photodiode, accurate to 1.5%.

The FS transforms the photons falling on it into pulses. Each photon gives a pulse, representing one photoelectron (p.e.), at a focal surface detector with a certain probability. This is a typical efficiency (product of quantum efficiency of the photocathode times the collection efficiency to collect the emitted p.e. on the first dynode). Typical values are 30÷35% and the efficiency will be measured with accuracy of better than 2% on ground. Each of the 200,000 pixels has their own efficiency, to be measured independently; they become 600,000 if three colours are used. This efficiency takes into account the filter (or filters) glued to the silica holding the photocathode effects.

During the launch and the flight, the transmittance of lenses and filters and the efficiency of detectors can deteriorate by vibrations of the MAPMTs, radiations on the filter(s), too strong illumination, change of gain, etc. This efficiency must be measured regularly during the flight and it must be done with light going directly from the light source to the FS, without any obstacle in between because, as seen earlier, the FS efficiencies are used to determine the lenses efficiencies. So, first the FS efficiencies have to be measured, then, the lenses ones.

The variations of the parameters are estimated from the experiments with acceleration in time so far carried. The degradation of ε, η, κ, g, T_l, T_f will be less than 5÷10% during the 5 year operation. The error in the reconstructed height of the light source by 10 km varies as $1/r^2$ and affects on r by only 5%, because JEM-EUSO observes EASs from high altitude, 400km. The values of κ and g may change by less than a few % due to the variation of the surrounding temperature. In addition to those, status monitor of each detector and electronics is necessary.

Absolute efficiency measurement should be completed on ground because onboard resources are limited. Only relative variation of the detector gain and efficiency, and the transmittance of the optics with time will be measured on board. If the variation of MAPMT gain is detected and not very big, it can be adapted by the change of the supplied high voltage and the trigger threshold in the front-end electronics, regularly. Bad detectors can be shut off completely if necessary. In the present baseline, onboard calibration is relative one, but observing the moonlight was evaluated as a possible absolute method.

The calibration method in flight is summarized in Table 4.5.1-1 and detailed in the following paragraphs.

Table 4.5.1-1. *Comparison of calibration methods. Comma means that each term before and after the comma is determined independently.*

Method	**Observables (product)**	**Comments**
LED on FS	$\varepsilon\,\eta\,g\,T_l^2\,T_f\,T_m,\,T_e$	T_M: reflectivity of the lid. T_e will be determined from the linearity check with light intensity.
LED behind the lens	$\varepsilon\,\eta\,g\,T_f,\,T_e$	T_e will be determined from the linearity check.
Night background	$\varepsilon\,\eta\,g\,T_l\,T_f\,T_e\,T_\alpha$	This is available during the science observation.
Moonlight	$\varepsilon\,\eta\,g\,T_l\,T_f\,T_e\,T_\alpha$	Candidate as absolute calibration source.
YAP	$\varepsilon\,\eta\,g$	The pixel with a YAP pulsar is used as a standard pixel to ensure the calibration accuracy by LED light sources.
Ground flasher	$\varepsilon\,\eta\,g\,T_l\,T_f\,T_e\,T_\alpha,\,\kappa$	GLS (Ground Light Source) can be deployed at many places because they are relatively less expensive. Multi-wavelength is available by band pass filters.
Airborne flasher	$\varepsilon\,\eta\,g\,T_l\,T_f\,T_e,\,\kappa$	The effect of atmospheric transmittance can be neglected, but the calibration cannot be done frequently.
Ground Lidar	$\varepsilon\,\eta\,g\,T_l\,T_f\,T_e\,T_\alpha,\,\kappa,\,r$	The transmittance of the atmosphere will be obtained as a function of height. It can be used as an artificial EAS to study the accuracy of the event reconstruction.

The instrument calibration will be described in the following sections for four categories:

- Pre-flight calibration
- On-board calibration
- Calibration in flight with on-ground instruments
- Atmospheric monitor calibration

4.5.2. Pre-flight calibration

4.5.2.1. Calibration of MAPMT

In this stage, MAPMTs are selected to satisfy the requirements and are sorted into several groups with the parameter of gain.

Photon detection efficiency (corresponding to the product of the quantum efficiency times the collection efficiency), uniformity of sensitivity, gain, and cross-talks are measured for each MAPMT with the optical filter. MAPMTs with similar gain will be used together for a PDM. The response to the various intensity of light and supplied voltage is studied and the database of MAPMT characteristics will be made. The measurement accuracy will be less than 5%.

Absolute efficiency measurement

One PMT per 10 PMTs is defined as a standard one, whose absolute efficiency is measured. This method was used for the absolute efficiency measurement of the PMTs for the photon yield measurement [78]. As shown in Fig.4.5.2.1-1, UV LED light (at 340 nm, 360 nm and 385 nm wavelength) is diffused in an integrating sphere. The variation of light intensity is monitored with a photo-diode, precisely calibrated at the National Institute of Standards and Technology (NIST, USA), during the PMT measurement. This method gives an absolute efficiency with a good accuracy. In order to obtain accuracy better than 1%, a faint light is required where the number of two p.e.s per pulse is less than 1%. The first integrating sphere has a role of splitter. The two spheres attenuate the light significantly by one millionth, so that a photo-diode and a PMT, which have quite different gains, can see the light simultaneously. The ratio of light intensity between the point where the PMT is attached and where the photo-diode is attached is measured in advance.

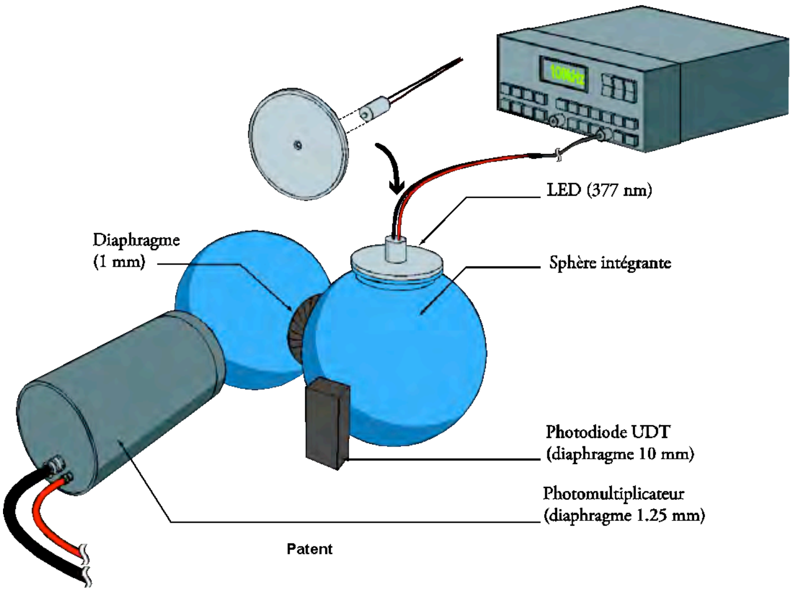

Figure 4.5.2.1-1. *Scheme of the absolute calibration system. UV light is diffused in an integrating sphere and detected simultaneously by the photo-multiplier (PMT) to be calibrated and a photo-diode precisely calibrated at NIST to obtain the PMT absolute efficiency precisely [78].*

The measurement of PMT consists of two parts: one is taking single p.e. spectrum in order to check the lost counts below the discrimination level; the other is done with a discriminator, and the number of coincident signals between the discriminator output and the LED pulser is counted. Taking single p.e. spectrum takes longer time because of the dead time of ADC, but counting can run faster (about 100 times) and then the efficiency measurement with good statistics can be done in a short time. This method gives an accuracy of the calibration by less than ~2% [78]. The advantage of this method is the independence of the light intensity and the emission pattern of the source (LED).

The apparatus for the absolute efficiency measurement has been already built for JEM-EUSO. Preliminary result about photon detection efficiency of an ultra-bialkali MAPMT was about 32% with reproducibility less than 1%, which is consistent with the previous measurement with relative systematic error of 15%. The measurement accuracy would be less than 2% even if taking into account the accuracy of the photo-diode. Spectroscopic absolute efficiency will be taken for some MAPMTs in the range between 300nm and 450nm with a Xenon lamp and a spectroscope.

Relative efficiency measurement for all the MAPMTs

As shown in Fig. 4.5.2.1-2, UV light from LEDs (340 nm, 360 nm and 385 nm) is attenuated and collimated to make a faint UV beam with a point spread function of ~0.1 mm. Light from 3 colour LEDs is diffused in an integrating sphere, and divided by optical fibers and collimated so that single photoelectron spectra for 9 MAPMTs can be taken simultaneously. The light source with the sphere can move on a XY stage so that two-dimensional distribution of photo-cathode sensitivity can be taken. The variation of the light intensity is monitored with a photo-diode attached to the sphere during the measurement. At present, a collimated UV LED light at 370 nm is used to characterize MAPMTs to be used for JEM-EUSO. This characterization system will be extended to measure the efficiency of ~10 MAPMTs in parallel.

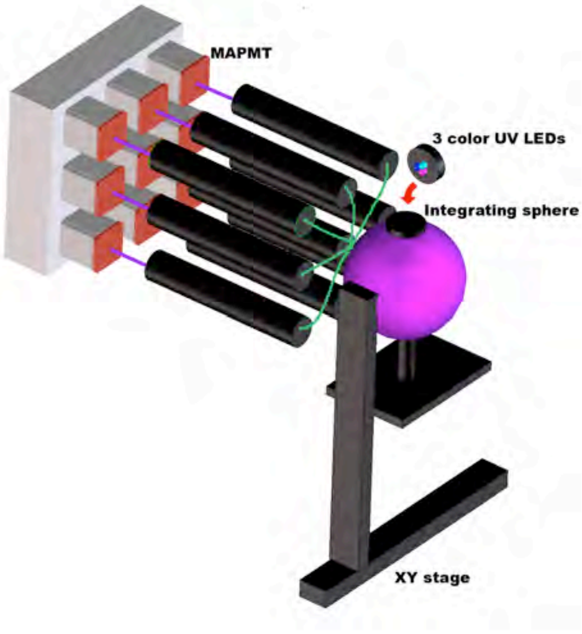

Figure 4.5.2.1-2. *Scheme of the MAPMT characterization system. Light from 3 colours LEDs is diffused in an integrating sphere, and divided by optical fibres and collimated so that single photoelectron spectra for 9 MAPMTs can be taken simultaneously. The light source with the sphere can move on a XY stage so that two-dimensional distribution of photo-cathode sensitivity can be taken. The variation of the light intensity is monitored with a photo-diode attached to the sphere during the measurement.*

The basic measurement is taking single photoelectron spectra of each pixel with faint UV light from LEDs at the three wavelengths. Linearity to light intensity and the gain variation with supplied voltage are taken for five kinds of conditions, respectively. Then two-dimensional distribution of photocathode efficiency is taken with 1 mm step. If 10 MAPMTs are measured simultaneously, about 1 year is necessary to finish the characterization of 10,000 MAPMTs estimated from the current measurements,. The absolute efficiency of all the MAPMTs will be determined if a MAPMT with known absolute efficiency is used as a reference in each measurement.

4.5.2.2. Calibration of PDM

After the selection and grouping, the MAPMTs are assembled as PDMs with electronics. First, it is confirmed whether the expected number of photoelectrons corresponding to the intensity of light is counted using the apparatus described in the previous section. Next, the PDM will be installed in vacuum as a simulated space environment to check the stability of the gain. The temperature of the voltage divider circuit will be monitored during the stability check.

In order to study the response of the MAPMTs at various positions on the focal surface, PDMs are illuminated with the angle distribution of light determined from the optics simulation. Thirdly, uniformity of photon detection efficiency, gain and count are checked with a realistic JEM-EUSO optics and parallel collimated UV light. For the calibration including the second and the third trigger circuits, emulated EAS images with a LED array light source are illuminated with a parabolic mirror or optical fibers. One of the candidate light source for the calibration with a real optics is a UV LASER light reflected by a rotating mirror to make a moving bright point on the focal surface like an EAS image.

4.5.2.3. Calibration of the telescope

We assemble the JEM-EUSO flight model and make a final calibration table of effective transmittance of the lenses, focal surface image, photon detection efficiency and gain of the detector, gain of the electronics circuit and cross talks with a collimated and parallel UV light. One of the candidate light sources is the combination of UV LASER and a mirror like for the PDM calibration.

4.5.3. Calibration in flight

The resources in flight are limited; hence, the calibration system onboard must be very simple and stable. However, we need to get enough information of the JEM-EUSO detector for data analysis and adjustment of gain, HV and discrimination level. The major features for the onboard calibration system (light sources) are:

- Spectro-radiometry in the range 330÷400 nm
- Appropriate light intensity for photon counting
- Background <10^4 photons/(pixel s)
- Light weight
- Low power consumption
- No movable components
- Monitoring function of the light intensity
- Structure and size to fit the JEM-EUSO telescope
- Uncertainty of the absolute intensity < 10 % (TBC)

In addition to the above features, the following conditions are required:

- The light source works stably during the JEM-EUSO operation
- Non-uniformity of the intensity < 20 % (TBC). (Uniformity is calibrated on ground before the launch.)

4.5.3.1. Efficiency measurement of the Focal Surface with LED light sources

Optical design

Several light sources are set on the support of the last lens before the focal surface and illuminate the focal surface. The light source should be small enough to create no obstruction. Fig.4.5.3.1-1 shows the intensity distribution on the focal surface calculated by a ray-tracing simulation code [65, 79]. The intensity is uniform within a factor of two. This uniformity is enough to observe single photoelectrons. The intensity of each light source is adjusted so that the number of photoelectrons per pulse is few enough (the probability of more than one p.e. is less than 2%). In order to obtain enough intensity on the focal surface (5×10^9 photons/s, 1 second exposure is assumed) with a single light source, the power should be larger than 10^{15} photons/s.

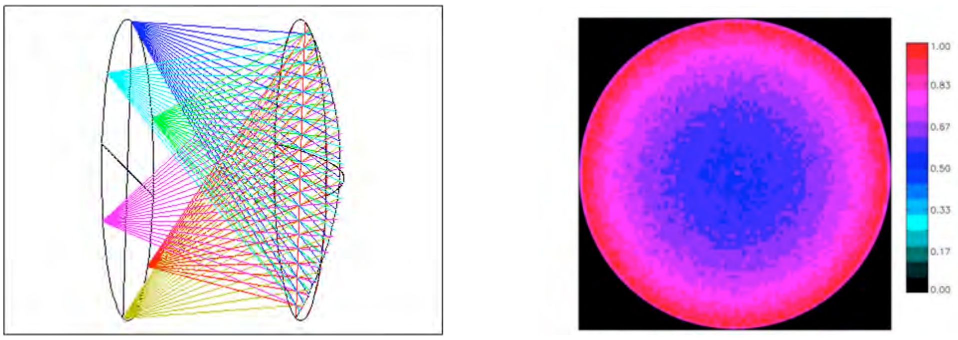

Figure 4.5.3.1-1. *Ray-tracing simulation when light sources are placed along the edge of the lens facing on the focal surface (left) and the intensity distribution at FS (right).*

Light source

Two or three kinds of LEDs with wavelength 340 nm, 360 nm and 385 nm, which have similar wavelengths of major fluorescence lines from Nitrogen, are used for the diffused light source. For redundancy, two pieces for each wavelength are used for one light source. Those LEDs have a light power of ~1 mW, so that they satisfy the requirement of low power consumption. The pinhole diameter and the LED-pinhole distance can be adjusted to define the emission solid angle and the photon flux diffused by a Teflon sheet (Fig.4.5.3.1-2). The stability of the light source is monitored by a photo-diode precisely calibrated at NIST. Instead of the Teflon sheet, an integrating sphere with 30 mm in diameter may be used as a diffuser. The emission angle distribution from an integrating sphere follows *cosθ* law, ideally and the intensity monitor by a photo-diode is easier.

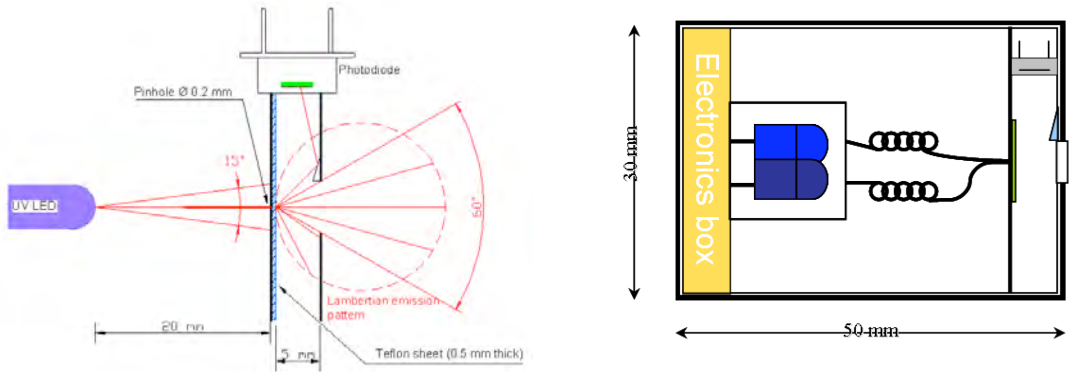

Figure 4.5.3.1-2. *Schematic figure of the LED light source for the on-board calibration. The light from LED is diffused by a Teflon sheet to illuminate large area, and a part of light is monitored by a photo-diode precisely calibrated at NIST. Three color LEDs are used in the range of 300÷400 nm [65].*

Since LEDs are semiconductor devices, it is necessary to study the radiation hardness. GaN based materials such as GaN, InGaN are used for UV or blue LEDs. Blue LEDs with GaN based materials are reported to be radiation hard up to 10^{13} protons/cm^2 [76]. We irradiated 70 MeV protons to candidate UV LEDs with wavelengths of 340 nm, 360 nm and 385 nm by up to 2×10^{11} protons/cm^2, which is more than the expected irradiation (1.6×10^{11} protons/cm^2) if JEM-EUSO is assumed to fly in the South Atlantic Anomaly (SAA) for 5 years all the time, and found no significant decrease in intensity. Generally, GaN based LEDs are radiation harder than GaAs based ones. Therefore GaN based LEDs will work in the JEM-EUSO environment. The photodiode will be shielded with 4 mm-thick aluminium to protect from irradiation effects.

Calibration of the detector and the electronics

Each channel of the front-end electronics will be calibrated with the LED light sources or with night sky background. Cosmic rays are observed with the resolution that single photoelectrons can be discriminated with. For the calibration purpose, single photoelectron spectra will be taken with higher resolution. In order to reduce the amount of data, this measurement will be done once a week or a month. Status of the detectors and the electronics will be monitored with simplified procedure several times per day. It will be checked whether each detector and electronics work with night sky background during the observation or the LED light source during the day. The average and the variance of the count for each channel are monitored every orbit.

4.5.3.2. Efficiency measurement of the lenses with a LED light source

Optical design

A light source is settled at the centre of the focal surface as shown in Fig.4.5.3.2-1. The light passing through the lenses is reflected by a diffused reflector on the rear of the lid and is detected by the focal surface detectors. Using the FS efficiency previously measured, the lens efficiency is determined.

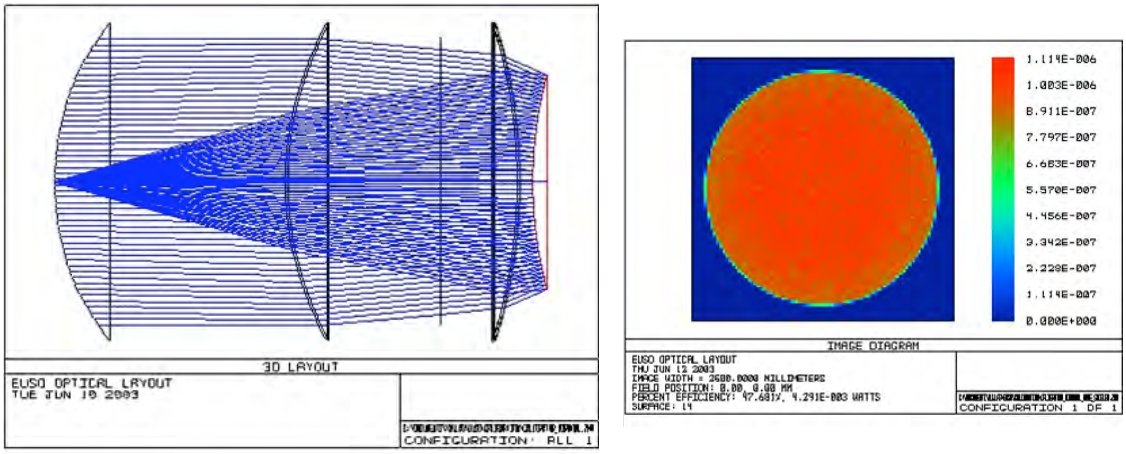

Figure 4.5.3.2-1. *Left: Ray-tracing simulation when a LED light source is settled at the centre of the focal surface and the light is reflected at the rear side of the lid. Right: the expected intensity distribution [65].*

Light source

Essentially the same box as that used for the measurement of the FS efficiency, diffused light source with LEDs at 340 nm, 360 nm and 385 nm, is adopted.

4.5.3.3. Natural light source (night sky background)

The balloon and Russian satellite experiments show that, outside of illuminated cities, the background of stars reflected on Earth is constant with a precision better than the desired resolution expected for the shower energy determination. Hence, that background can be used while data taking, outside of the showers. The Slow-mode is another way to look at that.

4.5.3.4. Man made sources on ground

Light sources are deployed on ground for the atmosphere monitoring and their light is observed by JEM-EUSO to obtain the attenuation factor of UV light in the atmosphere. As a light source, flasher and LIDAR are considered. Flasher is relatively less expensive, so that it is deployable at many places on ground. Wavelength dependence of the attenuation can be obtained by using band pass filters. The wavelength of on-ground LIDAR is 355 nm, the third harmonic of YAG:Nd. The atmospheric transparency can be studied as a function of height by detecting back-scattered light of LIDAR. Systematic errors in the energy and arrival direction determination of JEM-EUSO can be evaluated experimentally by reconstructing LIDAR events as simulated EASs.

Flashers

Ground flashers work as "standard candles" placed around all over the world during the JEM-EUSO mission. The flasher, schematically shown in Fig.4.5.3.4-1, consists of high intensity Xe lamps in short microsecond flashes.

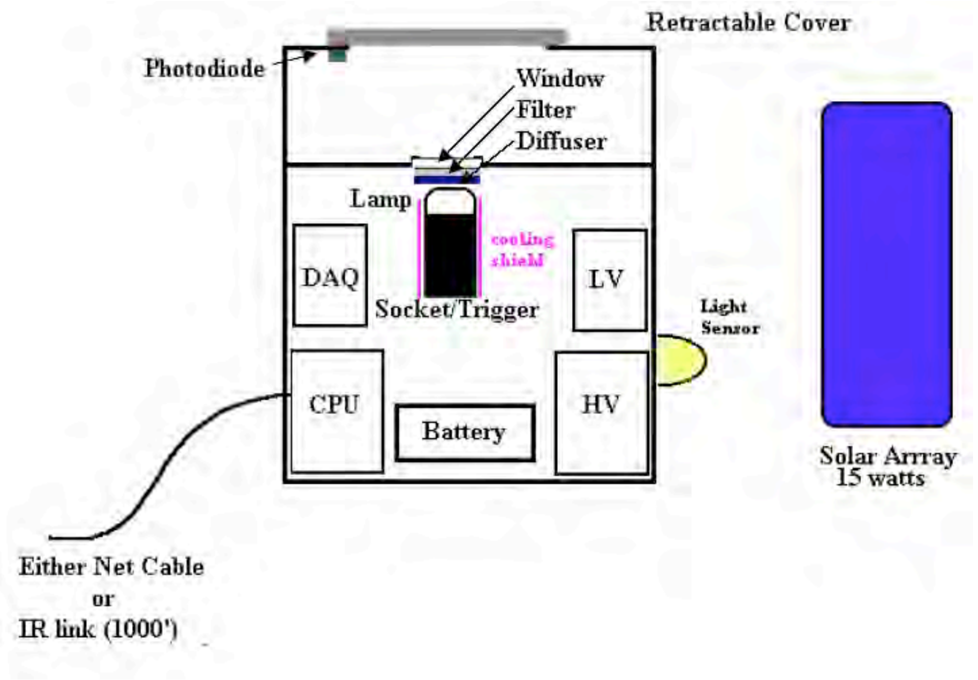

Figure 4.5.3.4-1. *Schematic figure of the on-ground Xe flasher station [65].*

There will be ~~20~~ a dozen ground-based units deployed at host stations in different geographical locations (Table 4.5.3.4-1) to cover various atmospheric conditions, and one airborne unit. ISS will fly over one flasher in average every night. The airborne unit is to be installed on an upward directed portal of a P3B research aircraft stationed at NASA Wallops Flight Facility. It flies under the orbit of ISS at the altitude of 1÷6 km above both land and sea every month during the JEM-EUSO mission. Xe lamps are used as a light source.

Table 4.5.3.4-1. *Candidate deployment sites of ground flashers.*

Place	Latitude	Altitude
Haleakala, HI	20° N	3.0 km
Climax, CO	39° N	3.5 km
Mt. Washington, NH	44° N	1.9 km
Jungfraujoch, Switzerland	47° N	3.5 km
Mt. Norikura, Japan	36° N	2.8 km
Mt. Hermon, Israel	33° N	2.0 km
Chacaltaya, Bolivia	16° S	5.3 km
Alma-Ata, Kazakhstan	43° N	3.0 km
Mexico City, Mexico	19° N	2.3 km
Kwajalan Atoll, USA	11° N	0.0 km

The Hamamatsu flash lamp L6404 has an light intensity of 2J per flash. The expected signal detected by JEM-EUSO is about 500 photoelectrons for clear nights (Fig.4.5.3.4-2). The maximum flash-to-flash variation for this lamp is ~3% and the spatially non-uniformity is less than 5% over a 60° field of view. The duration of over-flights range from 5 to 70 seconds, so that typically 100 flashes per over-flight will be observed by JEM-EUSO. Atmospheric transmittance will be determined with a few percent accuracy by repeating measurements.

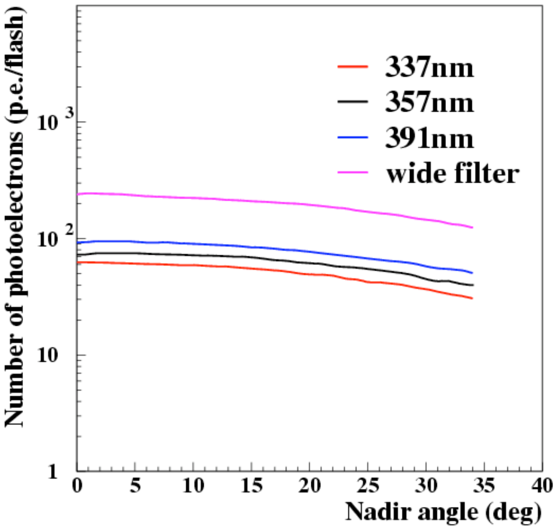

Figure 4.5.3.4-2. *Number of photoelectrons detected by JEM-EUSO from a flash of a on ground Xe flasher. The number of detected photoelectrons is shown as a function of the nadir angle of JEM-EUSO. Only the attenuation of Rayleigh scattering is taken into consideration in clear night condition. If Mie scattering is included, the intensity will decrease by a few 10% [65].*

Each ground flasher consists of four lamps with band pass filters at 337 nm, 357 nm and 391 nm, which corresponds to the wavelength of main N_2 fluorescence lines, and one broad band filter similar to that on JEM-EUSO. The intensity of the lamps is monitored by a photodiode precisely calibrated at NIST. These lamps will be controlled by way of the Internet and flash at ~30 Hz when JEM-EUSO flies over the station. The image of a ground flasher moves at ~ 0.03° / 0.03 s. If a light source passes through at the centre of the FoV, about 2000 flashes will be observed by JEM-EUSO and the atmospheric attenuation will be well determined.

If the onboard Lidar shoots at a ground light source, height dependence of the attenuation will be obtained. Accuracy and systematic error of the onboard Lidar will be estimated by comparing the data from the onboard Lidar and from the ground flasher. In order to use the ground flasher as a light source for absolute calibration, the factor of the attenuation in the atmosphere should be subtracted from the observation results. The transmittance of the atmosphere will be determined with Lidar or observation of standard stars like Vega in U band at the ground flasher stations. Averaging the intensity for appropriate time will reduce the effect of flickering stars.

When the lenses deteriorate (vibrations, radiations, dust, etc.) not only the transmittance will decrease, but also the PSF should increase (slight change of index, dispersion, shape of the Fresnel grooves…). Then a light source position on Earth will look bigger on the FS, with two results: less light per pixel and blurred image cause less accurate determination of EAS directions. The other is the slight raise of threshold for the showers. Since the ground flashers are point sources for JEM-EUSO, focusing quality of the optics can be checked. The increase of focal image is taken into account for the simulation and the data analysis.

Ground Lidar

Since we can emulate EASs with the third harmonic of NdYAG Laser (355 nm), ground Lidars may be an effective tool for calibration [65]. In order to emulate the EAS of 3×10^{20}eV with an elevation angle of ~20°, we need the output of 50 mJ at least. Once the power and the elevation angle of the Laser, we can determine the size of the receiver (~1 m in diameter). The signals back-scattered at 30 km and 60 km are about 800 photoelectrons and 20 photoelectrons in 2.5 μs. If we shoot 100 times, for example, more than 1000 photoelectrons will be observed and the atmospheric properties are determined well (Fig.4.5.3.4-3). We can measure the transparency with an accuracy of 5÷10% after ~100 shots.

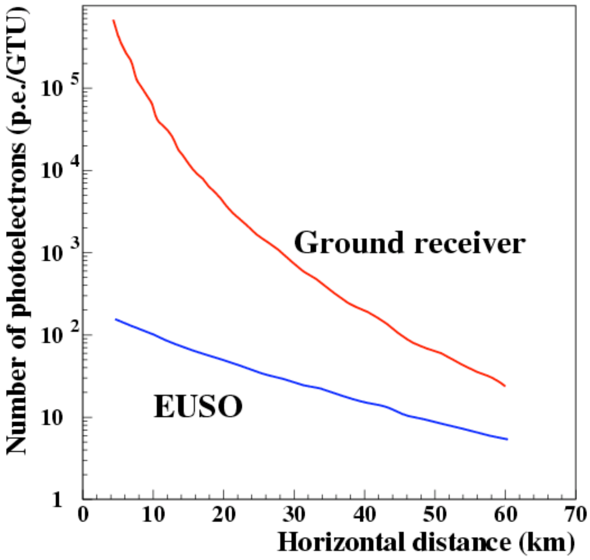

Figure 4.5.3.4-3. *Expected number of photoelectrons per GTU (2.5μs) detected by JEM-EUSO and a ground receiver from a ground Lidar (50 mJ/shot, 355 nm NdYAG third harmonic) shooting with elevation angle of 20° [65]. The ground Lidar receiver is assumed to be 1 m in diameter and 10% in quantum efficiency. More than several photoelectrons can be detected by JEM-EUSO up to 60 km in horizontal distance. The signal detected by the ground Lidar receiver is strong enough to characterize the atmosphere in detail after ~1000 shots.*

As a ground light source the shot in the elevation angle of 20÷30° is optimum and probably the fixed directional Laser may be robust and minimize the maintenance of the mechanical parts of the system. The Laser can be tuneable up to 10÷30 Hz. In these horizontal shots, the Laser beam reaches the top of the atmosphere after travelling ~30 km, where the Rayleigh scattering is dominant. The beam travels in pure molecular region for another 30 km and we can get the boundary condition for the Lidar equation, because we can know the ratio of the back-scattered intensity to the beam intensity in the pure molecular region. Then we can solve the Lidar equation to obtain the transmittance of the atmosphere as a function of height.

The Laser beam with an elevation angle of 20° can be seen as a track of 30÷50 km long from JEM-EUSO. If the scattering is dominated by the Rayleigh process, the number of photons at the entrance of JEM-EUSO can be calculated. The scattering angles of photons that JEM-EUSO will receive are always larger than 40°. In such large scattering angles, Rayleigh process usually dominates under good weather condition. We will use photons scattered above 3 km where the scattering is better described only by the Rayleigh process. Simultaneous operation of the on-board Lidar system and the ground Lidar system gives us more detailed information about the atmosphere and more redundant measurements. It will also reduce the systematic error in the measurement significantly. The systematic errors and the resolutions of arrival direction and energy determination determinations by JEM-EUSO can be evaluated experimentally by reconstructing Lidar events.

4.5.3.5. Onboard Lidar and Infrared camera

These instruments are mainly used to measure the height of the clouds top. They also give some knowledge on the atmosphere transparency between the shower and JEM-EUSO.

Onboard Laser

It is composed of only a laser, the receptor being the JEM-EUSO telescope. The two variables in a laser are the timing, which does not need to be monitored, and the emitted light intensity. Part of this light should be sent to a NIST photodiode.

Onboard Infrared camera

Its "calibration" is provided by the manufacturer. The camera measures the cloud top temperature which gives its altitude through a well known model.

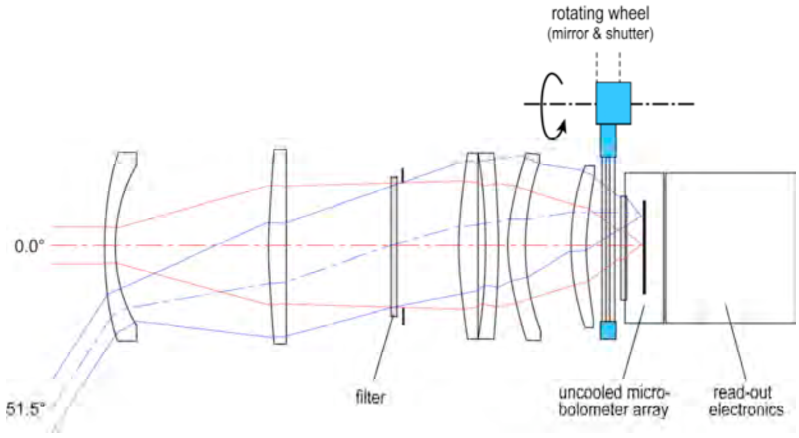

Figure 4.5.3.5-1. Schematic design of the Infrared camera calibration.

Between the microbolometer array sensor and the optics, a wheel can place a mirror in the path of the infrared rays (Fig.4.5.3.5-1) so the CCD will look at itself. If a regular thermometer is fixed to the sensor, it calibrates itself in an absolute way. The precision is 3K, corresponding to 200 m.

A better, but maybe not necessary, calibration can be realized if one can make the camera look at vacuum (during the day with an on-off mirror), or to some simple black bodies in the 11÷13 μm range. Then the precision would reach 1K.

4.5.3.6. Advanced options

YAP pulsars

In order to increase reliability of the calibration with LED light sources, calibration with YAP light pulsars are performed. YAP light pulsar consists of $YAlO_3$ scintillator and a ^{241}Am isotope and emits steady intensity of UV light at around 350 nm. YAP pulsars are used for calibration purpose in the field of high-energy physics experiments.

One YAP pulsar is put on a pixel per PDM. The pixel is dedicated to the calibration as a standard pixel to monitor the variation with time. The response to the LED light sources is compared with that to the YAP pulsar to guarantee the calibration accuracy with LEDs.

YAP pulsars have weak temperature dependence, so that it is calibrated well before the launch. The long-time stability of the light intensity of YAP pulsars should be checked in a laboratory.

Natural light source (moonlight)

In addition to the artificial light sources described above, light sources in Nature will be utilized which is considered to be stable for a long time. One of those sources is the reflection of the moonlight. The moon is one of the nearest astronomical objects and its spectrum has been measured precisely. When the moon with phase α is at the zenith angle of θ, the expected number of photoelectrons detected by JEM-EUSO of the reflected and scattered light by the Earth is expressed as the following equation [75]:

$$I_{Moon}(\theta,\alpha) = 40 \cdot \cos\theta \times 10^{-0.4\left(1.5|\alpha| + 4.3\times10^{-2}\alpha^4\right)} \qquad \text{[p.e./pixel/2.5μs]}$$

When the moon is full it is too bright to observe cosmic rays, but is within the dynamic range of the front-end electronics. Therefore, reflected moonlight could be a good calibration source. The stability of the intensity in various atmospheric conditions will be studied in detail.

Cross calibration with ground based experiments

Differences may arise in results of between JEM-EUSO and ground based experiments, especially in the energy spectrum. The difference in energy determination can be checked directly by observing a same shower, but it is very rare to observe 10^{20} eV showers at the same time. Observing Lidar beam shots at an observatory for ultra-high energy cosmic rays such as the Pierre Auger Observatory, the Telescope Array Experiment may give us information about mutual calibrations between JEM-EUSO and ground based experiments.

4.5.4. Operation

During the science observation, the count rate of each pixel is monitored and the average and the variance are calculated for each pixel every orbit. The photon detection efficiency and the linearity of each pixel are examined by the onboard LED sources during the day.

For precise calibration, single photoelectron spectra will be taken once a week with the LED light sources for each pixel. When JEM-EUSO flies over a ground light source, the instrument calibration and atmospheric monitor will be performed.

The calibration frequency is about once per day and 1÷5 hours per year will be used for the observation of ground light sources.

4.5.5. Summary

4.5.5.1. Specifications

Table 4.5.5.1-1. *Onboard calibration requirements.*

Code	Item	Required value	Note
CSR1	Observation wavelength	330÷400 nm	
CSR2	Accuracy on the calibration of the light intensity	< 18% (TBC)	

Table 4.5.5.1-2. *Onboard calibration technical readiness levels.*

Code	Item	Technical Readiness Level (TRL) and its reason when selected in Febr.'07	Verification status of TRL and reason (as of Apr.'08)	Expected TRL and activities at SDR time (Mar.'09)
CSR1	Observation wavelength	TRL3 Verified by two tyes of UltraViole LED (360 nm, 380 nm TBC).	TRL3 Choose two candidates of UltraViolet LED, and verify them by calculations based on the characteristics of the optics and detector.	TRL4 Verification by means of the evaluation of BB models, which consists of the combination of the elements of test manufactured calibration device, optics, and focal surface detector.
CSR2	Accuracy on the calibration of the light intensity	TRL3 Verified by a calibration device in lab.	TRL3 Verified by a calibration device in lab.	TRL4 Verification by BB model evaluation, which consists of the combination of the elements of test manufactured calibration device, optics and focal surface detector with help of simulation.

Table 4.5.5.1-3. *Onboard calibration temperature requirement (same for the focal surface detector and electronics).*

Item	Operation temperature	Non-Operation temperature
Detector	T_0±10°C (0°C < T_0 < +20°)	-30°C ~+50 °C
Electronics	-10°C ~+50 °C	-30°C ~+50 °C

Table 4.5.5.1-4. *Onboard calibration. Mass budget.*

Parts	BEE [kg]	Margin [%]	Total [kg]	Comments
LED light source	7	30	9	1 kg × 7 (TBC)
YAP	1	30	2	
Total	***8***		***11***	

Table 4.5.5.1-5. *Onboard calibration. Power budget.*

Item	BEE [Watt]	Margin [%]	Total [Watt]	Comments
LED light source. In operation	8	30	11	(TBC)
LED light source. Non operation	0	30	0	0

Table 4.5.5.1-6. *Onboard calibration. Telemetry budget.*

Item	BEE [kbps]	Margin [%]	Total [kbps]	Comments
LED light source	6	30	8	Details here below
Total data rate 30 Mbits/orbit (TBC) ≈ 6 kbps				
- Single photoelectron spectra:			4 Mbits/orbit (full data/week)	
- Data for ground flasher:			1.5 Mbits/orbit	
- Data for ground Lidar:			1.5 Mbits/orbit	
- Background monitor during science observation:			6 Mbits/orbit	
- Data for detection efficiency and linearity check:			15 Mbits/orbit (TBC)	

4.5.5.2. Cost

Table 4.4.5.2-1. *Cost, in MYen, for the JEM-EUSO calibration subsystem.*

Item	FY 2008	FY 2009	FY2010	FY 2011	FY 2012	FY 2013
Efficiency measurements of MAPMTs	10	38	5	4	3	0
Onboard LED light source	1	1	2	1	0	0
On ground flashers	9	10	10	14	38	10
On ground Lidars	0	1	1	7	32	3

Total = 210 M¥

4.5.5.3. Schedule

Table 4.4.5.3-1. *Schedule for the JEM-EUSO calibration subsystem development.*

Item	FY 2008	FY 2009	FY2010	FY 2011	FY 2012	FY 2013
Pre-flight MAPMTs calib.	Design & trial model	Fabrication	Calibration			
Onboard LED	Design Trial model	Fabrication	Testing			
Onboard YAP	Design	Trial model	Fabrication and Testing			
Ground flasher	Concept	Detailed design		Fabrication and Testing		Deployment
On ground Lidars	Concept	Detailed design		Fabrication and Testing		Deployment

4.5.5.4. Organization

Calibration subsystem: Ph. Gorodetsky (APC Paris), N. Sakaki (Aoyama)
Pre-flight calibration: N. Sakaki (Aoyama)
Onboard calibration: E. Pace (Univ. Firenze)
Ground flasher: M. Christl (MSFC/NASA)
Ground Lidar: N. Sakaki (Aoyama)

4.6. Support Sensors

JEM-EUSO has attitude sensors and one GPS, Global Positioning System.

The attitude sensor consists of a star sensor VSC (Visual Star Camera) and a gyroscope RLG (Ring Laser Gyroscope). The absolute attitude (< 0.05°) of JEM-EUSO is obtained by VSC, while RLG (with a total error less than 0.04°) is operated as the backup of VSC, which cannot work when star is not able to be seen.

The GPS is used to measure time with an absolute accuracy better than 1 μs.

We are planning to use the support sensors which are compatible with the sensors developed and used in MAXI (Monitor of All-sky X-ray Image). However, some improvements for GPS may be necessary to match the requirement of the higher time accuracy (< 1 μs) with respect that of the GPS in MAXI (< 10 μs) to accurately catch the instant of thunder light generation. The specifications of the MAXI support sensors are:

- VSC bias error: ±10”×10” (maximum)
- RLG total error: < 0.04°
- GPS time accuracy: < 10 μs

4.7. Bus System

Bus System concerns the structure part, the structural control mechanism system, the data processing unit, the power distribution unit, the electrical and thermal control system, as shown in Fig. 4.7-1 (as in Fig.4.1-3). Inner and outer interfaces are described in paragraph 4.7.5.

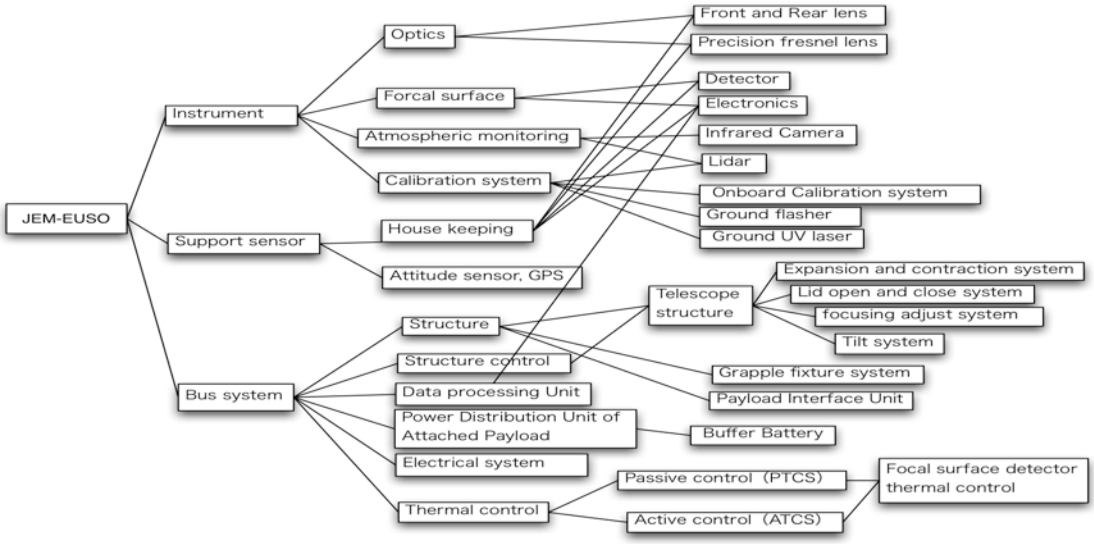

Figure 4.7-1. *Breakdown of the JEM-EUSO system.*

4.7.1. Structure part

4.7.1.1. Accommodation of JEM-EUSO to HTV

From the size point of view, the accommodation of JEM-EUSO into the HTV transfer vehicle has been studied through the Phase-A and was described in detail in the "Incidental Conditions Study Result Report" [80] submitted to JAXA in Nov. 2007.

One of the main results is that the so-called Case-C (2.6 m in diameter, of which the lateral part is cut) is determined as the current baseline which satisfies most of both the scientific and HTV envelop requirements (TBC).

4.7.1.2. Structural design

The front lens and its supporting structure are slotted into the pallet. Supporting structure without affecting the separation/latch mechanism such as TSM, HSM, HDM, and wiring of the flexible shaft cables on the pallet (Figure 4.7.1.2-1). In addition, the cylinder of the telescope is divided into three rings, and by moving these rings in the axis direction, the telescope is deployed. The overall drawings based on these design concepts are shown in Figs 4.7.1.2-4 and 4.7.1.2-3.

Observation state of JEM-EUSO to JEM/EF is shown in Figure 4.7.1.2-4. JEM-EUSO is planned to be attached to the EFU#2 port of JEM/EF. For this case, possible interference exists with the standard payload for EFU#4. The EFU#9 port can be used as a backup option without any physical interference. The corridor for EVA activity (30 inches width from the corner of the exposed facility) confirmed to be secured.

Radio interference with the PROX antennae located in the pressurized module, found to be less severe compared to the standard payloads even for the EFU#2, if telescope is shrunk to stowing mode and is tilted by 80° (see Figure 4.7.1.2-5).

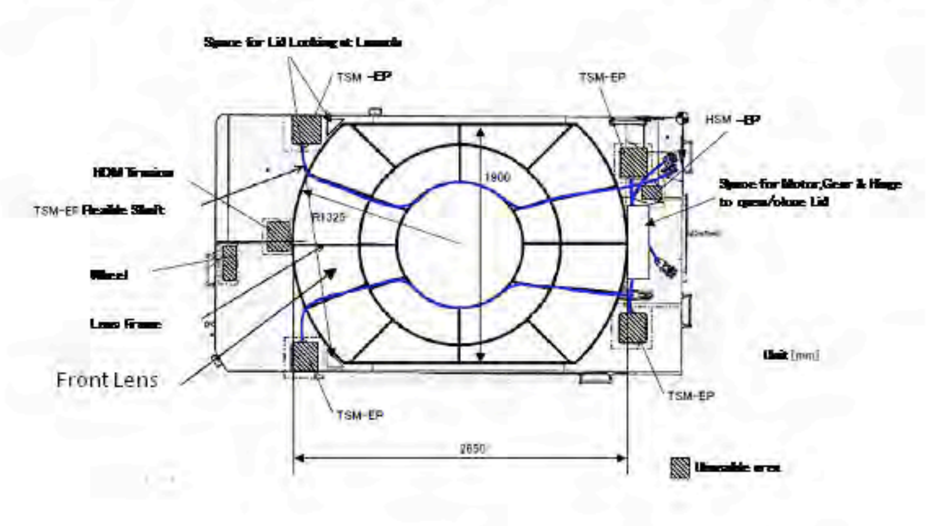

Figure 4.7.1.2-1. *JEM-EUSO in the HTV. Bottom view from nadir [80].*

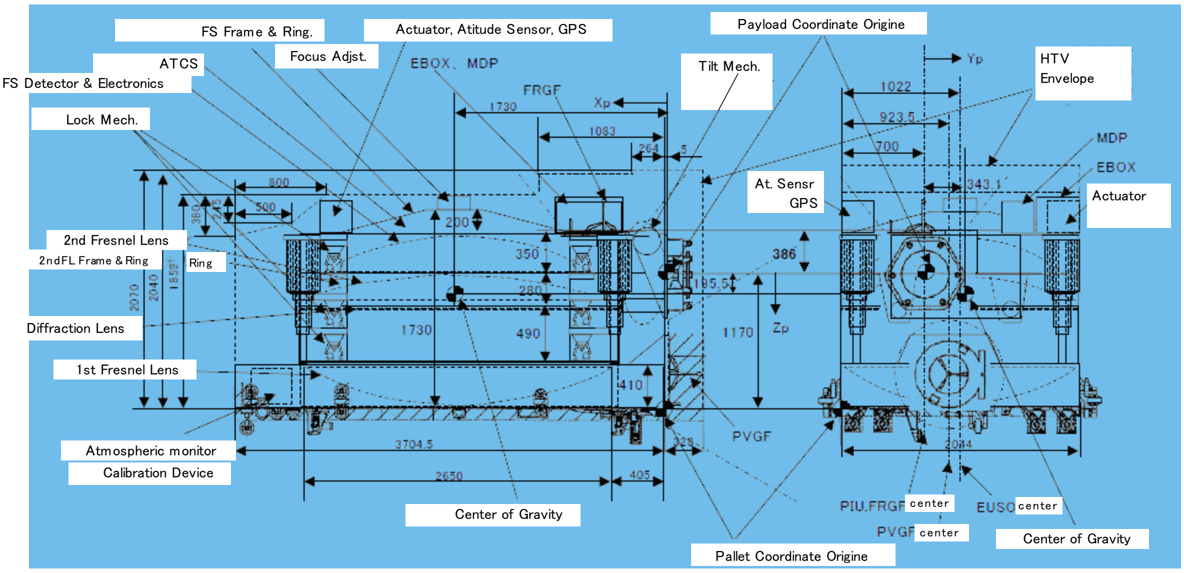

Figure 4.7.1.2-2. *Side view of JEM-EUSO (stowing configuration in HTV) [80].*

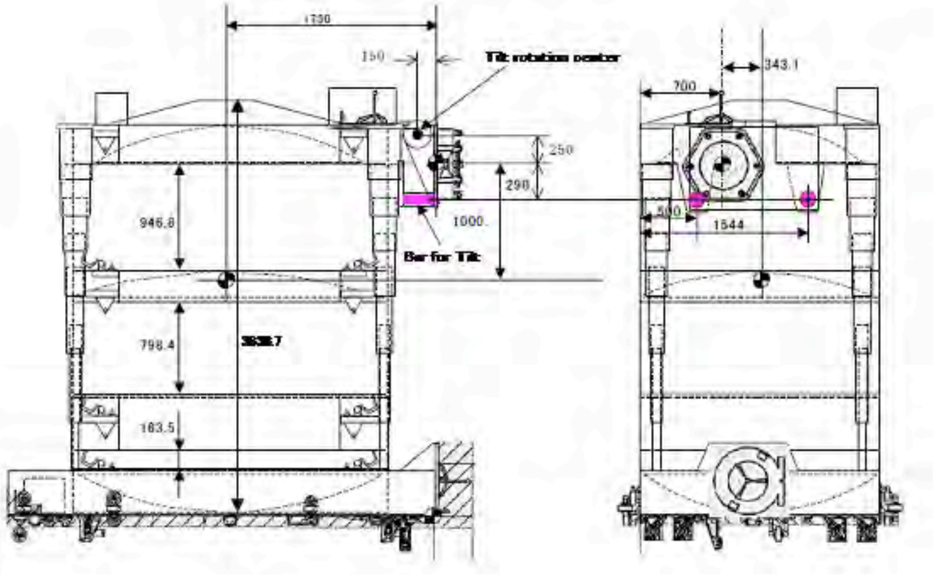

Figure 4.7.1.2-3. *Side view of JEM-EUSO (observation configuration) [80].*

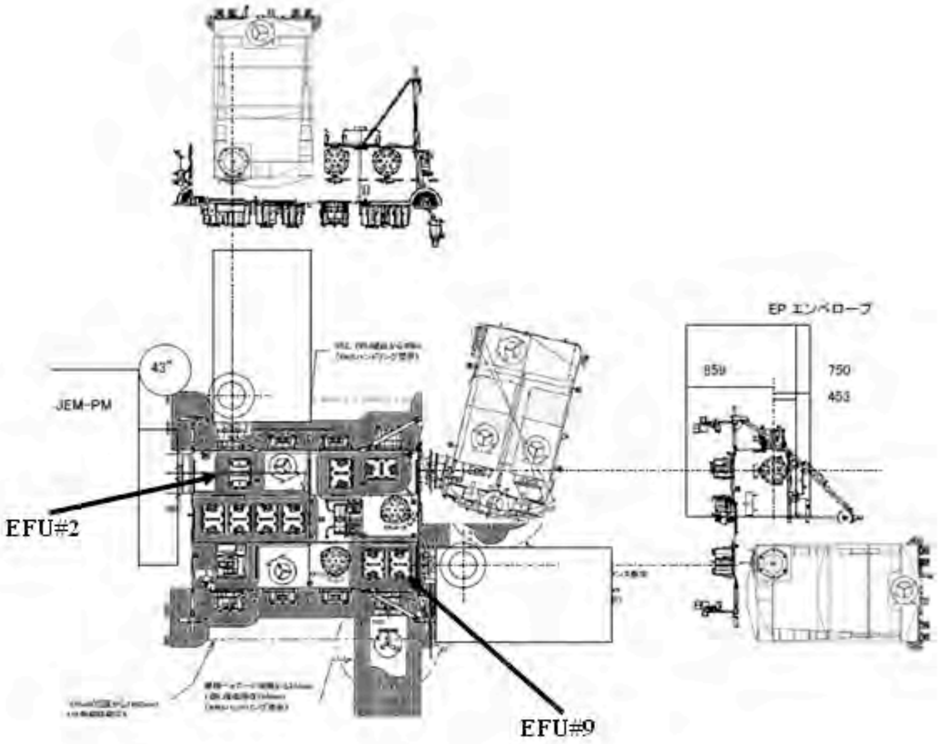

Figure 4.7.1.2-4. *Attached state of JEM-EUSO to EFU#2 or EFU#9 of JEM/EF [80].*

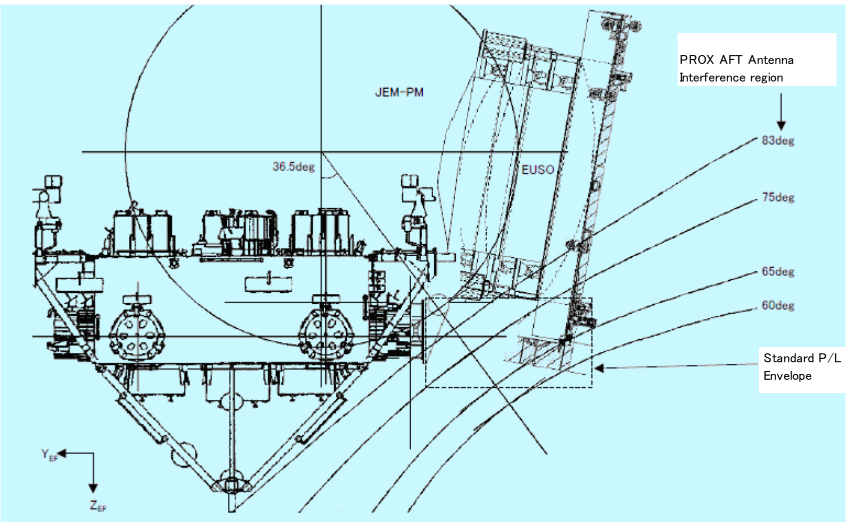

Figure 4.7.1.2-5. *PROX antenna interference in case of JEM-EUSO attached to EFU#2 tilted by 80° [80].*

4.7.1.3. Structural analysis

Structural analysis for the structure mentioned above has been done by the IHI AeroSpace engineering company [80].

Natural frequency analysis of observation state

The analysis of telescope in observation mode in deployed state was done. Natural Frequency turned to be as high as 1.7 Hz under the boundary condition that telescope was fixed to PIU (Payload Interface Unit). It is larger than the minimum required value of 1Hz. It can be increased to around 2 Hz by reinforcing PIU adapter. Figure 4.7.1.3-1 shows the model structure for the simulation.

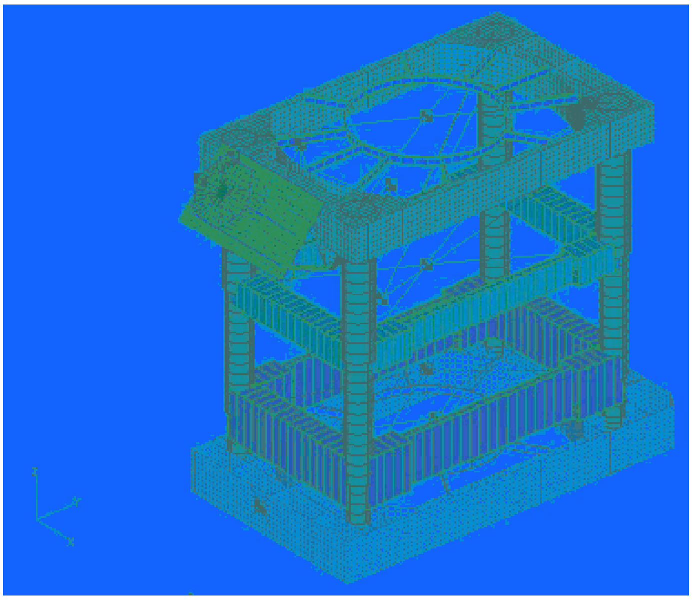

Figure 4.7.1.3-1. *Structural simulation model. Observation (deployed) state; 40° tilt angle [80].*

Natural frequency analysis of stowing state

We found that the minimum natural frequency was 25.6 Hz and that it satisfies the requirement of launch time rigidity, over 25Hz. Figure 4.7.1.3-2 shows the model to use in this analysis.

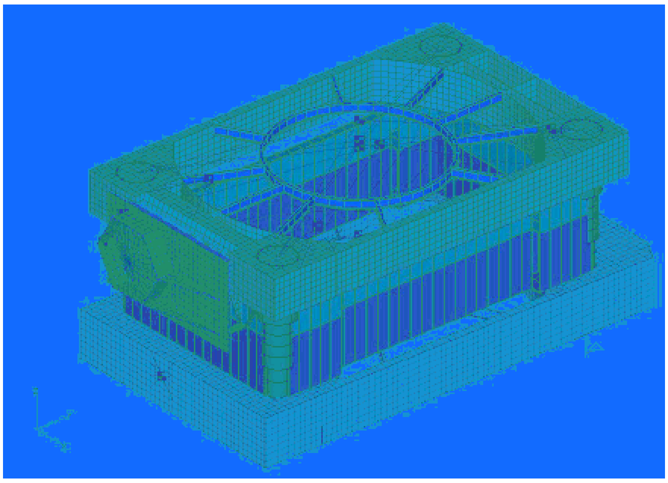

Figure 4.7.1.3-2. *Structural simulation model. Launch (stowed) state; 0° tilt angle [80].*

Static analysis of launch state

Static analysis was performed for various kinds of accelerated loads. The Margin of Safety (MS) value was calculated by stress in the structure and failure stress of material (A7075-T7351). The minimum MS was equal to 2.10 in the vicinity of the connection point between TSM and pallet frame. It means that the designed structure satisfied the strength requirement at launch; the results of the calculation in case of the load by which the minimum MS value is obtained is shown in Fig. 4.7.1.3-3.

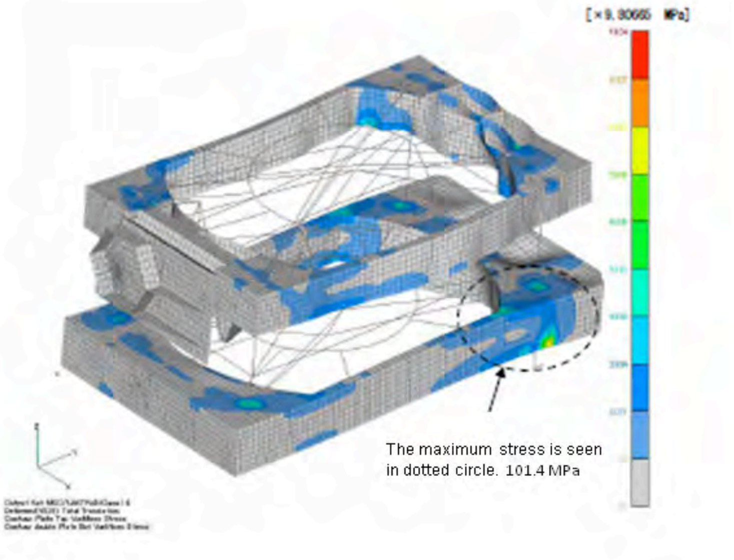

Figure 4.7.1.3-3. *Structural stress distribution [80].*

4.7.2. Structure control (mechanism) system

Regarding the Structure Control (Mechanisms) of the bus system, we studied the following points: opening/closing of lid, stowing/deploying mechanism, tilting mechanism and adjusting mechanism of focus.

4.7.2.1. Lid

Conceptual study and design of the lid were done by a company which has experience and expertise in Space engineering (what company?). We confirmed the durability for 30,000 times opening/closing operations for 5 years and estimated the mass (14.1 kg including the lid, driving mechanism, support structure, etc.) and driving power (around 3.4 W for opening operation for 6 seconds) (Figure 4.7.2.1-1).

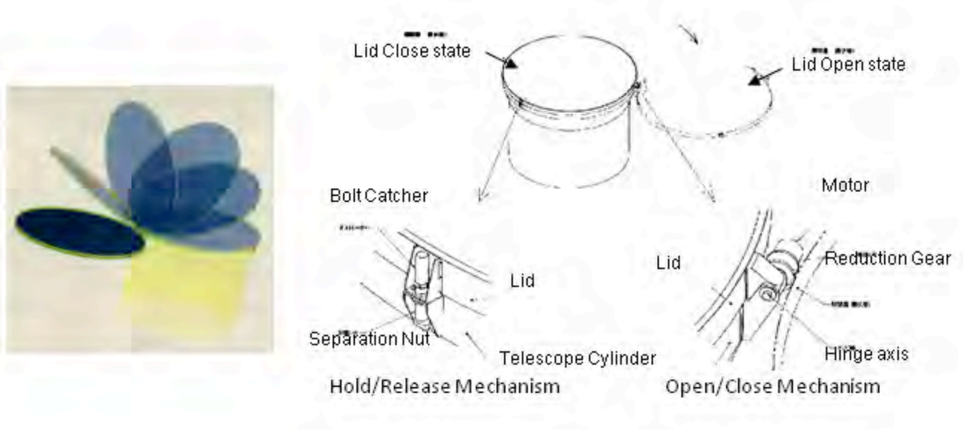

Figure 4.7.2.1-1. *Conceptual diagram of the lid opening/closing.*

Secondly, we have studied the MAPMT durability test. In the case that the lid in opening mode accidentally remains open even during the daytime, the focal surface may be exposed to diffusive light in the Earth daytime. We have tested that FS detector remains durable for a few years to continue the observation in the Earth night-time, as long as the high voltage is not applied. Even in that case, the detector could be partly be deteriorated by reflection on the mirror surface, such as the water surface of shallow lake, caused by the Sunlight on Earth. It would be better to keep the lid closed during the daytime in order to maintain the performance of the detector as long as possible. In addition, it is necessary to close the lid to protect the telescope from bad environmental conditions which are caused by approaching of HTV, re-boosting etc..

Based on these studies, we decided to design the lid and opening/closing mechanism with as high reliability as possible, then to repeat opening/closing action of the lid in every orbital cycle in the early stage of the operation. When we detect an anomaly in the mechanism, it will be appropriate to keep the lid in open state to avoid locking in the closed state, because we lose all the function of the instrument.

4.7.2.2. Deploying and stowing mechanism

The telescope cylinder is divided into three rings which are moved by four inflatable masts. Regarding the deploying/stowing mechanism of the telescope, Inflatable Sunshield In Space (ISIS) Telescope Mast$^{\mathrm{TM}}$ supplied by NORTHROP Grumman Company is confirmed to have excellent reliability. These four masts will be installed outside the telescope and extended synchronously (see Figure 4.7.1.2-2 and 4.7.1.2-3 for details).

4.7.2.3. Tilt mechanism

Tilt mechanism is installed near PIU (Payload Interface Unit) in order to tilt the whole telescope (Figure 4.7.1.2-2 and 4.7.1-2-3). To avoid radio interference of PROX antenna, the capability of tilt angle should be at least 80° (Figure 4.7.1.2-5). Thus we can assure 30÷40° of the required tilt angle for observation.

We studied of the tilt angle and its direction, using crepuscule line angle and beta angle as parameters. By evaluating the observable time (time period in which the whole FoV occupies night area on Earth) for the various tilt directions, we confirmed that the difference among each case was very small (maximum 25 seconds) (Figure 4.7.2.3-1).

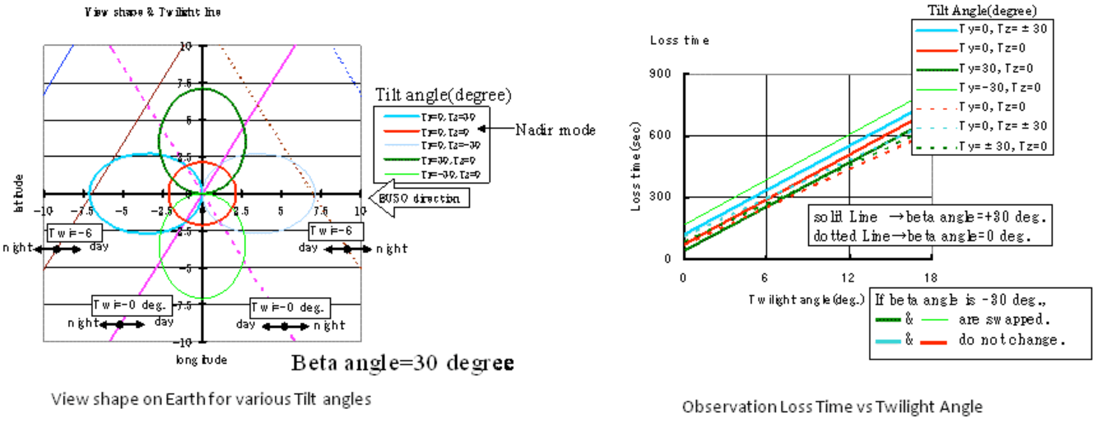

View shape on Earth for various Tilt angles

Observation Loss Time vs Twilight Angle

Figure 4.7.2.3-1. *Tilt angle analysis.*

4.7.2.4. Focusing adjustment mechanism

Figure 4.7.2.4-1 shows the conceptual design of the focusing adjustment mechanism.

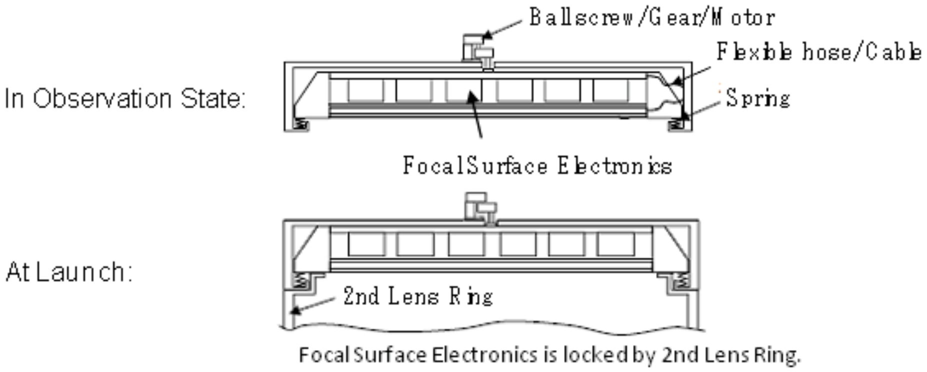

Figure 4.7.2.4-1. *Focusing adjustment mechanism [80].*

4.7.3. Data processing unit and power distribution unit

The following figure shows the overall system diagram including the relation between the mission and data processing unit/power distribution unit.

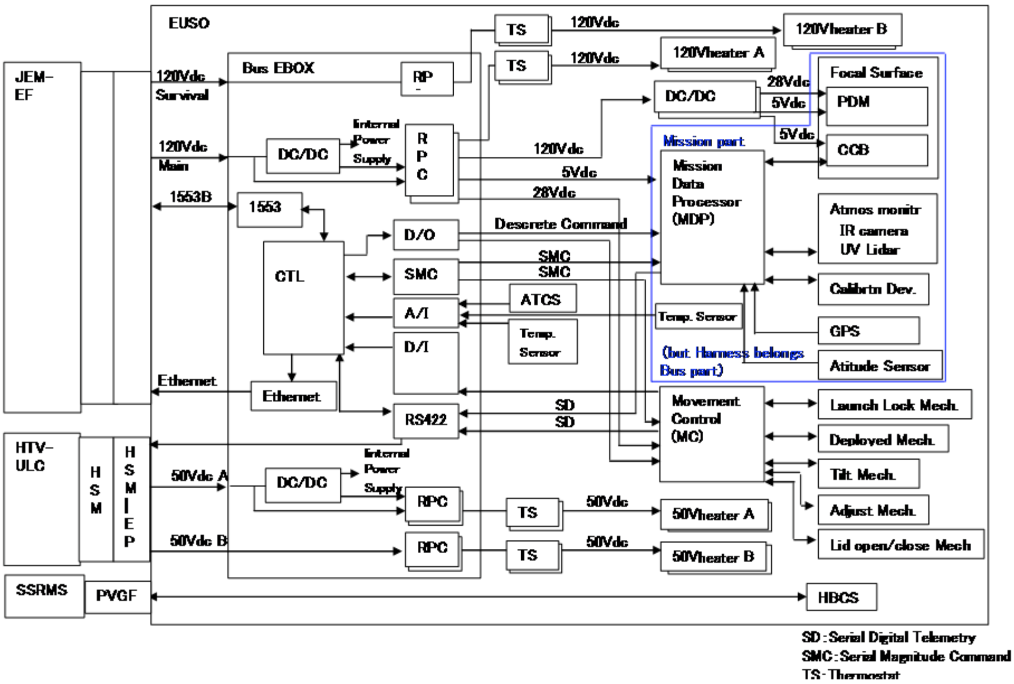

Figure 4.7.3-1. *Bus system block diagram*

4.7.3.1. Data processing unit

Data processing in the bus system consists of data processor (CTL) in the EBOX and movement controller (MC) outside the EBOX (Figure 4.7.3-1).

The major functions of data processor (CTL) in EBOX are:

- communication interface among JEM/EF, CTL by payload bus2 (1553B) and Ethernet,
- communication interface between mission system and CTL,
- acquisition of HK data of mission system,
- interface between power distribution unit in EBOX and CTL, and ON/OFF control of power supply by power distribution unit to each device,
- the function to start/stop the trigger of the installed JEM-EUSO software (JES), which processes the data observed by focal surface detector and atmospheric monitor; it is also necessary to have a rewritable and non-volatile memory for software storage,
- interfacial function of distributing the 1 PPS clock signal from GPS to MDP and VSC electronics (VSCE),
- interfacial function of ATCS.

Movement controller (MC) accepts signals from DP and controls movable mechanisms (telescope deploying/contracting, lid opening/closing, focus adjusting and telescope tilting) and then actuates these mechanisms into the required position/state. HK and position data are also acquired by MC and sent to CTL.

4.7.3.2. Power Distribution Unit

The major functions of power distribution unit (DC/DC inside/outside EBOX, Fig.4.7.13) are:

- receiving power from JEM/EF, transforming it into appropriate voltage and supplying required power to each device in the telescope, (ON/OFF actions of power supply can be controlled by CTL), and

- receiving survival electric power from JEM/EF, and supplying its power to each heater in JEM-EUSO system.

Optimization of power supply to FS electronics which consists of PDM, CCB and MDP was done. The following combination of 8 DCDC converters, realizes the least power conversion loss. Figure 4.7.3.2-1 shows the voltage distribution diagram.

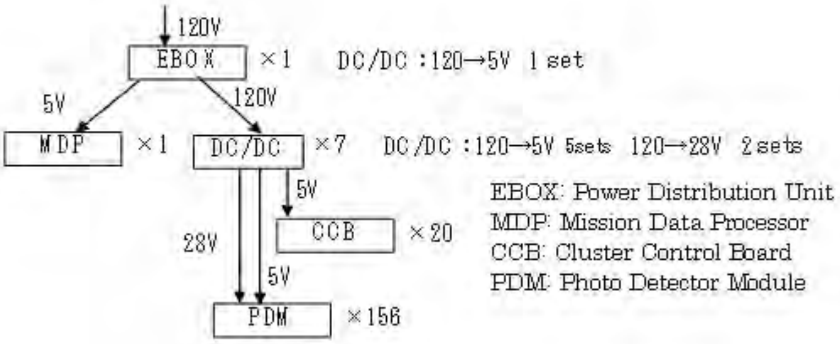

Figure 4.7.3.2-1. *Voltage distribution diagram [80].*

Power consumption rate of the telescope is much different between operating state (night-time) and non-operating state (day-time). In order to smooth the difference, we studied the utilization of buffer battery. Lithium-ion battery is preferable for a Space mission because of high energy density (165 Wh/kg), high Energy efficiency (96%) and low thermal loss and no memory effect, and more [81]. If the Depth of Discharge (DoD) is less than 25%, instead of full discharge (100% DoD), we would need a battery of over 4 times larger; however, battery life for 25%DoD will be expected 50 times longer than that of 100% DoD. In addition, in case of 25%DoD, charge/discharge of 40,000 times is possible [81]. In case of JEM-EUSO, as around 20,000 times charge/discharge is estimated for three years, then the operation for about six years will be possible with 25%DoD.

By smoothing the power by buffer battery, the necessary power of the mission such as 1400 W in operation and 360 W in non-operation become possible, even if the supplied maximum power from the bus is limited to 950 W. In this operation, necessary mass of battery is estimated about 47 kg, even in case of preparing two batteries for redundancy. Battery mass is included as item ‘buffer battery’ in the mass budget table referred to the bus system.

4.7.4. Thermal control and thermal analysis

4.7.4.1. Thermal control

Thermal control system is composed of active thermal control system (ATCS), passive thermal control system (PTCS) and PIU (Payload Interface Unit) cover.

If SiPM is used as focal surface detector, ATCS has to dissipate actively the heat by electronics devices to keep the detector at less than -15°C. As the electronics devices are installed near detector backside surface, they should also be cooled by ATCS. Supply of coolant from PIU structure for ATCS to detector surface frame is relatively easy by connecting flexible hose at tilt mechanism. EBOX for bus system box and movement controller (MC) installed on detector frame are also cooled by ATCS. Atmospheric monitor and calibration devices which are not installed on detector frame are cooled by PTCS because their heat generation rate is small, and also it is difficult to supply coolant for ATCS. ATCS diagram obtained from the above study is shown in Figure 4.7.4.1-1.

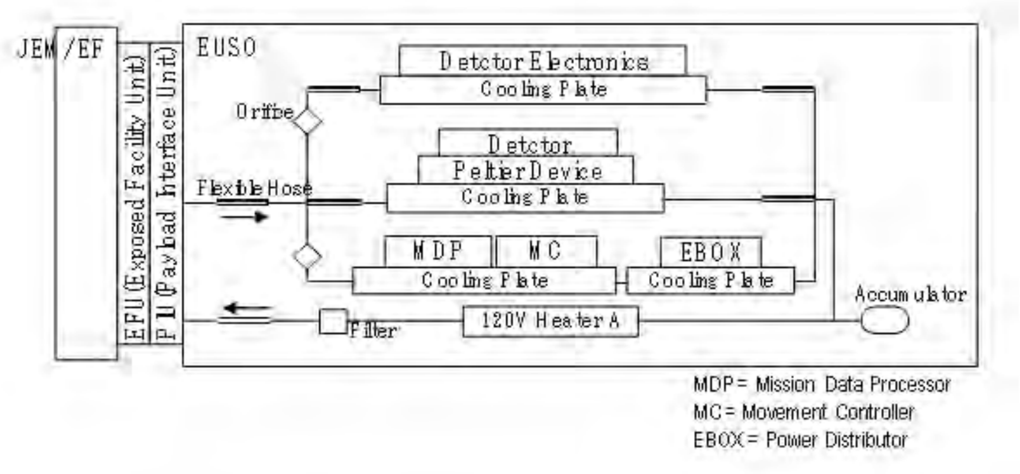

Figure 4.7.4.1-1. *ATCS block diagram [80].*

The devices requiring the Survival heaters are only atmospheric monitor, calibration system, and attitude sensors, which are cooled by PTCS. Then we estimate that these Survival heaters can satisfy the restriction of less than 100 W.

External surface of the cylinder structure of the telescope and the lid are thermally insulated by multi-layered insulation (MLI) material (PTCS). PIU cover is the cover which is used to insulate thermally PIU part during the launch phase.

4.7.4.2. Thermal analysis

The analysis was done for two cases: using MAPMT as a detector, and SiPM as a detector.

We understood that, in case of the MAPMT detector, a special cooling device was not necessary because it satisfied the temperature requirements, even if the energy consumption of PDM influenced the rise of the temperature of the focal surface detector.

As for the SiPM detector, if we succeed in making a design which insulates the sensor surface from the heated MLI, we estimate that the necessary quantity of the heat dissipation will be maximum around 50 W with the lid, and around 300 W without the lid (details in Annex).

4.7.5. Interface

4.7.5.1. Definition

JEM-EUSO bus system part has external interfaces to each part of JEM system, JEM operational control system/JEM experiment operation system, HTV un-pressurized carrier, JEMRMS (JEM remote manipulator system). Meanwhile, JEM-EUSO system part has internal interfaces to mission equipments in JEM-EUSO system, JEM-EUSO sensors, and so on.

4.7.5.2. External interface

JEM-EUSO bus system part has electrical, mechanical, thermal and electromagnetic interfaces to HTV un-pressurized carrier, JEM exposed facility and JEMRMS. The system part also has logical interfaces to JEM pressurized module/JEM inter-orbit communication system and JEM operational control system/JEM experiment operation system. Interfaces between JEM-EUSO bus system and each part/system are shown in Table 4.7.5.2-1.

Table 4.7.5.2-1. *External interfaces between JEM-EUSO bus system part and each part/system.*

	Electrical I/F	**Mechanical I/F**	**Thermal I/F**	**Elec.Magn. I/F**	**Logi.cal I/F**
HTV un-pressurized carrier	O	O	O	N/A	N/A
JEM exposed facility	O	O	O	O	N/A
JEMRMS	N/A	O	O	O	N/A
JEM pressurized module / JEM inter-orbit com.sys.	N/A	N/A	N/A	N/A	O
JEM operational cntl.sys. / JEM experiment oper.sys.	N/A	N/A	N/A	N/A	O
Legenda. O: interface exists; N/A: not applicable					

4.7.5.3. Internal interface

JEM-EUSO bus system part is interfaced with various equipments as shown in Figure 4.7.3-1. In addition, the following Table 4.7.5.3-1 shows the interface conditions for the major components (mechanics, power supply, communication, heat, etc.).

Table 4.7.5.3-1. *Internal interface conditions between JEM-EUSO and bus equipment*

Mission devices			Comments	Mechanical			Electric Power		Telemetry		Thermal		FoV	Others
				Dimension [mm]	Mass [kg]	Mechanical I/F	Power [W]	Voltage [V]	Telemetry speed [kbps]	No. channels Kind of signal	Thermal requirement [°C]	Thermal I/F	Temper. [deg]	
Optics	1st (front) lens		Lateral cut Cylinder Fig.4.7.1.2-1 Fig.4.7.1.2-2 Fig.4.7.1.2-3	2650x1900x15	173 (150)*	Fixed by lens frame. Frame is fixed by Ring.	--	--	--	--	In operating mode:T_0±10, $-30<T_0<+30$ In non-operating mode: -45~+55	Conductive heat transfer to/from lens frame. Radiation heat transfer to/from inner wall & lens (Earth, albedo rad. when lid is open).	±30	Accuracy of lens installation. Tab.4.7.6.1-1
	Iris			180x5	Included in lens frame								--	
	Precision Fresnel lens			2376x1900x10	55 (47)									
	2nd (rear) lens			2650x1900x15	166 (144)									
Atmosphere Monitoring	IR Camera			130x250x250 (TBC)	7 (5) TBC	Fixed by fastner to frame	11 (8) TBC	5 (TBC)	21 (16) TBC	TBD	-30~+60	Cooled by heat conduction to frame	±30	--
	Lidar	Laser unit etc.	Ryken type	450x350x250 (TBC)	22 (17) TBC		91 (70) TBC	28 (TBC)	4 (3) TBC	TBD			±15	--
		Power Sup.												
Calibration	Calibration device	LED light source	1xFocalSurface 6xRear lens	30Øx50x7pc. (TBC)	10 (7) TBC	Fixed by fastner to frame	11 (8) TBC	5 (TBC)	8 (6) TBC	TBD	TBD	Cooled by heat conduction to frame	--	--
		YAP pulser	137xFocalSurf.	5Øx1x137sheet (TBC)	1 (1) TBC	Sticked to each PMT						None		
Support Sensor	Attitude sensor VSG (Visual Star Camera) & RLG (Ring Laser Gyroscope)	VSC & Baffle	[MAXI] compatible JKX-99017 for VSC. NASDA-ESPC-3055 for RLG.	VSC=90x75x65 Bf=150x133x230 (TBC)	1 (TBC)	Fixed by fastner to Cold Plate	7.5 (TBC)	28 (TBC)	TBD	TBD	-40~+35 (TBC)	Cooled by cold plate for detector	18.4x13.4	VSC precision: <0.05° (TBC)
		VSC Electronics		110x110x176 (TBC)	1.2 (TBC)						-20~+70 (TBC)			
		RLG		250Øx180	5 (TBC)	Fixed by fastner to frame	35 (TBC)	TBD	TBD	TBD	TBD	TBD	--	RLG total error <0.04°
	GPS	Antenna	MAXI] comptible NASDA-ESPC-	40x50x15	0.1	Fixed by fastner to frame	2	5 (TBC)	TBD	TBD	-30~+60	None	--	GPS precision. <1μs (TBC)
		Electronics		70x50x40	0.3		0.3							
Electronics Circuit	Mission Data Processor	MDP	2 sets (1set=redundancy)	300x300x400 (TBC)	Board+ Cable: 105+112 (91+86) PMT: 159 (138) (TBC)	Fixed by fastner to Cold Plate	2 (1) (TBC)	5V x 2ch	Science Data: 233 (202) TBC Mission HK: 8 (6) TBC	Telemetry to/from EBOX via MDP: Discrete command x1ch (TBC) Serial magnitude command x1ch (TBC) Serial digital telemetry x1ch (TBC) Fig.4.7.3-1	Electronic devices: In operating mode: -10~+50 In non-operating mode: -30~+50 PDM: In operating mode: T_0±10, $0<T_0<+20$ In non-operating mode: -30~+50	Cooled by cold plate for MDP.	--	--
	Focal Surface Electronics & Detector	CCB (Cluster Control Board)	19 sets (TBC)	162x162x20 (TBC)		PDM are fixed by fastner to Support Frame or Cold Plate	17 (13) TBC	(5V+28V) x20ch (TBC)				Cooled by cold plate for detector		
		PDM (PMT, FEE, PDMCB)	137 sets (TBC) Fig.4.3.2.5-1	FS total: 2379x1900 PDM: 162x162x200 (TBC)			PDM: 311 (239) HV:94 (72) Converter Loss: 94 (72)							

4.7.6. Summary

4.7.6.1. Specifications

Table 4.7.6.1-1. *System requirements*

Item	Required value	Note
Enclosure structure	Primary natural frequency: more than 2 Hz (observation mode); more than 25 Hz (at launch). Performance of the light shielding: less than 1 GHz on the whole focal surface. Insulation performance: I/R emittance < 0.05	Protection of the instrument from the potential dangerous environmental elements [82] is required.
Opening and closing of the lid	Frequency: twice/orbit (90 minutes). Duration: less than 5 minutes. Endurance: more than 5 years, more than 30,000 times of opening and closing.	Redundancy in actuator electronic circuit is required.
Expansion mechanism	Stowing mode in HTV: should be settled in HTV envelope. Should not have a physical interference except with EFU#4, when placed in EFU#2 or EFU#9 of JEM-EF. Should be able to change repeatedly between stowing mode and observation mode during the mission.	HTV envelope: report about the results of the study of collateral conditions. Should be able to be expanded for the observation mode on JEM-EF.
Tilt mechanism	30° ~ 45°	Operating once every 6 months, approximately 10 times during the entire mission.
Focus adjustment mechanism	Moving range and step range of the optical system. Range: more than ±12.5 mm. Step: less tan 1.25 mm.	From ESA-EUSO study [83]
Accuracy of the installation of the lenses	Coaxial tolerance: within ±2.5 mm. Parallel Tolerance: within ±2.5 mrad. Accuracy of the position: within ±2.5 mm.	

Table 4.7.6.1-2. *System technical readiness levels.*

Item	**Technical Readiness Level (TRL) and its reason when selected in Febr.'07**	**Verification status of TRL and reason (as of Apr.'08)**	**Expected TRL and activities at SDR time (Mar.'09)**
Enclosure structure	TRL3 Structural analysis was done in ESA-EUSO Phase A [84].	TRL3 Perform a modal and structural analysis by means of FEM, then verify the concept design.	TRL3 Perform more detailed modelling of the expansion mast and others and to be verified by modal and structural analysis by means of FEM.
Lid	TRL3 Soft sail/sandwich panel, as in ESA-EUSO Phase A [84].	TRL3 Perform concept design by simple analysis and verify the endurance. Estimated weight 14.1 kg, driving power 3.4 W.	TRL4 Perform an inspection test of the function by means of the BB model of opening-closing mechanism, and verify basic functions.
Expansion mechanism	TRL3 Stowing capability in HTV was verified, concept of truss expansion mechanism.	TRL3 Verification of basic functions and estimation of weight (80 kg), doing analysis of the vibration and the structure of the JEM-EUSO concept design, which has 4 expanding masts in HTV.	TRL4 Perform quantitative evaluation of the weights, resistance, etc. of expanding masts and other expansion systems by a simulation, and then select an expansion system.
Tilt mechanism		TRL3 Perform the concept design of the tilt mechanism and estimate the weight (40 kg).	TRL3 Perform analysis of vibration and structure of the basic design, and verify functions.
Focusing length adjustment mechanism		TRL3 Redo the concept design of the adjusting mechanism and estimate the weight (20 kg).	TRL3 Perform analysis of vibration and structure of the basic design, and verify functions.
Heat control	TRL3 Heat analysis by means of a simple model was done during ESA-EUSO Phase A [85, 86].	TRL3 Analyze temperatures of lenses, focal surface, etc., by a simple model, then, Verify the in-plane distribution (4.5 °C) , which satisfies the required temperature, and estimate the quantity of heat discharge (without lid 300 W).	Verify the particularities, doing analysis of the heat by means of the detailed mathematical model of focal surface detector module.
System electronics		TRL3 Concept design on the move.	TRL4 Design the part regarding the interface with JEM/EF and do its BB model test.

Table 4.7.6.1-3. *System main pieces.*

Main system	**Related pieces**
Structure	Enclosure structure
	Lid
	Expansion mechanism (ring, expansion mast)
	Focus adjustment mechanism
	Lens frame
	Focal surface supporting structure
Temperature	ATCS system
Electricity	Power distributor
	Harness

IHI will be in charge of arrangement and procurement.

Table 4.7.6.1-4. *System temperature requirements.*

Item	**Operation temperature**	**Non-Operation temperature**
Fresnel lenses	T_0±10°C (-30°C < T_0 < +30°)	-45°C ~+50 °C
Focal surface	T_0±10°C (0°C < T_0 < +20°)	-30°C ~+50 °C (*)
System electronics circuit & battery	-10°C ~+50 °C	-30°C ~+50 °C
Atmospheric monitor	-30°C ~+60 °C (TBC)	-30°C ~+60 °C (TBC)

(*) from ESA-EUSO [87]

Table 4.7.6.1-5. *System HK requirements. (TBD)*

Table 4.7.6.1-6. *System mass budget.*

The column of margin in the table indicates the uncertainty of the BEE.
If the uncertainty is relatively large: 30%, small: 15%, no uncertainty: 0%.

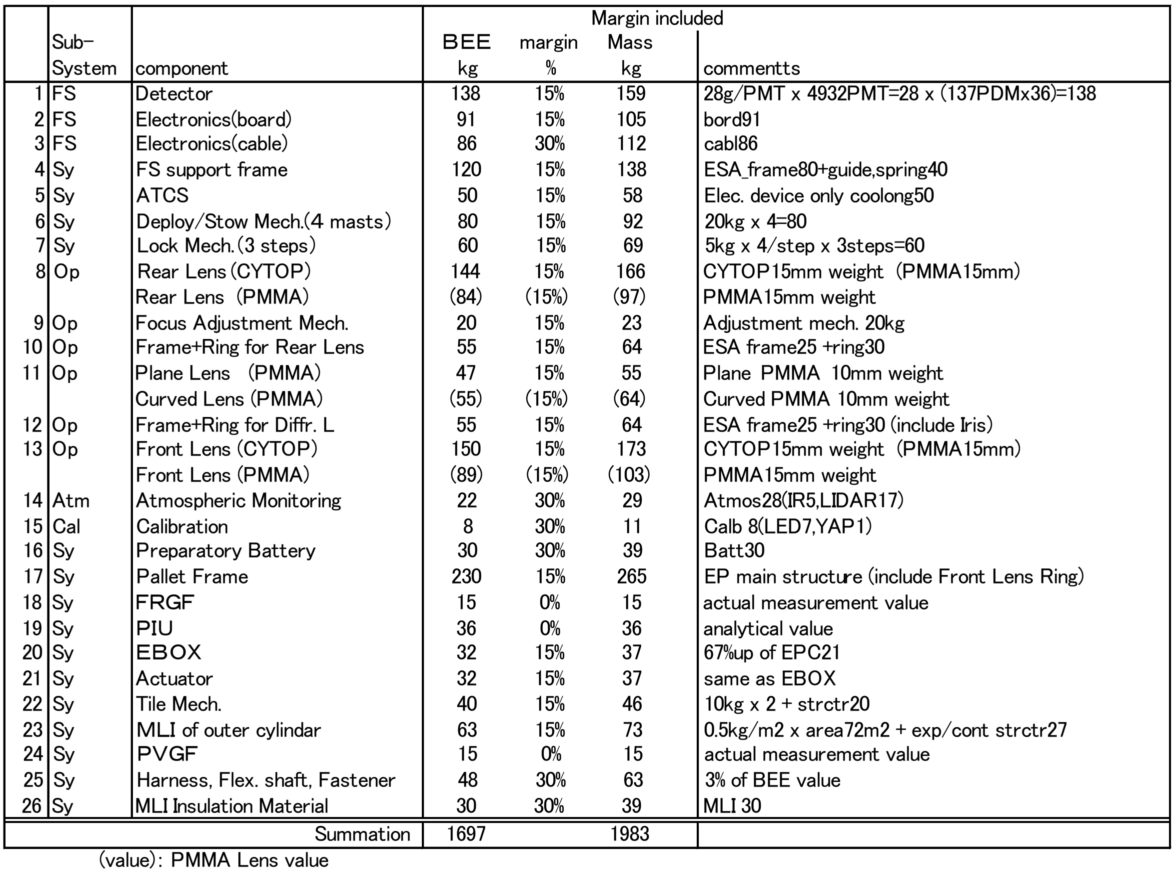

	Sub-System	component	BEE kg	margin %	Margin included Mass kg	commentts
1	FS	Detector	138	15%	159	28g/PMT x 4932PMT=28 x (137PDMx36)=138
2	FS	Electronics(board)	91	15%	105	bord91
3	FS	Electronics(cable)	86	30%	112	cabl86
4	Sy	FS support frame	120	15%	138	ESA_frame80+guide,spring40
5	Sy	ATCS	50	15%	58	Elec. device only coolong50
6	Sy	Deploy/Stow Mech.(4 masts)	80	15%	92	20kg x 4=80
7	Sy	Lock Mech.(3 steps)	60	15%	69	5kg x 4/step x 3steps=60
8	Op	Rear Lens (CYTOP)	144	15%	166	CYTOP15mm weight (PMMA15mm)
		Rear Lens (PMMA)	(84)	(15%)	(97)	PMMA15mm weight
9	Op	Focus Adjustment Mech.	20	15%	23	Adjustment mech. 20kg
10	Op	Frame+Ring for Rear Lens	55	15%	64	ESA frame25 +ring30
11	Op	Plane Lens (PMMA)	47	15%	55	Plane PMMA 10mm weight
		Curved Lens (PMMA)	(55)	(15%)	(64)	Curved PMMA 10mm weight
12	Op	Frame+Ring for Diffr. L	55	15%	64	ESA frame25 +ring30 (include Iris)
13	Op	Front Lens (CYTOP)	150	15%	173	CYTOP15mm weight (PMMA15mm)
		Front Lens (PMMA)	(89)	(15%)	(103)	PMMA15mm weight
14	Atm	Atmospheric Monitoring	22	30%	29	Atmos28(IR5,LIDAR17)
15	Cal	Calibration	8	30%	11	Calb 8(LED7,YAP1)
16	Sy	Preparatory Battery	30	30%	39	Batt30
17	Sy	Pallet Frame	230	15%	265	EP main structure (include Front Lens Ring)
18	Sy	FRGF	15	0%	15	actual measurement value
19	Sy	PIU	36	0%	36	analytical value
20	Sy	EBOX	32	15%	37	67%up of EPC21
21	Sy	Actuator	32	15%	37	same as EBOX
22	Sy	Tile Mech.	40	15%	46	10kg x 2 + strctr20
23	Sy	MLI of outer cylindar	63	15%	73	0.5kg/m2 x area72m2 + exp/cont strctr27
24	Sy	PVGF	15	0%	15	actual measurement value
25	Sy	Harness, Flex. shaft, Fastener	48	30%	63	3% of BEE value
26	Sy	MLI Insulation Material	30	30%	39	MLI 30
		Summation	1697		1983	

(value): PMMA Lens value

Note: By redesigning optics, we found that by using PMMA as material for lens, we could reach almost the same ability of CYTOP optics. Numbers in parentheses refer to the cases of PMMA. Gross weight with PMMA is 1584 kg (BEE) and 1853 kg with margin.

Table 4.7.6.1-7. *System. Mass budget for each component.*

Component	**BEE [kg]**	**Margin [%]**	**Margin included Mass [kg]**
Optics	471	16	545
Focal Surface	315	19	376
Atmospheric Monitor	22	30	29
Calibration	83	30	11
Bus System	881	16	1022
Total	***1697***		***1983***

Table 4.7.6.1-8. *System. Electric power budget.*

	Sub-system	Component	During Scientific Observation			
			BEE [Watt]	**Margin [%]**	**Total [Watt]**	**Comments**
1	OP	Focus Adjustment mech.	0	15	0	
2	Sy	Bus EBOX	138	15	159	EBOX 50 W, Convert loss 83 W, Supply loss 5 W.
3	Sy	Movement Control (MC)	0	15	0	
4	FS	FS Electronics	498	30	648	Estimated power 518 W for M36PMT; by DCDC optimization, 518-20 = 498 W.0
5	Atm	Atmospheric Monitor	78	30	102	IR camera 20 W, Lidar 70 W
6	Cal	Calibration	8	30	11	
7	Sy	Attitude Sensor	5	15	6	Estimation from MAXI data
		Total	***727***		***926***	
	Sub-system	**Component**	**During Non-scientific Observation**			
			BEE [Watt]	**Margin [%]**	**Total [Watt]**	**Comments**
1	OP	Focus Adjustment mech.	10	15	12	
2	Sy	Bus EBOX	147	15	170	EBOX 40 W, Convert loss 101 W, Supply loss 6 W.
3	Sy	Movement Control (MC)	10	15	12	
4	FS	FS Electronics	77	30	101	
5	Atm	Atmospheric Monitor	39	30	51	
6	Cal	Calibration	0	30	0	
7	Sy	Attitude Sensor	5	15	6	
		Total	***288***		***352***	

Table 4.7.6.1-9. *System. Electric power budget for each component.*

Component	During Scientific Observation			During Non-scientific Observ.		
	BEE [Watt]	**Margin [%]**	**Total [Watt]**	**Margin [%]**	**BEE [Watt]**	**Total [Watt]**
Optics	0	15	0	10	15	12
Focal Surface	498	30	648	77	30	101
Atmospheric Monitor	78	30	102	39	30	51
Calibration	8	30	11	0	30	0
Bus System	143	15	165	162	16	188
Total	***727***		***926***	***288***		***352***

Table 4.7.6.1-10. *System. Telemetry budget.*

	Component	BEE [kbps]	Margin [%]	Total [kbps]	Comments
1	Scientific Data	202	15	233	Trigger rate 0.1 Hz
2	Mission HK	6	30	8	1200 data every 2 seconds
3	Atmosphere Monitoring	19	30	25	IR camera (16) + Lidar (3)
4	Calibration	6	30	8	ESA-EUSO estimation
5	Bus H&S	9	15	11	1000 data each second
	Total	***242***		***285***	

Table 4.7.6.1-11. *System. Telemetry budget for each component.*

Component	BEE [kbps]	Margin [%]	Total [kbps]
Focal Surface	202	15	233
Atmosphere Monitoring	19	30	25
Calibration	6	30	8
Bus H&S	15	27	19
Total	***242***		***285***

4.7.6.2. Cost

The cost of bus is not mentioned in this document because the estimation by the engineering company is not determined yet. For reference, the cost estimation of the whole bus system was around 3 billion Yen in 2007, one year ago.

4.7.6.3. Schedule

The schedule for bus system by the engineering company in charge is in Figure 4.7.6.3-1.

4.7.6.4. Organization

Basic specifications will be provided by the mission side. Based on this, the engineering company, which is under contract to JAXA, will promote system development by cooperating closely with mission side.

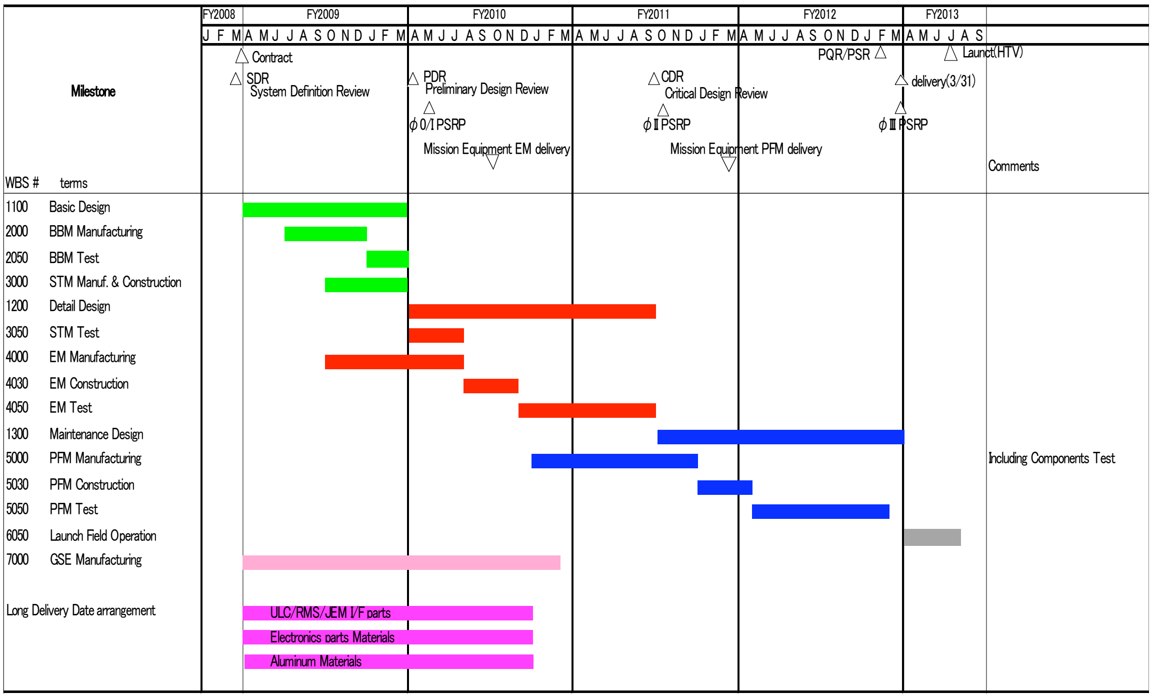

Figure 4.7.6.3-1. *System development schedule [80].*

5. Expected Performance

5.1. The End-to-End Simulation

In JEM-EUSO, a higher performance compared to ESA-EUSO (min) will be accomplished through improvements in both hardware and software, like new lens material, an advanced optical design, a focal surface device with a high quantum efficiency and a more efficient triggering algorithm.

The End-to-End simulation code has been developed considering hardware characteristics of the JEM-EUSO optical system, the focal surface detector and the output signal control circuit. Pseudo-observational data has been generated by executing the code for various EAS longitudinal developments pooled in the EAS database.

The accuracies of cosmic ray energy, arrival direction and longitudinal development can be estimated by reconstructing EAS profiles with the most suitable algorithm; the End-to-End simulation code is also used for successive improvements of the hardware system to upgrade their accuracies.

To progress of scientific researches, JEM-EUSO has set requirements for experimental accuracies as:

- expected number of events: more than 1000 events with energies above 7×10^{19} eV;
- threshold energy: 5×10^{19} eV;
- angular resolution: < 2.5°;
- energy resolution: < 30%;
- $X_{\max}$ resolution: < 120 g/cm^2.

The simulation code consists of three components: EAS generation, telescope simulation and EAS event reconstruction parts.

EAS generation code generates EAS longitudinal profile in atmosphere initiated by assumed chemical compositions for zenith angle of 0°÷90° and energy greater than $10^{18.5}$ eV. Air fluorescence and Cherenkov light emissions are also calculated taking into account their yields, absorption and scattering in atmosphere, and then the characteristics of the photons (wavelength, arrival time and spatial position of emission) on the optical lens of the telescope are evaluated.

In the telescope simulation code, characteristics of hardware responses to incident photons, photoelectrons and analogue/digital signals have been taken into account. Hardware performance on optical system, focal surface detector and output signal control circuit has been estimated. Finally pseudo-observational data including overall hardware responses will be generated.

In addition, EAS event reconstruction code determines EAS energy, arrival direction and longitudinal development from simulated pseudo-observational data produced by former two processes, and is used for evaluating their accuracies. This code also contributes as a feedback for the studies related to the development of analytical algorithms and hardware improvements aiming at the excellent telescope's capability with the best accuracies.

The scheme of the current End-to-End simulation chain is shown in Figure 5.1-1.

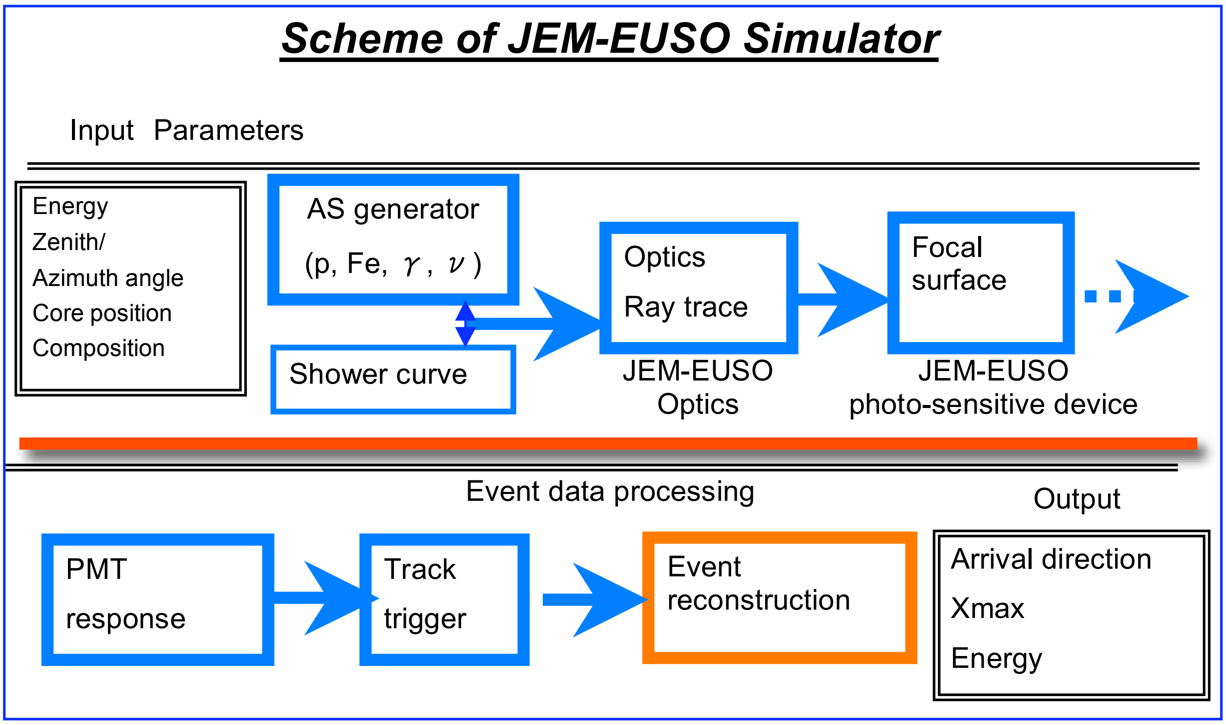

Figure 5.1-1. *Schematic view of the JEM-EUSO End-to-End simulation chain.*

5.2. Baseline Estimation

Taking into account the hardware improvements performed till now (December 2008) during the Phase-A study of the mission, we have set the following assumptions and conditions in the End-to End simulation chain to obtain the baseline estimation of the JEM-EUSO performance:

- Optics system: lenses 2.65 m diameter, side-cut; first and third lens: CYTOP; second lens: PMMA000;
- FS detector: array of ultra bialkali MAPMTs (6×6 pixels each);
- Time resolution (GTU): 2.5 μs;
- Track trigger method as event trigger;
- Standard background: 500 photons/(m^2 sr ns);
- EAS events with Cherenkov mark (golden events).

5.2.1. Effective acceptance

JEM-EUSO telescope will be installed at the external platform of the Japan Experiment Module (JEM) of the International Space Station, and will orbit around the Earth at a level of 430km (average) with a period of 90 minutes. EAS observation will be carried out in the Earth night-time, then a minimum duty cycle of 19% was estimated after taking into account the passage in a region of high background light intensity and actual data deficit ratio of EASs with a zenith angle less than 45° due to incomplete EAS reconstruction by a cloud shielding.

Observational acceptance of JEM-EUSO for EAS events depends on the primary EECR energy and arrival direction. Acceptance reaches the maximum value at a zenith angle of ~45° as a result of a larger integrated solid angle in azimuth and a smaller effective area projected on the perpendicular plane to the EAS axis with an increasing zenith angle.

Geometrical acceptance is expected as 5.2×10^5 km^2 sr with field of view ±30° . A time integrated acceptance could be 1.7×10^6 km^2 sr year, assuming a duty cycle of 19% and (2+3) years observations in (nadir and tilted mode). This is just 1060 times and 25 times larger than those of 10 years observation of AGASA and Pierre Auger ground-based observatories, respectively. In an actual observation, there will be untriggered events, events without Cherenkov mark in the field of view, and also missing events by incomplete reconstruction due to the small number of incident photons.

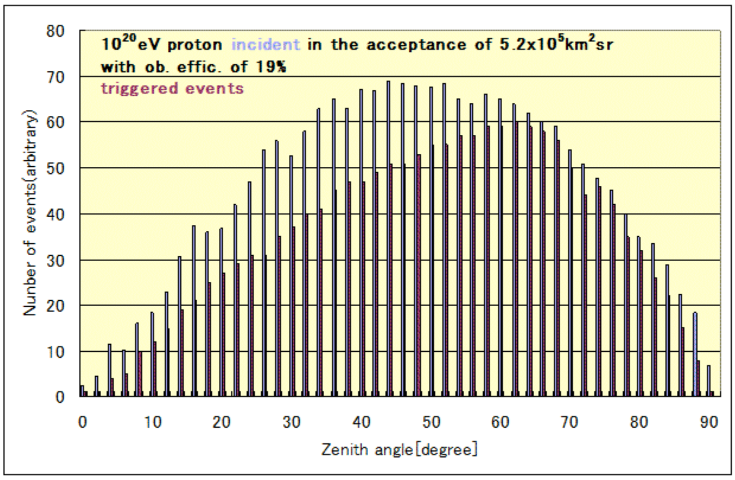

Figure 5.2.1-1. *Zenith angle dependence of the JEM-EUSO acceptance.*

In Figure 5.2.1-1, acceptance for EAS initiated by proton with energy 10^{20} eV is shown as a function of the zenith angle. A case of clear sky was assumed here. Acceptance for golden EASs with enough accuracy is also obtained to be 5.2×10^5 km^2 sr.

In the case of JEM-EUSO tilted mode observation, a larger volume of target atmosphere to observe EAS could be achieved (Fig.5.2.1-2, left); the field of view increases with the tilt angle, as shown in Figure 5.2.1-2, right.

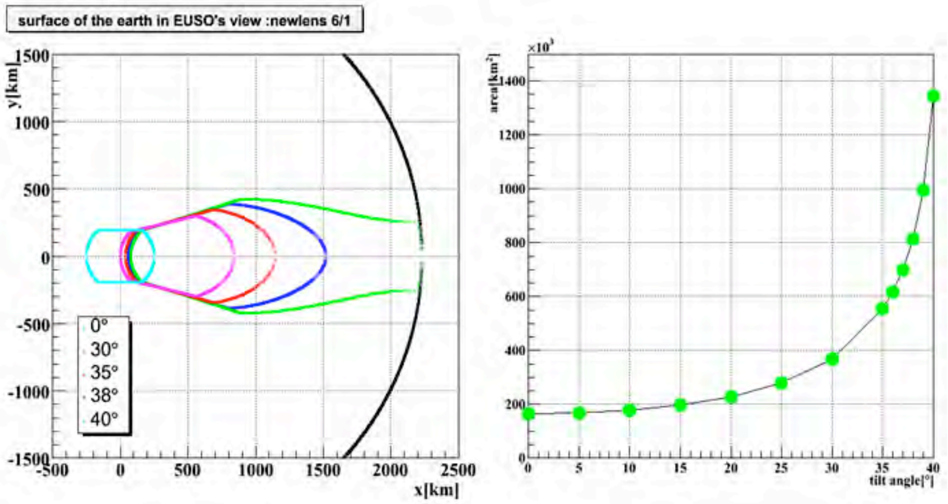

Figure 5.2.1-2. *The JEM-EUSO field of view at different tilt angles; shape (left) and area (right).*

5.2.2. Trigger efficiency

In JEM-EUSO, air fluorescence light from EAS has to be observed in a background light emitted from ground and airglow sources. Therefore, optimized EAS triggering method will be required to acquire the EAS events efficiently with the best S/N avoiding fake triggers.

Figure 5.2.2-1 shows the energy dependence of the JEM-EUSO trigger efficiency with an assumption of background light intensity of 500 photons/m^2/sr/ns. Track trigger method has been applied to the individual time profile of photo-electrons from MAPMT. The trigger efficiency for tilt mode observations with tilt angle of 30°, 35° and 38° is also shown.

The trigger efficiency at 10^{20} eV is 86% for nadir mode observation, and EAS threshold energy is estimated to be 5.0×10^{19} eV at 50% detection efficiency level. In addition, the trigger efficiency curve of EAS hit within a radius of 100 km in the field of view (red squares) shows how the threshold energy becomes lower than 2.7×10^{19} eV because of a better performance of optical system and smaller impact parameters.

The remaining three lines in Fig.5.2.2-1 show the trigger efficiency in case of tilted mode observations with different tilt angles. Although the threshold energy increases due to a longer distance from the EAS axis to JEM-EUSO, the increase of acceptance by tilt mode observation has an important advantage over it.

In Fig.5.2.2-2 the energy dependence of the effective acceptance with a combination of trigger efficiencies and an increase of field of view is shown. Relative advantage of tilt mode observation could be seen as 1.8 times and 2.4 times larger effective acceptance at 10^{20} eV and $10^{20.5}$ eV, respectively, than the nadir mode observation.

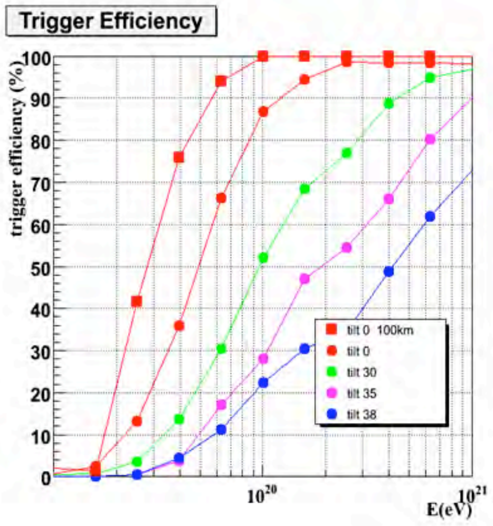

Figure 5.2.2-1. *The energy dependence of the trigger efficiency at different tilt angles.*

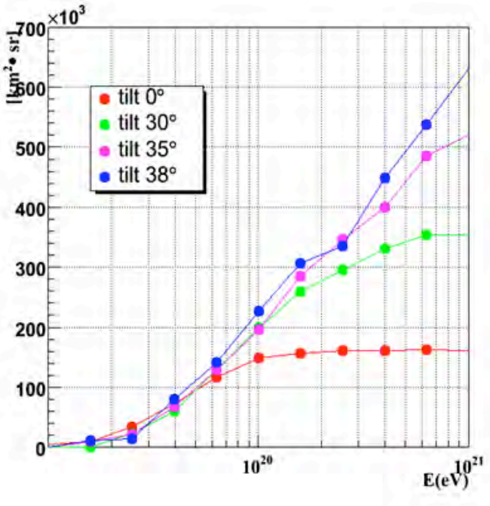

Figure 5.2.2-2. *The JEM-EUSO effective acceptance as function of energy and tilt angle.*

5.2.3. Expected number of triggered events

In JEM-EUSO, it is possible to estimate the expected number of triggered EAS events by taking into account primary cosmic ray energy spectra, geometrical acceptance (5.2×10^5 km^2 sr), a duty cycle of 19% and the trigger efficiency which depends on energy and zenith angle.

The expected number of triggered events is shown as the integrated numbers at any energies in Table 5.2.3-1. The expected number of events with energy > 7×10^{19} eV and > 10^{20} eV is almost

490/year and 64/year by JEM-EUSO, respectively, if the energy spectrum is assumed as a flux $J(E)E^3$ of 2.0×10^{24} [$eV^2\ m^{-2}\ s^{-1}\ sr^{-1}$] at 2×10^{20} eV and GZK cutoff in the spectrum.

A study in lower energy region is also important for what concerns the cross calibration with the Pierre Auger Observatory results and for a study of anisotropy with the highest statistics. JEM-EUSO has potential to study EAS around 3×10^{19} eV with more than 1000 events per year.

Table 5.2.3-1. *Expected number of JEM-EUSO trigerred events in 1 year.*

At energy >Log(E)	Nadir	Tilt angle 30°	Tilt angle 35°	Tilt angle 38°
19.7	1140	1200	1350	2080
19.8	490	560	680	1060
20.0	64	75	95	110
20.2	12	17	21	28
20.4	5.0	8.5	10	13
20.6	2.0	3.9	4.6	6.0
20.8	0.8	1.5	2.0	2.4
21.0	0.2	0.4	0.4	0.6

Moreover, the tilt mode observation with tilt angles of 30°, 35° and 38° can increase the statistics as shown in Table 5.2.3-1. About 110 events with energy > 10^{20} eV can be expected in the observation with a tilt angle of 38°. We plan two years in nadir mode and three years in tilt mode observation, then the expected numbers will be 1800 and 450 events for energies greater than 7×10^{19} eV and 10^{20} eV, respectively, in the planned period. Furthermore, 25 events with energy above $10^{20.5}$ eV will be expected by JEM-EUSO with a reality of the highest energy study.

5.2.4. Angular resolution

Arrival direction of triggered EAS is determined by reconstructing the length of the EAS image and its spatial position in atmosphere from the recorded photoelectron position and time transition in the focal surface coordinates. Image length changes depending on energy and zenith angle. A distortion in the EAS image by background photons affects the accuracy of the EAS axis reconstruction.

The angular resolution for triggered EAS events has been estimated with the assumption of 500 photons/($m^2\cdot sr\cdot ns$) as standard background photons. The angular resolution for proton-induced EAS of $10^{19.5}$ eV, 10^{20} eV, $10^{20.5}$ eV and 10^{21} eV is shown in Fig.5.2.4-1 as a function of zenith angles. Left and right panels show the resolution for EAS hitting within a radius of 200 km and 100 km in the JEM-EUSO field of view, respectively. The angular resolution becomes better for larger zenith angles because of a longer EAS image at the focal surface, and the requirement value of < 2.5° in angular resolution is satisfied above 45° zenith angle . Resolution of 1.0° can be estimated for EAS of energy greater than 10^{20} eV and zenith angle above 60º and it is enough resolution for the study of cosmic ray origin.

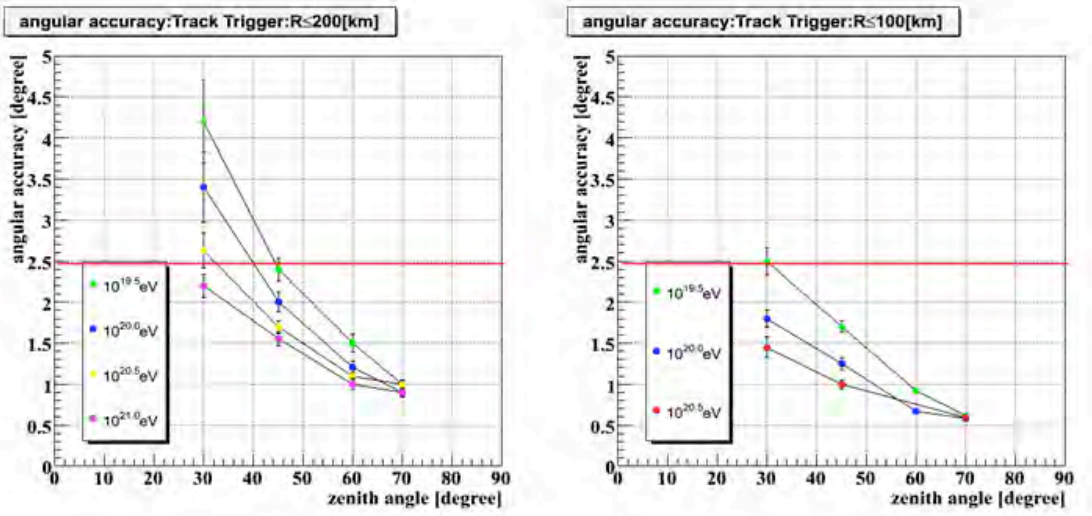

Figure 5.2.4-1. *Angular resolution as function of energy and zenith angle for events triggered within a region of 200 km (left) and 100 km (right) radius, centered in the JEM-EUSO field of view. Red line indicates the limit of 2.5°, requirement for the angular resolution.*

5.2.5. X_{max} resolution

After the determination of the EAS axis, the primary energy and the EAS $X_{\max}$ are obtained from the reconstructed longitudinal development estimated from produced photon numbers and fluorescence light yield at any position along the shower axis. The $X_{\max}$ resolution for proton-induced EAS of $10^{19.5}$ eV, 10^{20} eV, $10^{20.5}$ eV and 10^{21} eV is shown as a function of zenith angles in Fig.5.2.5-1. Left and right panels refer to EAS hitting within a radius of 200 km and 100 km in the JEM-EUSO field of view, respectively. The X_{max} resolution does not depend on zenith angles and values of 100 ÷ 200 g/cm^2 are estimated within a radius of 200 km in the field of view.

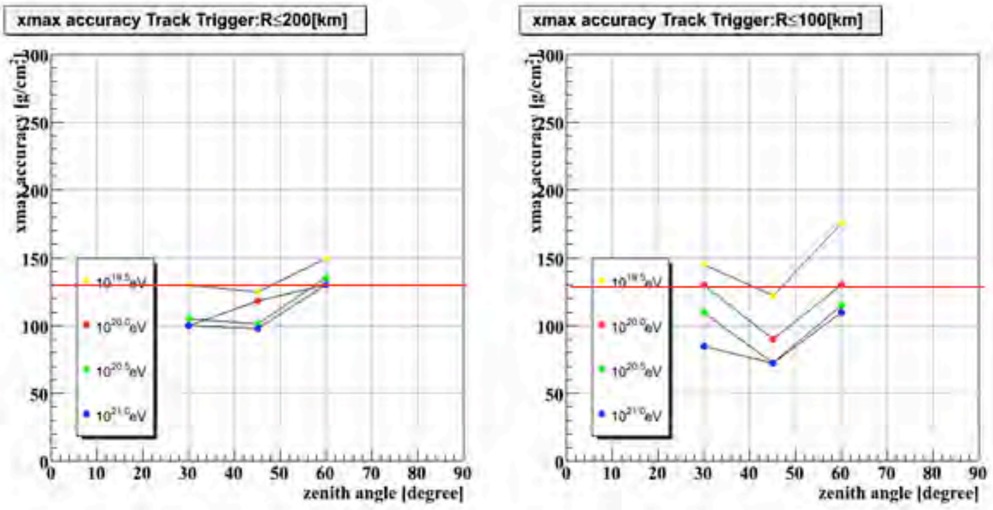

Figure 5.2.5-1. *The X_{max} resolution as function of energy and zenith angle for events triggered within a region of 200 km (left) and 100 km (right) radius, centered in the JEM-EUSO field of view. Red line indicates the limit of 120 g/cm^2, requirement for the X_{max} resolution.*

5.2.6. Energy resolution

Energy determination has been estimated by the reconstructed longitudinal structure. The energy resolution for EAS of $10^{19.5}$ eV, 10^{20} eV, $10^{20.5}$ eV and 10^{21} eV is shown in Fig.5.2.6-1 as a function of zenith angles. Left and right figures show the case of EAS hitting within a radius of 200 km and 100 km in the JEM-EUSO field of view, respectively. The energy resolution becomes better (<30 %) for EAS with zenith angle above 45°, and accuracy of 15% could be expected for EAS of more than 10^{20} eV in a radius of 100 km.

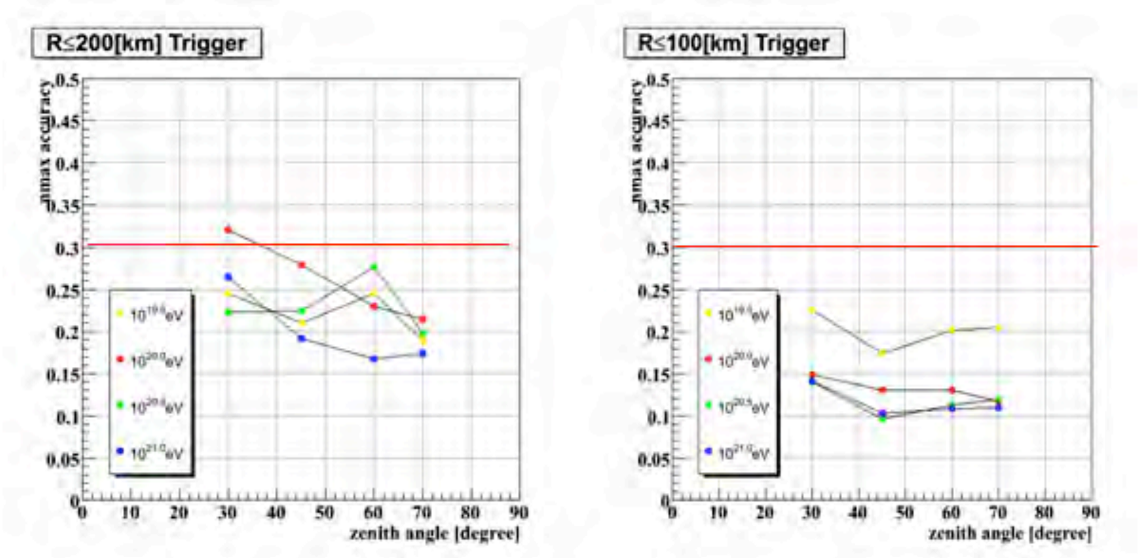

Figure 5.2.6-1. *The energy resolution as function of energy and zenith angle for events triggered within a region of 200 km (left) and 100 km (right) radius, centered in the JEM-EUSO field of view. Red line indicates the limit of 30%, requirement for the energy resolution.*

5.2.7. Detection sensitivity for UHE neutrinos

JEM-EUSO with a field of view of ±30° will cover the atmospheric mass of 2×10^{15} kg as a target matter for incident neutrinos. Observational targets will be the electromagnetic and hadronic EASs induced by an inelastic interaction between neutrino (i.e. electron, muon and tau neutrino) and atmospheric nucleus. For the detection of a neutrino-induced EAS, a rejection power greater than 10^{-4} is required to discriminate candidates from usual EASs of energy greater than $10^{19.5}$ eV accumulated with a rate of 6,300 events/year.

Neutrino-induced EASs are expected to develop at lower altitudes compared to those of proton/nucleus-induced EASs with same zenith angles because of the smaller interaction cross-section. Therefore, $X_{\max}$ is the most suitable observable to discriminate the neutrino-induced EAS candidates from the standard ones.

The $X_{\max}$ distribution of neutrino-induced EASs is shown in Figure 5.2.7-1 in case of 1×10^7 neutrinos of 10^{20} eV incident to the JEM-EUSO target volume of atmosphere with zenith angle in the full range 0÷95°. The generation probability of neutrino-induced EAS is 0.009% with energy dependence. Its distribution is almost uniform in the area of the target volume. On the other hand, proton-induced EASs of $10^{19.5}$ eV show a distribution with an average $X_{\max}$ of 810 g/cm^2 with 60 g/cm^2 in 1σ standard deviation as shown by the yellow region in the same Fig.5.2.7-1.

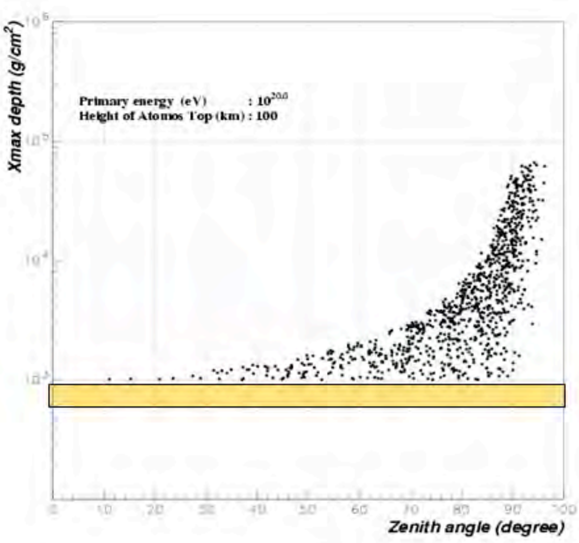

Figure 5.2.7-1. *The X_{max} distribution of neutrino-induced EASs in the JEM-EUSO target volume.*

Neutrino-induced EASs can be observed preferably if they are largely inclined because of a longer interaction mean free path, but they will be candidates in which the Cherenkov mark will not be observed. In addition of events with no Cherenkov mark due to the presence of clouds, the width of EAS profile (time duration) for different zenith angles is useful for the estimation of X_{max} as the autonomous method. Assuming a neutrino intensity of 1/km^2/day above 10^{19} eV and an effective acceptance of $2\pi \times 2\times10^{15}$ kg sr, the number of incident neutrinos in the JEM-EUSO target volume is estimated to be 2×10^4 per year. After taking into account the interaction probabilities of neutrinos and trigger efficiency for neutrino-induced EASs, the related X_{max} are calculated. In the case of X_{max} above 1,400 g/cm^2 for a rejection of background EASs, 2.1 neutrino-induced EASs per year are detectable by JEM-EUSO observation.

Figure 5.2.7-2 shows the detection sensitivity of JEM-EUSO (under nadir and tilt observation mode, blue and green line, respectively) in neutrino intensities. Expected fluxes of neutrinos from Z-burst model, GZK neutrinos, AGN origin and some top-down processes are also shown.

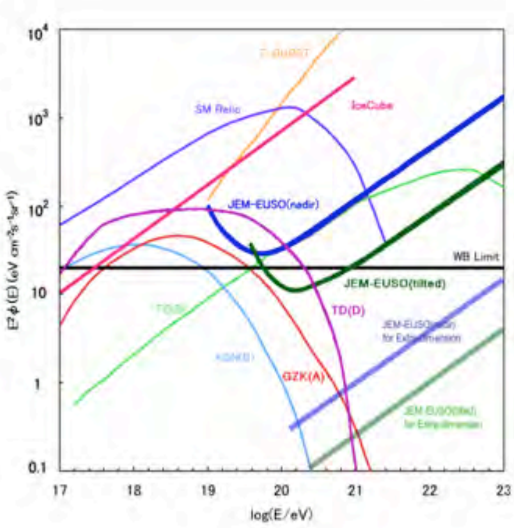

Figure 5.2.7-2. *The expected neutrino intensity under some model, and JEM-EUSO sensitivity to UHE neutrinos.*

5.2.8. Comparison with other experiments

The Pierre Auger Observatory in Argentina (southern hemisphere) covers an acceptance of 7×10^3 km^2 sr corresponding to 44 times AGASA extension; the Telescope Array experiment in Utah, USA, has observed with a surface detector (SD) acceptance of 1.4×10^3 km^2 sr. The acceptance of JEM-EUSO will be 5.2×10^5 km^2 sr, which is just 74 and 370 times larger than those of Auger and Telescope Array experiment, respectively, as listed in Table 5.2.8-1. The integrated exposure of JEM-EUSO is estimated as 1.7×10^6 km^2 sr year by 2 years nadir and 3 years tilt mode observation with a duty cycle of 19%. This exposure is comparable to 25 times of Auger and 85 times of Telescope Array hybrid observation for 10 years.

The number of events for EAS $>10^{20}$ eV observed by the Auger experiment is expected as 3/year assuming “GZK” energy spectrum. In case of JEM-EUSO (nadir mode), the statistics will be more than 18 times of Auger due to a larger integrated acceptance. Consequently JEM-EUSO will show much higher advantage in performing astrophysical studies by means of super GZK energy cosmic rays.

Though the Auger Observatory will accomplish a hybrid observation by surface detectors (SD) and air fluorescent telescopes (FD), the combined observational efficiency does not exceed ~10%. JEM-EUSO has an advantage in the EAS statistics exceeding by far that of Auger, therefore, much higher accuracy is expected from JEM-EUSO observation. Moreover, detection of neutrinos in this energy region will be a promising research task for JEM-EUSO thanks to the large acceptance which counterbalances the small interaction cross-section of neutrino.

Table 5.2.8-1. *Comparison between JEM-EUSO and other EECR observatories.*

Experiment / Observatory	Acceptance [km^2 sr]	Operational Year	Period [#years]	Observat. Efficiency [%]	Exposure [km^2 sr year]	Relative exposure to AGASA	Relative exposure to Auger South
AGASA	160	Stop	13	100	1.6×10^3	1	0.02
Auger South SD	7,000	2006-2015	10	100	7.0×10^4	44	1
Telescope Array							
SD	1,400	2006-2015	10	100	1.4×10^4	9	0.2
FD	6,700		10	10	6.7×10^3	4	0.1
Hybrid	1,400		10	10	6.7×10^3	4	0.1
Total					2.0×10^4	13	0.3
TUS	30,000	2009-2014	5	20	3.0×10^4	20	0.5
JEM-EUSO							
Nadir	520,000	2013-2014	2	19	2.1×10^5	130	3
Tilt	2,580,000	2015-2017	3	19	1.5×10^6	940	21
Total					1.7×10^6	1,060	25

5.3. Advanced Estimation

5.3.1. Reconstruction of observed events in cloudy sky

The expected cloud coverage will be nearly 30% in the field of view of JEM-EUSO. In this case, the EAS Cherenkov mark cannot be observed, and the shower profile under the cloud will not be measured. The average height of clouds is generally lower (around 4,000 m) in night-time than in daytime. Therefore, shower profiles with $X_{\max}$ will possible be reconstructed for EASs with zenith angle greater than 60°. With data of Cherenkov mark at the cloud, $X_{\max}$ can be estimated by the shape method. This method is used for the characteristic which the time width of shower profile is related to the height of $X_{\max}$. This method has already been studied in the Phase-A study of ESA-EUSO, and the accuracy of $X_{\max}$ determination was estimated to be 120 g/cm^2. This provides us a reliable analysis even for data taken in the cloudy sky and the observation efficiency will be increased by 20% larger than that in the observation under the clear sky.

5.3.2. Performance with advanced optics and photosensitive device

Performance advancement in JEM-EUSO has been estimated taking into account the further improvements foreseen in the hardware part of the EECR telescope system.

A first improvement concerns an interference filter which has highly transmission coefficient only around the wavelengths of the EAS fluorescence light; consequently, the signal-to-noise ratio, $S/\sqrt{N}$, becomes better by 1.4 times due to the shielding of background lights. Secondly, the ratio $S/\sqrt{N}$ will be better by 1.6 times with the modification to a half size pixel of the focal surface detector and, thirdly, the ratio will be better by 2.0 times thanks to a time resolution of 0.5×GTU (baseline design). Figure 5.3.2-1 (left) shows the trigger efficiency under the assumptions of all the three improvements mentioned above. The threshold energy at 50% trigger efficiency is improved as $10^{19.3}$ eV and $10^{19.9}$ eV for nadir mode and tilt mode (38°) observation, respectively. The effective acceptance of JEM-EUSO with advanced design can be estimated as shown in Figure 5.3.2-1 (right). The effective acceptance in tilt mode will exceed that of nadir mode observation at energy of $10^{19.3}$ eV, and 2.4 times, 3.3 times and 4 times larger acceptance will be achieved in 38° tilt mode observation for events of $10^{20.0}$ eV, $10^{20.5}$ eV and $10^{21.0}$ eV, respectively. The expected numbers of observed events, with the advanced design of JEM-EUSO, are listed in Table 5.3.2-1, by considering observation periods of 2 years in nadir and 3 years in tilt mode.

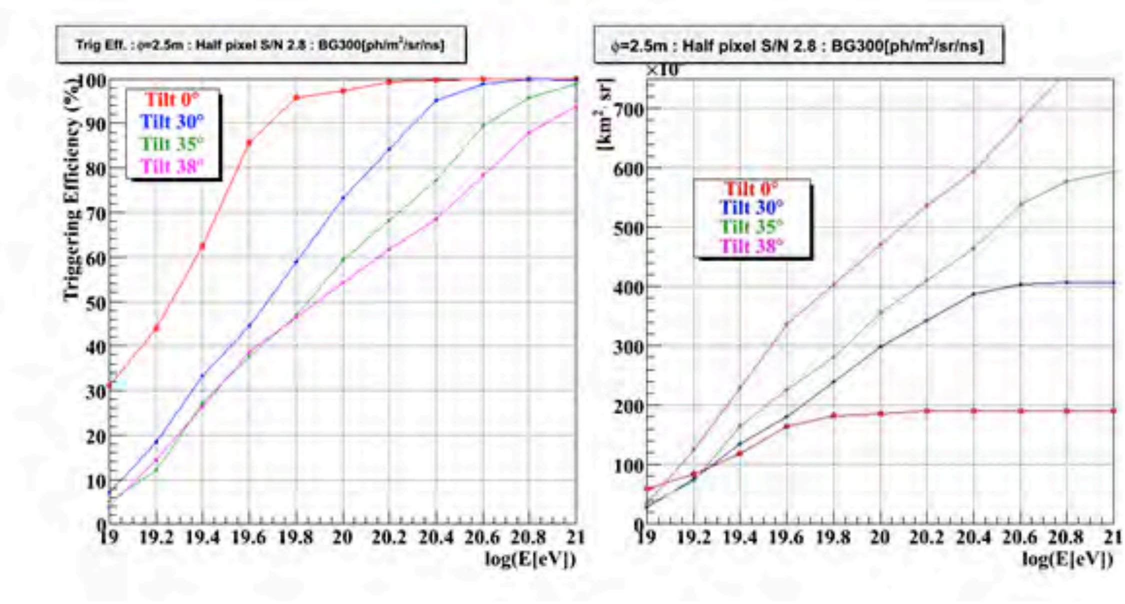

Figure 5.3.2-1. *Trigger efficiency (left) and effective acceptance (right) for JEM-EUSO with advanced design.*

Table 5.3.2-1. *The number of observed events in baseline and advanced estimation.*

Primary energy	Observation mode	Baseline	Advanced ×2.2 [(a)]	Advanced ×2.8 [(b)]
>7×10^{19} eV	Nadir (#obs/year)	290	410	420
	Tilt 38° (#obs/year)	390	920	990
	Total (#obs in 5 years)	***1750***	***3580***	***3810***
>1×10^{20} eV	Nadir (#obs/year)	64	71	72
	Tilt 38° (#obs/year)	110	180	190
	Total (#obs in 5 years)	***458***	***682***	***714***

The " advanced" option depends on the improvements considered, which influence the Signal-to-Noise ratio:
(a) Interference filter and half-size pixel → 2.2×S/√N
(b) Interference filter, half-size pixel and half GTU → 2.8×S/√N

5.4. Summary

The End-to-End simulation chain developed for the JEM-EUSO experiment is ready and several executions have been done. EAS generation code generates EAS longitudinal profile in atmosphere initiated by assumed chemical compositions for zenith angle of 0-90° and energy of >10$^{18.5}$eV. Air fluorescence and Cherenkov light emissions are also calculated taking into account their yields, absorption and scattering in atmosphere, and then the characteristics of the photons (i.e. wavelength, arrival time and spatial position of emission) on the optical lens of the telescope are evaluated. In the telescope simulation code, characteristics of hardware responses to incident photons, photoelectrons and analogue/digital signals have been taken into account. Hardware performance on optical system, focal surface detector and output signal control circuit has been estimated. Finally, pseudo-observational data including overall hardware responses will be generated. In addition, EAS event reconstruction code determines EAS energy, arrival direction and longitudinal development from simulated pseudo-observational data produced by former two processes, and it is used for evaluating their accuracies. This code also contributes as a feedback for the studies related to the development of analytical algorithms and hardware improvements aiming at the excellent telescope's capability with the best accuracies.

Taking into account the hardware improvements performed till now (December 2008) during the Phase-A study of the mission, we have set the following assumptions and conditions in the End-to End simulation chain to obtain the baseline estimation of the JEM-EUSO performance:

- Optics system: lenses 2.65 m diameter, side-cut; first and third lens: CYTOP; second lens: PMMA000;
- FS detector: array of ultra bialkali MAPMTs (6×6 pixels each);
- Time resolution (GTU): 2.5 μs;
- Track trigger method as event trigger;
- Standard background: 500 photons/(m^2 sr ns);
- EAS events with Cherenkov mark (golden events).

The JEM-EUSO performance estimated by the baseline simulation can be summarized as:

Trigger Efficiency and Expected Numbers of Observed Events. The trigger efficiency at 10^{20}eV is 86% for nadir mode observation, and EAS threshold energy is estimated to be 5.0×10^{19}eV at 50% detection efficiency level. In addition, the trigger efficiency curve of EAS hitting within a radius of 100 km in the field of view have shown that the threshold energy becomes lower than 2.7×10^{19} eV because of a better performance of optical system and smaller impact parameters. The threshold energy for tilt mode observation become higher by 70% due to a longer distance from the EAS axis to JEM-EUSO, however, a increase of acceptance by tilt mode observation has an important advantage over it. Energy dependence of effective acceptance with a combination of trigger efficiencies and an increase of field of view has been evaluated. Relative advantage of tilt mode observation could be seen as 1.8 times and 2.4 times larger effective acceptances at 10^{20} eV and $10^{20.5}$ eV, respectively than nadir mode observation. Integrated apertures of JEM-EUSO is estimated as 2.1×10^{5} km^{2} sr year and 1.5×10^{6}km^{2} sr year for nadir and tilt mode observation respectively, therefore we plan the 2 years nadir mode and 3 years tilt mode observation; the expected numbers will be 1800 and 450 events for energies $>7\times10^{19}$eV and $>10^{20}$eV, respectively, in planned 2 years nadir mode and 3 years tilt mode observation.

Angular Resolution. The requirement of < 2.5º in angular resolution is satisfied with energy of $>10^{19.5}$eV and zenith angle of >45º. In addition, resolution of 1.0º can be estimated for EAS of $>10^{20}$eV and >60º and it is enough resolution for the study of cosmic ray origin. Expected resolutions will improve and satisfy the requirement even for EAS with energy around $10^{19.5}$eV when EASs hit at the center of JEM-EUSO field of view.

X_{max} Resolution. This resolution does not depend on zenith angles; X_{max} resolution values of $100\div120$ g/cm^{2} are estimated within a radius of 200 km in the field of view.

Energy Resolution. Energy resolution becomes to be <30% for EAS with zenith angle above 45º and accuracy of 15% could be expected for EAS of $>10^{20}$eV in a radius of 100km.

6. Operation

In the present chapter, we describe the scenario of JEM-EUSO launch, attachment to JEM port, commissioning and regular operation; the sketch of the ground segment for regular operation is mentioned.

6.1. Launch and Attachment to JEM/EF Port

As the baseline for the JEM-EUSO accommodation on HTV, we employ the side cut scheme described in Sect.4.7.1.

After HTV docks in the ISS Docking Port, the Space Station Remote Manipulator System (SSRMS) takes out JEM-EUSO and pass it to the JEM Remote Manipulator System (JEMRMS). JEM-EUSO is installed onto EFU#2 port of JEM/EF where JEM-EUSO is expanded to operational shape using autonomous mechanism (see Figures 4.7.1.2-2 and -3 for JEM-EUSO storage and deployment). Throughout these processes, two grapple fixtures on JEM-EUSO are needed for SSRMS and JEMRMS. The configuration of grapple fixture for JEM-EUSO and Payload Interface Unit (PIU) is designed as in the case for standard JEM/EF payload [88]. EFU#2 Port accommodates 2.5 tons payload with up to 3 kW power supply capacity and heat wasting capability.

Figure 6.1-1 (same as Fig.4.7.1.2-4) shows the JEM-EUSO location on the EFU#2. For this configuration, possible interference exists with the standard payload on EFU#4. On the other hand, the JEM-EUSO has more than one meter margin to the pressurized module and is secured against External Vehicular Activities (EVA).

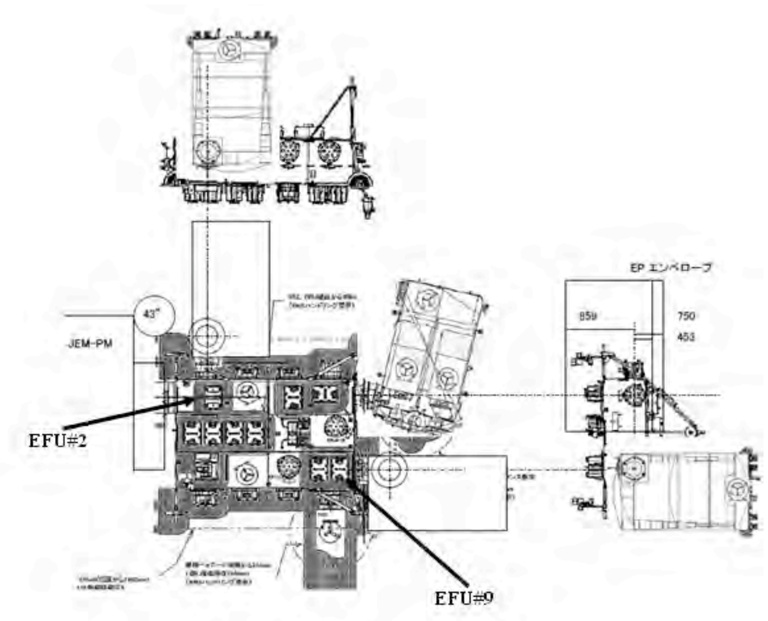

Figure 6.1-2. *Configuration of JEM-EUSO on EFU#2 port [80].*

6.2. Commissioning

For a first few months after deployment, we will devote to commissioning of the JEM-EUSO telescope. In this phase we will perform pilot EECR event observation and establish the performance index of >90% level by adjusting the equipment and finalizing operational parameters. This index will be defined by the rate of the observed EECR events which satisfy the required quality. The analysis procedure will be verified with the actually observed air shower event data.

6.3. Observation Phase

In the observation phase, the operation scheme is characterized by the local solar time on the orbit, mainly observation at nighttime and standby under daylight with ~90-minute-cycle of regular routines as the orbital period. Besides normal operation, the active safety measures are required to coup with sudden incident during the observation. Especially against the possible malfunctioning in daytime, the even more elaborate functions need to be ready to minimize the damage by daylight.

In order to design the system of the elementary function such as opening the lid and sequence of those functions, or command system, we have defined about 200 commands so far. This number will rise according to ongoing hardware development and other requirements. These commands are implemented in the emulating software that has been developed for test command flow of possible operational occasions such as regular observation.

6.3.1. Regular Observation

In the regular observation phase, EECR observation is started at the termination of the twilight and is halted before the dawn. The observation is not halted under the moonlight unless the case of crescent moon when the background noise rate is too high to acquire good quality data. Due to too short night-time to secure warm-up time and efficient observation time on the orbit, regular observation is fully suspended in a few days around the full moon.

In every orbital period, the standard routine is repeated every ~90 minutes. Taking the local solar time being 12 hours as the origin, this routine is described as follows.

Mid-day to twilight:

i) Starting up sub-systems. Setting operational parameters on each subsystem. Apply HV on MAPMT to operational level. Starting MAPMT pre-observation calibration sequence.

Twilight to dawn:

ii) Opening lid. Starting trigger logic. Starting data acquisition (DAQ; start of EECR observation).

iii) Before dawn. Stopping DAQ (termination of EECR observation). Halting trigger logic. Shutting lid. Starting post-observation calibration.

iv) Ramping down HV on MAPMT to stand-by status (see following description). Data downlink upon request. Halting sub-systems.

The time of EECR observation is shortened by the presence of well waxed moon above the horizon. JEM-EUSO accommodates the system for issuing clearance or blocking the command execution. The act of opening lid, for example, is permitted only if sunshine, twilight and intense moonlight are absent. In case of applying HV on MAPMT to the operational level, the status of lid mechanism should be normal. This is a typical example of fail-safe scheme to take into account the possibly happening worst case that both power-off HV and shutting lid would be out of control. During the regular operation, this system stationary alerts HK data and status from subsystems are stationary alerted. The presences of thundercloud or/and intense man-made light sources are also monitored for putting active safety measures in motion.

During the daytime, the lid is closed to protect JEM-EUSO telescope from severe degrading. To reduce the power consumption, powers for subsystems except essential components are off. Even in this case, the MAPMT power supply is left on but the voltage on the first dynode is controlled to minimize the effect by stray light.

The downlink of scientific, HK and subsystem monitor data is practiced during the daytime. In ordinary occasion, prompt accessibility to those data are not mandatory. The size and frequency of downlink highly depend upon the JEM-EUSO operation. For example, the flexibility of downlink protocol increases if the common data storage and computing facility is equipped on the JEM pressurized module.

6.3.2. Trouble shooting

Throughout JEM-EUSO operation at any phase, it is possible that the potential trouble or malfunction of subsystems occur. This, to wide degrees, would possibly result in spoiling scientific capability of the entire mission. To recover such occasion, we investigated a number of possible situations, likely or not, and studied for trouble shooting. The following is an example case of trouble shooting scheme on malfunctioning of the lid mechanism.

In the regular operation, one may assume the trouble shooting against malfunctioning by the following measures:

1) Less frequent lid operation;
2) Lid kept open.

In each case, we aim at salvaging the quality of data even in trouble shooting operation. In case 1) and 2), we relieve the required lower limits of the performance indices of 70% and 50%, respectively (TBC).

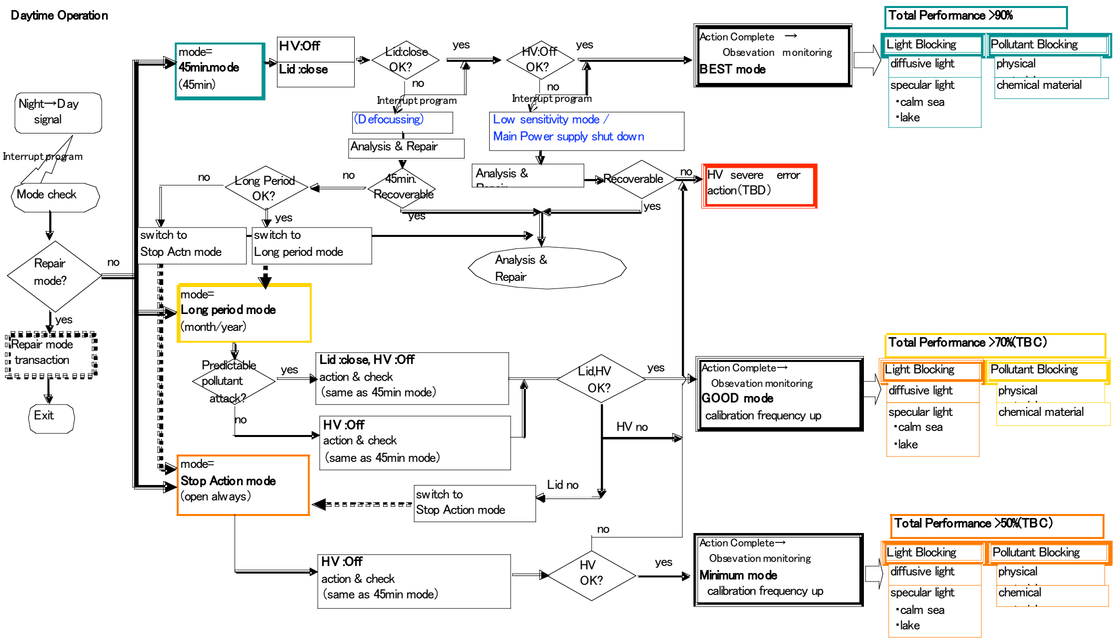

Figure 6.3.2-1. *Flowchart of lid trouble shooting.*

In Fig.6.3.2-1 we summarize the measures for lid trouble shooting. The basic scheme is described in the following. For example, if the malfunction of lid is found in daytime, the regular operation is suspended even before the terminator. In this case, sounding the lid mechanism and related subsystems is carried out to fix the trouble as early as possible. In similar occasion in the nighttime, emergent ramping down of HV on MAMPT and defocusing of the focal surface detector are alerted to secure the focal surface detector itself. In the case HV system is also failure, the main power is also switched off. Unless the trouble is solved in short time scale, the operation is shifted in the above mentioned 1) or 2) for long-term trouble shooting. In case of 2), the lid is only tried to be closed to avoid the polluting the lens such as when HTV approaches ISS. Currently, further more serious cases of troubles are in argument.

6.3.3. JEM-EUSO telescope pointing

The optical axis of the JEM-EUSO telescope stationary is pointed downward to the ground for EECR observation and protection against sunshine. In first two years, JEM-EUSO telescope is pointed toward the nadir (nadir mode) and then moved upward toward by ~40 degrees (tilt mode). The scientific merit of tilt mode is the enhancement of sensitivity against EECRs with higher energies. It is planned to only once change the pointing direction at the beginning of tilt mode operation; however, the operation of JEM-EUSO may require changing the tilt angle or reverting back to nadir mode. The mechanism for such control will be equipped.

6.4. Ground Segment

In the present section we describe the Ground Segment and related activities during the regular operation, which have been applied in the past- and present-running Space experiments.

The principal components of the Ground Segment are ISS ground station, JEM Mission Control Room (MCR) and our own Space Operation and Data Centre (SODC). The end-to-end communication is established via NASA's Tracking and Data Relay Satellite (TDRS). Among them, SODC is the primary component for JEM-EUSO during the regular scientific operation and consists of the following three units providing the key functionalities:

- Unit_1 [Mission activity planning/telecommand unit]
- Unit_2 [Data processing/system monitor unit]
- Unit_3 [Data management and archiving unit]

6.4.1. Mission activity planning and telecommand unit

Mission activity planning and telecommand unit is responsible for uplink of telecommands and operational parameters to JEM-EUSO. This unit includes the mission planning task. The mission plan, in which the detailed operational command sequence is defined, is renewed every several days taking into account the ISS orbital motion and other conditions. It is ideal that the mission plan is autonomously carried out onboard; however, it is possible that changes of the plan are required according to the increasing background level or/and JEM and ISS operational constraints. In Unit_1, the telecommands for such remote controls are generated and are uplinked to JEM via MCR.

In addition, Unit 1 has the function to enable development and test of telecommands, related software, system patches, and more. To debug and to verify the action of newly developed telecommand, Unit_1 accommodates the test facility that includes principal subsystems.

6.4.2. Data processing and system monitor unit

The main task of the data processing and system monitor unit is reception and processing of the downlink data (scientific, monitor, HK, etc). Here all the data is transferred to SODC via MCR. The data are sorted into two classes, requiring frequent-possible downlink or not.

The scientific data such as EECR event data are supposed to be downloaded as little frequent as even once a day. These data are processed in the quick-look analysis to give the preliminary information to the scientists. In this analysis, the calibration data such as MAPMT calibration and atmosphere monitoring are reflected.

On the other hand, monitor data from subsystems, HK data, MAMPT calibration data are required to be available permissively more frequently. These datasets go through pile-line process and are delivered to ground staffs on duty.

6.4.3. Data management and archiving unit

Data management and archiving unit is responsible for all data management, data distribution and the development of related software. It should be noted that the scientific data will be public-domain after a certain period (details to be determined).

Unit_3 manages raw data from JEM-EUSO, calibration data, atmospheric data, HK data and analyzed scientific data plus related information (e.g. ISS attitude). The user interface is also developed and delivered with transparent data to retail users. The reconstruction software and subsystem manuals are also managed in this unit.

6.4.4. SODC staff on duty

We will establish 24-hour operation of SODC mainly to monitor the system status. It is expected that about 20 persons of permanent staff and visiting researchers participate in SODC activities during regular operation. The significant part of tasks, such as mission plan uplink, is performed in daytime on the ground.

The activity in each SODC unit co-runs along with the regular operation. For each unit, we will designate the responsible scientist. In daytime, operating staffs are deployed with a ratio of 2:2:1 for Unit 1:2:3. During night, at least two staffs are on duty to monitor the system and anytime responsible scientists and subsystem experts are in touch. In the commissioning phase, Principal Investigator (PI) and these key persons will devote to establishing the operation scheme.

7. Development Plan

According to the JAXA documents on “Call for proposal for the mission candidates of 2nd phase utilization of JEM/EF”, the JEM-EUSO development plan is divided into two parts: the feasibility study phase (2007 and 2008 fiscal years) corresponding to Phase-A, and the development phase (years after 2008 fiscal year) corresponding to Phase-B and later. At the end of 2008 fiscal year, the evaluation shall be made whether the plan is advanced into Phase-B or not. The launch opportunity is estimated in 2013. The schedule map for the development plan is shown in Table 8-4-1.

7.1. Feasibility Study Phase

We have done the conceptual design and preparation study Phase-A for 2 years (2007-2008).

7.1.1. Plan

The test model, including the key elements of the telescope, is manufactured, assembled and tested in feasibility study phase. Two sets of main elements (front lens, rear lens, diffractive optical elements, and photo-detector module) will be manufactured and assembled in the prescribed positions to make the test apparatus. This apparatus plays the role of elemental test model of telescope functions. A beam of UV laser is impinged from the front lens to the focal surface and the path along the optics, transmittance of the optics and sensitivity of the detectors are measured and compared with those designed. An air shower is simulated by a swing of the beam to verify the trigger efficiency of the trigger electronics. The data measured in this test apparatus will be used in the software simulator of JEM-EUSO telescope to estimate the performance of the entire telescope in terms of arrival direction and energy of the extreme energy particles, and X_{max} of the EAS and energy threshold.

The prototype of the atmospheric monitor is manufactured to design the actual atmospheric monitor effectively.

Mechanical parts such as lid, enclosure cylinder and the tilt mechanism are manufactured and their technical robustness was verified. Radiation and vibration/impact tests will be done for important parts of these mechanisms.

The air-fluorescence observation from EAS has been well established in ground-based experiments such as HiRes and Pierre Auger Observatories. However JEM-EUSO will challenge to observe the EAS from the Space for the first time. In order to make sure the ability of our instrument, we are planned balloon experiments with laser and detectors.

Furthermore we join TUS (Track Ultraviolet Setup) experiment on the Russian Foton satellite that will be the pathfinder of JEM-EUSO. The end-to-end verification of the air-fluorescence observation from orbit will be performed by TUS that will be launched in 2011.

7.1.2. Implementation structure

RIKEN will work as a hub of corporations of Space organization (JAXA, NASA, ESA), universities, and research institutions in Japan (Konan Univ., Saitama Univ., KEK, NAOJ, etc.) and international partners(Univ. Alabama in Huntsville, etc.) in feasibility study phase. Major members of JEM-EUSO Collaboration are listed with their responsibilities:

Table 7.1.2-1. *Division of major roles for the JEM-EUSO implementation.*

Responsibility	**Responsible(s)**
Project PI	Toshikazu Ebisuzaki (RIKEN)
Instrument Manager	Fumiyoshi Kajino (Konan Univ.)
Project Science	Yoshiyuki Takahashi (RIKEN, Univ. Alabama in Huntsville)
Project Manager	Hiroshi Mase (RIKEN)
Optics System	Roy Young (NASA/MSFC), Yoshiyuki Takizawa (RIKEN)
The Whole Focal Surface	Hirohiko M. Shimizu (KEK), Yoshiya Kawasaki (RIKEN)
Focal Surface Detector	Yoshiya Kawasaki (RIKEN)
Focal Surface Electronics	Marco Casolino (Univ. Roma “Tor Vergata”), Tokonatsu Yamamoto (KonanUniv.)
Calibration System	Philippe Gorodetsky (APC Paris), Naoto Sakaki (Aoyama Gakuin Univ.)
Atmospheric Monitor	Valentin Mitev (CSEM Neuchatel), Satoshi Wada (RIKEN)
End-to-End Simulation	Dmitry Naumov (JNRD Dubna), Naoya Inoue (Saitama Univ.)
System	JAXA

Below is the organization of JEM-EUSO in development stage.

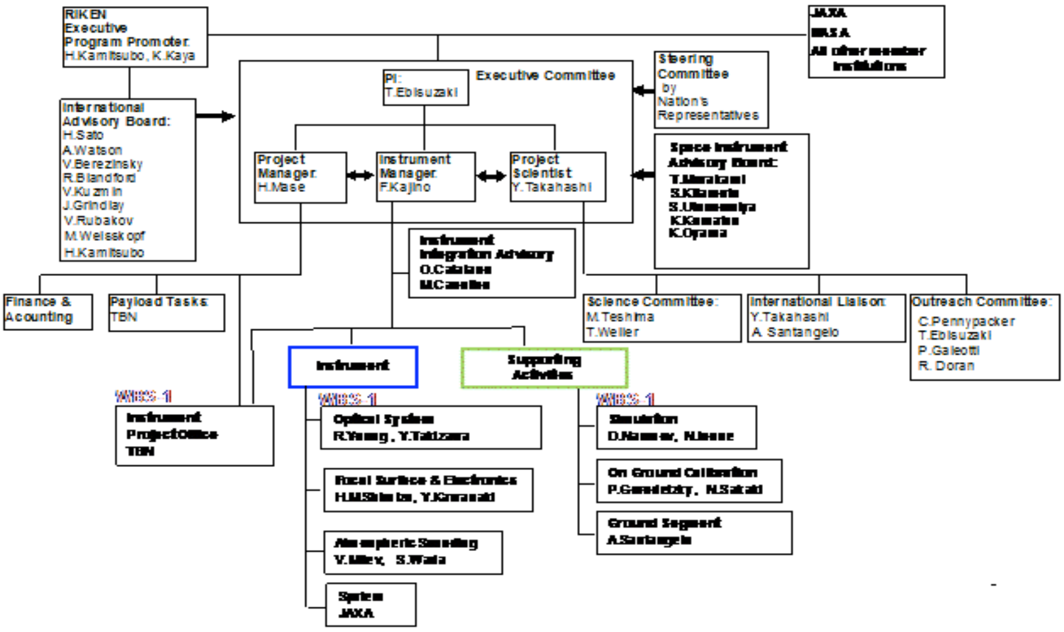

Figure 7.1.2-1. *Organization of JEM-EUSO in development stage (as Nov.08).*

7.2.Development Phase

The organization for the development phase will be discussed and determined by RIKEN, JAXA and participating organizations during feasibility phase taking into account the opinions of the International Science community.

7.3. Cost Budget

Total cost, including the manufacturing cost and the observation operating cost, is estimated about 12 billion Yen, in which we estimate 9 billion Yen for the mission and 3 billion Yen for the bus system.

Japan will pay the bus system cost taking the responsibility of integration, and the mission cost will be shared by Japan, USA, Europe and other countries with almost the same share. Basically, each part will pay around 3 billion Yen.

The following tables summarize the cost for the development year by year, including a rough draft of the charges of each country. We will fix the details of each cost by negotiating with relevant institutes by SDR (System Definition Review Mar., 2009).

Table 7.3-1. *JEM-EUSO breakdown of the development cost year by year.*

mission ready ↓ (Fiscal year 2013)

unit : million YEN=0.01M$

Cost Breakdown		Fiscal year 2008	Fiscal year 2009	Fiscal year 2010	Fiscal year 2011	Fiscal year 2012	Fiscal year 2013	Fy '14	Fy '15	Fy '16	Fy '17	Fy '18	SUM
Mission	Optics	24	411	1,040	720	656	449						**3,300**
	F S(Detector)	40	442	422	345	295	56						**1,600**
	FS(Electronics)	30	464	419	350	290	47						**1,600**
	Atmospheric Monitoring	10	402	350	284	89	15						**1,150**
	Calibration	20	50	18	26	73	13						**200**
	Operation & Ground Supp.	0	0	0	0	30	30	120	120	120	120	120	**660**
	Mission sum	124	1,769	2,249	1,725	1,433	610	120	120	120	120	120	8,510
Bus System		150	500	750	1,000	500	100						3,000
Contingency		10.00	90.00	126.00	115	83	66						490
	Summation	**284**	**2,359**	**3,125**	**2,840**	**2,016**	**776**	**120**	**120**	**120**	**120**	**120**	12,000

Table 7.3-2. *JEM-EUSO development cost share year by year.*

unit : million YEN=0.01M$

Cost Share		Fiscal year 2008	Fiscal year 2009	Fiscal year 2010	Fiscal year 2011	Fiscal year 2012	Fiscal year 2013	Fy '14	Fy '15	Fy '16	Fy '17	Fy '18	SUM
Japan	RIKEN	45	120	300	300	300	225	40	40	40	40	40	1,490
	University	13	30	54	83	180	80						440
	JAXA (Mission)	40	50	250	250	250	230						1,070
	JAXA (System)	150	500	750	1,000	500	100						**3,000**
	JApan sum	**248**	**700**	**1,354**	**1,633**	**1,230**	**635**	**40**	**40**	**40**	**40**	**40**	6,000
USA		**30**	**830**	**925**	**607**	**386**	**22**	40	40	40	40	40	3,000
EU,Korea,Mexico		**6**	**829**	**846**	**600**	**400**	**119**	40	40	40	40	40	3,000
	Summation	**284**	**2,359**	**3,125**	**2,840**	**2,016**	**776**	**120**	**120**	**120**	**120**	**120**	12,000

Table 7.3-3. *JEM-EUSO cost share of development & manufacturing by each country.*

unit: million YEN=0.01M$

Cost Share		Japan	France	USA	Swiss	Russia	Korea	Italy	Germany	Mexico	Spain	**Summation**
Mission	Optics	588		2,712								**3,300**
	FS Detector	80		5		29		45	436			**3,200**
	Electronics	80	47	5			515	465	50	14	29	
	PDM manufacturing	1,280	30				30	30	30			
	Atmospheric Monitoring	385	445		320							**1,150**
	Calibration	29	23	55		45		5	28	15		**200**
	Operation & Ggoround Supp.	313	40	100	9	40	40	40	40	19	19	**660**
Bus System		3,000										**3,000**
Contingency	mission	122.5	25	122.5	14	5	25	25	25	2	2	**367.5**
	system	122.5										**122.5**
	合計	**6,000**	**610**	**3,000**	**343**	**119**	**610**	**610**	**609**	**50**	**50**	**12,000**

8. Preparation Status

8.1. JEM-EUSO Working Group

JEM-EUSO working group (WG) has been approved by the Steering Committee for Space Science of ISAS/JAXA on June 2006. RIKEN acts as a hub of corporations: Konan Univ., Aoyama Gakuin Univ., Saitama Univ., etc. are performing research in each role.

Research communication meeting is usually held monthly and coordination of each other's researches is managed.

8.2. Activity of Planning Committee at RIKEN Discovery Research Institute

RIKEN Discovery Research Institute has settled "Planning Committee for promoting JEM-EUSO" (Chairperson: Professor Fumitaka Sato, Konan University).

The Committee discussed the scientific impacts of JEM-EUSO and its organizational problems to promote it.

A report was submitted to the director of RIKEN Discovery Research Institute, Dr. Koji Kaya.

The committee concluded as follows:

i) Scientific impacts of JEM-EUSO mission will be very high. It will open up the new astronomy with charged particles to explore extreme Universe.

ii) It is appropriate to submit the proposal of Phase-A study of JEM-EUSO from RIKEN, because: 1) it had the responsibility of the development of the focal surface in ESA-EUSO; 2) it has experience of the first phase utilization of ISS/JEM: the Monitor of All-sky X-ray Image (MAXI) and the Space mission of High Energy Transient Explorer-2 (HETE-2).

iii) It is necessary to clarify the responsibilities and role sharing between RIKEN and JAXA, when JEM-EUSO mission will be selected.

iv) JEM-EUSO mission is the international scientific project promoted by Japanese Science Community. Eight countries, Italy, France, German, Switzerland, USA, Russia, the Republic of Korea and Mexico will participate in JEM-EUSO. It is necessary to form an appropriate organization and a well-thought-out practicable plan in the Phase-A study.

8.2.1. Selection as the mission candidates of 2^{nd} phase utilization of JEM/EF

Based on the above report, we applied recruitment of the mission candidates of 2^{nd} phase utilization of JEM-EF of which the deadline was Feb. 2007.

Then our mission was adopted as a candidate in May 2007. Thus RIKEN and JAXA made a contract for collaborative scientific research and they started two-year conceptual design and preparatory research.

8.2.2. International Collaboration Meeting and International Symposium

The following International Collaboration Meetings and International Symposium have been organized from January 2007 to December 2008:

Jan.2007	The first JEM-EUSO International Collaboration Meeting

Mar.2007	International Symposium on "Astronomy and astrophysics of the Extreme Universe". Proceedings will be published soon.
Jun.2007	The first International JEM-EUSO meeting (Wako, Japan). The first International Advisory Board meeting (Wako, Japan).
Nov.2007	The second International JEM-EUSO meeting (Wako, Japan).
Jan.2008	The second International Advisory meeting (Wako, Japan). The advisory report is attached as Annex of this document.
Jun.2008	The third International JEM-EUSO meeting (Wako, Japan).
Dec.2008	The fourth International JEM-EUSO meeting (Turin, Italy).

8.2.3. Preparation of budget and improvement of organization at RIKEN

Following the report by the above Planning Committee, RIKEN did a budgetary request of 2008, as a part of the budget of fundamental scientific research. Then RIKEN succeeded in getting about 45 million Yen as a part of JEM-EUSO manufacturing cost of which RIKEN is in charge. In addition, "The research of extreme energy particles" was included in the midterm plan (Apr.1 2008 ~ Mar.31 2013) of RIKEN, as a part of fundamental scientific research. Furthermore, RIKEN is planning to ask an increase in budget paid by RIKEN, in the budgetary request of 2009.

Using the above budget as a resource, we have formed the Research Advancement Group of Extreme Space, in the Advanced Science Institute of RIKEN set up in 2008 (organization detailed in Annex, at the end of this report). This was highly advised by the above Planning Committee and by the third International Advisory Board meeting, and the collaboration between MAXI and JEM-EUSO, which will use the JEM/EF equally, for the Space observation, became ready. They will collaborate closely. In addition, an International Cooperation Research team was set up on Jul. 1, 2008. The team is composed of main members from main countries. Mr. Yoshiyuki Takahashi is in charge of team head, as well as responsible for USA. The role of this team is to monitor the International situation and to do the coordination of technology and budget, by supporting the applications for budget in each country.

We are also negotiating for the increase of the mission budget for stowing JEM-EUSO on the ISS Space Station, in cooperation with the section in charge of JAXA. The universities other than RIKEN are planning to apply subventions for large scale scientific research (specially-promoted, particular field, academic foundation, etc.), and they have already started preparing the application.

8.3. Preparation Status in each Country

JEM-EUSO is an international project that can be realized by international cooperation. At present time, confirmation of international role-sharing is in progress, mainly by Japan and USA. Regarding the mass for the launch, we will get to work on NASA and ESA through the participants of USA and Europe during the examination phase after the adoption, toward the regeneration of international sharing.

8.3.1. U.S.A.

USA is in charge of optics of JEM-EUSO and also is contributing to detector, trigger method and ground flashers for calibration. NASA selected the USA participation to ESA-EUSO, permitting the expenditure of 36 M$ for the entire mission. However, this plan has been frozen because ESA postponed the ESA-EUSO Phase-B. NASA/MSFC, as the hub of JEM-EUSO in USA, is requesting to permit resumption on this plan. All members of ESA-EUSO including new members have announced the desire of immediate resumption of this plan to join in JEM-EUSO.

NASA/JSC (Johnson Space Center) that is in charge of the utilization of JEM in NASA, has shown a positive response to the use of EFU#2 for JEM-EUSO. NASA has the right of usage of 49% of JEM-EF.

8.3.2. Europe

At ESA as well as in Europe, distrust of ISS and Space Shuttle increased since last autumn. Since then, as it was decided that all the ISS stowing experiments will not to be included in the budget of the scientific section, this experiment cannot be paid with this budget. However, gaining support from other departments such as Manned Space Station Department is considered favorable. Preparation status in each country is as follows:

In Italy, "Studio di Astrofisica delle Alte Energie (AAE) - Proposta di nuove Missioni ed Occasioni di missione (2° anno)" was adopted by the Italian Space Agency, as a preparatory study of the JEM-EUSO in Italy, and 74 kEuro of expense was accepted. This will allow a full-scale qualification for the budget requirement, and the above is a preparatory budget allocation. In addition, JEM-EUSO was adopted as "Italo-Japanese collaborative scientific research program", and 100 kEuro budget has been allocated by the Italian Ministry of Foreign Affairs ("Ministero degli Affari Esteri, Direzione Generale per la Promozione e Cooperazione Culturale") for JEM-EUSO in the fiscal year 2008.

French JEM-EUSO team will submit their proposal to the CNES (Centre National d'Études Spatiales) and to the CNRS, and a preparatory meeting among CNES, CNRS, and the Director of RIKEN Discovery Research Institute, was held in March in Paris. In addition, JEM-EUSO was adopted as the new “Franco-Japanese collaborative scientific research program”, sponsored by CNRS.

In Germany, the group of Mr. M. Teshima of Max-Planck-Institut (MPI) obtained 1MEuro, as 5 years’ R&D cost for the development of the JEM-EUSO detector (SiPM) from the internal budget of MPI. In addition, Prof. A.Santangelo of University of Tübingen, a key figure of German JEM-EUSO team, is planning to do an application of around 4 MEuro, from September to October in 2008, as a matching fund between German Aerospace Center (Deutsches zentrum für Luft-und Raunfahrt) and MPI.

In addition, Poland, Slovakia, Spain and Switzerland show their intention to participate.

8.3.3. Korea

Prof. I. Park of Ehwa, as leader of the team, is developing an electric circuit for triggering purposes to be stowed in the telescope and MEMS mirror for the deflection of the Lidar beam.

8.3.4. Mexico

Universidad Nacional Autonoma and Benemerita and Universidad Autonoma de Puebla are showing their intention to participate.

8.3.5. Russia

SINP MSU and Dubna JINR announced to participate in JEM-EUSO. Japan JEM-EUSO team will join TUS experiment to verify the technologies (photomultipliers and readout electronics) that will be used in JEM-EUSO. TUS is promoted by MSU and will be scheduled to launch in 2009. Possibility of cooperation in detector developments is under discussion

8.4. Development Schedule

The following table shows the JEM-EUSO development schedule (as Dec.2008).

Table 8.4-1. *JEM-EUSO development schedule.*

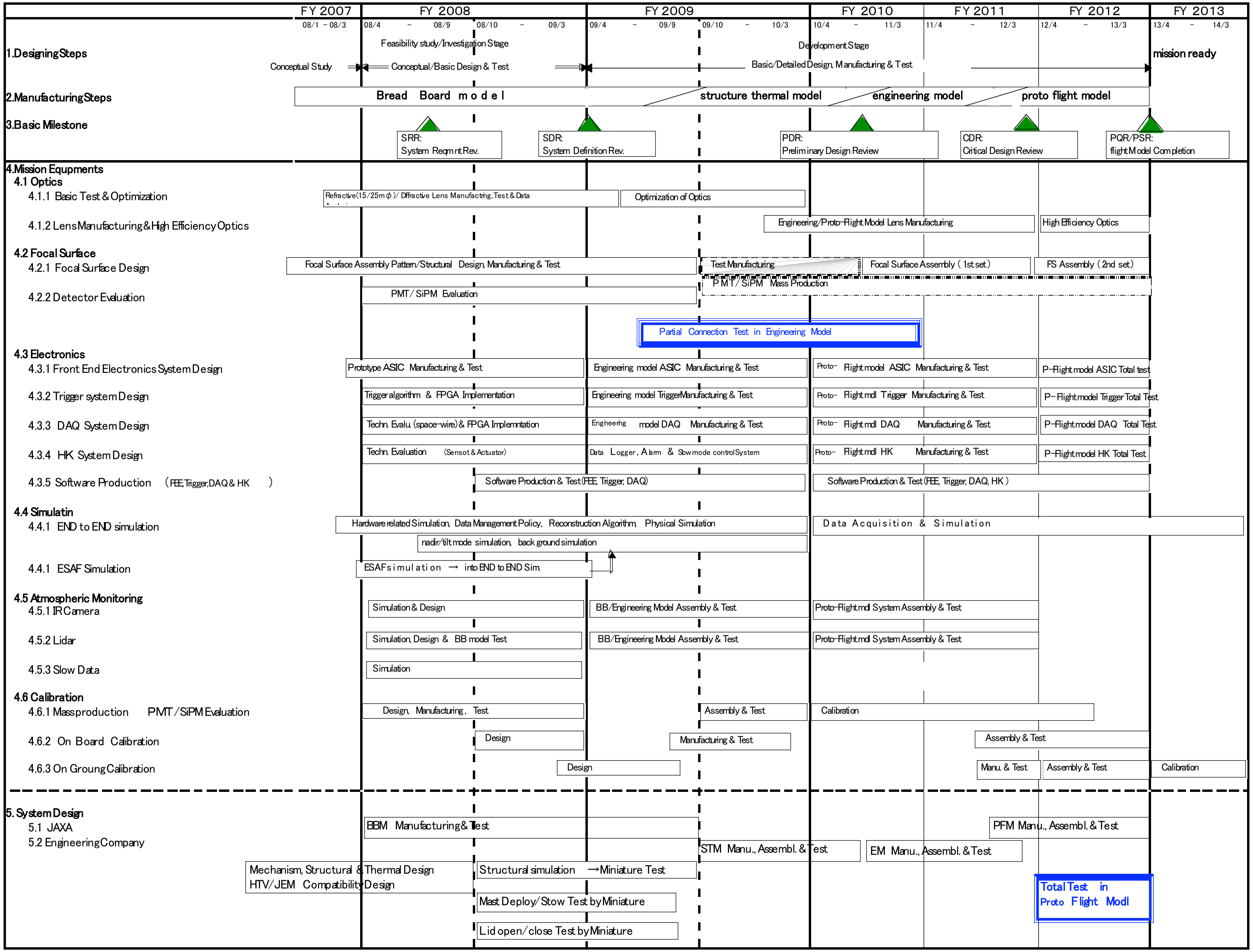

References

[1] Penzias, A.A. and Wilson, R.W. 1965, *Astrophys. J.* 141, 419.

[2] Greisen, K., 1966, *Phys. Lett.* 16, 148.

[3] Zatsepin, G. T. and Kuz'min, V. A. 1966, *JETP Phys. Lett.* 4, 78.

[4] Berezinsky, V. Kachelriess, M. and Vilenkin, A., *Phys.Rev. Lett.* 79, 4302, 1997.

[5] Aloisio, R. Berezinsky, V., and Kachelrieb, M., *Physical Review, D.* 69, 094023, 2004.

[6] Sakar, S. and Toldra, *R. Nucl. Phys..* B621, 495, 2002

[7] Berezinsky, V. and Kachelrieb, M., *Physical Review, D.* 63, 034007, 2001.

[8] Birkel, M. and Sarkar, S., *Astropart. Phys.* 9, 297 1998.

[9] Barbot, C. and M. Drees, M., *Phys. Lett. B 533*, 107 2002; *Astropart. Phys.* 20, 5 2003.

[10] Navarro, J. F., Frenk, C. S., and White, S.D.M, *Astrophys. J.* 462, 563, 1996

[11] Moore, B. *et al*. *Adtrophys. J. Lett.* 524, L19, 1999

[12] Fukushige, T. Kawai, A. and Makino, J.,*Astrophys. J.*, 606, 625-634, 2004.

[13] Diemand, J., Kuhlen, M., Madau, P. *astro-ph*/0611370, 2006.

[14] Takeda, M. *et al*. 1999, *Astrophys. J.*, 522, 255.

[15] Gorbunov, D.S. and Troitsky, S.V. *Astroprt. Phys.* 23, 175; Abbasi, R. U.et.al, 2006, *Astrophys. J.*, 636, 680.

[16] Auger Collaboration, Science 318, 896, 2007.

[17] Ghisellini, G. *et al*., arXiv:0806.2393.

[18] Takami, H., private communication / Takami, H., and Sato, K., arXiv:0710.0767

[19] Takami, H., Yoshiguchi, H. and Sato, K. *Astrophys. J.*, 639, 803-815, 2004.

[20] Berezinsky, V., Blasi, P. and Vilenkin, A., *Phys.Rev.D,* 58:103515,1998

[21] Berezinsky, V. Mikhailov, A.A. *Phys. Rev. D.*, 58, 10315, 1998.

[22] Medina-Tanco, G. and Watson, A., *Astropart. Phys.* ,12, 25, 1999.

[23] Weiler, T. J. *Phys. Rev. Lett.*, 49, 234, 1982.

[24] Weiler, T. J. *Astrophys. J.,* 285, 495, 1984.

[25] Ringwald. A. and Wong, Y.Y.Y., *J. Cosmol. Astropart. Phys.* 12, 005, 2004.

[26] Medina-Tanco, G., Teshima, M. and Takeda, M. *Proc. 29th ICRC Tsukuba*, 747.

[27] Abbassi, R.U. et al., *Phys. Rev. Lett.* 100, 101101, 2008.

[28] Pierre Auger Collaboration, *Phys. Rev. Lett.* 101, 061101, 2008.

[29] Medina-Tanco 2008, private communication.

[30] Berezinsky,V.S. and Grigorieva, S.I, 1988, *Astron.Astrophys.* 199, 1.

[31] Stecker, F.W. *Nature*, 1989, 342, 401.

[32] Landau, L.D. and Pomeranchuk, I.J., Dokl.Akad.*Nauk SSSR*, 92,535, 1953.

[33] Migdal, A.B., *Phys. Rev.* ,103,1811, 1956.

[34] Vankov, H. P., Inoue, N., and Shinozaki, K., *Physical Rev. D*, 67, 043002 , 2003.

[35] Sakaki, N. *International Journal of Modern Physics*, 20, 7020-7022, 2005.

[36] Pierre Auger Collaboration, 2008, *Astropart. Phys.,* 29, 243-256.

[37] Semikov, DV. for the Pierre Auger Collaboration, *Proc. of Int. Cosmic Ray Conf.*

[38] Gelmini, GB; Kalashev, OE and Semikoz, DV., 2005, arXiv:astro-ph/0506128.

[39] Coppi, P.S., and Aharonian, F.A. 1997, *Astrophys. J. Letters*, 487, L9-L12.

[40] Kifune, T. 1999, *Astrophysical Journal,* 518, L21-24.

[41] Coleman, S. and Glashow, S.L., 1999, *Phys. Rev. D*, 59, 116008.

[42] Lieu, R. and Hillman, L.W. 2003, *Astrophys. J.,* 585, L77-L80.

[43] Palimares-Ruiz, S.,Irimia,A.,and Weiler, T.J, *Physical Rev. D*, 73, 083003, 2006.

[44] Waxman, E and Bahcall, J., *Phys.. Rev.. D*, 59, 23002, 1999.

[45] Asano, K. private communication, Asano, K., Nagataki S., *Astrophys. J.* 640 L9-L12, 2006.
[46] Anchordoqui, L.A., Feng, J.L. and Goldberg, H., *Physics Lett. B*, 535, 1-4, 302-308, 2002.
[47] Kachelriess, M., Serpico, P. and Teshima, M., *Astropart. Physics*, 26 378, 2006.
[48] Tinyakov, P. G. and Tkachev, I. I., *Astropart. Phys.* 18, 165, 2002.
[49] Harari, D., Mollerach, S. and Roulet, E. , JHEP 9908, 022, 1999.
[50] Prouza, M. and Smida, R., *Astron. Astrophys.* 410, 1 (2003)
[51] Jain, A., Jain, P. Mackay, D.W., and Palston, J., *International Journal of Modern Physics A*, 17, 533-554, 2002.
[52] Sato, H. and Tati, T., *Prog. Theor. Phys.* 47, 1788, 1972.
[53] Yamaguchi, Y., *Prog. Theor. Phys.,* 2003, 110, 611., Y. Yamaguchi, *Prog. Theor. Phys.,* 111, 545, 2004.
[54] Amelio-Camelia, G. *et. al.*, *Nature*, 393, 763, 1998.
[55] Ellis, J., Mavromatos, N.E., and Nanopoulos, D.V., *Phys. Rev. D*, 63, 124025, 2001.
[56] Thomas, R. J. *Journal of Geophysical Research*, 86, 206, 1981.
[57] Onoma, F. *et al. Annales Geophysicae*, 23, 2385, 2005.
[58] Horinouchi, T. Nakamura, T., and Kosaka, J. *Geophysical research Letters*, 29, 2007.
[59] Iwagami, N. *et al. Advance in Space Research*, 2005, 35, 1964.
[60] Jacobson, A.R. and Shao, X., *Journal of Geophysical Research,* 107, D22, 4661, 2002.
[61] Jacobson, A.R., *Journal of Geophysical Research,* 108, D24, 4778, 2003.
[62] Gurevich, A.V, and Zybin, K.P., *Physics,Letters,*A329, 341-347, 2004.
[63] Pasko, V.P. and George, J.J. *Journal of Geophysical Research*, 107, A12, 1458, 2002.
[64] Fishman, G.J. *et al*., *Science*, 264, 131, 1994.
[65] EUSO Collaboration, “EUSO Red Book – Report on the Phase A Study”, EUSO-PI-REP-005, 2004.
[66] EUSO-OM Team, “Optics Module Design”, EUSO-DESIGN-001-2, 11 September 2003.
[67] Catalano, O., *Il Nuovo Cimento*, 24-C, N.3, 445-470, 2001.
[68] Cuneo, S., “The housing of the MAPMT of the EUSO detector”, EUSO-FS-REP-007, 2003
[69] Bleurvacq, N., C. Chapron, Ph. Gorodetsky, E. Plagnol, “The Focal Surface mechanical supporting structure”, EUSO-FS-REP-011, 2003.
[70] Kawasaki, Y., N. Sakaki, M. Takeda, “Characters of MAPMT”, EUSO-FS-REP-006, 2003.
[71] Takahashi, Y. et al., *Proc. 29th ICRC*, 8, 351, 2005.
[72] BepiColombo, http://esa.int/esaSC/120391_index_0_m.html
[73] Zong, J. et al., *Photogrammetric Engineering and Remote Sensing*, 68, 821, 2002.
[74] Hasler, A.F., et al., *Journal of Applied Meteorology*, 30, 257, 1991.
[75] Montanet, F., “EUSO Duty Cycle: Moon and Sun Effects”, EUSO-SIM-REP-009, 2004.
[76] Khanna, S.M., et al., *IEEE Trans.Nucl.Sci*, 51, 3585, 2004.
[77] Adams, J.H., Christl, M., & EUSO Collaboration, *Proc. 28th ICRC*, 919, 2003.
[78] Lefeuvre, G., Phd Thesis, Univ. Paris 7 Denis Diderot, 2006.
[79] Pace, E., “Proposal for EUSO Instrument Calibration Ssystem”, TR1, Univ. Firenze, 2003.
[80] IHI Aerospace Engineering Co., Ltd., “Conceptual design support/achievement report (Vol.3) about the missions candidate of 2nd phase utilization of JEM-EF”, 2008.
[81] Fontani, L., “Battery on-board study for EUSO experiment”, EUSO-IM-TN-003, 2003.
[82] De Masi, A., Attinà, P., “EUSO Instrument System Specification”, EUS-SP-AI-0002, 2003.
[83] EUSO-OM Team, “Optics Module design Document”, EUSO-OM-DESIGN-001, 2003.
[84] De Masi, A., Attinà, P., “EUSO Instrument System Design Report”, EUS-RP-AI-0005, 2003.
[85] De Masi, A., Attinà, P., “EUSO Instrument Structure and Thermal Control Specification”, EUS-SP-AI-0003, 2003.
[86] De Masi, A., Attinà, P., “EUSO Instrument Structure and Thermal Control Design Report”, EUS-RP-AI-0007, 2003.
[87] Catalano, O., Maccarone, M.C., Petrolini, A., Santangelo, A., Scarsi, L., “EUSO IIDD Instrument Interface Definition Document (Phase A Study)”, EUSO-IIDD-001, 2003.
[88] “Kibo JEM/EF Platform Utilization handbook”, JDX-2006150.

List of Acronyms

… in preparation …

Annex A – Temperature Analysis

The temperature analysis of MAPMT was done by RIKEN using a simple model, which does not take into accounts possible shadows caused by surrounding structures. On the other hand, the analysis in case of SiPM was done using a mathematical model by the engineering company (IHI AeroSpace) which has experience in Space experiments; this model is more accurate because it takes into consideration shadows caused by surrounding structures.

Temperature analysis of MAPMT

The M36 photomultiplier is the MAPMT currently defined as baseline for JEM-EUSO. The M36 was analyzed using the simple model by RIKEN. The telescope was considered to be a cylindrical shape. The observation time was 45 minutes, a half of one ISS orbital cycle (~90 min).

Regarding to the electric power setting, we examined the following two cases:

(a) Large electric power: necessary 641W in the night-time (the sum of: PDM, CCB, MDP, EBOX_mission 498W; EBOX_bus 138W; Altitude Sensor 5W), and 229 W in the daytime as BEE value of M36 PMT.

(b) Small electric power: necessary 383 W×1.3=498 W (night-time), and 77×1.3=101 W (daytime) only for PDM as margin included value (30%) of M36.

The temperature and the necessary heat sink were obtained as follows.

Case (a). To achieve allowable temperature (temperature on the focal surface: less than 30°C), if the function of the lid is normal, cooling power around -50 W is required. Figure A-1 shows the results. If the lid remains open and its function is suspended, the albedo of the Sun enters the telescope during daytime. Thus, larger cooling power is required (around -285 W).

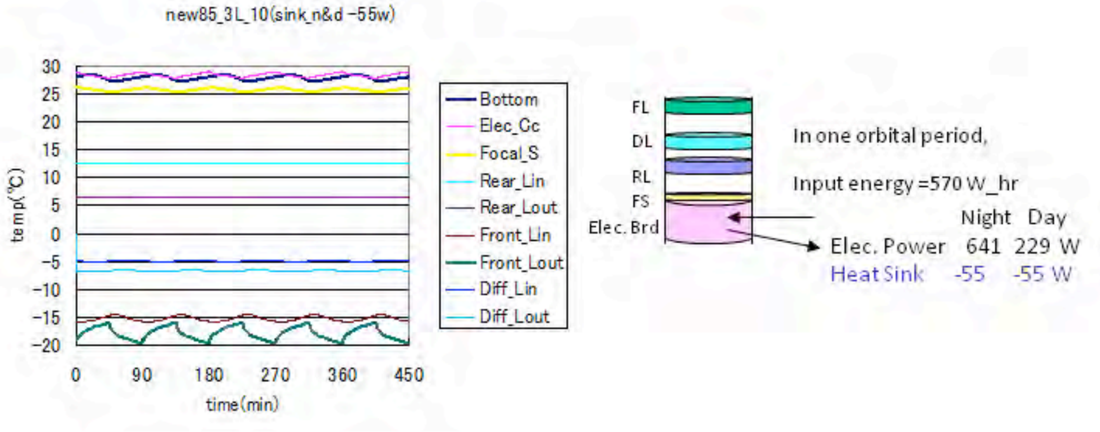

Figure A-1. *Temperature distribution in case a large electric power is needed.*

Case (b). To achieve allowable temperature (temperature on the focal surface: less than 30°C), if the function of the lid is normal, it is necessary to remove only the energy consumption of PDM, and we concluded that a special cooling device to satisfy the temperature requirements of the focal surface detector is not necessary. Figure A-2 shows the results. However, if the lid remains open and its function is suspended, the albedo of the Sun enters the telescope during the daytime. Thus, larger cooling power is required (around -145 W).

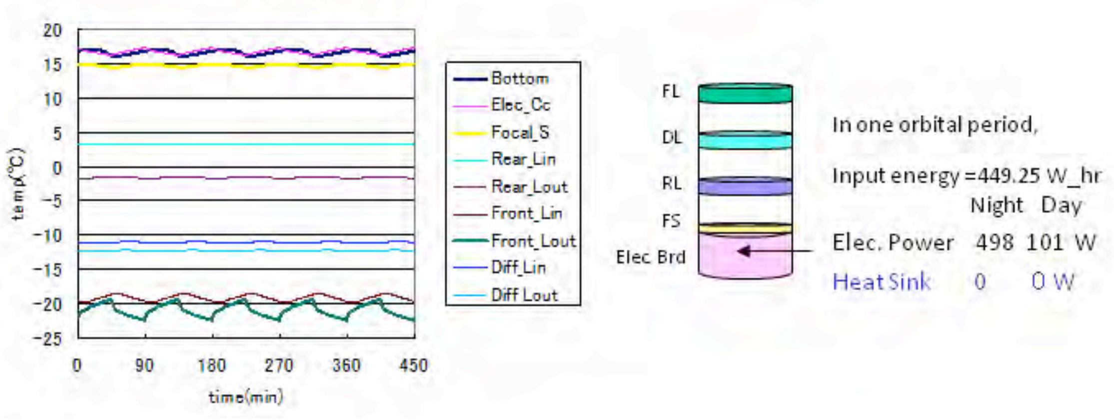

Figure A-2. *Temperature distribution in case a small electric power is needed.*

Temperature analysis of SiPM

Figure A-3 shows the model of JEM-EUSO and the time conditions for the observation. After the analysis, the temperature variation of the inner lens surfaces was 4.5°C maximum with the lid, and less than 1°C without the lid. In this analysis, the lens was considered as monolithic, and there was no modelling of the frame and the ring. In addition, we did not take into consideration the heat conduction between the lens and the MLI, which is the external cylinder of the telescope. However, we are highly confident to achieve the target temperature variation, less than 10°C, by thermally combining the divided lens by the metallic frame and ring, and by making effort in designing to reduce the heat conduction between MLI of the external cylinder of the telescope.

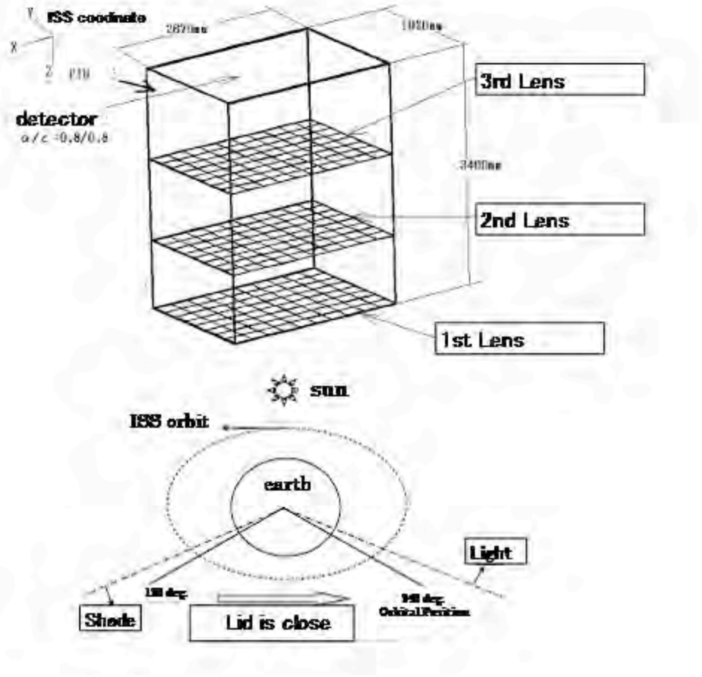

Figure A-3. *Model of JEM-EUSO and observation time.*

Furthermore, assuming the SiPM detector, the necessary quantity of heat dissipation to keep the sensor surface less than -15°C, dissipating the generated heat by the electric devices associated with the detector, was at maximum around 100 W with the lid, and at maximum 350 W without the lid. In this analysis, we considered that there was only MLI on the sensor surface, and that the thermal input around 50 W caused by the heated MLI by the radiation to the sensor surface, is included. Thus, if we succeed in making the design to insulate heat flow between the sensor surface and the MLI, we estimate that the necessary quantity of the heat dissipation will be maximum around 50 W with the lid, and around 300 W without the lid. If we cool the sensor surface till -15°C with the Peltier device, and dissipate the heat to ATCS, the necessary electric power to cool using the Peltier device will be about 2.7 times of the necessary heat dissipation. So we estimate the necessary electric power to keep the sensor surface -15°C, to be around 135 W maximum with the lid, and around 800 W maximum without the lid. All the above results show the efficacy of the lid. Moreover, we also understand that the thermal impact in case of lid trouble is large. Fig.A-4 shows the not homogeneities of each lens from the temperature point of view.

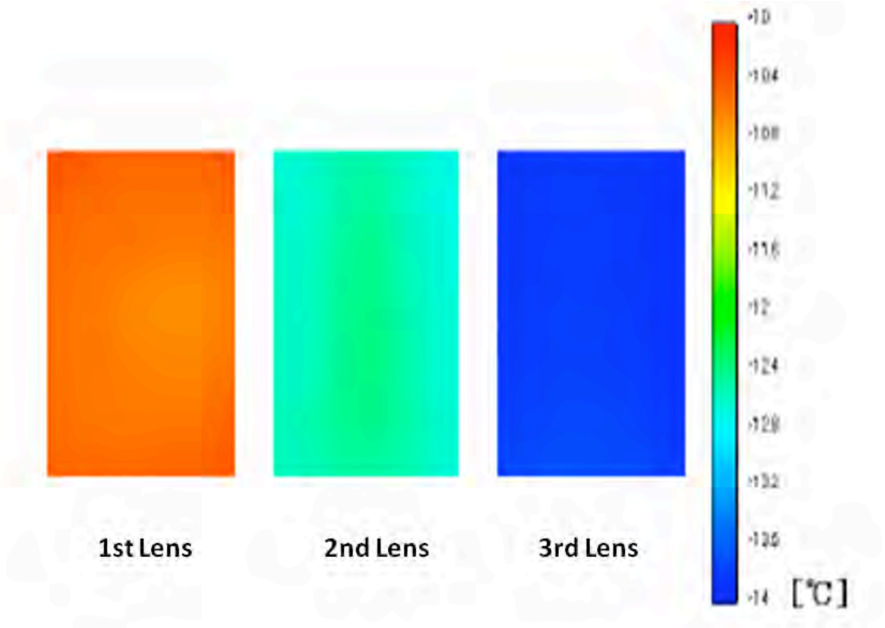

Figure A-4. *Contour of lens temperature (b=0°, with opening/closing of the lid).*

Annex B – Recommendations by International Advisory Board

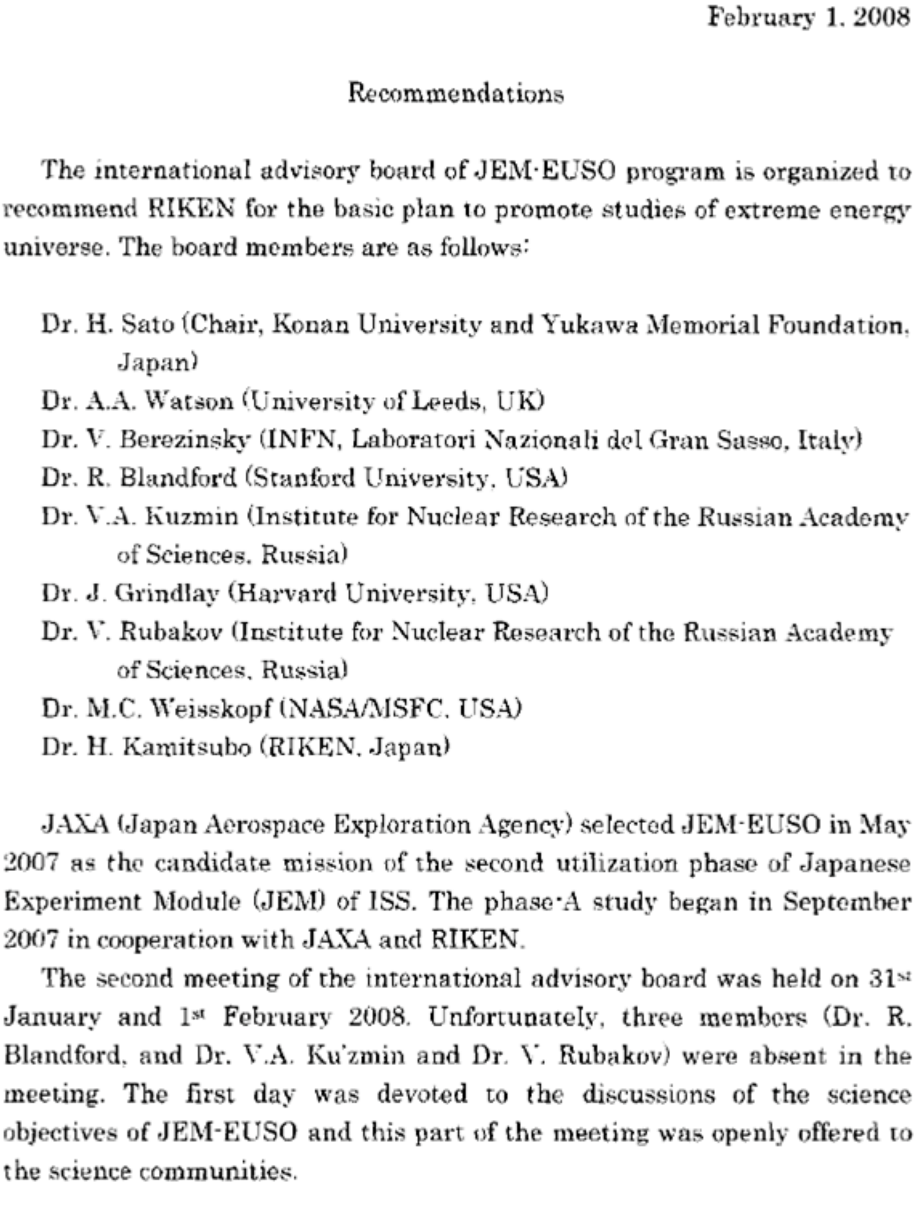

February 1. 2008

Recommendations

The international advisory board of JEM-EUSO program is organized to recommend RIKEN for the basic plan to promote studies of extreme energy universe. The board members are as follows:

Dr. H. Sato (Chair, Konan University and Yukawa Memorial Foundation, Japan)
Dr. A.A. Watson (University of Leeds, UK)
Dr. V. Berezinsky (INFN, Laboratori Nazionali del Gran Sasso, Italy)
Dr. R. Blandford (Stanford University, USA)
Dr. V.A. Kuzmin (Institute for Nuclear Research of the Russian Academy of Sciences, Russia)
Dr. J. Grindlay (Harvard University, USA)
Dr. V. Rubakov (Institute for Nuclear Research of the Russian Academy of Sciences, Russia)
Dr. M.C. Weisskopf (NASA/MSFC, USA)
Dr. H. Kamitsubo (RIKEN, Japan)

JAXA (Japan Aerospace Exploration Agency) selected JEM-EUSO in May 2007 as the candidate mission of the second utilization phase of Japanese Experiment Module (JEM) of ISS. The phase-A study began in September 2007 in cooperation with JAXA and RIKEN.

The second meeting of the international advisory board was held on 31st January and 1st February 2008. Unfortunately, three members (Dr. R. Blandford, and Dr. V.A. Ku'zmin and Dr. V. Rubakov) were absent in the meeting. The first day was devoted to the discussions of the science objectives of JEM-EUSO and this part of the meeting was openly offered to the science communities.

Based on the discussions in this 2nd meeting, we recommend the following.

1) Science Objectives

JEM·EUSO will be the first space observatory to detect air showers induced by the extreme energy cosmic-rays. It is designed to detect, in a few years of operation, more than a few thousands of events with energy greater than 7× 10^{19}eV. This number exceeds the critical value to observe all the sources at least once within one hundred Mpc even when the Greisen·Zatsepin·Kuzmin (GZK) suppressions at work. Hence, JEM·EUSO is very likely to initiate a new astronomy with these charged particles (10^{19}eV<E<10^{21}eV). Because they are deflected by only several degrees by galactic and extragalactic magnetic fields, these extreme energy particles can be traced back to the origin in the measured arrival direction, just like in the usual astronomy with photons. A sign of the spatial small-scale clustering of the events was also reported by AGASA. On November 9, 2007, the Pierre Auger Observatory reported the likely small-scale correlation of the arrival directions of 27 cosmic-rays with the positions of nearby active galactic nuclei (AGNs) and also, a mid-scale clustering around Cen·A. Details of the new observation by the Pierre Auger Observatory are reported by one of its leading members (AW) and discussed in the meeting. The board concludes that this important result of the Pierre Auger Observatory strongly supports the main objectives of JEM·EUSO which has an exposure per year about 60 times larger than that of the Pierre Auger Observatory.

One of the board members (VB), at this meeting, presented the predictions of neutrino flux based on various conventional and unconventional physics in this meeting. According to his report, JEM·EUSO has an ability to detect the predicted neutrino fluxes for many models and in the negative case to set significant constraints.

In conclusion, the board approved the soundness and compelling nature of the science objectives of JEM·EUSO and recommends the executive committee to keep the efforts along this line.

2) International Collaborations

JEM·EUSO has been promoted by international collaborations among ten countries: those are Japan, USA, France, Italy, Germany, Mexico, Republic of Korea, Russia, Spain, and Switzerland. Organizational structure and role-sharing among international partners are appropriate, beside the part of software development. The board recommends to executive committee to strengthen the software development of both on-board electronics and analysis in ground.

3) Organization in RIKEN

RIKEN, as the PI institution, is expected to perform the major role and contribution to the JEM-EUSO mission, in cooperation with JAXA, NASA, and all other member institutions. The designs, productions, integrations, and verifications of the parts of the telescope will be carried out by many institutions, individually and cooperatively, and in parallel to other sub-systems. RIKEN has an obligation and ability to promote such an international collaboration project: it has a great heritage of successful promotion of several major international projects. RIKEN-RAL laboratory and RIKEN-BNL center are such examples. The board believes that a central organization for the common ground is necessary to be established in RIKEN so that all the participants and the community to get together and to bring in their contributions. It is most desirable to include the world experts of various related fields to make the frontier of extreme universe science synergistically very effective and productive.

Ohmori Material Fabrication Laboratory has unequaled technologies for the precise fabrication of optical devises in world wide. The advisory board believes that their contribution is essential for the manufacturing of optics of JEM-EUSO.

MAXI (Monitor of All-sky X-ray Image), being developed and fabricated under the collaboration among JAXA, RIKEN, Osaka University, Tokyo Institute of Technology, and Aoyama Gakuin University, Nihon University, and Kyoto University will explore the all-sky energetic sources, via nearly continuous coverage of a large fraction of the entire sky in X-rays; it will be launched in early 2009 as the first phase mission of JEM-EF and its hardware is presently near completion. MAXI will be operated for several years after the launch. From both technical and scientific aspects, the heritage of MAXI, as the preceding mission for exploration of the energetic universe, is critically important to the successful completion of the JEM-EUSO mission. Furthermore, one of the members (JG) pointed that the objectives of MAXI includes the monitoring of time variation of AGNs which are the promising candidates of the origin of the EECRs. The board recommends that JEM-EUSO team may strengthen their cooperation with the RIKEN MAXI members, for synergetic evolution of pioneering studies of extremely energetic universe.

Dr. H. Sato

H. Sato

Dr. J. Grindlay

Dr. A. A. Watson

Dr. M.C. Weisskopf

Dr. V. Berezinsky

Berezinsky

Dr. H. Kamitsubo

上坪宏道

Annex C – Research Advancement Group of Extreme Space

(As of July 1st, 2008).

Group Head: Kazuo Makishima (Makishima Cosmic Radiation Lab., Chief Scientist)

(1) Cosmic X-ray Research Team

[Team Head: Kazuo Makishima Chief Scientist (Makishima Cosmic Radiation Lab.)]

Tatehiro Mihara	Senior Scientist (Makishima Cosmic Radiation Lab.)
Nobuyuki Kawai	Senior Visiting Scientist (Research Advancement Group of Extreme Space)
Atsumasa Yoshida	Visiting Scientist (Research Advancement Group of Extreme Space.)

(2) Optics Fabrication and Application Research Team

[Team Head: Hitoshi Omori Chief Scientist (Omori Materials Fabrication Lab.)]

Kazutoshi Katahira	Full-time Researcher (Omori Materials Fabrication Lab.)
Kouki Maekawa	Associate Visiting Researcher (Omori Materials Fabrication Lab.)
Yosuke Hachisu	Associate Visiting Researcher (Omori Materials Fabrication Lab.)

(3) Particle Astrophysics Research Team

[Team Head: Toshikazu Ebisuzaki Chief Scientist (Ebisuzaki Computational Astrophysics Lab.)]

Yoshiyuki Takizawa	Researcher (Ebisuzaki Computational Astrophysics Lab.)
Yoshiya Kawasaki	Associate Visiting Researcher (Ebisuzaki Computational Astrophysics Lab.)
Hiroshi Mase	Associate Visiting Engineer (Ebisuzaki Computational Astrophysics Lab.)
Fumiyoshi Kajino	Senior Visiting Scientist (Research Advancement Group of Extreme Space)
Naoya Inoue	Visiting Scientist (Research Advancement Group of Extreme Space)
Masahiro Teshima	Senior Visiting Scientist (Research Advancement Group of Extreme Space)
Masaki Fukushima	Senior Visiting Scientist (Research Advancement Group of Extreme Space)
Hirohiko Shimizu	Senior Visiting Scientist (EN'YO Radiation Lab.)

(4) Solid State Laser for Astronomical Observation Research Team

[Team Head: Satoshi Wada Research Unit Leader (Solid-State Optical Science Research Unit)]

Akinori Saito	Associate Visiting Researcher (Solid-State Optical Science Research Unit)
Takayo Ogawa	Associate Visiting Engineer (Solid-State Optical Science Research Unit)

(5) International Cooperative Propulsion Research team

[Team Head (adjunct): Yoshiyuki Takahashi (Prof. Department of Physics, Univ. of Alabama)]

Toshikazu Ebisuzaki	(Ebisuzaki Computational Astrophysics Lab., Chief Scientist)
Philippe Gorodetzky	(Astro-Particle and Cosmology Lab., Prof. Emeritus at CNRS)
Piergiorgio Picozza	(Istituto Nazionale di Fisica Nucleare (INFN), Prof. Univ. of Roma)
Andrea Santangelo	(Prof. Institute for Astronomy and Astrophysics, Univ. of Tübingen)
Il Hung Park	(Prof. Department of Physics, Ewha Womans Univ.)